UNIVERSITÀ DI PISA

Ion Acceleration by Solitary and Shock Waves Driven by Laser- Plasma Interactions

---

Scuola di Dottorato Galileo Galilei
Dipartimento di Fisica, E. Fermi
Largo Bruno Pontecorvo, 3, Ed. C
University of Pisa
56127 Pisa, Italy

Doctor of Philosophy
in
Applied Physics

January 3, 2013

Student:

Amritpal Singh Nindrayog

Academic Supervisors:

Prof. Francesco Pegoraro
Dr. Andrea Macchi

Contents

1 Introduction **6**
- 1.1 Background and motivation . . . 6
- 1.2 Particle acceleration with laser . . . 7
- 1.3 Solitary and Shock Waves in Plasma . . . 9
- 1.4 Layout of the thesis . . . 10

2 Laser Pulse Interaction with Overdense Plasma **12**
- 2.1 Outline . . . 12
- 2.2 Ultrashort Laser Pulse Amplification . . . 12
- 2.3 Electron Dynamics and Ponderomotive force in Non-relativistic regime . . . 14
- 2.4 Motion of electron in relativistic laser field . . . 17
- 2.5 Ponderomotive Force in Relativistic Regime . . . 19
- 2.6 Laser Interaction with plasma . . . 21
  - 2.6.1 Basic laser pulse parameters . . . 21
  - 2.6.2 Propagation of laser beam in plasma . . . 22
- 2.7 Collisional absorption . . . 24
- 2.8 Collisionless Absorption . . . 25
  - 2.8.1 Resonance Absorption . . . 26
  - 2.8.2 Brunel vacuum heating . . . 27
  - 2.8.3 Relativistic $\mathbf{j} \times \mathbf{B}$ heating . . . 29
- 2.9 Hot electron generation . . . 30

3 Laser-Driven Ion Acceleration **32**
- 3.1 Target Normal Sheath Acceleration (TNSA) . . . 33
  - 3.1.1 Introduction . . . 33
  - 3.1.2 Basic theoretical model . . . 34
- 3.2 Radiation Pressure Acceleration (RPA) . . . 36
  - 3.2.1 Hole-boring RPA: Thick targets . . . 37
  - 3.2.2 Light-sail Regime: Thin targets . . . 40
- 3.3 Shock Acceleration . . . 42

4 Electrostatic Solitons and Shock Waves in Collisionless Plasmas **45**
- 4.1 Waves in Unmagnetized plasma . . . 45
  - 4.1.1 Plasma Oscillations . . . 46
  - 4.1.2 Electron Oscillations in Warm Plasmas: Langmuir waves . . . 47
  - 4.1.3 Ion Acoustic Waves in Electron-Ion Plasma . . . 48
- 4.2 Nonlinear Effects on Ion Acoustic Waves . . . 50
  - 4.2.1 Nonlinear Plasma Oscillations . . . 51
  - 4.2.2 Ion Acoustic Solitary wave . . . 52
  - 4.2.3 Shock wave in Collisionless Plasma . . . 53

4.3 Nonlinear Wave Methodology . . . 54
4.3.1 Reductive perturbation method . . . 55
4.3.2 Sagdeev pseudo-potential method . . . 59
4.4 Particle reflection . . . 62
4.5 Landau Damping of Electrostatic Waves . . . 64
4.5.1 Electrostatic Ion Acoustic Waves and conditions for Landau Damping . . . 66
4.6 Particle Trapping . . . 67

5 Particle-In-Cell (PIC) Code 69
5.1 Introduction . . . 69
5.2 Basic Model Equations . . . 69
5.3 Lagrangian and Eulerian approach . . . 70
5.4 Numerical PIC Approach . . . 71
5.4.1 How the code works . . . 71
5.4.2 The Particle approach . . . 72
5.5 Numerical Algorithm . . . 74
5.5.1 The Discrete Model Equations . . . 74

6 Solitary versus Shock wave Acceleration in Laser Plasma Interactions 76
6.1 Introduction . . . 76
6.2 Simulation with Linear Polarization . . . 77
6.2.1 Solitary wave dynamics and ion acceleration . . . 77
6.2.2 Effects of the ion energy distribution . . . 80
6.2.3 SAW breaking in the expanding sheath . . . 81
6.2.4 Collective Oscillations of the Warm Plasma Foil . . . 82
6.2.5 Long pulse excitation: Multi-peak structures . . . 84
6.2.6 Effect of target density on ion dynamics and SAW generation . . . 86
6.2.7 Criterion for SAW or Shock generation versus Target density . . . 89
6.3 Simulation with Circular Polarization . . . 90
6.4 Test Particle Simulations . . . 92

7 Ion Temperature and Two-Dimensional Effects on the Formation of Shock and Solitary waves 95
7.1 1D PIC Simulations . . . 95
7.2 Simulation results for $a_0 = 4$ amplitude . . . 96
7.2.1 Proton Ion Simulations (Z/A = 1) . . . 96
7.2.2 Carbon Ion Simulations . . . 100
7.3 Simulation Results for $a_0 = 1$ amplitude . . . 102
7.3.1 Warm ion simulations . . . 102
7.4 2D Simulation Results . . . 104
7.5 Simulations with Circular Polarized Pulses . . . 106

8 Conclusion and Future work 109
8.1 Conclusion . . . 109
8.2 Future work . . . 110

Bibliography 111

Abstract

This thesis presents a theoretical study of the interaction of intense, ultrashort laser pulses with overdense plasmas. Main objectives are to understand the basic phenomenon which leads to the formation of non-linear electrostatic coherent wave structures in form of either solitary ion acoustic waves (SAW) or collisionless shock waves (CSW). These different types of waves have been classified according to Sagdeev's theory and related formulas have been used for comparison with the numerical results. The particular focus is on the effect on ion acceleration, by means of ion refection by the moving electrostatic field associated to the shocks/solitons. An extensive numerical study by 1D PIC simulations has been performed and in particular the differences arising between linearly polarized pulses and circularly polarized pulses have been discussed. In a cold plasma, ion bunches produced by "hole boring" (HB) radiation pressure acceleration at the target surface may propagate in the bulk as solitary waves. The acceleration mechanism of these ion bunches has been discussed pointing out a distinction between shock acceleration (SA) and HB acceleration, also with respect to some recent experimental results. Stability of (SAW) or (CSW) and ion reflection from them has been found to be strongly dependent on the initial velocity distribution of ions. The effect of both the ion and the electron temperature on the generation and evolution of solitary acoustic waves have been discussed.

CHAPTER 1

Introduction

1.1 Background and motivation

Lasers are one of the most significant inventions of the twentieth century. Since the invention of laser in 1960 [1], lasers are continuously gaining importance in the field of plasma physics. Up-to now, this technology has been vastly improved, from powerful lasers for industrial purposes to spectrally narrow banded continuous wave lasers for microscopic measurements of fundamental constants. When laser made its debut in 1960, at that time different groups across the world were working to understand the behavior of matter in the presence of an external applied field. Lasers invention comes as an excellent source to boost up these studies to a new level. The invention of pulse amplification of lasers opened many excited research opportunities in the field of laser-matter interactions. The first enhancements in the laser intensity of the order of $10^{15}\mathrm{Wcm}^{-2}$ were feasible at the end of the $1970\mathrm{s}$ by the $\mathrm{Q}-$switching and mode locking experiments which provide high peak power in nanosecond or picosecond duration pulses. The last three decades have witnessed an outstanding progress in the development of ultrashort laser pulses and many multi-disciplinary fields of ultra-fast science phenomenons.

A major dramatic breakthrough in 1985, with the invention of chirped pulse amplification technique (CPA) [2] have led to the advent of new solid-state laser sources that can deliver very short pulses of few tens of femtosecond (fs) which opened up many innovative opportunities in the domain of ultrashort ultra-intense laser physics. These ultrashort laser pulses allow to reach very intense fields and provide a strong increase in obtainable peak power. For example: a laser pulse of $100\mathrm{mJ}$ and a pulse duration of $100\mathrm{fs}$ corresponds to a peak power of $1\mathrm{TW}$ $(10^{12}\mathrm{W})$, when focused to a $10\mu\mathrm{m}$ diameter, it gives us an intensity $\simeq 5\times10^{18}\mathrm{Wcm}^{-2}$ at the focus. Thus ultrashort laser pulses can deposit a certain amount of energy in a very short interval of time and opens many innovative approaches in laser matter interactions which are complex but very enrich in physics. Up-to now, over the past 10 years, laser intensities have increased by more than four orders of magnitude and reached up-to $10^{21}\mathrm{W}/\mathrm{cm}^2$ while pulse durations have shortened below 10 femtosecond [3]. The field strength at these intensities is of the order of teravolt/cm which is 100 times the Coulomb field that binds the electrons to the nucleus.

Therefore, it is now possible to create solid - density plasmas within a fraction of laser cycle by ultrafast ionization and to study the laser interactions with plasmas in a regime where electrons oscillate at relativistic velocities in the laser field. Due to the extreme light pressure $\mathrm{P}=2\mathrm{I}/\mathrm{c}$ of the order of giga- to terabar at the relativistic laser intensities, leads to a variety of novel and highly nonlinear phenomenons which are of great interest for basic physics as well as for a number of scientific applications such as high-order harmonics, electron and ion acceleration, X-ray and particle sources, in thermonuclear inertial confinement fusion and in ultrafast optical devices. So the development of new diagnostic techniques has marked a turning point for the comprehension of a variety of non-linear effects and provide direct informations on distributions of density and fields during the interaction.

1.2 Particle acceleration with laser

Depending upon the laser and plasma parameters, the sub-field of the particle acceleration can be divided into two domains of laser matter interactions. It was realized in 1979 by Tajima and Dawson [4] that a laser pulse propagating in a plasma can excite electron plasma waves which being longitudinal can be used to accelerate particles within the plasma. Thus plasma based particle acceleration opened an exciting field of extreme gradient beyond $1\mathrm{TV/m}$ and with the present advances in laser technology having available laser intensities of $10^{21}\mathrm{W/cm^2}$, electrons can be accelerated up-to GeV energies. An electromagnetic pulse interacting with a plasma is termed as relativistically intense when its intensity is so high that the velocity of the electrons oscillating in the transverse field of the pulse approaches the velocity of light. The required intensity for this regime is $\sim 10^{18}\mathrm{W/cm^2}$ for a pulse wavelength of $\lambda = 1\mu\mathrm{m}$. When the relativistically electromagnetic pulse interacts with a plasma, strong nonlinear effects come into play [5, 6]. As at such high intensities, the quiver velocity of electrons becomes comparable to the velocity of light and the effect of relativistic mass increase becomes significant such that $m_{\text{eff}} = \gamma m_e$ where $\gamma = 1/\sqrt{1 - \mathbf{v}_q^2/c^2}$, $\mathbf{v}_q$ is the quiver velocity of electrons.

On the contrary, ions can be efficiently accelerated up-to several tens of mega electron-volt per nucleon ($\sim \mathrm{MeV}$) energies with the interaction of short ($< \mathrm{ps}$) laser pulses of intensity $\mathrm{I}\lambda^2 > 10^{18}\mathrm{W/cm^2}$ with overdense plasma and is one of the active areas of research in the past few years. Ions, because of their higher inertia than electrons, are not directly driven by the laser pulse and mostly relies on the generation of the hot electrons. There are several mechanisms feasible at current accessible laser intensities which lead to forward acceleration of high quality ion beams due to the generation of large electric fields set by the laser accelerated electrons at the target interface. Ions having energies up-to several MeVs had been observed in several high intensity laser matter interaction experiments with different targets [7, 8, 9]. The isotropic ion emission with low brilliance in these experiments are not so attractive as ion accelerators for applications. In the year 2000, some experimentalists [10, 11, 12] observed an intense emission of multi$-\mathrm{MeV}$ protons from solid targets irradiated by high intensity laser pulses. The outstanding characteristics of laser accelerated proton beams with high degree of collimation and beam laminarity were quite impressive and generated an enormous interest both in fundamental research and in the potential possible applications. The findings of forward proton emission of multi$-\mathrm{MeV}$ energy triggered discussions for their applications as ion source for the injection into conventional particle accelerators[4]. An important application proposed for laser driven protons is to employ them in radiation therapy as the protons or light ions, differently from electrons or $\mathrm{X}-$rays deliver most of their energy at the end of their path at the so called Bragg peak[13]. Due to their large mass, protons have little lateral side scatter in the tissue, the beam does not broaden much and stay focused on the tumor shape, delivering small dose side effects to the surrounding tissues. The second physical reason is that energy loss is dominated by coulomb collisions for which the cross section strongly grows with decreasing energies such that the stopping process becomes progressively more and more efficient. This property of protons and ions makes them suitable for highly localized energy deposition and give an edge to their role in several potential applications such as ion beam cancer therapy, laser triggering and control of nuclear reactions, fast ignition of Inertial Confinement Fusion targets and production and probing of warm dense matter.

While the potential role of protons in so many applications was apparent, the details of the physics behind the proton acceleration up-to $\sim \mathrm{MeV}$ energies were not clear. A debate arose on the actual location of the region where the protons were accelerated and consistently, on the mechanism driving the acceleration. To support the experiments[10, 11, 12] performed in year 2000, Wilks *et al.*[14] introduced the theoretical interpretation of proton acceleration with so called Target Normal Sheath Acceleration

(TNSA) model. According to TNSA model, the ions get accelerated due to the space-charge field generated at the rear side of the target by highly energetic "fast" electrons accelerated at the target front surface, crossing the target bulk and escape in vacuum from the rear side. A brief discussion about TNSA mechanism is described in sec.3.1 of Ch.3. Although the TNSA generated proton beams are highly laminar and of very low emittance, their broad energy spectrum is not optimal for most potential applications. Hence this issue motivates the search of other ion acceleration mechanisms.

The other important mechanisms for ions acceleration which have been explored previously in astrophysics context includes the radiation pressure acceleration (RPA) and collisionless shock acceleration (CSA). These two mechanisms RPA and CSA are attracting a substantial amount of experimental and theoretical attention due to the predicted superior scaling in terms of laser-ion conversion efficiency and monoenergetic ion acceleration. According to RPA, a highly intense electromagnetic wave carries strong momentum which may be delivered to a non-transparent (absorbing or reflecting) target. RPA is related to the generation of steady ponderomotive force (PF) which acts inversely to particle mass. At the surface of an overdense plasma, the electrons due to their lighter mass than ions, get strongly pushed inwards by the PF, creating an electrostatic, back-holding charge separation field which in turn accelerates the ions by delivering the EM wave momentum. While on the other side, according to CSA mechanism, the strong intense laser pressure, pushes and compresses the target inwards at nearly relativistic speeds and such a strong compression and acceleration may lead to generation of strong nonlinear collisionless shock waves which further may accelerate ions during propagation within the plasma bulk. A detailed discussion about the RPA and CSA mechanism have been reported in Ch.3. Since the above defined RPA and CSA may have similar ion energy spectrum and makes it difficult to distinguish the related ion acceleration. Therefore simple analytically affordable models are extremely useful to understand and distinguish these basic acceleration mechanisms. We will show by numerical PIC simulations that CSA does lead to acceleration of ions in the bulk while RPA which actually occurs at the target front surface does not accelerate ions within the bulk.

Now considering a linearly polarized laser and define the normalized amplitude a_0 of the laser vector potential as

$$a_0 \equiv \frac{\mathbf{p}_q}{m_e c} = \frac{e\mathbf{E}_{\text{L}}}{m_e c \omega_{\text{L}}} = 0.85(I_{18}\lambda_\mu^2)^{1/2}. \tag{1.1}$$

where $\mathbf{p}_q$ is the quiver momentum of electrons and $\mathbf{E}_{\text{L}}$ is the laser electric field. The dimensionless parameter a_0 is frequently used to characterize the importance of relativistic effects. When $\text{I}_{18}\lambda_\mu^2 > 1.4$ we have $a_0 > 1$ and electrons oscillate at relativistic velocities. This leads to relativistic effects which modify the propagation of the EM laser wave in a plasma[15, 16]. Consequently, the propagation of such relativistic intense laser pulses is allowed even in the overdense plasmas. The motion of electron in electromagnetic field is determined by the Lorentz force ($-e[\mathbf{E} + \mathbf{v} \times \mathbf{B}]$). An electron irradiated by a laser pulse with $a_0 \ll 1$ performs harmonic oscillation transverse to the laser propagation. For $a_0 \geqslant 1$, due to the effect of the magnetic term $\mathbf{v} \times \mathbf{B}$, the force becomes nonlinear and the electrons oscillate along the laser direction. Due to the shape of the pulse, the effective electron mass and therefore the effective electron plasma frequency ($\omega_{\text{eff}} = \omega_p/\sqrt{\gamma}$) gain a intensity dependence and as a result, the interaction gets highly nonlinear. Nonlinearity is a fascinating element of nature whose importance has been appreciated for many years when considering large amplitude wave motions observed in various fields, *e.g.,* fluids and plasmas, astrophysics, particle physics, laser plasma interactions *etc.* The nonlinearity which arises through the generation of higher order harmonics at different frequencies[17], the nonlinear Lorentz force and the ponderomotive force etc., is the source of many physical phenomenons such as relativistic plasma transparency, laser pulse self focusing [18], excitation of nonlinear plasma waves and the generation of coherent electrostatic structures such as solitary waves, shock waves and

vortices etc[19, 20].

1.3 Solitary and Shock Waves in Plasma

Localized large amplitude waves called solitons or solitary waves[21] which propagate in a medium without spreading and have particle like properties, represent one of the most striking aspects of nonlinear phenomenons. Nonlinear effects play an important role to undergo steepening of the leading edge of the wave. It is frequently found in plasma dynamics that the dispersion effects become significant as the steepness of the wave front increases. With this nonlinear deformation, the portion of the wave profile characterized by high velocities tend to overtake the portion characterized by low velocities such that a discontinuity is ultimately formed which lead to wave steepening. In the system of wave equations, the nonlinearity, i.e., the dependence of the behavior of the wave packet on its amplitude and the generation of high order harmonics with large wave numbers, can enhance dissipation or trigger instabilities of the wave packets. Solitary waves are formed due to the balance between the effect of nonlinearity and the dispersion (when dissipation is negligible). The study of solitary waves is important to understand the particle or energy transport mechanisms in plasmas and plays an important role in the wide spectrum of research related to nonlinear plasma physics [22]. In general, it is possible for a high intensity laser to excite nonlinear plasma waves and by this transfer energy into the plasma. The solitary waves in plasmas are interesting localized wave modes, occur in the form of modulated wave packets in the form of electrostatic [23] or electromagnetic solitons [24] nonlinearly coupled to the space charge fields. These nonlinear structures can be created in the laboratory or externally launched in laboratory plasma under control conditions. However, if the dissipative effects are comparable to or dominant over the dispersion effects, the shock wave may generate within the system.

Solitary waves are formed in laser-plasma interactions when the laser ponderomotive pressure depletes the local electron density which get accumulated at the two edges and provide the trapping of electromagnetic radiations in the form of a soliton. Inside the soliton, due to the variation in the amplitude of the pulse, the ponderomotive force (nonlinearity) sustains the space charge field (dispersion). Such envelope soliton structures provide the mechanism for the penetration of intense laser pulses into an overdense plasma[25] and can be considered as a solution for transporting laser energy deep into the overdense regions. The solitons propagate with relativistic velocities, can be extremely useful for the charge particle acceleration [4]. A detailed description about the solitary waves in relativistic laser plasmas and the balance between the nonlinearity and dispersion by the complex set of nonlinear partial differential equations has been reported in $\mathrm{Ch.4}$

The other nonlinear structure which we observe in our numerical simulation is a shock wave. A shock wave in a broad sense is a transition layer which causes a change in the state of the plasma and which is stationary (on the average) in time in its reference frame. In laboratory plasma, the transition layer generally propagates through the plasma, changing the plasma state as it flows. Historically, the first study about the shock formation have been carried out by Ernest Mach in a gas dynamics. Mach observed in his experiment that when the relative velocity v_{rel} between the fluid and the obstacle (e.g bullet) reached the range of values for which the the ratio with the sound speed (c_s) was greater than one; *i.e*, when Mach number $\mathrm{M} = v_{\text{rel}}/c_s > 1$ (i.e. supersonic), a discontinuity appeared in density, velocity and temperature in the spatial region close to the obstacle. In this case the flow is too fast for the disturbances generated by the obstacle to propagate large distances upstream and we call it that the flow is shocked. In collision dominated plasmas, the density rise across a shock occurs in a distance of the order of few collision mean free paths (λ_{coll}) while in a collisionless shock, the thickness over which the shock occurs can be much larger. The attention here will be focused on the collisionless shocks (CS)

which results in particle acceleration, in order to develop an useful theoretical framework for interpreting the numerical simulation results illustrated in Ch.6 and Ch.7.

In laboratory experiments, first evidence of CS waves had been reported in 1965[26], since then the research on this topic has developed into its own discipline. In the theoretical investigation of laminar CS waves which have been first proposed by Sagdeev in his review paper[27], dispersion limits the nonlinear steepening of the wave and a trailing or leading edge wave train is generated. Dissipation can enter by few processes such as particle reflection and particle trapping, which leads to damping of the wave train. For small Mach number shocks, the kinetic theory of laminar shock waves is fairly complete[27, 28] and insights many microscopic physics processes taking place during collisionless shock formation. Later, the insight into the CS waves formation and the introduction of the equivalent Sagdeev pseudo-potential method clarified many open points and determined the direction of future shock research. Nowadays electrostatic collisionless shocks can be generated by laser produced hydrogen plasma and is the area of high interest at the moment because of monoenergetic ion acceleration from the collisionless shock waves. A detailed discussion about generation of collisionless shock wave and the related ion acceleration have been performed in Ch.3 and Ch.4.

1.4 Layout of the thesis

This PhD dissertation is a report of numerical study of nonlinear electrostatic wave generation (solitary and shock waves) and ion acceleration with high intensity lasers. The work described in this thesis has been carried out in Plasma Physics group, University of Pisa, led by Prof. Francesco Pegoraro. The purpose of the numerical study performed in the field of laser-overdense target interaction is to study the generation of nonlinear solitary and collisionless shock waves in plasma and to understand the physics behind the monoenergetic ion acceleration. The thesis is structured as follows.

Chapter-2: Provides an introduction about the laser pulse propagation and interaction with overdense plasma. Electron dynamics and its acceleration with ponderomotive force in the non-relativistic as well as in relativistic regime have been described. The various regimes of laser pulse absorption in plasmas at low, moderate and at relativistic intensities are discussed.

Chapter-3: Three important ion acceleration mechanisms, i.e Target Normal Sheath Acceleration (TNSA), Radiation pressure acceleration (RPA) and Collisionless Shock Acceleration (CSA) are discussed.

Chapter-4: A linear analysis of ion acoustic waves followed by the nonlinear analysis of ion acoustic solitons and shock waves are discussed. A general description of solitons and shock waves in plasmas is provided. Reductive perturbation and Sagdeev pseudo-potential method are explained to find out solutions of occurrence of ion acoustic solitons and collisionless shocks. Particles reflection, particle trapping and damping of the electrostatic solitary waves have been explained.

Chapter-5 A brief study about Particle in cell method is presented in this section. The simulation code PHIC (based on the PIC method) is used throughout this work and is described in detail by putting into the context of other simulation codes and methods.

Chapter-6 1D PIC Simulation results of solitary and shock wave generation by linear polarized laser interaction with overdense target are presented in this section. Role of initial ion distribution in generation of these nonlinear electrostatic waves have been discussed. Circular polarized simulations have been discussed to explain the role of pulse polarization and the role of electron temperature in generation of collisionless solitary and shock waves. Test particles simulations are performed to distinguish the hole-boring HB − RPA and collisionless shock acceleration mechanism.

Chapter-7 Role of initial ion distribution in collisionless shock stability and related monoenergetic ion acceleration has been discussed for linear polarized pulses at moderate intensities of $10^{18} - 10^{19}\mathrm{W/cm^2}$. 2D PIC simulations have been performed to understand the shock deceleration and related instabilities. Role of initial electron temperature and generation of non-linear electrostatic perturbation in form of solitons and shock waves for the circular polarized pulses have been prescribed.

Chapter-8: The main results of this work are summarized and our conclusions and prospects for the future work are presented in this chapter.

CHAPTER 2

Laser Pulse Interaction with Overdense Plasma

2.1 Outline

A large variety of nonlinear phenomenons occurs during the laser-matter interaction which modifies the matter physical parameters and effects the further laser interaction with matter. Analyzing the laser-matter interactions, one has to consider a number of physical processes that occur within the matter under the influence of the electromagnetic (EM) fields generated by the laser pulse. Depending on the laser pulse parameters (*i.e.* pulse profile, duration and intensity etc.), the laser induces many processes on the front side of target such as surface melting, evaporation, ablation and ionization which fundamentally effects the laser pulse propagation and the physics of the laser energy transfer to the target. The laser pulse may encounter either a very steep density gradient by interacting directly with an almost undisturbed overdense target or an extended region of the underdense preplasma formation, where the pulse interact firstly with the free electrons over a long distance and excite strong plasma waves and instabilities [29].

In this chapter, we focused on the certain fundamental aspects and on the main physical parameters which characterize the laser-matter interactions. Section 2.2 is devoted to the physics and technology concerned with the amplification of ultrashort laser pulses triggered by chirped pulse amplification. In ultrashort laser pulse interactions, the electrons are the main energy carriers. So the dynamics of free electron both in the non-relativistic as well as in relativistic laser field will be described in section 2.3 and 2.4. The phenomenon of ponderomotive acceleration for non-relativistic and relativistic regimes will be discussed in section 2.3 and 2.5 respectively. In the section 2.7 and 2.8, we will review a few major absorption mechanisms to the laser-overdense plasma interaction.

2.2 Ultrashort Laser Pulse Amplification

The development of compact table-top tera-watt laser systems delivering intense, ultra-short pulses relies on the major advancement in technology of chirped pulse amplification (CPA) developed in mid eighties [2, 30]. The CPA technique was originally developed for the microwave devices (*e.g.* radars) to overcome the power limitations of radars[31]. In 1985, it was realized by Mourou and his group[2], that CPA technique can also be applied to optical domain for laser science technology and the first CPA laser was successfully demonstrated in 1988[30]. Since then this technique has been extensively used by applying to many conventional master-oscillator-power-amplifier (MOPA) laser systems in which a small prototype laser pulse is passed through a chain of optical power amplifiers. A simple schematic of CPA laser system is shown in Fig. 2.1

A modern CPA laser consists of the following main parts: femtosecond oscillator, stretcher, amplifier, compressor and focusing system. In a CPA laser system, a short laser pulse is first stretched to a much longer duration by means of strongly dispersive “stretcher or expander” (i.e. a grating pair). In the

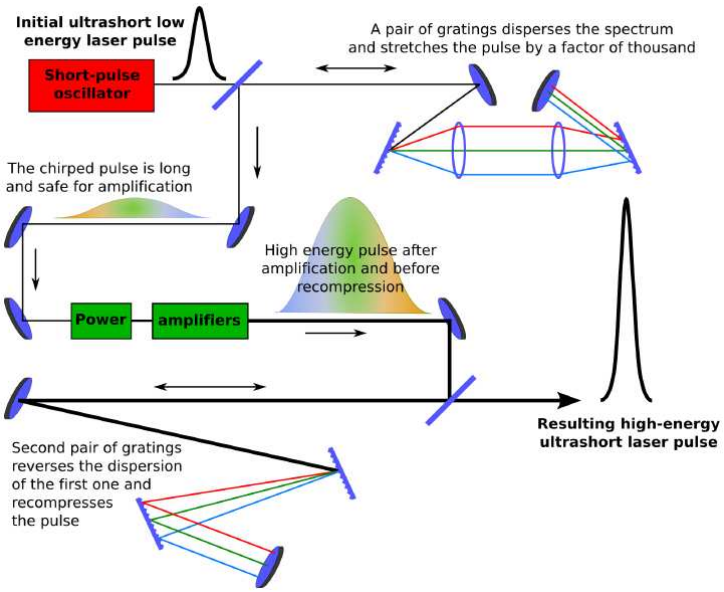

Figure 2.1: Schematic of CPA system, indicating pulse width and intensity at different stages of amplification. In a first step, the short pulse generated by oscillator get stretched by a pair of gratings. The stretched pulse then get amplified by various acceleration stages, before it enter the final mixed glass amplifier. At the end, the pulse get re-compressed by another pair of gratings. Reprinted from [32].

stretcher, the gratings are arranged in such a way that the low frequency component of the laser pulse travels a shorter distance than the high frequency component. The pulsed get stretched in time by several order of magnitude without the loss of bandwidth. An expanded pulse has its frequency changing with time so called as a "chirped" pulse. The term "chirped" came from the radar technology where it was used earlier for pulse manipulation. After the passage from stretcher, the laser pulse becomes positively chirped[1] and has longer duration than the original one by factor of $10^3 - 10^5$. The chirped pulse has an increased pulse width and hence a low peak intensity. The intensity of the stretched pulse is sufficiently low and is suitably safe to introduce this pulse into the gain medium to amplify it by a factor of 10^6 or even more. After the gain medium, the amplified pulses passes through the dispersive "compressor", an element having opposite dispersion to stretcher. This compressor provides a negative chirp of the same order to compensates for the positive chirp introduced by a stretcher and re-compresses the pulse temporally to a duration similar to the input pulse. After passing through the compressor, consequently a very high intensity pulse, having peak power of the order of $\sim \mathrm{terawatt(TW)}$ values is obtained.

Thus CPA technique makes it possible to achieve very high peak power lasers and to miniaturize the laser systems to build them on a tabletop. In order to use this scheme, it is necessary to stretch and then re-compress the pulse without the loss of bandwidth and without distortion. The most advanced CPA lasers are built on the basis of Ti:sapphire and Nd:glass. The solid state Ti:sapphire laser has many advantages over the dye-based laser of earlier generation such as large lasing bandwidth, very good thermal conductivity and excellent mechanical properties. The development of ultrashort high intensity lasers and the state of the art techniques used for generation and amplification of these lasers is beyond the scope of the present work and detailed information can be found in these review papers [33, 34, 35].

[1] A laser pulse is called positively chirped if lower frequency light travels ahead of higher frequency light and is negatively chirped if opposite holds.

2.3 Electron Dynamics and Ponderomotive force in Non-relativistic regime

Considering the motion of free electron in a plasma under the influence of plane, monochromatic electromagnetic wave, the spatial and temporal electric ($\mathbf{E}$) and magnetic ($\mathbf{B}$) field components are described as

$$\mathbf{E}(\mathbf{r},t) = \mathbf{E}_0 \cdot \cos(\omega t - \mathbf{k}\cdot\mathbf{r}) \tag{2.1}$$

$$\mathbf{B}(\mathbf{r},t) = -\frac{1}{\omega}\cdot\nabla\times\mathbf{E}(\mathbf{r},t) = \mathbf{B}_0\cdot\sin(\omega t - \mathbf{k}\cdot\mathbf{r}) \tag{2.2}$$

where ω is the angular laser frequency in the plasma and $\mathbf{k}$ is the propagation vector. The dynamics of the free electron motion under the influence of electromagnetic fields is governed by the Lorentz force, $\mathbf{F} = -e\cdot(\mathbf{E} + \frac{\mathbf{v}_e}{c}\times\mathbf{B})$. From the Newton's second law, the electron equation of motion for a non-relativistic case reads as

$$\frac{d\mathbf{p}_e}{dt} = m_e\frac{d\mathbf{v}_e}{dt} = -e\cdot\left[\mathbf{E}(\mathbf{r},t) + \frac{\mathbf{v}_e}{c}\times\mathbf{B}(\mathbf{r},t)\right], \quad \text{where} \quad \mathbf{v}_e = \frac{d\mathbf{r}}{dt} \tag{2.3}$$

where $\mathbf{v}_e$ and $\mathbf{p}_e$ represents the velocity and momentum of the electron. Now, in the linear and non-relativistic approximation, we neglect the magnetic field term, because for weak fields $|\mathbf{v_e}| \ll c$. Thus the linear equation of motion simplifies to

$$\frac{d\mathbf{p}_e}{dt} = m_e\frac{d\mathbf{v}_e}{dt} = -e\cdot\mathbf{E}(\mathbf{r},t) \tag{2.4}$$

Considering now the case of an laser electric field $\mathbf{E}(\mathbf{r},t)$ for a linearly polarized pulse, propagating along the $z-$axis (*i.e.* wave vector $\mathbf{k}$ = k $\hat{z}$). Assuming the initial electron position and velocity are $|\mathbf{r}_e(t=0)| = 0$ and $|\mathbf{v}_e(t=0)| = 0$ respectively, then the solution of the above Eq. (2.4) reads as:

$$|\mathbf{r}_e| = \mathrm{r}_q\cos(\omega t - \mathbf{k}\cdot z), \qquad |\mathbf{v}_e| = \mathbf{v}_q\sin(\omega t - \mathbf{k}\cdot z) \tag{2.5}$$

where r_q is the quiver amplitude of the electron excursion in the laser field and v_q is the oscillatory quiver velocity of the electron and is given by

$$\mathrm{r}_q = \frac{e\mathrm{E}_0}{m_e\omega^2} \qquad \text{and} \qquad \mathbf{v}_q = \frac{e\mathrm{E}_0}{m_e\omega} \tag{2.6}$$

The time averaged energy acquired by the electron as a result of this oscillatory motion is expressed in terms of the average kinetic energy over one laser cycle and is actually known as the ponderomotive potential or ponderomotive energy(will discuss below in detail): $\Phi_p = \langle\mathcal{E}_{\text{kin}}\rangle_{\mathrm{T}} = \langle\frac{1}{2}\mathrm{m_e}\mathbf{v}_e^2\rangle_{\mathrm{T}}$. The ponderomotive potential can also be expressed in terms of the laser electric field E_0 or laser intensity I as:

$$\Phi_p = \frac{e^2}{4m_e\omega^2}\cdot\mathrm{E}_0^2 = \frac{e^2}{2m_e\varepsilon_0\omega^2 c}\cdot\mathrm{I} \tag{2.7}$$

From above equation, the laser electric field strength and the laser frequency can be defined in practical units as,

$$\mathrm{E}_0 = \left(\frac{2\mathrm{I}}{\varepsilon_0 c}\right)^{1/2} \simeq 2.75\times10^{11}\cdot\sqrt{\mathrm{I}_{16}} \quad [\mathrm{V/m}] \tag{2.8}$$

$$\omega = \frac{2\pi c}{\lambda_{\mathrm{L}}} \simeq \frac{1.88\times10^{15}}{\lambda_{\mathrm{L}}(\mu m)} \quad [\mathrm{s}^{-1}] \tag{2.9}$$

where I_{16} is the laser intensity in terms of $10^{16}\mathrm{Wcm}^{-2}$. Taking into account the above dependencies, one can define in practical terms the quiver amplitude, quiver velocity and the ponderomotive potential as follows.,

$$\mathrm{r}_q = 13.7 \times \sqrt{\mathrm{I}_{16}}. \quad (\lambda_{\mathrm{L}}[\mu m])^2 \quad [nm] \tag{2.10}$$

$$\frac{\mathbf{v}_q}{c} = 0.086 \times \sqrt{\mathrm{I}_{16}}. \quad (\lambda_{\mathrm{L}}[\mu m]) \tag{2.11}$$

$$\Phi_p \approx 933 \times \mathrm{I}_{16}. \quad (\lambda_{\mathrm{L}}[\mu\mathrm{m}])^2 \quad [\mathrm{eV}] \tag{2.12}$$

For a laser pulse of wavelength $0.8\mu\mathrm{m}$ at intensity I_{16}, an electron has the ponderomotive energy around $\Phi_p \approx 0.6\mathrm{keV}$, the quiver velocity is $\mathbf{v}_q \approx 0.07\mathrm{c}$ and the quiver amplitude of the oscillatory motion is $\mathrm{r}_q \approx 9\mathrm{nm}$. When the ponderomotive potential Φ_p becomes comparable to the electron rest energy, *i.e.* $\mathcal{E} = \mathrm{m_e c^2} \approx 511\mathrm{keV}$, the relativistic approach of the electron is considered. For a laser pulse in the near-infrared and visible wavelength ranges, the relativistic regime for the electron starts at intensities larger than $\approx 10^{18}\mathrm{W/cm}^2$.

It is worth considering now the motion of electrons in the laser-matter interactions since they response quickly to the "realistic" electromagnetic field, gain energy from the wave and carry it further into the matter. However, to be more specific, laser pulses are not plane waves, but have finite width and duration. In general, a laser pulse will be described by an envelope function having its transverse and longitudinal profiles, multiply by an oscillating function. A general representation of the electric and magnetic fields of the laser pulse can be given in the form

$$\mathbf{E}(\mathbf{r},t) = \mathrm{Re}\left(\tilde{\mathbf{E}}(\mathbf{r},t)e^{-i\omega t}\right) = \frac{1}{2}\tilde{\mathbf{E}}(\mathbf{r},t)e^{-i\omega t} + \mathrm{c.c.}, \qquad \text{and}$$

$$\mathbf{B}(\mathbf{r},t) = \mathrm{Re}\left(\tilde{\mathbf{B}}(\mathbf{r},t)e^{-i\omega t}\right) = \frac{1}{2}\tilde{\mathbf{B}}(\mathbf{r},t)e^{-i\omega t} + \mathrm{c.c.}, \tag{2.13}$$

the envelope functions are supposed to vary with time on the slower time scale than the oscillating period $\mathrm{T} = 2\pi/\omega$. We assume that the fields are averages to zero over a period, i.e. $\langle \mathbf{E}(\mathbf{r},t)\rangle = 0$ while for the envelope function $\langle \tilde{\mathbf{E}}(\mathbf{r},t)\rangle \neq 0$. The assumption of two separate time scales describe the electron motion as the superposition of a slow term(denoted by subscript s) and a fast "oscillating" term (with subscript o) such as

$$\mathbf{r}(t) = \mathbf{r}_s(t) + \mathbf{r}_o(t), \qquad \langle \mathbf{r}_o(t)\rangle = 0, \qquad \langle \mathbf{r}_s(t)\rangle = \mathbf{r}_s(t) \tag{2.14}$$

It is possible under suitable conditions to describe the "slow motion" by a dynamic equation with slowly varying force known as the ponderomotive force and will study the motion of an "oscillating center" over which a fast oscillation is overlapped.[2]

We first derive the ponderomotive force in non-relativistic regime, keeping terms of the order $\sim \mathbf{v}_e/c \ll 1$ and then later discuss it in the relativistic regime. A crucial assumption is that the spatial variation of the field envelope across an oscillation is very small. Since the oscillation amplitude is less than $\lambda = 2\pi\mathrm{c}/\omega$, the scale of spatial variation of $\tilde{\mathbf{E}}$ will be sufficiently larger than λ. This assumption allows to expand the field as follows

$$\mathbf{E}(\mathbf{r}(t),t) = \mathbf{E}(\mathbf{r}_s(t) + \mathbf{r}_o(t),t) \simeq \mathbf{E}(\mathbf{r}_s(t),t) + (\mathbf{r}_o(t)\cdot\nabla)\mathbf{E}(\mathbf{r}_s(t),t) \tag{2.15}$$

[2]This is analogous to the guiding center approximation to study the electron motion in an inhomogeneous magnetic field which means that while rotating along the field lines with cyclotron frequency, the charge particle also get drifted slowly along these field lines.

The equations for the oscillating component of the lowest order are

$$\frac{d^2\mathbf{r}_o}{dt^2} = \frac{d\mathbf{v}_o}{dt} \simeq -\frac{e}{m_e}\mathbf{E}(\mathbf{r}_s(t),t) \simeq \frac{-e}{2m_e}\tilde{\mathbf{E}}(\mathbf{r}_s(t))e^{-i\omega t} + \text{c.c.}, \tag{2.16}$$

such that $\mathbf{r}_o = \text{Re}(\tilde{\mathbf{r}}_o e^{-i\omega t})$ and $\mathbf{v}_o = \text{Re}(\tilde{\mathbf{v}}_o e^{-i\omega t})$ where

$$\tilde{\mathbf{r}}_o = \frac{e}{m_e\omega^2}\tilde{\mathbf{E}}(\mathbf{r}_s(t)) \qquad \text{and} \qquad \tilde{\mathbf{v}}_o = -\frac{ie}{m_e\omega}\tilde{\mathbf{E}}(\mathbf{r}_s(t)) \tag{2.17}$$

Now by averaging the Newton's equation of motion we have[3]

$$m_e\frac{d\mathbf{v}_s}{dt} = -e\langle\mathbf{E}(\mathbf{r}(t),t)\rangle - \frac{e}{c}\langle\mathbf{v}\times\mathbf{B}(\mathbf{r}(t),t) \tag{2.18}$$

For the electric field average term we have

$$\begin{aligned}\langle\mathbf{E}(\mathbf{r}(t),t)\rangle &\simeq \langle\mathbf{E}(\mathbf{r}_s(t),t) + (\mathbf{r}_o(t)\cdot\nabla)\mathbf{E}(\mathbf{r}_s(t),t)\rangle \\ &= \frac{1}{4}(\tilde{\mathbf{r}}_o(t)\cdot\nabla)\tilde{\mathbf{E}}(\mathbf{r}_s(t),t) + \text{c.c} \\ &= \frac{e}{4m_e\omega^2}(\tilde{\mathbf{E}}(\mathbf{r}_s(t),t)\cdot\nabla)\tilde{\mathbf{E}}(\mathbf{r}_s(t),t) + \text{c.c}\end{aligned} \tag{2.19}$$

Similarly for the magnetic force term, we have

$$\langle\mathbf{v}\times\mathbf{B}(\mathbf{r}(t),t)\rangle \simeq \frac{1}{4}\tilde{\mathbf{v}}_o\times\tilde{\mathbf{B}}_o(\mathbf{r}_s(t),t) + \text{c.c} \tag{2.20}$$

Now by using $c\nabla\times\mathbf{E} = -\partial_t\mathbf{B} = i\omega\mathbf{B}$, the above equation becomes

$$\begin{aligned}\langle\mathbf{v}\times\mathbf{B}(\mathbf{r}(t),t)\rangle &\simeq -\frac{ie}{4m_e\omega}\tilde{\mathbf{E}}(\mathbf{r}_s(t),t)\times\left(-\frac{ic}{\omega}\nabla\times\tilde{\mathbf{E}}(\mathbf{r}_s(t),t)\right) + \text{c.c} \\ &= -\frac{ec}{4m_e\omega^2}\tilde{\mathbf{E}}(\mathbf{r}_s(t),t)\times\Big(\nabla\times\tilde{\mathbf{E}}(\mathbf{r}_s(t),t)\Big) + \text{c.c}\end{aligned} \tag{2.21}$$

Putting the electric and magnetic field terms in Eq. (2.18), we thus get

$$\begin{aligned}m_e\frac{d\mathbf{v}_s}{dt} &\simeq -\frac{e^2}{4m_e\omega^2}\Big((\tilde{\mathbf{E}}(\mathbf{r}_s(t),t)\cdot\nabla)\tilde{\mathbf{E}}(\mathbf{r}_s(t),t) - \tilde{\mathbf{E}}(\mathbf{r}_s(t),t)\times(\nabla\times\tilde{\mathbf{E}}(\mathbf{r}_s(t),t))\Big) \\ &= -\frac{e^2}{4m_e\omega^2}\nabla\mid\tilde{\mathbf{E}}(\mathbf{r}_s(t),t)\mid^2 = -\frac{e^2}{2m_e\omega^2}\nabla\langle\mathbf{E}^2(\mathbf{r}_s(t),t)\rangle \equiv \mathbf{F}_p\end{aligned} \tag{2.22}$$

The last equality term defines the ponderomotive force $\mathbf{F}_p$, which describes the dynamics of the oscillation center such that the cycle averaged position and velocity is

$$m_e\frac{d^2\langle\mathbf{r}\rangle}{dt^2} = m_e\frac{d\langle\mathbf{v}\rangle}{dt} = \mathbf{F}_p = -\nabla\Phi_p \tag{2.23}$$

describing the ponderomotive potential Φ_p by envelope function, the Eq. (2.7) can be rewritten as

$$\Phi_p = \Phi_p(\langle\mathbf{r}\rangle) = -\frac{e^2}{2m_e\omega^2}\langle\mathbf{E}^2\rangle \tag{2.24}$$

[3]We here use the general property that, if $A(t)$ and $B(t)$ are real, "quasi-monochromatic" oscillating functions of time and their complex representation is defined as $A(t) = \text{Re}(\tilde{A}e^{-i\omega t})$ and $B(t) = \text{Re}(\tilde{B}e^{-i\omega t})$, where $\tilde{A}$ and $\tilde{B}$ are either constants or slowly-varying functions of time. Then $\langle A(t)B(t)\rangle = \text{Re}(\tilde{A}\tilde{B})/2 = \tilde{A}\tilde{B}/4 + \text{c.c}$. In particular, $\langle A^2(t)\rangle = |\tilde{A}^2|/2$.

Thus any spatial variation of laser intensity will act to push the electrons from the high intensity region to the low intensity region through the ponderomotive force, which is proportional to the laser intensity gradient. A similar ponderomotive force is expected to occur on the ions but due to their inertia ($m_i \gg m_e$), the effect will be negligibly small than that on electrons.

From Eq.(2.23), the Ponderomotive force density f_p, can be defined as,

$$f_p = n_e \mathbf{F}_p = -\frac{n_e m_e}{4} \nabla \mathrm{v}_q^2 = -\nabla \mathrm{P}_{\text{rad}} \tag{2.25}$$

where P_{rad} is the light pressure (or radiation pressure). The Ponderomotive force density may lead to steepening of the electron density gradient around the critical density. The competition between radiation pressure ($\mathrm{P}_{\text{rad}} = \mathrm{n_e m_e v}_q^2/4$) and the thermal pressure ($\mathrm{P}_{\text{th}} = \mathrm{n_e K_B T_e}$) influence the energy transfer process of laser to the target. The influence of the ponderomotive force in the absorption mechanisms for short laser pulse (ps), has been investigated in various experiments and by different theoretical models [36, 37] which we will discuss below in section 2.8.

2.4 Motion of electron in relativistic laser field

The motion of electron in electromagnetic wave is described by the Lorentz force $\mathbf{F}$, therefore writing the Eq. (2.4) for relativistic regime, it becomes

$$\mathbf{F} = \frac{d\mathbf{p}_e}{dt} = \frac{d}{dt}(\gamma m_e \mathbf{v}_e) = -e(\mathbf{E} + \frac{\mathbf{v}_e}{c} \times \mathbf{B}) \tag{2.26}$$

where γ is the relativistic factor

$$\gamma = \frac{1}{\sqrt{1 - \mathbf{v}_e^2/c^2}} = \sqrt{1 + \frac{\mathbf{p}_e^2}{m_e^2 c^2}} \tag{2.27}$$

Electric and magnetic fields are defined by Maxwell equations by using the vector potential $\mathbf{A}(\mathbf{r}, t)$ in the coulomb gauge $\nabla \cdot \mathbf{A} = 0$ such that

$$\mathbf{E} = -\frac{1}{c}\frac{\partial \mathbf{A}}{\partial t} \qquad \text{and} \qquad \mathbf{B} = \nabla \times \mathbf{A} \tag{2.28}$$

Putting Eq. (2.28) in Eq.(2.26) and solving for the vector identity [4], we get the first basic equation for electron momentum $\mathbf{p}_e$

$$\frac{d\mathbf{p}_e}{dt} = \frac{e}{c}\frac{\partial \mathbf{A}}{\partial t} + \frac{e}{c}\left[(\mathbf{v}_e \cdot \nabla)\mathbf{A} - \nabla(\mathbf{v}_e \cdot \mathbf{A})\right] \tag{2.29}$$

the second basic equation for electron energy is obtained by multiplying Eq. (2.29) with $\mathbf{v}_e$

$$\frac{d(\gamma - 1)m_e c^2}{dt} = e\mathbf{v}_e . \frac{\partial \mathbf{A}}{\partial t} \tag{2.30}$$

Assuming electrons are initially at rest and a plane electromagnetic wave of infinite laser pulse is propagating along $z-$axis (as shown in Fig.2.2a), therefore $\mathbf{A} = \mathbf{A}_\perp(z, t)$. Now let the "$\perp$" subscript refer to the vector components of the fields and momentum in the transverse yz plane, e.g. $\mathbf{p}_\perp = (p_x, p_y)$ and $p_\parallel = p_z$. Solving the Eqs. (2.29) and (2.30) to find the electron momentum $\mathbf{p}_e = (p_\parallel, \mathbf{p}_\perp)$. We obtain the conservation laws:

$$\mathbf{p}_\perp - e\mathbf{A}_\perp = \textit{const}$$

[4] by using the vector identity $\mathbf{v} \times \nabla \times \mathbf{A} = \nabla(\mathbf{v} \cdot \mathbf{A}) - (\mathbf{v} \cdot \nabla)\mathbf{A}$

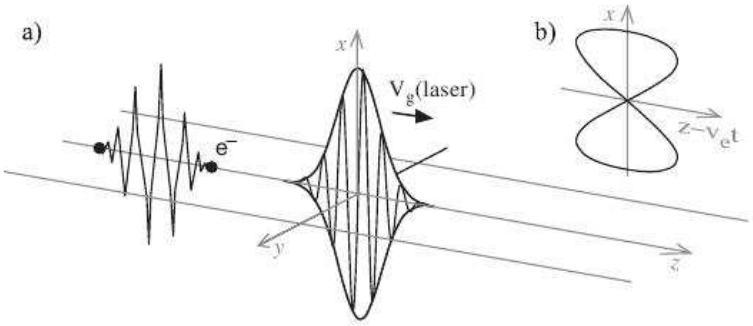

Figure 2.2: (a) A relativistic laser pulse propagating from left to right on the $z-$axis has passed an electron. Its electric field $\mathbf{E}$ points along the $\hat{\mathbf{x}}-$direction and the magnetic field (not shown here) along $\hat{\mathbf{y}}-$ direction. The electron has moved along a zig-zag shaped trajectory in the $\hat{\mathbf{x}}$- $\hat{\mathbf{z}}$ plane and stopped at rest after the passage. (b) "Figure of Eight" electron trajectory in a frame moving with the mean forward velocity of the electron, i.e. average rest frame of electron.

$$(\gamma - 1)m_e c^2 - p_{\|}c = const \tag{2.31}$$

the first constant is usually called the canonical momentum. Solving the above terms in Eq. (2.31) using $\mathbf{p}^2 + m_e^2c^2 = (m_e c\gamma)^2$ and $\mathbf{p}^2 = p_{\|}^2 + \mathbf{p}_{\perp}^2$ we get the following relations;

$$p_{\|} = m_e c(\gamma - 1) \qquad \text{and} \qquad p_{\|} = \mathbf{p}_{\perp}^2/2m_e c \tag{2.32}$$

The relation $p_{\|} = m_e c(\gamma - 1)$ has an intuitive interpretation in terms of momentum and energy delivered by the EM field along the propagation direction $\hat{\mathbf{z}}$. In non-relativistic case, free electron simply oscillates in the laser electric field perpendicular to the propagation vector $\mathbf{k}$, while in the relativistic regime $\mathbf{v}_e \times \mathbf{B}$ term of the Lorentz force becomes significant and for $\gamma \gg 1$, the electron also moves in the direction of laser pulse.

The nonlinear parameter of laser plasma interaction is the dimensionless amplitude A_0 of the vector potential $\mathbf{A}$ of the laser pulse. This dimensionless amplitude can be expressed as

$$a_0 = \frac{eA_0}{m_e c} = \frac{eE_0}{m_e c\omega} \tag{2.33}$$

where $E_0/m_e\omega = \mathbf{v}_q$ is the the quiver velocity of the oscillating electrons and is transverse to the $\mathbf{k}-$vector of the $\mathbf{E}-$field.

The fully relativistic equations of motion of an oscillating electron in an electromagnetic plane wave was solved by many authors [38, 39]. For higher laser field amplitudes, the orbit reveals a more complicated trajectory. For example, consider an electron which is under the influence of super-intense laser field propagating in the $z-$direction. The plane electromagnetic wave is described by

$$\mathbf{A}_{\perp}(\mathbf{z}, t) = A_0[\hat{\mathbf{x}}\delta\cos(\omega\tau) + \hat{\mathbf{y}}(1 - \delta^2)^{1/2}\sin(\omega\tau)] \tag{2.34}$$

where $\tau = t - z/c$ is the retarded time and $\delta \leq 1$ parameter defines the polarization of the wave: for $\delta = 1$ or 0, the wave is linearly polarized along $\hat{\mathbf{x}}$ or $\hat{\mathbf{y}}$ while for $\delta = 1/\sqrt{2}$, wave is circularly polarized. From this we get the values of $\mathbf{p}_{\perp}$ and $p_{\|}$ such that[40]

$$\mathbf{p}_{\perp} = (p_x, p_y) = \frac{eA_0}{c}(\delta\cos(\omega\tau), (1 - \delta^2)^{1/2}\sin(\omega\tau)),$$

$$p_{\parallel} = p_z = \frac{1}{4m_e c}\left(\frac{eA_0}{c}\right)^2 [1 + (2\delta^2 - 1)\cos(\omega\tau)] \tag{2.35}$$

We now obtain the electron trajectories in implicit form by integrating Eq. 2.35 w.r.t $(\omega\tau)$. The electron trajectory reads as[5]

$$kx_e(t) = \hat{x} = -a_0\delta\sin(\omega\tau), \qquad ky_e(t) = \hat{y} = a_0(1-\delta^2)^{1/2}\cos(\omega\tau)$$

$$kz_e(t) = \hat{z} = \frac{a_0^2}{4}(-\omega\tau + \left(\delta^2 - \frac{1}{2}\right)\sin(2\omega\tau)) \tag{2.36}$$

Electron is pushed parallel to the direction of laser propagation along $z-$ direction. In Eqs. (2.36), the z- term of the electron motion shows two distinct contributions: a net drift in the laser propagation direction and a superimposed $2\omega-$oscillation (twice per laser cycle). Since for circular polarized pulses, $2\delta^2 - 1 = 0$, therefore the average drift with constant velocity $v_{\rm D}$ along $z-$axis is given by[41]

$$\frac{v_{\rm D}}{c} = \frac{a_0^2}{a_0^2 + 4} \tag{2.37}$$

So for circular polarization in such frame, the orbit is a circle. For linear polarization, the electron orbit is closed in the frame where the average velocity vanishes, and such orbit gives rise to well known "Figure-of-Eight" electron motion in a time averaged co-moving frame of reference (as shown in Fig. 2.2b) and a helical orbit in the laboratory frame. From the electron trajectory (Eq. 2.36), the electron return to its initial position in the perpendicular plane, but is moved in the direction of the laser pulse propagation by a distance $\Delta z = \int v_{\rm D}(t)dt$. Therefore the electron is accelerated in direction of laser intensity gradient with increasing intensity and decelerated when it feels decreasing laser intensity. This acceleration and deceleration in the direction of intensity gradient is due to the ponderomotive force.

2.5 Ponderomotive Force in Relativistic Regime

For a "realistic" laser pulse, difference in the dynamics arise from the fact of relativistic mass increase at high quiver velocities and the non-vanishing $\mathbf{B}-$component in the Lorentz force. For an relativistic EM wave, which is described by the vector potential $\mathbf{A}(\mathbf{r}, t)$ such that $\mathbf{E} = -(1/c)\partial_t\mathbf{A}$. From this, it can be shown that $\mathbf{p}_\perp \simeq e\mathbf{A}/c$ holds even for the relativistic regime, provided the amplitude varies significantly over large distances than the wavelength. Relativistic effects make the relativistic refractive index nonlinear. The inhomogeneity of the laser field leads to a nonlinear force experienced by the charged particle[42]. By solving the Eqs. (2.29) and (2.30), the nonlinear force can be obtained

$$\frac{dp_{\parallel}}{dt} = -\frac{e^2}{2m_e\gamma}\frac{\partial \mathbf{A}_\perp^2}{\partial z} \tag{2.38}$$

this nonlinear force is proportional to the square amplitude of the laser pulse and composed of an averaged part and oscillating part with period π/ω which is a half of the laser period. Rewriting Eq. (2.38) in more general form with time-averaged momentum through a laser period $\langle\mathbf{p}\rangle$

$$\frac{d\langle\mathbf{p}\rangle}{dt} = \mathbf{F}_p = -\frac{e^2}{2m_e\langle\gamma\rangle}\nabla\langle\mathbf{A}^2\rangle \tag{2.39}$$

[5] we write the equations in dimensionless units, normalizing the coordinates to $1/k = \lambda/2\pi = c/\omega$ and using $\hat{\mathbf{r}} = k\mathbf{r}$.

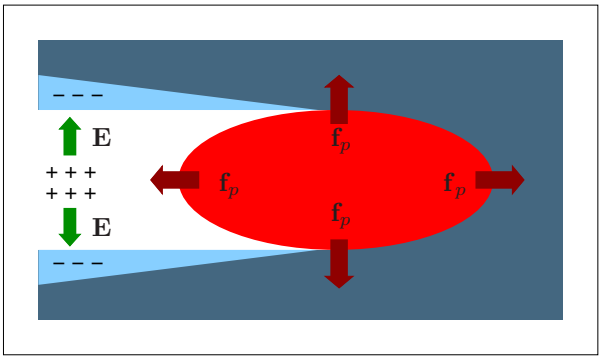

Figure 2.3: The sketch shows the ponderomotive action by a laser pulse while propagating into a plasma. The ponderomotive force ($\mathbf{F}_p \propto -\nabla\langle\mathbf{E}^2\rangle$) expels electrons out of the beam axis, modifying the electron density and creating a space charge field.

where γ is the relativistic average factor

$$\langle\gamma\rangle = \sqrt{1 + \frac{\langle\mathbf{p}\rangle^2}{(m_e c)^2} + \frac{e^2\langle\mathbf{A}^2\rangle}{(m_e c)^2}} \tag{2.40}$$

taking into account the average momentum $\langle\mathbf{p}\rangle$ and the oscillation momentum $\mathbf{p}_{\text{osc}} = e\mathbf{A}/m_e c$. A relativistic generalization of the ponderomotive force can be obtained by replacing the electron mass with the effective mass $m_e\gamma$ and requires a more sophisticated mathematical treatment [43, 42, 16]. Since the energy is $m_e(\gamma - 1)c^2$, we eventually arrive at a very similar expression as of Eq. (2.22) and is written as

$$\mathbf{F}_p = -\frac{m_e c}{2\langle\gamma\rangle}\nabla\langle\gamma\rangle^2 = -m_e c^2\nabla\langle\gamma\rangle \tag{2.41}$$

Eq. (2.41) can be simplified only as the part related to the oscillation momentum $\langle\mathbf{A}^2\rangle$ and ignoring the $\langle\mathbf{p}\rangle^2$ component which is coordinate of time. We obtain the ponderomotive force[6] as,

$$\mathbf{F}_p = -m_e c^2\nabla\left(1 + \frac{e^2\langle\mathbf{A}\rangle^2}{m_e^2 c^2}\right)^{1/2} = -m_e c^2\nabla\left(1 + \frac{e^2\langle\mathbf{E}\rangle^2}{m_e^2\omega^2}\right)^{1/2} \tag{2.42}$$

In an oscillating, quasi-monochromatic electromagnetic field described by the vector potential $\mathbf{a}(\mathbf{r}, t)$, whose envelope is sufficiently smooth in space and time, the relativistic ponderomotive force in a compact form can be written as [16],

$$\mathbf{F}_p = -m_e c^2\nabla(1 + \langle\mathbf{a}^2\rangle)^{1/2} = -\nabla m_{\text{eff}} c^2 \tag{2.43}$$

where $m_{\text{eff}} \equiv m_e\gamma = m_e(1 + \langle\mathbf{a}^2\rangle)^{1/2}$ is the electron effective mass[7], describes that the oscillating momentum leads to an increase of the effective inertia of the oscillating center. The relativistic ponderomotive force is responsible for the average electron motion observed in the laboratory frame and can be written as the negative gradient of the ponderomotive potential, i.e. $\mathbf{F}_p = -\nabla\Phi_p$

$$\Phi_p = m_e c^2(\langle\gamma\rangle - 1) = m_e c^2(\sqrt{1 + \langle\mathbf{a}^2\rangle} - 1) \tag{2.44}$$

According to the "Lawson-Woodward theorem", in case of plane wave with slowly varying amplitude, the ponderomotive force can't accelerate electrons and thus any free charge cannot gain the kinetic

[6] in the present definition we explain the ponderomotive force as the slow-varying effective force describing the cycle-averaged motion of the oscillation center of the electron in a nonuniform field, over a time scale longer than the the oscillation period. We ignored the fast oscillating components here to describe the ponderomotive force

[7] In which γ is the relativistic factor and can be explained as $\gamma = \sqrt{1 + \langle\mathbf{a}^2\rangle}$ where $\mathbf{a}(\mathbf{r}, t) = e\mathbf{A}/m_e c$ and angular brackets denote an average over the oscillation period.

energy from the laser pulse. However, in reality for the femtosecond laser pulses, which are usually tightly focused and their amplitude changes on a very short time scale, this theorem is not valid. The other most important consequence of Eq. (2.43) is that electrons are scattered out of focus, i.e. expelled from regions where the electric field is large. The scattered electrons which get accelerated in the direction of laser propagation can gain a maximum kinetic energy $\mathcal{E}_{\text{kin}} = (\gamma - 1)\mathrm{m_e c^2}$, of the order of the laser ponderomotive potential.

The above discussion reveals that ponderomotive force is extremely useful in describing and understanding the intense laser interactions with matter. For a standard bell shaped laser pulse e.g. Gaussian both in the propagation and transverse directions, the ponderomotive force is such to push the electrons out of the high intensity region. The pulse attempts to remove electrons out of its path due to self-focusing and self-compression. This ponderomotive displacement of electrons will create a space-charge field which in turn accelerate ions. Fig.2.3 shows the radial electrostatic field generated by the expulsion of the electrons in the transverse direction. In several regimes, due to the charge separation between electron and ions, a mechanical equilibrium between ponderomotive and electrostatic forces on electrons get established over such short times and distances that it is appropriate to assume that the ions, and thus the whole medium, feel "directly" a pressure that is given by the ponderomotive force times the number of electrons per unit volume (i.e. the electron density).

2.6 Laser Interaction with plasma

2.6.1 Basic laser pulse parameters

A laser pulse is described here by an envelope function, having transverse and longitudinal profiles. The laser intensity is defined as the energy flux density averaged over the fast oscillations

$$I(\mathbf{r},t) = \left\langle \frac{c}{4\pi} |\mathbf{E}\times\mathbf{B}| \right\rangle = \frac{c}{8\pi}|E_0(r,t)|^2 = \frac{c}{8\pi}\left(\frac{a_0 m_e c\omega}{e}\right)^2 \tag{2.45}$$

The dimensionless parameter a_0 described in Eq.(2.33) defines the boundary between the non-relativistic and relativistic regime of electrons in a monochromatic EM wave. In the relativistic regime, the quiver momentum of electron starts exceeding the rest mass momentum of the electron. So at higher laser intensities, the pulse is characterized by a dimensionless quantity a_0, known as laser strength parameter or laser pulse amplitude and related with laser intensity I as,

$$I\lambda_{\text{L}}^2 = a_0^2 \times 1.37\cdot 10^{18}\mathrm{W}\mu\mathrm{m}^2/\mathrm{cm}^2 \qquad \text{or}$$

$$a_0 = \frac{eE_0}{m_e\omega c} \approx \sqrt{\frac{I\lambda_{\text{L}}^2}{1.37\times 10^{18}\frac{\mathrm{W}}{\mathrm{cm}^2}\mu\mathrm{m}^2}} \tag{2.46}$$

Thus, $a_0 = 1$ corresponds to the equality of the rest and averaged kinetic energy of the electron oscillating in the laser field. So one can read from the dimensionless amplitude $a_0 = \mathbf{v}_q/c$ to measure the "relativisticness" of the interaction. When $a_0 \geq 1$, the quiver velocity of the oscillating electrons $\mathbf{v}_q$ reaches close to the velocity of light c and electron motion is considered as relativistic

$$\mathbf{v}_q = \frac{eE_0}{\gamma_{\text{L}} m_e\omega} \tag{2.47}$$

where $\gamma_{\rm L}$ is the relativistic factor of the laser field[8] If the average electron momentum is much lower than the oscillation momentum ($\langle \mathbf{p} \rangle \ll e\mathbf{A}$), then $\gamma \approx \gamma_{\rm L}$ where γ is the relativistic average factor of electron explained above in Eq. (2.40). Present day laser system allow to reach focused intensities above $10^{21}\mathrm{W/cm}^2$ for $\lambda = 0.8\mu\mathrm{m}$, so that strong relativistic regimes with $a_0 \approx 10$ are at the forefront of current research.

2.6.2 Propagation of laser beam in plasma

When a laser pulse interacts with a plasma, the free electrons and ions that constitute the plasma will respond to small scale deviations of their distribution and will be displaced slightly in an electromagnetic wave of frequency ω. Subsequently to a distortion of the charge neutrality, the particles within the plasma tend to oscillate with a frequency known as electron plasma frequency The resonance frequency of the resulting oscillations is known as the plasma frequency ω_p. depending on their mass m, charge Ze and density n

$$\omega_{p,e} = \sqrt{\frac{4\pi n_e e^2}{m_e}}, \qquad \omega_{p,i} = \sqrt{\frac{4\pi n_i Z^2 e^2}{m_i}} = \omega_{p,e}\sqrt{\frac{Zm_e}{m_i}} \tag{2.48}$$

where $\omega_{p,e}$ and $\omega_{p,i}$ are electron and ion plasma frequency respectively. From the Drude model of conductivity in which the plasma is considered as an electron cloud having uniform background of immobile ions and collisions are neglected. So the plasma dielectric constant (relative permittivity) of the electron ensemble can be expressed as [44]

$$\varepsilon(\omega) = 1 - \frac{4\pi n_e e^2}{\gamma_{\rm L} m_e \omega^2} = 1 - \frac{\omega_p^2}{\gamma_{\rm L}\omega^2} \tag{2.49}$$

where $\omega_p = \omega_{p,e}$ reads the plasma frequency. With the help of dispersion relation for electromagnetic waves in relativistic plasmas, we can find the laser frequency ω as

$$\omega^2 = \frac{\omega_p^2}{\gamma_{\rm L}} + k^2 c^2 \tag{2.50}$$

The correlation between the plasma frequency ω_p and laser frequency marks a fundamental boundary between conducting and dielectric behavior for the laser pulse interaction with plasma and divides the properties of the plasma into underdense (transparent) if $\omega > \omega_p$ and overdense (opaque) if $\omega < \omega_p$ plasmas. The electron density n_e at which the the plasma frequency ω_p becomes equal the laser frequency ω is called the critical density n_c. This density denotes the boundary between underdense and overdense plasma as shown in Fig. 2.4.

$$n_c = \frac{m_e \omega^2}{4\pi e^2} = 1.1 \times 10^{21}\mathrm{cm}^{-3}\lambda_{\mu m}^{-2} \tag{2.51}$$

where $\lambda_{\mu m}$ is the laser wavelength in micron. The relativistic effect is equivalent to an increase of the critical density, $n_{\rm eff} = n_e/\gamma_{\rm L}$ in which the plasma can be theoretically transparent

$$n_c < n_e < \gamma_{\rm L} n_c \tag{2.52}$$

[8] here in our definitions, given the value for I, the peak value of the dimensionless vector potential $a(\vec{r}, t)$ of the plane wave will be given by peak dimensionless amplitude of electric field and is a_0 for linear polarization (LP) and $a_0/\sqrt{2}$ for the circular polarization (CP) such that for LP, $\gamma_{\rm L} = \sqrt{1 + a_0^2}$ and for CP, $\gamma_{\rm L} = \sqrt{1 + \frac{a_0^2}{2}}$.

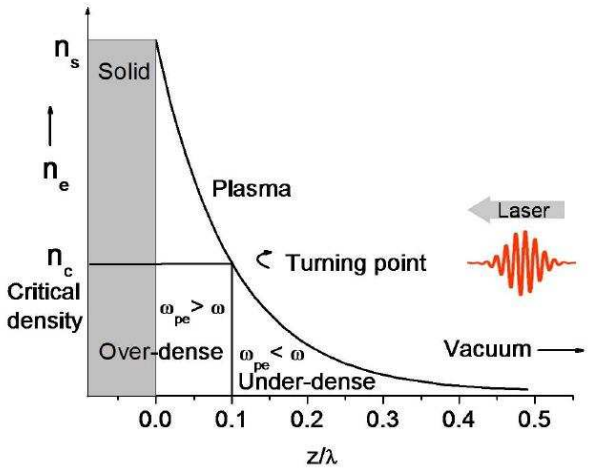

Figure 2.4: Schematic of the typical electron density profile in the Laser-produced plasma

Relativistic effects make the refractive index nonlinear. A typical laser pulse has a radial dependence shape of I(r) with $dI/dr < 0$ and the corresponding radial nonlinear "refraction" index n_{NL} can be written as

$$n_{\text{NL}}(r) = \sqrt{1 - \frac{\omega_p^2(r)}{\gamma_{\text{L}}(r)\omega^2}} = \sqrt{1 - \frac{n_e}{\gamma_{\text{L}}(r)n_c}} \tag{2.53}$$

ω_p is supposed to depend on r. The relativistic factor γ_{L} introduces a nonlinear dependence of the refractive index upon the electric field. As a consequence, when laser pulse propagates in a plasma with increasing density along the propagation axis, the refractive index n_{NL} becomes imaginary when $n_e > \gamma_{\text{L}} n_c$, showing an increase of cut-off density for the laser pulse and the laser is thus reflected. With respect to the non-relativistic case for a given wavelength, the plasma critical density (n_c) increases by a factor γ_{L} and the pulse propagate towards denser plasma layers and the effect is known as relativistic Self-Induced Transparency (SIT) or overdense penetration[45].

Numerical simulations explains that EM wave propagating in the overdense plasmas leads to strong instabilities and heating of electrons that absorbs the energy of propagating laser[46]. Since the plasma frequency (ω_p) and γ_{L} has dependence on r, one has $dN_r/dr < 0$ and the plasma acts as a lens to the laser light. There exists a critical power [47]

$$P_c \simeq 1.7 \times 10^{10}\text{W}\frac{\omega^2}{\omega_p^2} = 17\text{GW}\frac{n_c}{n_e} \tag{2.54}$$

Above the critical power P_c, the laser light self focuses into a filament and can be self guided on long distances much longer than the Rayleigh length.

For $\omega > \omega_p$, the refractive index has real values as solving Eq.(2.50), the wave vector k describes the electromagnetic wave propagation through the plasma. For $\omega < \omega_p$, the nonlinear refractive index $n_{\text{NL}}(r)$ has both the real and imaginary values which results in occurrence of the reflection as well as absorption phenomenons. The electric and magnetic field decay exponentially. Thus the laser pulse can not propagate in overdense plasma, an evanescent component will anyhow penetrate into the over-dense region up-to some characteristic length, known as the collisionless skin depth $l_s = c/\omega_p$. The laser pulse penetration depends not only on the target electron density but also on the target size (l) when the latter becomes smaller or closer to one wavelength. In such examples, the nonlinear and reflection coefficents can be calculated for a sub-wavelength foil modeled as a Dirac delta-like profile [48], obtaining a self-

induced transparency threshold as

$$a_0 > \pi \frac{n_e}{n_c} \frac{l}{\lambda} \equiv \zeta \tag{2.55}$$

Laser absorption and charged particle acceleration

In contrast to the previous sections, where the laser interaction with the plasma is discussed, here we will discuss about the various laser absorption mechanisms in the overdense plasma. The energy coupling to the overdense plasma becomes one of the main research topic due to important role played by the absorption energy efficiency in a large number of effects and application such as high energy particle generation, ICF ignition methods[49], ultrafast radiation emission *etc*. During the past decades, important experimental and theoretical progresses were registered on the route of understanding and modeling the absorption mechanisms of ps and $\mathrm{sub-ps}$ laser pulses at intensities between $10^{12}\mathrm{W/cm^2}-10^{16}\mathrm{W/cm^2}$ [50, 51]. For these longer pulses of moderate intensities, collective resonance absorption and collisional inverse bremsstrahlung[52, 53] processes are the main absorption mechanisms. For the ultrashort, high intensity ($10^{17}\mathrm{W/cm^2}$ and above) laser pulse interactions with overdense targets, a couple of new collisionless processes being found responsible for the coupling of laser energy to targets such as Brunel effect [54] or vacuum heating[55], $\mathbf{j} \times \mathbf{B}$ heating[56], different skin effects [57] *etc*.

2.7 Collisional absorption

In vacuum, due to the momentum and energy conservation, the free electron does not gain energy from the EM laser wave. Electrons oscillates in the electric field of the wave or if the field is strong enough, drifts along the laser propagation direction. However, after the laser pulse passes by, electrons ends up again with its initial energy. In plasma, the presence of ions makes the condition different. Free electron can collide with ions and thereby can gain some thermal energy from their oscillatory motion and thus transfer EM energy of the laser into the kinetic energy of plasma. For laser intensities of the order $10^{12} - 10^{14}\mathrm{Wcm^{-2}}$, the plasma is gradually heated due to electron-ion collisions. The collisions were justifiably the dominant absorption mechanism in this intensity regime. Related absorption mechanisms such as normal skin effect, anomalous skin effect, collisional absorption lead to the heating of electrons. In order to get the absorption processes in the laser plasma interactions, one may introduce the collisional damping term in the Lorentz equation of motion for the electrons and ions. The equation of motion of the electron fluid, Eq. (2.3) in a high frequency laser electric $\mathbf{E}(\mathbf{r}, t)$ and magnetic $\mathbf{B}(\mathbf{r}, t)$ field in the presence of collisions reads as:

$$m_e \frac{\partial \mathbf{v}_e}{\partial t} = -e \cdot (\mathbf{E} + \frac{\mathbf{v}_e}{c} \times \mathbf{B}) - m_e \nu_{ei} \mathbf{v}_e \tag{2.56}$$

where $\mathbf{v}_e$ represents the velocity of electron fluid and ν_{ei} is the electron-ion collisional frequency.

The thermal behavior is ensured from particles collisions. The rate of momentum transfer between the particles depends upon the collision frequencies. Electrons in the intense laser field get accelerated up to very high velocities whereas the ions due to their much higher inertia, stay almost at rest and do not respond much onto a high frequency laser field. The electron-ion collision frequency for an electron having velocity $\mathbf{v}_e \gg \mathbf{v}_i$ is given by [16, 52]

$$\nu_{ei} = \frac{4\sqrt{2\pi}}{3} \cdot \frac{Z n_e e^4}{(4\pi\varepsilon_0)^2 \sqrt{m_e} (K_B T_e)^{3/2}} \cdot \ln(\Lambda) \simeq 2.91 \times 10^{-6} \cdot \frac{Z n_e[cm^{-3}]}{T_e[eV]^{3/2}} \cdot \ln(\Lambda)[s^{-1}] \tag{2.57}$$

In above, the factor coulomb logarithm $\ln(\Lambda)$ is defined as, $\ln(\Lambda) = b_{\max}/b_{\min}$[9], where $b_{\max}$ and $b_{\min}$ are the maximum and minimum value of the impact parameter b[52].

If the number of collisions per wave cycle are large $\nu_{ei} \gg \omega$, it gives rise to *collisional skin effect* where the EM wave can enter only to the outer skin of the plasma up-to the depth $l_s \approx 0.16\lambda_{\rm D}$ and get damped. An analytical solution of the collisional absorption coefficient η_{abs} for the long exponential density profile having scale length ($l_s \gg \lambda_{\rm D}$) can be derived using the WKB−approximation [52, 29]

$$\eta_{abs}^{nse} = 1 - \exp\left(-\frac{8\nu_{ei}l_s}{3c}\cos^3\theta\right) \tag{2.58}$$

the above absorption coefficient η_{abs}^{nse} is for normal collisional skin effect. By solving the heat flow including the collisional absorption coefficient , we can derive the formula for the surface temperature scaling of the electron population [29, 57].

$$T_e = 119\left(\frac{n_e}{10^{23}\mathrm{cm}^{-3}}\right)^{1/12} Z^{1/2}\left(\frac{I}{10^{15}\mathrm{W/cm}^2}\right)^{1/3}\left(\frac{t_p}{100\mathrm{fs}}\right)^{1/6}\mathrm{eV} \tag{2.59}$$

where $\mathrm{T_e}$ is the electron temperature and t_p is the laser pulse duration. Nevertheless, these collisions do not mediate considerable energy transfer due to much higher ion mass than that of electron and only the part of $2\mathrm{m_e/m_i}$ of electron energy can be transferred between the particles in each collision. Thus for the plasma interaction with less intense $(10^{12} - 10^{14}\mathrm{Wcm}^{-2})$ and relatively long nanosecond (ns) laser pulses, the collisional absorption can be very efficient and can considerably transfer more than 80% of the total laser energy into plasma.

2.8 Collisionless Absorption

For ultra-short laser pulses of intensities $\gtrsim 10^{15}\mathrm{W/cm}^2$, the substantial energy transfer can not be explained by the electron-ion collisions. This is mainly because of two reasons, First, at higher intensities, the electron quiver velocity $\mathbf{v}_q$ may exceed than the thermal velocity $\mathbf{v}_{\rm th}$ and Secondly, the collision frequency scales as $(\mathrm{K_B T_e})^{-3/2}$ (from Eq.2.57), therefore the plasma electrons temperature rises sufficiently fast that collisions become ineffective during the interaction and hence the collective motion over-weigh the collisions [29]. Several models for *collisionless absorptions* have been developed in order to account for the higher absorption rates which make explicit use of the short pulse interactions with overdense plasmas[29, 36]. Recalling the electron temperature scaling of Eq (2.59) from [29, 58], we have

$$T_e \sim I^{4/9} t_p^{2/9} \tag{2.60}$$

The condition for collisionless absorption is fulfilled if a short $45\mathrm{fs}$ laser pulse of intensity $\mathrm{I} > 10^{15}\mathrm{Wcm}^{-2}$ is interacting with overdense plasma ($n_e = 10^{23}\mathrm{cm}^{-1}$) and the electron gains temperature of ~ 400 eV. Following the Eq. (2.57), in which the collision frequency scales as $T_e^{-3/2}$, implies a scaling fall off as

$$\nu_{ei} \sim I^{-2/3} t_p^{-1/3} \tag{2.61}$$

The second limiting effect occurs when the electron quiver velocity becomes comparable to the thermal velocity, which reduces the effective collision frequency further [59]

$$\nu_{\rm eff} \simeq \nu_{ei}\frac{\mathbf{v}_{\rm th}^3}{(\mathbf{v}_q^2 + \mathbf{v}_{\rm th}^2)^{3/2}} \tag{2.62}$$

[9] The minimum distance $b_{\min}$ is given by the classical distance of closest approach such that $b_{\min} = l_{ca}$ while the very distant interactions are screened by the surrounding charged particles, so there is a finite value for the interaction range $b_{\max} = \lambda_{\rm D}$. Therefore $\Lambda = \frac{\lambda_{\rm D}}{l_{ca}} = \frac{9N_{\rm D}}{Z}$ where $N_{\rm D} = (4\pi\lambda_{\rm D}^3 n_e)/3$ is the total number of particles in the Debye sphere.

So an electron temperature of 1 keV corresponds to the thermal velocity $v_{\text{th}} \simeq 0.05$, therefore collisional absorption starts to turn off for laser irradiances $\mathrm{I} \geq 10^{15}\mathrm{W/cm}^2$ and could not account for the high absorption mechanism which also observed experimentally as well as numerically [60]. There are number of collisionless absorption mechanisms which dominate couple laser energy to the plasma.

2.8.1 Resonance Absorption

This concept was first given by Ginzburg [53], who explains that the collisionless light absorption via collective processes occurs most efficiently for densities near the critical density $(n_e = n_c)$. This mechanism is complicated since the plasma oscillation is longitudinal and the EM wave of laser beam is transverse. A plasma wave is excited only if the EM wave enters the plasma obliquely (for $\theta > 0$) and with p−polarization for electric field to have a component directed into the plasma. The laser penetrates through the plasma up-to the surface of electron density $n_e = n_c \cos^2\theta$, where the reflection starts to occurs when $\theta > 0$. The electric field vector has projection along the density gradient n and the laser field skins from the reflection surface to the critical density surface where it may linearly excite electron plasma waves which leads to plasma heating. The excitation works well when the laser frequency is in resonance with the eigen-frequency of plasma, i.e. at critical density n_c, where $\omega = \omega_p$, hence coined the name resonance absorption.

Under oblique incidence of electromagnetic pulse in an inhomogeneous plasma, the pulse get reflected before it reaches the resonance condition *i.e* $n_{\text{eff}} < n_c$ (Eq. (2.52)) while for a steep density gradient, the electric field may tunnel into the critical density region and excite the plasma resonantly[52, 61]. The power converted into plasma oscillation can be determined by the "driver" electric field $\mathbf{E}_d$, which depends upon free-space value of the laser electric field ($\mathbf{E}_{\text{L}}$), angle of incidence (θ) and on the density gradient scale length $L = (d\ln N/dx)^{-1}$ in the following way

$$\mathbf{E}_d = \frac{\mathbf{E}_{\text{L}}\phi(\xi)}{\sqrt{2\pi kL}} \tag{2.63}$$

where $k = 2\pi/\lambda$ is the laser wave vector and $L^{-1} \equiv |\frac{d}{dx}\log N_e|_{x=x_c}$. Efficiency of resonance absorption ξ depends upon the plasma density scale length L and the laser angle of incidence θ. For long density linear scale length profile, usually defined by the inequality $L \gg 1/k$, the dimensionless parameter ξ is defined as $\xi = (kL)^{1/3}\sin\theta$ and commonly known as Ginzburg function. Based on theoretical [53] and numerical work [62] and following the above scaling , the maximum efficiency of absorption achieved is $\xi = (kL)^{1/3}\sin\theta \approx 0.8$. To a good approximation, the function for a cold plasma wave as shown in

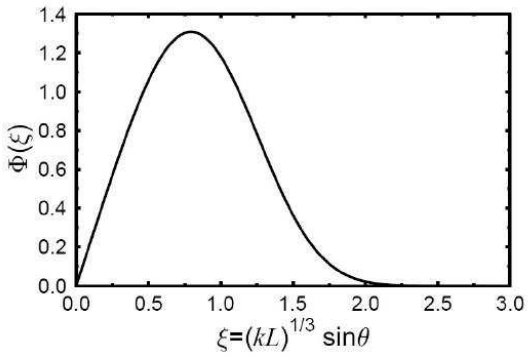

Figure 2.5: self similar behavior of resonance absorption for long density scale lengths which relates the effective plasma wave driving field to the transverse field strength. The Denisov function characterizing the efficiency of resonance absorption for $\mathrm{Lk} \gg 1$. The parameter ξ is defined as $(\mathrm{kL})^{1/3}\sin\theta$. Reprinted from [61]

Fig. 2.5, is

$$\phi(\xi) = 2.3\xi \exp\left(\frac{-2\xi^3}{3}\right) \tag{2.64}$$

where $\phi(\xi)$ is the defined as the Denisov function describing the angular dependence of $\mathbf{E}_d$ as a function of parameter ξ. From the graph shown in Fig.2.5, for resonance absorption there is an optimum angle at which maximum energy is transferred to the plasma. The maximum absorption angle can be deduced as $\theta = \sin^{-1}[0.8(c/\omega L)^{1/3}]$ and the fractional resonance absorption rate, can be found by determining the size of the decaying electric field at the critical density[29].

$$\eta_{ra} = \frac{1}{2}\phi^2(\xi) = \frac{1}{2}\left[2.3\xi \exp\left(\frac{-2\xi^3}{3}\right)\right]^2 \tag{2.65}$$

For the optimum value of $\xi = 0.8$, the fractional absorption is approximately $\eta_{ra} = 0.5$. This electron plasma wave propagates into the plasma which are formed at higher intensities and get damped by particle trapping or wave breaking and give rise to a population of very fast and hot electrons. Up-to $\sim 50\%$ optimum absorption may occur by resonance absorption [62, 63]. Resonance absorption mechanism efficiently works only for large scale plasma density profiles. The other collisionless absorption mechanism which occurs for the steep density gradients is known as the "Brunel vacuum heating" and $\mathbf{j} \times \mathbf{B}$ heating.

2.8.2 Brunel vacuum heating

This mechanism first described by Brunel [54], with the original title "*not so resonant resonance absorption*. The resonance absorption cease to work for steep density gradients. This mechanism is more efficient and the strong energy absorption is accounted by the oscillating electrons that are dragged into vacuum and then sent back into the plasma with velocity $\mathbf{v} \simeq \mathbf{v}_q$. If the quiver velocity of electrons $\mathbf{v}_q$ in the laser field exceeds the plasma density scale length L, i.e. when $\mathbf{v}_q/\omega > \mathrm{L}$, the resonance break down since the wave is destroyed and built fresh at each cycle. In such conditions the absorption occurs by so called "Brunel vacuum heating" in which electrons are directly heated by the obliquely incident laser field.

We will now derive a model based on capacitor approximation, in which the magnetic field is ignored (neglsecting $\mathbf{v} \times \mathbf{B}$ term). Assuming that the laser electric field $\mathbf{E}_{\mathrm{L}}$ has some component $\mathbf{E}_d$ normal to the target surface which pulls the electrons back and forth across the equilibrium. Consider a $\mathrm{p-}$polarized pulse obliquely incident at angle θ on a steep density gradient overdense plasma. A resonant plasma wave is formed at the critical density having driving electric field such as

$$\mathbf{E}_d = 2\mathbf{E}_{\mathrm{L}} \sin\theta \tag{2.66}$$

In the first half laser cycle $(0 < \omega \mathrm{t} + \phi < \pi)$, the electrons are pushed inside the plasma which start oscillations along the density gradient and gain very low energy because the electric field is strongly attenuated within the plasma. In the second half $(\pi < \omega \mathrm{t} + \phi < 2\pi)$, these thermal electrons are dragged out of the target into vacuum well beyond the thermal Debye sheath $\lambda = \mathbf{v}_{\mathrm{th}}/\omega_p$, where $\mathbf{v}_{\mathrm{th}}$ is the thermal velocity of plasma electrons. Here the electrons gain very high energy of the order of ponderomotive potential $\Phi_p = m_e c^2\sqrt{1 + a_0^2/2} - 1$. Many electrons are ejected at the same time which create a self consistent electric field. Due to both, the self consistent field and the oscillating laser field, most of the electrons turn around, accelerated back into the plasma and acquires a velocity

$\mathbf{v}_d \simeq 2\mathbf{v}_q \sin\theta$.[10]. We assume that all the electrons which return back into plasma, lose their energy to the solid. The average energy density absorbed per laser cycle is $P_a = \frac{\Sigma}{\tau_p}\frac{m\mathbf{v}_d^2}{2}$ where $\Sigma = N_e \delta x$ is the surface number density of plasma by which we can estimate the number of ejected electrons N_e and the thickness of the ejected layer δx, up-to which the field pulls a sheath of electrons and τ_p is the laser pulse duration. Now comparing P_a with the incoming laser power $P_L = \frac{cE_L^2 \cos\theta}{8\pi}$, we get the fractional absorption rate

$$\eta_a \equiv \frac{P_a}{P_L} = \frac{4a_0}{\pi}\frac{\sin^3\theta}{\cos\theta} \tag{2.67}$$

From Eq. (2.67), the mechanism tends to become more efficient with greater incident angles θ and with increasing laser irradiance, $I\lambda^2 \propto a_0$. In general, not all the electrons turn back into plasma, so we rewrite the Eq. (2.66) by taking into account the reduced driver field amplitude due to imperfect reflectivity, it becomes,

$$\mathbf{E}_d = (1 + \sqrt{1-\eta_a})\mathbf{E}_L \sin\theta \tag{2.68}$$

Second, taking into account that the return velocities of the electrons become relativistic at laser intensities above $10^{18}\mathrm{W/cm}^2$, thus we add relativistic kinetic energy of the electrons $\mathcal{E}_{\text{kin}} = (\gamma - 1)m_e c^2$ in the absorption power P_a. Using these both corrections, we get an implicit expression for the fractional absorption

$$\eta_B = \frac{1}{\pi a_0} f\left[(1 - f^2 a_0^2 \sin^2\theta)^{1/2} - 1\right]\frac{\sin\theta}{\cos\theta} \tag{2.69}$$

where $f = 1 + \sqrt{1-\eta_a}$ is the field amplification vector.

The schematic of the Brunel absorption is illustrated on left side of Fig 2.6 where the electric field is perpendicular to the target and the electron acceleration is normal to the target surface. The geometry of Brunel heating is quite similar to that of resonance absorption but the mechanism is different. Particularly the Brunel heating mechanism occurs in large and steep density gradient in which the resonance mechanism breaks down. The energy deposited by the Brunel heating is transported by hot electrons in the form of bunches ejected once per laser period. The average energy of electrons is $\mathcal{E}_{\text{kin}} \sim \Phi_p$ and the energy distribution is considered as Maxwellian as the electrons are accelerated in different phases of the laser electric field. The mechanism of Brunel heating works well for intermediate intensities of order

[10] Assuming the plasma is highly overdense, the electric field penetrates only to a skin depth $\sim \mathbf{v}/\omega_p$, up-to where the electrons can move unhindered into the plasma and eventually get absorbed in latter. In such a way, a population of "hot electrons" is formed in about every laser cycle.

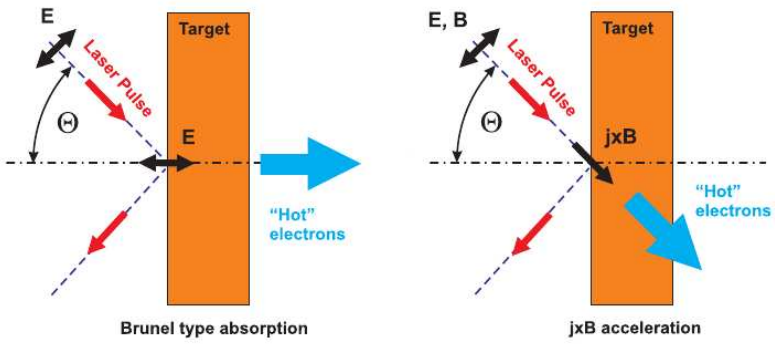

Figure 2.6: Schematic of Left: Brunel and Right: $\mathbf{j} \times \mathbf{B}$, collisionless laser absorption mechanisms which lead to acceleration of hot electrons.

$10^{16}\mathrm{W/cm^2}$, the absorption can be as high as 70% [29]. But for relativistic laser intensity $10^{18}\mathrm{W/cm^2}$ and above, i.e. $a_0 > 1$, the absorption by Brunel heating rarely exceeds 10% and the absorption mechanism "$\mathbf{j} \times \mathbf{B}$ heating" is more efficient.

2.8.3 Relativistic j × B heating

$\mathbf{j} \times \mathbf{B}$ heating is an important collisionless absorption mechanism which plays significant role in short-pulse high intensity laser-matter interactions. The characteristics of "$\mathbf{j} \times \mathbf{B}$" mechanism over the Brunel mechanism is that it works well with all the arbitrary laser polarization directions (except circular). Secondly, due to the driving high frequency $\mathbf{j} \times \mathbf{B}$ component, leads to heating in an analogous fashion and the electrons get accelerated in the laser propagation direction twice every full laser cycle. The energy gain of the electrons is of the order of the ponderomotive potential Φ_p of the laser field

$$\Phi_p = m_e c^2(\gamma - 1) = m_e c^2 \left(\sqrt{1 + \frac{a_0^2}{2}} - 1 \right) \tag{2.70}$$

The $\mathbf{j} \times \mathbf{B}$ mechanism, is most efficiently effective for normal incidence where the laser electric field vector is parallel to the plasma density profile [29] and becomes more significant at relativistic quiver velocities, i.e. $a_0 > 1$. The schematic of the $\mathbf{j} \times \mathbf{B}$ absorption is illustrated on the right side of Fig 2.6.

Relativistic $\mathbf{j} \times \mathbf{B}$ heating was theoretically first predicted by Kruer and Estabrook [56] and then later experimentally confirmed by Malka [64]. This mechanism is of more relevance at relativistic laser intensity. When the laser pulse intensity is sufficiently high (of the order $\gtrsim 10^{18}\mathrm{W/cm^2}$), the $\mathbf{v} \times \mathbf{B}$ component of the Lorentz force becomes important and the electrons are accelerated in addition by the magnetic field component of the Lorentz force. As discussed in sec.2.5, for a steep density plasma profile, the ponderomotive force pushes away the electrons from areas of high intensities along the field gradient. Similar to Brunel heating, electrons gain energy at step-like density profile by propagating into the overdense region. Electrons are accelerated perpendicular to the surface into the overdense plasma region, as the field gradient is directly normal to the critical surface, which later ejected from the rear side into the vacuum. Due to the action of self consistent field created by the ejected electrons, the electrons return into the plasma where they feel no restoring force after passing the thin skin depth and get absorbed in the plasma. The electrons continues their motion until the laser pulse is on and form a hot electron tail in the energy spectrum.

Now we will illustrate the differences arising between linear and circular polarization of the laser pulse. Assuming a step-like density profile and considering the normal incidence of an elliptically polarized pulse, neglecting the relativistic and thermal effects, the vector potential inside the plasma can be written as

$$\mathbf{A}(x,t) = \frac{A(0)}{\sqrt{1+\varepsilon^2}} \mathrm{e}^{-x/l_s} (\hat{\mathbf{y}} \cos\omega t + \varepsilon \hat{\mathbf{z}} \sin\omega t) \tag{2.71}$$

where $l_s = c/\sqrt{\omega_p - \omega^2}$ and ε is the ellipticity $(0 < \varepsilon < 1)$. Using $\mathbf{B} = \nabla \times \mathbf{A}$ and $\mathbf{P}_\perp = e\mathbf{A}/c$ for the electrons transverse momentum, the longitudinal $-e\mathbf{v} \times \mathbf{B}$ force on the electrons can be written as [40]:

$$\mathbf{F}_x = -\frac{e^2}{2m_e c^2} \partial_x \mathbf{A}^2 = F_0 e^{-2x/l_s} \left(1 + \frac{1-\varepsilon^2}{1+\varepsilon^2} \cos 2\omega t \right) \tag{2.72}$$

The term F_0 in above equation is

$$F_0 = \frac{e^2 A^2(0)}{2 l_s m_e c^2} = m_e c^2 \frac{a^2(0)}{2 l_s} \tag{2.73}$$

Taking the cycle average of Eq. (2.72), we recover the secular ponderomotive force[11] independent of polarization, as explained in Eq. (2.22). This second oscillating term at 2ω frequency vanishes for circular polarization (where $\varepsilon = 1$) which leads to a very different laser-plasma coupling between linear and circular polarization at normal incidence. $\mathbf{j}\times\mathbf{B}$ heating becomes the more significant absorption process than the Brunel heating, when the magnitude of $\mathbf{v}\times\mathbf{B}$ driving term becomes larger than the electric field component normal to the surface, i.e. $\mathbf{v}_q\mathbf{B} > \mathbf{E}\sin\theta$. The Brunel heating mechanism is superseded by $\mathbf{j}\times\mathbf{B}$ mechanism at ultra-high intensities, i.e. $\geq 10^{20}\mathrm{Wcm}^{-2}$ as the electrons motion across the density gradient along the polarization axis is dominated by the motion in the forward direction.

Apart from the above mentioned mechanisms, there exist various mechanisms for laser energy absorption such as vacuum heating, normal and anomalous skin effects etc and each covers different regimes of their existence with respect to density scale lengths, polarization properties and laser incidence geometries. Due to the complex dynamics of the laser interaction processes, today it becomes a challenge to investigate the relevant process contribution to a single experiment result. If at relativistic regime, the $\mathbf{j}\times\mathbf{B}$ acceleration mechanism is the dominant one, Brunel absorption might occur at the sides of the hole. Later Wilks etal[36] explained with PIC simulations, the potential importance of the heating mechanisms in the relativistic regimes along with the occurrence of other processes such as hole boring and the magnetic field generation which plays an important role in fast particle acceleration.

2.9 Hot electron generation

All of the collisionless absorption mechanisms discussed above, by one way or another, results in strong heating of fraction of electrons to much higher energy than the initial bulk plasma having temperature $\mathrm{T_c}$. These supra-thermal electron component generally known as "hot (fast) electrons" has a Maxwellian form with a characteristic temperature $\mathrm{T_h} \gg \mathrm{T_c}$. With the interaction of short fs laser pulses with overdense plasma, these hot electrons bunches oscillate in the transverse laser field and driven into the target at 2ω via the $\mathbf{j}\times\mathbf{B}$ heating mechanism, further get accelerated by coherent electric field, having monochromatic beam-like tail with some energy spread. Hot electron generation is mainly due to specific acceleration mechanisms such as resonant absorption and $\mathbf{j}\times\mathbf{B}$ heating etc. The characteristic feature of these absorption mechanisms and their dependence on the laser parameters (such as intensity, wavelength, incidence angle etc.) will reflect the generation of hot electrons population. Thus the presence/absence of hot electrons will features the presence/absence of related specific absorption mechanism in the laser plasma coupling.

The temperature of the fast electrons $\mathrm{T_h}$ is of the order of the cycle averaged oscillation energy in the electric field of laser in vacuum and also estimated from the ponderomotive potential, $\Phi_p = \mathrm{K_B T_h} \approx \mathrm{m_e c^2}(\gamma - 1)$. The $\mathbf{j}\times\mathbf{B}$ mechanism is considered to be the main source of hot electrons for intensities of the order $\sim 10^{19}\mathrm{W/cm^2}$ and above. The higher the intensity of the laser pulse, the higher is the fraction of the laser energy which get converted into hot electrons. Upto $20-30\%$ [64, 65] for intensities around $10^{19}\mathrm{W/cm^2}$ or even upto 40% for $5\times10^{20}\mathrm{W/cm^2}$[12] of the laser energy is transferred to the supra-thermal electron population and the temperature of the hot electrons increases up-to several MeV. Considering bi-Maxwellian electron distribution, the ponderomotive hot electron scaling law proposes

[11] Actually some authors identify the ponderomotive force with the whole nonlinear force including the oscillating components. We here, keep the definition of the ponderomotive force related to the slow, non-oscillating motion as developed in sec 2.3.

an approximately $(\mathrm{I}\lambda^2)^{0.5}$ dependence of $\mathrm{T_h}$ to laser intensity [36]

$$K_B T_h \approx 0.511 \left[\left(1 + \frac{I_{18}\lambda^2}{1.37} \right)^{1/2} - 1 \right] \mathrm{MeV} \tag{2.74}$$

This scaling was supposed to be valid in general when laser plasma interaction density is close to the critical density. Depending upon the laser conditions (such as spot size, pulse length, prepulse) this constraint may be satisfied for a wide range of intensities. The scaling of the hot electron temperature varies with laser intensity, laser pulse duration and laser incidence angle and is still under debate. The uncertainty in plasma conditions around the laser plasma interaction region may be responsible for the discrepancies in $\mathrm{T_h}$ scaling with intensity [66, 65]. These fast electrons growth have been observed and characterized in several experiments and for different interaction conditions [66, 65, 67, 68]. Beg *etal* [8] found an empirical scaling of hot electrons $\mathrm{T_h}$ to be effectively scales as $(\mathrm{I}\lambda^2)^{0.3}$ at laser intensity of $\mathrm{I} \sim 10^{19}\mathrm{W/cm^2}$. $\mathrm{T_h}$ is found experimentally to increase as $(\mathrm{I}\lambda^2)^{0.34\pm0.04}$ for laser intensities from $10^{18} - 10^{21}\mathrm{W/cm^2}$ which suggests that the ponderomotive scaling of $(\mathrm{I}\lambda^2)^{0.5}$ overestimates the growth of fast electrons with laser intensity [69]. Although the hot electrons are much less in number than the thermal electrons, but their population often carries more energy. Acceleration and transport of these hot electrons is of particular interest in recent years and play a fundamental role in many vital applications such as in ICF ignition methods and more importantly in proton and heavier ion acceleration from the overdense targets and will be briefly discussed in the following Chapter.

CHAPTER 3

Laser-Driven Ion Acceleration

With the rapid development of laser technology and having wide potential applications of ion beams in laser fusion [70] and proton therapy [71], ion acceleration has received great attention in the area of laser interaction with overdense plasma. Acceleration of ions by super-intense laser pulses was boosted in the year 2000 when three experiments (Clark etal [10], Snavely etal [12] and Maksimchuk etal [11]) independently reported the observation of multi-MeV protons from few microns thick metallic target. The emission of protons from the metallic targets whose chemical composition doesn't include Hydrogen sound very surprising, but was explained soon after that protons get originated from impurities which are ordinarily present on the metallic surface in the form of thin layers of water or hydrocarbons. Although all authors in principle agreed upon the proton origination from the metallic target surface but the opinions differ about the question, whether the source layer of the observed protons is located on the front [10] or on the rear side of the target[12, 11, 72]. Later, the controversy of ion acceleration has also been expanded with the origin of heavy ions[73].

A direct interaction of protons and heavier ions in a field of current available laser systems is by far not strong enough to accelerate these particles to $\sim \mathrm{MeV}$ energies. Similar to Eq.(2.46), which explains the relativistic threshold for electrons, i.e. $I_e\lambda^2 = 1.37 \times 10^{18}\ \frac{\mathrm{W}}{\mathrm{cm}^2}\mu\mathrm{m}^2$, one can derive the intensity where the kinetic energy of oscillating proton in the laser field equals to its rest energy [74]

$$I_p\lambda^2 = \left(\frac{m_p}{m_e}\right)^2 I_e\lambda^2 \approx 5 \times 10^{24} \qquad \mathrm{W}\mu\mathrm{m}^2/\mathrm{cm}^2 \tag{3.1}$$

which corresponds to a laser pulse amplitude $a_0 = 1836$ in which the ions finally reach relativistic velocities within one laser cycle and the acceleration process enters into the so called Piston Regime [75]. This laser intensity is far beyond the present laser technology yet and might be feasible in the future with the new concept of optical parametric amplification $(\mathrm{OPA-CPA})$[76]. Energetic ions observed in the laser-matter interaction have been accelerated not directly by the laser fields but by the plasma fields which are formed by the laser heated electrons. However, these plasma electrons can mediate the forces of laser fields on ions by generating strong quasi-static electric fields which arises from the local charge separation. These fields which vary on a time scale comparable to the laser pulse duration, can be of same magnitude as that of the fast oscillating laser fields, giving the ions a significantly longer time to accelerate.

The laser energy can be efficiently transferred to the plasma electrons by various mechanisms leading to different ion acceleration scenarios, depending on the laser parameters e.g. intensity and temporal contrast of the pulses and on the target properties such as shape and size of the target. In this section, the two main ion acceleration scenarios will be discussed, that provide sufficiently strong electric fields to the particles over a sufficiently long time. According to the first scenario, ions can be accelerated in the vicinity of the laser focus at the target front surface by the "ponderomotively" expelled electrons, leaving behind a positive space charge of ions. This mechanism is commonly known as radiation pressure acceleration ("RPA"). [11]. The second scenario includes the ion acceleration at the target rear side, by which the fast electrons accelerated at the target front surface, crossing the target bulk and escape

in vacuum from the rear side, as a result a space-charge field in the form of thin Debye sheath being generated that provides strong and long lasting electric fields which accelerate the ions. This mechanism is commonly known as target normal sheath acceleration ("TNSA"). [12, 14]. In recent years, there is one more acceleration mechanism which is of high interest, is the "Shock acceleration" mechanism [77, 78] which can accelerate high energy ions $(\sim \mathrm{MeV})$ of monoenergetic nature[79]. According to this, when the laser intensity is of the moderate range, i.e. $10^{18} - 10^{21}\mathrm{W/cm^2}$, the light pressure ranges up-to terabar values, sweeps out and compress the laser produced plasma, pushing its surface at relativistic speeds. Such a strong compression and acceleration may generate strong shock waves propagating in the bulk of plasma which accelerate ions. In moderately overdense and hot plasmas, where the shocks are of collisionless nature, shock acceleration may lead to both higher ion energy and narrow ion spectrum and can be the dominant acceleration mechanism than the widely studied TNSA and RPA mechanism. Below we will discuss these three ion acceleration mechanisms in brief.

3.1 Target Normal Sheath Acceleration (TNSA)

3.1.1 Introduction

TNSA scheme was first suggested by Wilks etal [14] in agreement with its original use [7], as an explanation for the energetic ions (protons of order $\sim 58\mathrm{MeV}$) which was observed normal to both the rear surfaces of a wedge-shaped target in an experiment performed at the NOVA− Peta-watt laser facility of LLNL, USA [12], According to TNSA model, a very intense current of high energy "hot (fast)" electrons is generated at the front side. As the electrons travel with relativistic velocity (see sec 2.9 of Ch.2), these hot electrons cross the rear side boundary and attempt to escape in the vacuum at the rear side while the ions due to their heavy mass almost remain at rest. Therefore the charge imbalance generates a sheath field $\mathbf{E}_s$, normal to the rear surface. If the hot electrons have density n_e and temperature T_h, the typical spatial extension of the sheath L_s will be related to electric field $\mathbf{E}_s$ as

$$\mathbf{E}_s \sim \frac{T_h}{eL_s} \tag{3.2}$$

The protons will thus be accelerated perpendicular to the target into the rear side hemisphere until they compensate the electron charge. Assuming a steep interface and n_h and T_h as the only parameters, L_s can be roughly estimated as the Debye length of fast electrons

$$L_s \sim \lambda_{\mathrm{Dh}} = \sqrt{\frac{T_h}{4\pi e^2 n_h}} \tag{3.3}$$

Assuming a simple scaling of hot electrons T_h, for a laser irradiance of intensity $I\lambda^2 = 10^{20}\mathrm{W/cm^2}$ and a fractional absorption $\eta_f = 0.1$, we find $n_h \sim 8 \times 10^{20}\mathrm{cm^{-3}}$, $T_h = 5.1 m_e c^2 = 2.6\mathrm{MeV}$, $\lambda_{\mathrm{Dh}} = 4.2 \times 10^{-5}\mathrm{cm}$ and $\mathbf{E}_s \sim 6 \times 10^{10}\mathrm{V/cm}$. This huge electrostatic field is by far stronger than that of the electric field of the laser wave, so will back-hold most of the escaping electrons, ionize the atoms at the rear side and start to accelerate ions. In a rough estimate, a test ion crossing the sheath would acquire a energy $\mathcal{E}_i \sim eZ\mathbf{E}_s L_s = ZT_h$, with a scaling $\mathrm{I}^{1/2}$ if $T_h \approx \Phi_p$(ponderomotive energy) given by Eq. (2.74) holds. Due to the hydrocarbons or water containments on the surface of the non-treated targets, the protons are in a favorable condition for acceleration and are more rapid in following the electrons by screening the sheath field than other heavy ions because of their initial position, located at the maximum of the field and their higher charge-to-mass ratio. The heavy ions can also be efficiently accelerated from the cleaned targets[1].

[1] Several cleaning techniques such as target heating and laser ablation have been adopted and tested to remove almost all

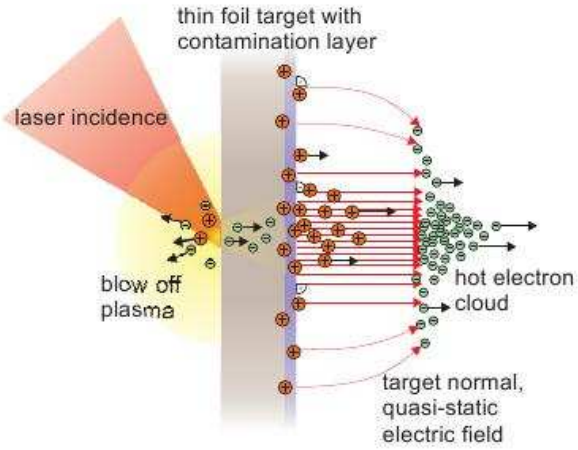

Figure 3.1: TNSA mechanism: Electrons heated at the front side pass through the target, escape to the rear side in vacuum. A strong quasi-static electric field normal to the target surface builds up between electron cloud and the ionized target which accelerate the ions.

The accelerated ions leave the target together with the co-moving electrons forming a quasi- neutral plasma sheath. The plasma density in this sheath drops quickly after the detachment from the target while the temperature remains high in this sheath, recombination effects are negligible for propagation lengths in the range of several meters[82]. After the very early stage of acceleration, the process is described as collisionless plasma expansion in vacuum, the electrons move ahead of the ions front until almost the whole of the electron energy has been transferred to ions. The energy transfer from electrons to ions is almost due to the large mass difference. Most of the fast electron energy is delivered to ions and particularly to protons if the latter dominate the acceleration in proper conditions. The accelerating electrostatic field is parallel to the normal vector of the target rear surface, therefore the mechanism is called as "Target normal sheath acceleration". The schematic for this mechanism is sketched in Fig. 3.1.

After its discovery, the essential features of the TNSA mechanism has been supported by several experiments and it provided the experiments many ideas to test the ion acceleration schemes with different shape of targets. In particular, the schemes for beam optimization and control have been designed on the basis of TNSA. As the sheath field is almost perpendicular to the target surface, it is possible to focus the protons by shaping the target [83, 84]. The simple dependence of the electrostatic field on the density scale length at the rear side has been confirmed by performing a long scale length plasma at the rear side of target surface [85], by showing the proton energy decrease and suppression of acceleration with increasing L_s. The suppression of proton beam by removing the surface impurities provide a confirmation to accelerate efficiently the heavier ions such as carbon [86].

3.1.2 Basic theoretical model

The essential features of TNSA mechanism have been supported by several experiments and has become the reference framework to interpret observations of multi$-$MeV protons from the target rear side. First of all, we assume an electrostatic approximation which lead to the formulation of a simple set of equations, so that the electric field $\mathbf{E}_s = -\nabla\Phi$ where the potential Φ satisfies the Poisson's equation

$$\nabla^2\Phi = 4\pi e(n_e - \sum_j Z_j n_j) \tag{3.4}$$

the protons and other contamination layers from the target to accelerate heavy ions[80, 81]

where the summation is over each species of ions, having charge Z_j and density n_j. In a laser solid interaction, the electron density n_e can be described as of qualitatively two distinct populations of electrons having densities n_c and n_h such that $n_e = n_c + n_h$. In the simplest approach, only the "hot" electrons will escape the target vicinity, shielded from the ion attraction by their slow successors where the main part of the hot electrons population will be trapped in the coulomb potential (formed due to charge separation) and constitute an exponential sheath on the target rear side. So thermal effects can be neglected for the cold population (n_c), while n_h can be described by a one temperature Boltzmann distribution as

$$n_h = n_{0h} \cdot \exp\left\{\frac{e\Phi}{K_B T_h}\right\} \tag{3.5}$$

where Φ is the Coulomb potential of the ionized target. The above equation is a reasonable approximation to account for the presence of the self-consistent sheath field which will be retained as long as the laser pulse drives hot electrons through the target. The expression in Eq. 3.5 has actually been used in many works on TNSA[87, 88, 89] but can lead to serious problems[2] when the main goal is the evaluation of the maximum energy of the accelerated ions.

In most of the cases, it is appropriate to consider two different ion species, a light (L) and an heavy (H) population and by this way it is possible to model the acceleration of light ion species which is present on the surface of a solid target made of heavy ions. Depending upon the description of the ion population and to describe TNSA theoretically, there are two main categories of models named "static" and "dynamic" models which provide simplified analytical descriptions and are helpful to interpret the experimental data. In static models, it is assumed that the light ions (or the most energetic ones) are accelerated in the early stage of the sheath formation, while the heavy ions may be assumed as stationary or immobile. In such conditions, the effect of the light ions on the electrostatic potential Φ is usually neglected with the aim to provide more accurate description of the sheath depending on the assumptions of hot electron distribution. The second category is of dynamic models where the system is described as a neutral plasma in which the ions acquire kinetic energy in the course of sheath evolution. In most cases, a unique ion component is considered, i.e. a approach which is strongly connected to to the classical problem of plasma expansion in vacuum [90]. In a cold fluid description, the ions are described as follows:

$$\frac{\partial \mathbf{u}_j}{\partial t} + \mathbf{u}_j \cdot \nabla \mathbf{u}_j = -\frac{Z_j e}{m_j}\nabla\Phi \tag{3.6}$$

$$\frac{\partial n_j}{\partial t} + \nabla \cdot (n_j \mathbf{u}_j) = 0 \qquad \text{where} \quad j = (L, H) \tag{3.7}$$

and if the ions are described kinetically, then their phase space distribution can be described by Vlasov equation,

$$\frac{\partial f_j}{\partial t} + \mathbf{v} \cdot \nabla f_j - \frac{Z_j e}{m_j}\nabla\Phi \cdot \frac{\partial f_j}{\partial \mathbf{v}} = 0 \tag{3.8}$$

Most of the studies proposed in the literature both before and after the TNSA experiments and the related specific models of TNSA developed so far can be considered as suitable simplifications of the previous equations, and can be obtained further with physically motivated assumptions by selecting one of the two above mentioned categories or suitable combination of them. All of the models proposed so far to describe TNSA, to a large extent are phenomenological, i.e. they need some physical quantities as input parameter which are not precisely known. The best model in this context may be considered the one which provides the best fit of experimental data with the lowest set of target and laser parameters, and the one which give directions towards improvement of the acceleration process for future applications.

[2] These issues have been discussed at the end of this section after Eq. (3.10).

Quasi-static model

Starting approximation of static model includes the time scale of $\mathrm{sub-ps}$ laser pulses, an isothermal hot electron population, immobile heavy ions and the light ions to be sufficiently few in number to neglect their effect on the evolution of the potential and thus can be treated as test particles. In this approximation, we used Eq.(3.5) to describe the hot electrons and neglecting thermal effects for cold electrons, the potential in planer geometry is calculated as

$$\frac{\partial^2 \Phi}{\partial x^2} = 4\pi e \left[n_{0h} e^{e\Phi/T_h} - (Z_{\mathrm{H}} n_{0\mathrm{H}} - n_{0c}) \right] \tag{3.9}$$

where Subscript $_{\mathrm{H}}$ is for proton. The corresponding electron density, electric field and the energies of test protons can be calculated moving in such potential. The solution of Eq.(3.9) in the semi-infinite region $x > 0$ is calculated as [91]

$$\Phi(x) = -\frac{2T_h}{e} \left\{ \ln \left(1 + \frac{x}{\sqrt{2e}\lambda_{\mathrm{Dh}}} \right) \right\} \tag{3.10}$$

where λ_{Dh}, the Debye length of hot electron have been defined in Eq.(3.3). However, the electrostatic potential $\Phi(x)$ leads to an infinite acceleration of test protons which are initially at zero energy at $x = 0$. Therefore from Eq.(3.5), solving mathematically, $\Phi \to -\infty$ as $x \to +\infty$, which means the self-consistent electrostatic potential must diverge at large distances from the target. This is not a pathological consequence of the one dimensional approximation but is related with the fact that the Boltzmann relation implies the existence of particles with infinite kinetic energy, which is not physically meaningful[92]. So this unphysical behavior can by assuming an upper energy cut-off $\mathcal{E}_c$ in the electron distribution, such that $\Phi \to -\mathcal{E}_c$ as $x \to +\infty$ and electric field turns to zero at a finite distance[93].

More detailed discussion about this acceleration mechanism is out of the scope of this thesis, since the main acceleration mechanism explained in our simulation results is acceleration of ions from the front surface of the target. e.g. by radiation pressure acceleration mechanism and by collisionless shock formation which we will discuss below.

3.2 Radiation Pressure Acceleration (RPA)

This mechanism of ion acceleration has gained a lot of interest in the past few years [94, 95, 48, 96], where the particles are directly accelerated by the laser radiation pressure. Acceleration of solid objects via the radiation pressure of intense light from the long times, has been considered as a route to achieve extremely high velocities. The basic principle of this idea was first proposed by Marx in 1966 [97], giving a proposal for any human propelled macroscopic object to reach velocities approaching the speed of light. The efficiency approaches 100% as the object reaches the speed of light. Later this idea was implemented to a thin foil target being accelerated entirely as soon as short pulsed highly power laser systems were available.

RPA mechanism accelerates ions from the front side of the target in the vicinity of the laser focus due to the electrostatic fields which arise inside the target from the ponderomotive expulsion of plasma hot electrons where they form a compressed electron cloud. When a plane monochromatic EM wave of intensity I and frequency ω normally incident on the plane surface of a target (at rest), the electrons are pushed inside the target by the ponderomotive force (Eq. 2.70), while the ions are still immobile due to their heavy mass. The electrons are pushed inwards by ponderomotive force, leaving behind a charge separation layer and creating an electrostatic, back-holding field E_s that in turn acts on the ions and leads to acceleration. As soon as the electron density exceeds the critical density ($n_e > n_c$), the condition of

a sharp boundary is given and the pressure imposed on the electron layer might be described by the radiation pressure P_{rad} and is given by

$$P_{\text{rad}} = \frac{1}{2}\varepsilon_0 E_s^2 = (1 + R - T)\frac{I}{c} = (2R + A)\frac{I}{c} \tag{3.11}$$

where R, T and A are the reflection, transmission and absorption coefficients of the target and is well known derived by Fresnel formulas [98] as a function of the refractive index and thus of wave frequency. Energy conservation implies $R + T = 1 - A$, i.e. the fraction of the EM wave intensity that is converted into internal energy of the target[3].

Radiation pressure is basically the flow of delivered momentum per unit target surface and can be computed when the EM fields at the surface are known. RPA measurements at low intensities in the range from $10^{12} - 10^{19}\mathrm{W/cm^2}$ tells that it plays no role and indeed is not a measurable effect over-most at these intensities. RPA is dominated in this intensity regime by foil expansion driven by the thermal pressure of the plasma or in the higher intensity regime $> 10^{19}\mathrm{W/cm^2}$ by foil decompression due to TNSA. If the laser pulse is linearly polarized, it has been found experimentally as well as numerically that rear -surface acceleration (TNSA) produces high energy particles with small divergence and of higher efficiency than that of front surface acceleration[99, 73]. Later, it was numerically predicted that using linearly polarized lasers of intensity above $10^{23}\mathrm{W/cm^2}$ which is not experimentally accessible yet, RPA might be the main dominant mechanism than any other acceleration schemes [75].

Successfully exploring RPA requires a means of suppressing hot electron production at the target front surface. This may seems impossible task given the high values of electric field but becomes possible using circularly polarized pulses at normal incidence. For circular polarized, normal incidence laser interactions, RPA can be revealed at much lower intensities $10^{18}\mathrm{W/cm^2}$[95] in which the electrons are effectively in a trapped orbit close to their origin and do not propagate through the target thus suppressing TNSA. Due to the normal incidence of the laser, the Resonance and Brunel absorption are disbanded and for circular polarized (CP) pulses, the ponderomotive pressure $\sim \nabla\mathbf{E}^2$ is quasi-static and follow the laser beam temporal envelope in magnitude. Thus for CP pulses, the generation of hot electrons is suppressed since the longitudinal component of the Lorentz force vanishes[95]. Therefore for CP pulses, the scaler value of the electric field vector is constant and the ponderomotive pressure $\sim \nabla\mathbf{E}^2$ oscillates with a period of once per optical cycle and hence $\nabla\mathbf{E}^2 = const$ for $\mathrm{I} = const$. Constant pressure on electrons in the target allows a charge sheath to develop, i.e. ions are offset with respect to ions and hence the formation of an accelerating field.

In general, RPA consist of two different stages: a) hole boring stage HB−RPA:- where the electrons are piled up to an equilibrium and creates a restoring electrostatic field since the target ions are still immobile in that early stage. Later the ions are set into motion layer by layer due to this electrostatic field. The target rear surface almost remains stationary in this case. b) light sail stage LS − RPA:- where the entire target ions begin to move ballistic due to the electrical field created by the displaced and compressed electron layer which acts as an accelerated plasma mirror. We will concentrate more on the “hole boring acceleration stage” for circular and linear polarized pulses and to compare the ion acceleration mechanism occurred within the target due to the collisionless “electrostatic shocks”.

3.2.1 Hole-boring RPA: Thick targets

In the first measurements of ion acceleration in the forward direction, the possibility of relevant contribution of accelerating ions at the front side of target was conceived [100]. Later, few more experiments

[3] Other limiting cases include a perfect mirror ($\mathrm{R} = 1$, $\mathrm{T} = \mathrm{A} = 0$, so $\mathrm{P_{rad}} = 2\mathrm{I/c}$), a perfectly absorbing medium ($\mathrm{A} = 1$, $\mathrm{R} = \mathrm{T} = 0$, so $\mathrm{P_{rad}} = \mathrm{I/c}$) and a transmitting non-absorbing target ($\mathrm{A} = 0$, $\mathrm{T} = 1 - \mathrm{R}$, so $\mathrm{P_{rad}} = 2\mathrm{RI/c}$)

suggested that in particular laser and target conditions, the energy of the "front side ions" is comparable to or even exceed than that of "rear side" ions [101, 102]. As a consequence, the mechanism of ion acceleration in such regions is extensively investigated.

To derive the expression for the ion velocity in the non-relativistic case, (i.e. ion front velocity is slow compared to c), we first solve the equations for the momentum balance. It is assumed that the plasma is overdense so that the light beam is perfectly reflected from the plasma surface. Now a intense laser beam of constant intensity I is driving into a target of uniform density. At the front surface of plasma, the intense radiation pressure of the laser pulse pushes an overdense target inwards, steepening the density profile and bending its surface. To provide a dynamical picture of ion acceleration in the charge separation layer, we consider only the action of steady ponderomotive force which would be fully appropriate for circular polarized pulses at normal incidence. During the initial stage, the electrons are pushed inside the target by the ponderomotive force (see Ch.2, sec2.5 for detail), piles up to densities $n_e = n_{p0}$ (see Fig.3.2a) leaving behind a charge separation layer. This give rise to a restoring electrostatic field $\mathbf{E}_x$. Assuming that the time scale of electrons and ions is well separated because of the large mass difference, so that at any time the electrons can be considered in mechanical equilibrium, i.e. $\mathbf{E}_x$ and the ponderomotive force balance each other. To describes the ion motion analytically, we use simplified profiles of density and fields as shown in Fig.3.2. In Fig.3.2a, electrons have piled up under the action of ponderomotive force while the ions are still immobile and are at equilibrium. The model parameters n_{p0}, x_d and $\mathbf{E}_x$ are related to each other by the Poisson equation, charge conservation and the pressure balance condition such as

$$P_{es} = \int e n_e \mathbf{E}_x dx = P_{\text{rad}} = \frac{2I}{c} \tag{3.12}$$

The length $l_s = x_s - x_d$ is the penetration distance of the ponderomotive force into the target ($l_s = c/2\omega_p$). Since the electric force $\mathbf{E}_x$ decreases linearly with distance in the region $x_d < x < x_s$, ions with initial position in this range all reach to the $x = x_s$ point at the same time τ_b and a singularity appears in the ion density as shown in Fig.3.2c. Then the ions cross this electron layer and travel inside the target until they encounter the next layer of stationary ions. Due to much less inertia of electrons than that of ions, the compressed electron layer (Fig.3.2c) adjusts itself immediately. Now again the next stationary layer of ions experience the electrostatic field and get accelerated in the same manner. This cyclic acceleration of ions which proceeds by layer to layer resulting in the characteristic loops in the ion phase space (see results sec 6.3 for CP case in Ch.6), continues until they don't reach to target rear side.

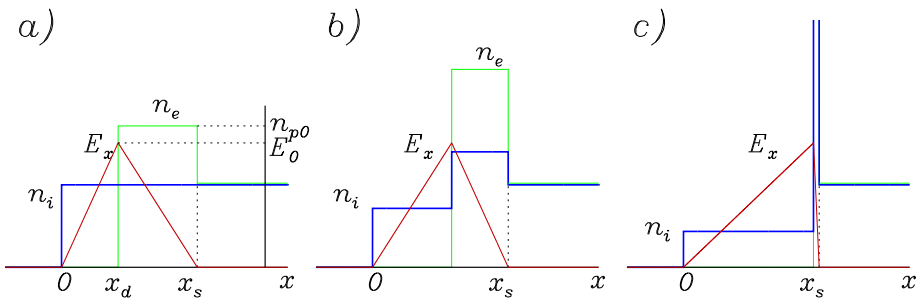

Figure 3.2: Schematic of the ion density n_i, electron density n_e and electrostatic field $\mathbf{E}_x$ at three different stages of ion acceleration. Figure reprinted from [103]

When an EM wave impinges on the target front surface, the intense radiation pressure of the laser pulse pushes the overdense target inwards with a velocity $\mathbf{v}_{\text{hb}}$ commonly known as hole-boring velocity, which can be estimated by balancing the electromagnetic fields and mass momentum flows in the instantaneous rest frame [77]

$$\frac{2I}{c} \sim 2n_i(m_i\mathbf{v}_{\text{hb}})\mathbf{v}_{\text{hb}} = \frac{2n_e}{Z}Am_p\mathbf{v}_{\text{hb}}^2 \tag{3.13}$$

where P_{rad} is the radiation pressure on the surface layer which is moving at velocity $\mathbf{v}_{\text{hb}}$. At this point, we will define a dimensionless piston parameter Ξ,

$$\Xi = \frac{I}{m_i n_i c^3} = \frac{I}{\rho c^3} = \frac{Z}{A}\frac{n_c}{n_e}\frac{m_e}{m_p}a_0^2 \tag{3.14}$$

where ρ is the mass density of the plasma. So we can determine $\mathbf{v}_{\text{hb}}$ as

$$\mathbf{v}_{\text{hb}} \sim \sqrt{\frac{I}{\rho c}} = \sqrt{\frac{I}{m_i n_i c}} = \sqrt{c^2\Xi} = a_0 c\left(\frac{Z}{A}\frac{m_e}{m_p}\frac{n_c}{n_e}\right)^{1/2} \tag{3.15}$$

The fastest ions form a narrow bunch of velocity $\mathbf{v}_{\text{max}}$ that penetrates into the overdense plasma detaching from the surface layer, such that the maximum velocity of the detached ion bunch can be $\mathbf{v}_{\text{max}} = 2\mathbf{v}_{\text{hb}}$[95]. Neglecting numerical factors, this leads to the following estimates and scaling for $\mathbf{v}_{\text{max}}$ and the corresponding energy per nucleon of the detached ion bunch for non-relativistic regime

$$\mathcal{E}_{\text{max}} = \frac{1}{2}m_i\mathbf{v}_{\text{max}}^2 = 2m_i c^2\Xi \tag{3.16}$$

The estimate for $\mathcal{E}_{\text{max}}$ shows a scaling with the laser intensity I and is more favorable than the $\text{I}^{1/2}$ scaling of TNSA. This suggests that the RPA effects become more important for higher intensities. From Eq.(3.15), $\mathbf{v}_{\text{max}}$ can be described as

$$\mathbf{v}_{\text{max}} \sim 2\mathbf{v}_{\text{hb}} = 2\sqrt{c^2\Xi} \tag{3.17}$$

the ion velocity depends simply on the laser intensity and target density in this scenario.

As $\mathbf{v}_{\text{hb}}$ does not become negligible with respect to c, one has to take into account that the effective radiation pressure P_{rad} on the surface moving with velocity $\mathbf{v}_{\text{hb}}$ in the lab frame and can be demonstrated by the Lorentz transformation [4] such that:

$$P_{\text{rad}} = \left(\frac{2I}{c}\right)\frac{1-\mathbf{v}_{\text{hb}}/c}{1+\mathbf{v}_{\text{hb}}/c} \tag{3.18}$$

The EM momentum flow, i.e. the radiation pressure P_{rad}, must balance the momentum flow difference equal to $n_i(2\gamma_{\text{hb}}m_i\mathbf{v}_{\text{hb}})\mathbf{v}_{\text{hb}}$. Thus the global momentum balance equation Eq. (3.13), with relativistic correction can be written as

$$\left(\frac{2I}{c}\right)\frac{1-\mathbf{v}_{\text{hb}}/c}{1+\mathbf{v}_{\text{hb}}/c} \sim n_i(2\gamma_{\text{hb}}m_i\mathbf{v}_{\text{hb}})\mathbf{v}_{\text{hb}} \tag{3.19}$$

[4] The relativistic correction is equivalent to the energy depletion of the incident radiation in the adiabatic approximation and can be shown easily by the heuristic model of radiation pressure in which the number of reflected photons per unit surface N with energy momentum $(\hbar\omega, \hat{x}\hbar\omega/c)$ contained in a short bunch of duration τ, corresponds to an intensity $I = N\hbar\omega/\tau$. If the surface is moving with velocity $\mathbf{v} = \beta c$, the frequency of the reflected photons is $\omega_r = \omega(1-\beta)/(1+\beta)$ and the reflected time would be $\tau_r = \tau/(1-\beta)$. Thus the resulting pressure will be $P = \frac{|\Delta p|}{\Delta t} = \frac{N\hbar}{c}\left(\frac{\omega+\omega_r}{\tau_r}\right) = \frac{2I}{c}\left(\frac{1-\beta}{1+\beta}\right)$

where $\gamma_{\text{hb}} = (1 - \mathbf{v}_{\text{hb}}^2/c^2)^{-1/2}$. Solving for the $\mathbf{v}_{\text{hb}}$ expression relativistically which yields

$$\frac{\mathbf{v}_{\text{hb}}}{c} = \frac{\Xi^{1/2}}{1 + \Xi^{1/2}} \tag{3.20}$$

So the relativistic correct expression for the ion energy per nucleon becomes [104, 105]

$$\mathcal{E}_{\text{max}} = 2m_i c^2 \frac{\Xi}{1 + 2\Xi^{1/2}} \tag{3.21}$$

and the scaling with I is turned down to $\text{I}^{1/2}$ at very high intensity. The simulations show that the final energy spectrum observed in the results is determined by the highly transient stage of equilibrium collapse and wave breaking which follow the formation of the singularity. Even referring for a planer geometry, the hole boring process is associated with the ion acceleration from the front side of the target[5].

The above equations (3.16) and (3.21) applies to thick target, i.e. much thicker than the the skin depth in which the ion acceleration by the space-charge field occurs. Ion acceleration in form of bunching and by wave breaking occurs as long as the laser pulse is on and pushing the adjacent surface layer deep into the target by a repeated cycle of charge separation. If the target and laser parameters do not vary much over an acceleration cycle, all the ions get accelerated to an energy $\mathcal{E}_{\text{max}}$ and the HB process which in general of non-stationary nature, might also be described by the quasi-stationary model [104]. Now if the target is thin enough that all the ions get accelerated before the end of laser pulse, in such case the laser pulse is able to further accelerate the ions since they are not screened by the background plasma surface. For example, if the target is of the order of $\sim x_s$ Fig.3.2c, the density profile ends up at the null point of the ponderomotive force and the acceleration cycle is repeated again over the same ions. Thus higher ion energies are expected for such thin targets. Now all the ions have the same velocity and undergo the light sail acceleration which we will discuss now in the next section.

3.2.2 Light-sail Regime: Thin targets

The thin target regime of RPA has been named "Light sail"(LS) as the term is appropriate to refer to a thin object of finite inertia, having low mass and large surface so that it can be significantly accelerated by the boosted action of the radiation pressure. Marx raised this idea by using calculations based on the simple model of a flat, perfect mirror boosted by a plane wave. Marx's concept faced some controversies but later Simmons etal [106] discussed this topic finally by concluding *"whatever his mistakes, at least Marx was more right than his critics"*. The analytic solution and scaling laws provided by the basic model[106] illustrate some appealing features of $\text{LS} - \text{RPA}$ such as high efficiency in the relativistic limit and the possibility to reach up-to very energy with present-day laser and target technology.

Let us consider the sail as a plane mirror of mass M, moving with velocity $\mathbf{V} = dX/dt$ in the laboratory frame S. We assume the mirror to have a reflectivity $R = R(\omega)$, which is defined in the frame where sail S is at rest. A quasi-monochromatic plane wave if intensity I impinges at normal incidence on the sail. The equation of motion for a moving target (sail) in the laboratory frame S can be obtained similarly to Eq.(3.19) with the help of Lorentz transformation into the instantaneous rest frame $S^{'}$ where the force on the target is given by radiation pressure $F^{'} = 2I^{'}R(\omega^{'}A/c)$ where A is the sail surface, $I^{'}$ and $\omega^{'}$ is the intensity and frequency in $S^{'}$ frame. Neglecting absorption for simplicity $(i.e. A = 0)$, we obtain the equation of motion for the light sail as

$$\frac{d}{dt}(\beta\gamma) = \frac{2I(t_r)}{\sigma c^2} R(\omega^{'}) \frac{1-\beta}{1+\beta}, \qquad \frac{dX}{dt} = \beta c \tag{3.22}$$

[5]Notice that in the literature, different definitions such as laser piston [104] or sweeping acceleration[99] are also used to refer to the same process.

where X is the position of the sail, $\beta = \mathbf{v}/c$ is the sail velocity in units of c, $\gamma = (1-\beta^2)^{-1/2}$, $\omega^{'} = \omega[(1-\beta)/(1+\beta)]^{1/2}$ is the laser frequency in the rest (sail) frame and $\sigma = m_i n_i l$ is the mass density per unit surface. The laser intensity I is a function of the retarded time $t_r = t - \frac{X}{c}$

The existing analytical solutions of Eq.(3.22) depends on the suitable expressions for $R(\omega)$. The simplest case is that of a perfectly reflecting mirror ($R = 1$) and a laser pulse of constant intensity I (for detailed derivation, see [106]). The normalized kinetic energy $K(t)$ is given by

$$\frac{K(t)}{mc^2} = \gamma(t) - 1 = \sinh(u) + \frac{1}{4\sinh(u)} - 1 \tag{3.23}$$

$$u \equiv \frac{1}{3} a \sinh(3\Omega t + 2), \qquad \text{where} \qquad \Omega \equiv \frac{Z}{A}\frac{m_e}{m_p}\frac{a_0^2}{\zeta} \tag{3.24}$$

in which ζ has been defined in Eq.2.55 (Ch.2). Asymptotically, $K(t)/mc^2 \simeq (3\Omega t)^{1/3} - 1$. Most significant quantities can be obtained for an arbitrary pulse shape $I(t)$ as a function of the dimensionless pulse fluence $F = \int I dt$ (the pulse energy per unit surface). For $R = 1$, one obtains for $\beta = \beta(t_r)$ [106]

$$\beta(t_r) = \frac{[1+F(\tau)]^2 - 1}{[1+F(\tau)]^2 + 1} \tag{3.25}$$

$$F(t_r) = \frac{2}{\sigma c^2}\int_0^{t_r} I(t^{'}) dt^{'} \tag{3.26}$$

From above equation, we can define the instantaneous efficiency η, as the variation of the sail's energy at the retarded time t_r divided by the electromagnetic power delivered at the sail at the same (retarded instant), i.e. by $I(t_r)$ the ratio between the mechanical energy delivered to the sail and the incident pulse energy as

$$\eta = \frac{2\beta(t_r)}{1+\beta(t_r)} = 1 - \frac{1}{[F(t_r)+1]^2} \tag{3.27}$$

Thus $\eta \to 1$ is obtained in the relativistic limit $\beta(t_r) \to 1$, which is reached when $F \to \infty$[6].

The scalings and estimates implied by Eqs. (3.25) and (3.27) are very useful for ion acceleration by super-intense pulses as they imply that laser parameters needed for interstellar travel are still far away. Let us use a thin solid foil for the sail having density ρ and thickness l, such that $\sigma = \rho l$. Thus the final energy per nucleon $\mathcal{E}_{\text{max}}$ as a function of the total fluence $F = F(\infty)$ is given by

$$\mathcal{E}_{\text{max}} = m_p c^2[\gamma(\infty) - 1] = m_p c^2 \frac{F^2}{2(F+1)} \tag{3.28}$$

where F in practical units is given by

$$F \simeq 2.2 \frac{F}{10^8 \text{J/cm}^2}\left(\frac{\rho}{1\text{g/cm}^3}\right)^{-1}\left(\frac{l}{10\text{nm}}\right)^{-1} \tag{3.29}$$

where F is the laser energy per unit surface and in terms of dimensionless parameters is given by

$$F \simeq \frac{2m_e c^2 n_c a_0^2 \tau \lambda}{m_i n_i l c^3} = 2\pi \frac{Z}{A}\frac{m_e}{m_p}\frac{a_0^2 \tau}{\zeta} \tag{3.30}$$

[6] This result follows from the photon number conservation such as N photons carrying a total energy $N\hbar\omega$, being reflected during short time intervals such that β does not vary significantly. Then the reflected photons have total energy $N\hbar\omega_r$ and the energy transferred to the mirror is $N\hbar(\omega - \omega_r) = N\hbar\omega[2\beta/(1+\beta)]$, thus the efficiency is $\eta = 2\beta/(1+\beta)$

a constant intensity has been assumed in above equation and τ is the laser pulse duration in units of the period $T = 2\pi/\omega = \lambda/c$. With the present day laser technology where target manufacturing can produce films of few nm thickness, e.g. Diamond-Like carbon foils, the values of $a_0^2\tau \sim 10^3$ seems affordable. Thus in principle it seems feasible to reach values of $F > 1$ approaching a regime which can accelerate relativistic ions with high efficiency and a more favorable scaling with the pulse energy at $F \gg 1$.

3.3 Shock Acceleration

Acceleration of particles by collisionless shocks in plasmas is a problem of central interest in astrophysics [107] as well as in laser-plasma physics[78]. Such collisionless shocks are abundant in space and in astrophysical plasmas, e.g. the Earth's bow shock, supernova remnants, interplanetary traveling shocks where in many circumstances the particle transport is caused by wave-particle interactions. The existence of an ion component that is reflected by the shock front is actually a direct signature for the formation of the collisionless, electrostatic shock waves in the basic fluid theory [28, 108, 109], where the electrons are assumed to be in Boltzmann equilibrium. In the frame moving at shock velocity, ions are reflected by the shock if the height of the electrostatic potential barrier Φ_{max} at the front is such that

$$Ze\Phi_{\text{max}} > m_i \mathbf{v}_i^2/2 \tag{3.31}$$

where $\mathbf{v}_i$ is the velocity of the ion component in the shock frame. Behind the shock front, the fields have an oscillating behavior. In a simple picture of ion acceleration by collisionless shocks; ions which are initially at rest, get reflected by the shock front (which acts as the moving wall), and acquire a velocity in lab frame, i.e. $\mathbf{v}_i \simeq 2\mathbf{v}_s$, where $\mathbf{v}_s$ is the shock front velocity.

Nowadays, it is possible to replicate the astrophysical conditions in the laboratory and study of collisionless shock phenomenon has received greater intention from last two decades. Collisionless shock (CS) can be generated in laboratory by interacting a strong laser pulse with overdense plasma [110] as well as by underdense plasma created by using gas jet targets [111] or by the effect of long prepulses in solid targets[102]. The generation of shock waves driven by laser pulses is well known in the moderate intensity($\text{I} = 10^{18}-10^{21}$ W cm^{-2}), nanosecond pulse regime. In a overdense plasma, rapid heating and ablation pressure at the surface may drive a shock wave propagating towards bulk and the study of such propagation may yield information on the equation of state of warm dense matter[112]. In the interaction of super-intense laser pulses with overdense plasma, the light pressure ranges from gigabar to terabar values and, like a piston, may sweep out and compress the laser-produced plasma and push its surface at nearly relativistic speeds. Such combination of strong compression and acceleration is often described as the generation of strong collisionless shock waves propagating towards the bulk of the target. Collisionless shocks with a relatively low Mach number have been investigated in laboratory plasmas since 1970s [113]. Recently theoretical and numerical study also infer about the occurrence of high Mach number collisionless shocks in laser plasma [114].

Ion acceleration by the CS waves is of high interest at the moment and receiving more attention because the energy spectrum of the accelerated ions is ideally monoenergetic, which is quite useful for many kinds of applications. Experimentally in laser-matter interactions, the ion acceleration by CS shocks have been reported in an underdense plasma [111], overdense plasmas [115] and in a gas jet target [79]. Ion acceleration by collisionless shocks in the target bulk is more prominent in case of linearly polarized (LP) pulses as the oscillating component of the $\mathbf{v} \times \mathbf{B}$ drives a sweeping oscillation at 2ω of the density profile which overlaps to the steady effect of the ponderomotive force and causes

strong absorption and fast electron generation. Moreover with the rapid development of laser technology and with the present availability of ultrashort and ultra-intense pulses with focused intensity exceeding $10^{21}\mathrm{W/cm^2}$, makes it possible to conduct laser-plasma interaction without pre-plasmas of large scale lengths where ion acceleration by CS may be examined and tested in more detail.

Numerically, Denavit first observed shock acceleration in their PIC simulations [77]. Later collisionless electrostatic shocks with Mach numbers $\mathrm{M} = \mathbf{v}_s/c_s = 2-3$ have been reported by Silva *etal*[78] where the sound speed is estimated using the fast (hot) electrons temperature $T_h \simeq m_e c^2(\sqrt{1+a_0^2/2}-1)$. The shocks are generated at the target front surface with a velocity close to $\mathbf{v}_{\text{hb}}$ given by Eq.(3.20) consistently with the assumption that they are driven by piston action of the radiation pressure. By estimating the shock velocity with respect to hole-boring velocity $\mathbf{v}_s \simeq \mathbf{v}_{\text{hb}}$[7] in the strongly relativistic limit $a_0 \gg 1$, the condition to obtain radiation pressure driven supersonic shocks and can be written as

$$a_0 > \frac{1}{2\sqrt{2}}\frac{n_e}{n_c} \tag{3.32}$$

As long as the shock velocity $\mathbf{v}_s$ is constant, the reflected ions from the shock front should have velocity $2\mathbf{v}_s$ and produce a monoenergetic peak in the spectrum. Such a peak would evolve into a spectral plateau due to the further acceleration in the sheath field at the rear side of the target [78]. A similar signature was interpreted experimentally as an evidence of front side contribution to ion acceleration [101] with respect to TNSA acceleration at the rear side of the target. Later an interplay between collisionless shock acceleration (CSA) and TNSA has been widely study through numerical simulations by d'Humieres *etal* [116] and Chen *etal* [117]. Very recently CSA has been indicated as the mechanism responsible for monoenergetic proton acceleration up-to $\sim 20\mathrm{MeV}$ energy in the $\mathrm{CO_2}$ laser pulse interaction with Hydrogen gas jets at an intensities up-to $6.5\times10^{16}\mathrm{W/cm^2}$ corresponding to $a_0 = 2.5$[79]. The particular temporal profile of the laser pulse, i.e. $100\ \mathrm{ps}$ train of $3\ \mathrm{ps}$ pulses, require to be essential for the acceleration mechanism, since no spectral peak is observed for a smooth, non-modulated pulse. Comparison with PIC simulations suggests that the multi-peak modulated pulses lead to efficient generation of supra-thermal electrons. It was found that these shocks are formed due to strong electron heating (rather than radiation pressure) in the density gradient which further accelerate monoenergetic beams of protons. However CSA generated by these supra-thermal electrons fall somehow out of the "collective acceleration" paradigm and only a minor fraction of the ions are accelerated by the shock.

In the context of ion acceleration by laser, we prefer to reserve the term "shock" for the regime described above which implies the generation of a "true" electrostatic shock wave, able to propagate into the plasma bulk and drive a ion acceleration there. The formation of true shocks may be inhibited for circular polarization because of the reduced electron heating. According to the fluid theory, a shock wave launched with some velocity $\mathbf{v}_s$ requires the sound speed ($c_s = \sqrt{T_e/m_i}$) and indirectly the electron temperature to be hot enough to prevent the Mach number $\mathrm{M} = \mathbf{v}_s/c_s$ from exceeding the critical value $\mathrm{M_{cr}} \simeq 6.5$ above which one does not have a shock but a pure piston [109]. The detailed discussion for CP simulations have been prescribed in Ch.6 and Ch.7.

In addition to collisionless shocks, the standard fluid theory [27, 28] also predicts electrostatic solitary waves (or solitons) propagating at the velocity $\mathbf{v}_{\text{sol}}$. A necessary and general condition for such solitons to exist is that the electrostatic potential energy jump Φ_{max} has a peak value

$$Ze\Phi_{\text{max}} < m_i\mathbf{v}_{\text{sol}}^2/2 \tag{3.33}$$

[7] The use of two terminology can be understood in such a way that the hole boring and shock acceleration may produce similar type of ion spectrum, because wave breaking at the plasma surface in hole-boring RPA produces ion bunches having maximum velocity $\simeq 2\mathbf{v}_{\text{hb}}$ (see section 3.2.1) as if those ions were reflected from the surface, while at the same time $\mathbf{v}_s \simeq \mathbf{v}_{\text{hb}}$ may occur [78].

so that the background ions are not reflected by these solitary waves. Assuming the electrons in isothermal Boltzmann equilibrium, the condition in Eq. (3.33) poses an upper limit on the Mach number $\mathrm{M} = \mathbf{v}_{\text{sol}}/c_s = 1.6$, where $c_s = \sqrt{T_e/m_i}$ is the speed of sound. The other condition is that the soliton must be supersonic, i.e. $\mathrm{M} > 1$. However, generation of electrostatic solitons may lead to ion acceleration in some circumstances, e.g. the soliton formed within the bulk when reach to rear side of the target, the wave breaking occurs in the expanding rear sheath due to the effect of plasma flow [118]. A detailed discussion about solitary versus shock wave formation and related ion acceleration has been prescribed in $\mathrm{Ch}.6$

CHAPTER 4

Electrostatic Solitons and Shock Waves in Collisionless Plasmas

In a harmonic wave solution, we genrally assume a plane wave of the form $exp\iota(\mathbf{k}.\mathbf{r} - \omega t)$ and the linear wave propagation is studied by considering one of the Fourier component at a time in the small amplitude limit. There are numerous processes via which an unstable mode can saturate and obtain large amplitude. When the amplitude of the wave is sufficiently large, nonlinearity can not be ignored. The nonlinearities occur due to: ion reflection from the wave front, trapping of the particles in the wave potentials, nonlinear Lorentz force, ponderomotive force *etc*. The nonlinearities due to particle reflection and particle trapping considerably increase the richness and variety of wave motion which exist in a plasma and significantly influence the condition required for the formation of localized electrostatic excitations. Below we will discuss such similar nonlinear phenomena and the occurrence of coherent structures such as electrostatic solitary waves and the transition from these solitary waves to collisionless shock waves.

4.1 Waves in Unmagnetized plasma

In this section, we will investigate some of the oscillatory modes (or waves) which can be supported by a homogeneous, unmagnetized plasma. By plasma modes or waves, we refer to propagating linear oscillations. These are obtained by considering the equilibrium state for species $j = e, i$, say $S_0 = [n_{j0}, u_0 = 0, \Phi = 0]$ and then assuming small amplitude harmonic oscillations around that state in the form $S_1 = [n_{j1}, u_1, \Phi_1]$. By small, we mean that say, $n = n_0 + n_1$, for any given species, where $|n_1/n_0| \ll 0$. The "linearized" version of the dynamical equations[1] will be solved to provide the oscillating quantities. In search for a solution of a linear equation, one considers a quantity "A" which is an oscillatory function of a space variable x and of time t. In our case, in a multi-variable problem, we deal with a system of linear equations, so this oscillating function may model any relevant plasma state variable, i.e. the number density n, the electric potential Φ etc. The linear equations may be Fourier transformed in both space and time, thus reducing the differential equations to a set of algebraic equations. Now, we may assume that each perturbed quantity has the mathematical form

$$A(\mathbf{r}, t) = \bar{A} \exp i\,(\mathbf{k} \cdot \mathbf{r} - \omega t) \tag{4.1}$$

where the real part is implicitly assumed. This form describes a wave in which the amplitude n is in general complex, allowing for a non-zero phase constant $\Phi = kx - \omega t$. The ω is the angular frequency while the wave-vector $\mathbf{k}$ gives both the direction of propagation and the wavelength $\lambda = 2\pi/k$. $\bar{A}$ is the

[1] To linearize the fluid equations is to consider a small real parameter, say $\varepsilon \ll 1$ and substitute $n = n_0 + \varepsilon n_1, u = 0 + \varepsilon u_1$ and so on. Isolated terms in ε^1 then give the linearised system while higher order terms $\sim \varepsilon^2, \varepsilon^3$.. are neglected (within the linear analysis).

amplitude of the oscillation. A point of constant phase on the wave form moves such that

$$\frac{d\Phi}{dt} = \mathbf{k} \cdot \mathbf{v}_{\text{ph}} - \omega = 0$$

where the wave phase velocity is

$$\mathbf{v}_{\text{ph}} = \frac{\omega}{k}\hat{\mathbf{k}} \tag{4.2}$$

The phase velocity of a wave may exceed the speed of light, since no information is carried at $\mathbf{v}_{\text{ph}}$. Information is carried by a modulation of the wave in either amplitude or frequency e.g. a wave pulse having a Gaussian envelope.

In general, a wave may contain many different frequencies and can then be described as a sum e.g. $A = \sum_j A_j e^{i(k_j x - \omega_j t)}$ or an integral over many such single frequency components each described by Eq. (4.1). In such cases, the quantity A is a wave packet (or wave group) and is confined within an "envelope" of varying amplitude. Each component within the envelope may have its own phase velocity, but the quantity which has a physical meaning is the velocity of the envelope, i.e. the velocity at which energy is transported by the wave and is known as the "group velocity" and is given by:

$$v_g = \frac{d\omega}{dk} \tag{4.3}$$

There is a relation between ω and $\mathbf{k}$ and is determined by the physical properties of the system. The function $\omega(\mathbf{k})$ is called the dispersion relation for the wave. Both the $\mathbf{v}_{\text{ph}}$ and v_g can be inferred from this dispersion relation. We will now identify the different wave modes that occurs in an unmagnetized plasma and will find the dispersion relation $\omega(\mathbf{k})$ for each.

4.1.1 Plasma Oscillations

Here, we will use the fluid dynamics by treating the electrons and ions separately as fluids under the influence of electromagnetic forces, generally called as *two-fluid formalism* for plasma. Considering a two species (electron-ion) plasma with $Z = 1$. In the simplest case of plasma with the following assumptions: (1) plasma is infinite, neutral, uniform and at rest (2) no magnetic field, i.e. $\mathbf{B} = 0$, (3) for the cold plasma approximation, neglecting thermal motions $(T \simeq 0)$, (4) the ions are fixed in space and are in a uniform distribution, (5) collisionless plasma, (6) considering the electrons motion only along the $x-$axis. Out of the full set of two fluid and Maxwell equations, the relevant equations for the electron fluid are the continuity and momentum equations, coupled to Gauss's law:

$$\frac{\partial n_e}{\partial t} + \nabla \cdot (n_e \mathbf{u}_e) = 0 \tag{4.4}$$

$$m_e n_e \left[\frac{\partial \mathbf{u}_e}{\partial t} + (\mathbf{u}_e \cdot \nabla)\mathbf{u}_e\right] = -e n_e \mathbf{E} \tag{4.5}$$

$$\nabla \cdot \mathbf{E} = 4\pi\rho = 4\pi e(n_i - n_e) \tag{4.6}$$

Simplifying the above set of equation by linearizing[2] it and by assuming that the oscillation introduces only a small perturbation to the equilibrium state of plasma. Using the above defined assumptions, the above set of equations becomes:

$$-i\omega n_1 = -i\mathbf{k} n_0 \mathbf{u}_1 \tag{4.7}$$

[2] Linearizion is done by writing variables as the sum of the equilibrium, labeled with suffix "0" and a small perturbation labeled with suffix "1" such that $n_e = n_0 + n_1$ and similarly the other variables.

$$-i\omega m_e \mathbf{u}_1 = -e\mathbf{E}_1 \tag{4.8}$$

$$4\pi e n_1 = -i\mathbf{k}\mathbf{E}_1 \tag{4.9}$$

This is a homogeneous system of three algebraic equations in the three variables n_1, $\mathbf{u}_1$ and $\mathbf{E}_1$. Eliminating n_1 and $\mathbf{E}_1$ and equating for $\mathbf{u}_1$, we get the electron plasma frequency ω_p

$$\omega = \sqrt{\frac{4\pi n_0 e^2}{m_e}} \equiv \omega_p \tag{4.10}$$

Therefore in order for an electron density oscillation to be supported in a cold, uniform plasma, the frequency of the oscillation must be equal to the plasma frequency. Since ω is constant and independent from wave vector $\mathbf{k}$, so the phase velocity $\mathbf{v}_{\text{ph}}$ and group velocity v_g of such oscillations is zero which means that the charge oscillation do not propagate through plasma. This oscillation is a fundamental mode of the plasma and has many ramifications. In the next step, we will investigate its importance.

4.1.2 Electron Oscillations in Warm Plasmas: Langmuir waves

Considering now a plasma satisfying all assumptions given in the previous section but having a "warm" plasma with a temperature $T_e \neq 0$. Thus electrons make streaming into adjacent layers of the plasma with their thermal velocities and will carry information about what is happening in the oscillating region. So in such a warm plasma, the pressure gradient term $-\nabla p_e$ needs to be included in in the momentum equation (4.5). The electron motion is effectively one dimensional and have only one (translational) degree of freedom. The relevant specific heat then at constant volume $c_v = K_B/2$ and at constant pressure $c_p = 3K_B/2$ per electron, giving the specific heat ratio $\gamma_e = c_p/c_v = 3$. Therefore the corresponding perturbations of electron pressure and density are related as

$$-\nabla p_e = -\gamma_e K_B T_e \nabla n_e = -3K_B T_e \nabla n_e = -3K_B T_e \nabla(n_0 + n_1) = -3K_B T_e \frac{\partial n_1}{\partial x}\hat{x} \tag{4.11}$$

Adding the above pressure term in the right hand side of the momentum equation (4.5) and after linearizing and imposing oscillatory solutions, the momentum equation for electron fluid becomes

$$m_e n_0 \frac{\partial \mathbf{u}_1}{\partial t} = -en_0\mathbf{E}_1 - 3K_B T_e \frac{\partial n_1}{\partial x}$$

$$-i\omega m_e n_0 \mathbf{u}_1 = -en_0\mathbf{E}_1 - 3K_B T_e i\mathbf{k} n_1 \tag{4.12}$$

Putting n_1 and $\mathbf{E}_1$ from Eq. $(4.7 - 4.9)$, we have

$$im_e\omega n_0 \mathbf{u}_1 = \left[en_0\left(\frac{-4\pi e}{i\mathbf{k}}\right) + 3K_B T_e i\mathbf{k}\right]\frac{i\mathbf{k}n_0}{i\omega}\mathbf{u}_1$$

$$\omega^2 \quad = \quad \omega_p^2 + \frac{3K_B T_e}{m_e}k^2 \quad = \quad \omega_p^2(1 + 3k^2\lambda_D^2) \tag{4.13}$$

where $\lambda_D = (K_B T_e/4\pi n_e e^2)^{1/2}$ is the Debye length. Eq.(4.13) is the Bohm-Gross dispersion relation for the Langmuir waves. From this, we can deduce the phase speed of the the Langmuir wave as

$$\mathbf{v}_{\text{ph}} = \left(\frac{K_B T_e}{m_e}\right)^{1/2}\left(3 + \frac{1}{k^2\lambda_D^2}\right)^{1/2} \tag{4.14}$$

The above dispersion relation is only valid for wave-vector much longer than the Debye length (*i.e.* $k\lambda_D \ll 1$). When the wave-vector $\mathbf{k}$ is less than or of the order of Debye length (*i.e.* $k\lambda_D \geq 1$), the phase speed of electrons becomes comparable to the thermal speed and it becomes possible for individual electrons to transfer energy between adjacent compression and rarefactions in the wave which results in energy transfer and damp the wave.

By using the expression for the thermal velocity $\mathbf{v}_{\text{th}} = \sqrt{\frac{2K_BT_e}{m_e}}$, the Eq.$(4.13)$ can be rewritten as

$$\omega^2 = \omega_p^2 + \frac{3}{2}k^2\mathbf{v}_{\text{th}}^2 \tag{4.15}$$

Eq.(4.15) is the dispersion relation for electron oscillations in warm plasmas, also known as Langmuir waves. Since in this case, ω is a function of $\mathbf{k}$, the group velocity will be different from zero. Differentiating the above equation, we get the group velocity

$$v_g = \frac{d\omega}{dk} = \frac{3k\mathbf{v}_{\text{th}}^2}{2\omega} = \frac{3\mathbf{v}_{\text{th}}^2}{2\mathbf{v}_{\text{ph}}} \tag{4.16}$$

The perturbation associated to the oscillation propagates through the plasma at the group velocity v_g. It is clearly seen from Eq.(4.16) that the group velocity v_g is always less than $(3/2)^{1/2}\mathbf{v}_{\text{th}}$ which in the non-relativistic case is always much less than c. Electron plasma waves are longitudinal waves, i.e. the oscillation is along the direction of propagation. When thermal motion are "turned on", the resulting thermal pressure gradients at the finite wave number k, convert the longitudinal plasma oscillations into propagating energy transport modes, called as "Langmuir waves". Thus the key of the Langmuir waves propagation is thermal pressure of the warm electrons. The proton pressure is negligible because they oscillate with an amplitude that is very small compared to electrons. In the following, we will study the ion motion in warm plasma.

4.1.3 Ion Acoustic Waves in Electron-Ion Plasma

In above, for the Langmuir wave analysis, we have ignored the ion motion by justifying that the ion thermal speed is negligibly small compared to the electron thermal speed, *i.e.* $T_i \ll T_e(m_i/m_e)$. However, the ion motion is not ignorable in a second type of plasma waves which exist at finite temperature, known as ion acoustic waves. These waves propagate with frequencies far much below the electron plasma frequency such that the electrons remain locked electro-statically to ions, keeping the plasma charge neutral. If $Z = 1$, for this type of oscillations, we therefore may assume the "plasma approximation" i.e. $n_i \simeq n_e = n$ and so here do not use Poisson's equation. We will investigate this type of oscillations by using continuity and ion momentum equation in an homogeneous, unmagnetized ($\mathbf{B} = 0$), infinite, collisionless, warm (ions having temperature $T_i \neq 0$) plasma. Under these conditions, the momentum equation of ion fluid becomes:

$$m_i n_i \left[\frac{\partial \mathbf{u}_i}{\partial t} + (\mathbf{u}_i \cdot \nabla)\mathbf{u}_i\right] = Zen_i\mathbf{E} - \nabla p_i \tag{4.17}$$

In this case, it is useful to write the electric field as a function of potential Φ, i.e. $\mathbf{E} = -\nabla\Phi = -i\mathbf{k}\Phi$. The ion pressure term $-\nabla p_i$ can be written similarly as we done for the electron fluid, i.e. from Eq. (4.11), for ion fluid it becomes: $-\frac{\partial p_i}{\partial x} = -\gamma_i K_B T_i \frac{\partial n_i}{\partial x}$.

After linearization and imposting perturbation terms (as done before for electron momentum equation), the ion momentum equation becomes;

$$-i\omega n_0 m_i \mathbf{u}_1 = -en_0 i\mathbf{k}\Phi_1 - \gamma_i K_B T_i i\mathbf{k}n_1 \tag{4.18}$$

As the electrons having temperature T_e respond rapidly to the electric field and redistribute themselves in equilibrium with potential Φ_1 and will follow the Boltzmann relation:

$$n_e = n_e \exp\left(\frac{e\Phi}{K_B T_e}\right) \simeq n_0 \left(1 + \frac{e\Phi_1}{K_B T_e} + ...\right) \tag{4.19}$$

From above equation, one can deduce the first order density perturbation of electrons (and of ions, since $n_e = n_i$) such as

$$n_1 = n_0 \frac{e\Phi_1}{K_B T_e}. \tag{4.20}$$

Similarly we can deduce the linearized ion fluid continuity equation from Eq. (4.7),

$$i\omega n_1 = n_0 i\mathbf{k}\mathbf{u}_i \tag{4.21}$$

Now we have obtained an homogeneous system of three equations, i.e Eqs.$(4.18), (4.20)$ and (4.21) in three variables $n_1, \mathbf{u}_1, \Phi_1$. Solving the above three equations for the ion acoustic dispersion relation, we get

$$\omega^2 = k^2 \left(\frac{\gamma_e K_B T_e + \gamma_i K_B T_i}{m_i}\right) \tag{4.22}$$

Now in an ion acoustic wave with respect to Langmuir electron waves, the individual thermal electrons, due to $m_e \ll m_i$, can travel over many wavelengths during a single wave period, i.e. move very rapidly and the electrons distribution may be assumed to be isothermal. Therefore the electrons effective one dimensional specific heat ratio is $\gamma_e = 1$ while the ions suffers one-dimensional compressions in the plane wave, so $\gamma_i = 3$. Eventhough the electrons provide the restoring force to the ion acoustic waves, the inertia of the protons and electro-statically locked electrons is entirely that of the heavy protons. Rewriting Eq. (4.22):

$$\frac{\omega}{k} = \left(\frac{K_B T_e + 3K_B T_i}{m_i}\right)^{1/2} \equiv c_s \tag{4.23}$$

where c_s is the speed of sound in the plasma. From Eq. (4.23), for an ion acoustic wave, both the phase and group velocity will be equal to c_s (for lower values of ω and k), as clear from a graphical representation in the (k, ω) plane showing a straight line in Fig.4.1b.

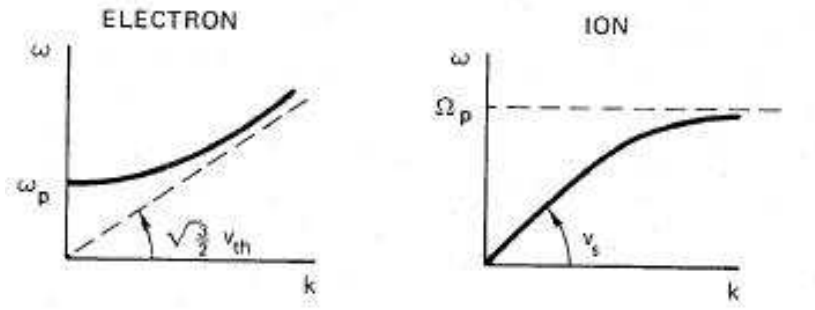

Figure 4.1: Dispersion relation for electrostatic waves, Langmuir waves and Ion acoustic waves in an unmagnetized plasmas. Reprinted from [119].

Charge separation effects on Ion-acoustic waves

In order to obtain a more accurate expression for the dispersion relation for the ion-acoustic waves, one must use the Poisson's equation to link the potential Φ and the local electron and ion density perturbations, which now will have to indicate with different symbols , *i.e.* n_{i1} and n_{e1} respectively. In such case, the linearized set of equations, i.e. continuity, momentum and Poisson's equations, used are

$$i\omega n_{i1} = n_0 i\mathbf{k}\mathbf{u}_1 \tag{4.24}$$

$$-i\omega n_0 m_i \mathbf{u}_1 = -en_0 i\mathbf{k}\Phi_1 - \gamma_i K_B T_i i\mathbf{k} n_{i1} \tag{4.25}$$

$$\frac{\partial^2 \Phi_1}{\partial x^2} = 4\pi e n_{i1} - n_{e1} \tag{4.26}$$

from the above Poisson's equation, the electron density n_{e1} is given by linearized Boltzmann relation, i.e from Eq. (4.20) and the ion density n_{i1} can be calculated from the continuity equation such as

$$n_{e1} = n_0 \frac{e\Phi_1}{K_B T_e} \qquad \text{and} \qquad n_{i1} = \frac{k}{\omega} n_0 \mathbf{u}_1 \tag{4.27}$$

By using the set of equations above, we get a more accurate expression for the dispersion relation of ion acoustic wave

$$\frac{\omega}{k} = \left(\frac{K_B T_e}{m_i} \frac{1}{1 + k^2 \lambda_D^2} + 3\frac{K_B T_i}{m_i} \right)^{1/2} \tag{4.28}$$

When $T_i \ll T_e$, we ignore the ion pressure term T_i and the waves restoring force is provided by the electron pressure. The character of these ion acoustic waves get modified when their wavelength becomes of the order of the Debye length *i.e.* $k\lambda_D \sim 1$, then the dispersion relation get modified to

$$\frac{\omega}{k} = \left(\frac{K_B T_e / m_i}{1 + k^2 \lambda_D^2} \right)^{1/2} = \mathbf{v}_{\text{iaw}} \tag{4.29}$$

which means that for for $k\lambda_D \gg 1$, the waves frequency approaches the ion plasma frequency $\Omega_p \equiv \sqrt{4\pi n e^2/m_i} \simeq \omega_p \sqrt{m_e/m_i}$, where ω_p is the electron plasma frequency as explained in Eq.(4.10). Eq. $(4.28 - 4.29)$ revealed that, for high frequencies (short wavelength λ_D), the ion acoustic waves turn into a constant-frequency wave (see Fig.4.1b). Thus there is a complementary behavior between Langmuir waves and ion acoustic waves: the former are basically constant frequency but become constant velocity at large k while the latter are basically constant velocity, but becomes constant frequency at large k.

In the following sections, we will explore the nonlinear effects in the ion acoustic waves and how they give rise to solitons and shock waves by using the K-dV perturbation method and Sagdeev pseudo-potential method and later will prescribe the conditions in which these solitary acoustic waves breaks and convert into collisionless shock waves.

4.2 Nonlinear Effects on Ion Acoustic Waves

Nonlinearity is a fascinating element of nature whose importance has been appreciated for many years when considering large amplitude wave motions observed in various fields, *e.g.*, fluids and plasmas, astrophysics, particle physics, quantum fields, chemical, biological and geological systems. The nonlinearity evidently modifies the pattern of motion of a wave described by the linear theory, i.e. the pattern which is harmonic in the linear approximation, becomes distorted and display a number of changes

in the course of time, for instance from a sine wave to a lopsided triangular waveform (nonlinear periodic wave). The nonlinearities in the plasmas contribute to the localization of waves, leading to different type of interesting coherent nonlinear wave structures. Such structures have been reported in laser plasmas interactions in the form of electrostatic [23] or electromagnetic solitons [24], collisionless shocks [78], ions and electrons phase space holes [20] *etc*. They arise out of interplay between some of the mechanisms in physical systems such as diffraction, dispersion, dissipation and nonlinearly.

4.2.1 Nonlinear Plasma Oscillations

In general, in a plasma; the dissipative effects ultimately set a limit on the steepness of the wave front and in a collisionless plasma, the chief mechanism responsible for the function is dispersion. The increasing steepness of the leading edge of the wave as a result of nonlinearity, implies the generation of higher harmonics in the wave[120]. These two effects (i.e. nonlinearity and dispersion) are responsible for the interesting features of the asymptotic wave motion which further develop the spontaneous production of intense oscillations as a consequence of the competition between dispersion and nonlinearity. We will now explain the possible nonlinear distortion to the harmonic wave profile in a collisionless plasma by considering the evolution of so-called simple waves. Consider now a one-dimensional simple wave equation for the velocity amplitude of a wave in a plasma fluid such as

$$\frac{d\mathbf{u}}{dt} \equiv \frac{\partial \mathbf{u}}{\partial t} + \mathbf{u}\frac{\partial \mathbf{u}}{\partial x} = 0 \tag{4.30}$$

above equation is the convective derivative in a fluid and describes the disturbance evolution as long as no friction or other force come into play. The term on the left hand side when expanded into a Fourier series, contains a large number of wave-wave interaction terms, as a result super-position and coupling of different wavelengths imply the deformation of the wave profile. Now, let us assume that the initial wave $\mathbf{u}(x,t) = A\sin[k(x-u_0t)]$, is injected into the plasma with u_0 being the convection speed. During the propagation through plasma, the main effect on the shape of the disturbance arises from the second nonlinear term $(\mathbf{u}\frac{\partial \mathbf{u}}{\partial x})$ which can be written as $\mathbf{u}k\cos[k(x-u_0t)]$ or $\frac{1}{2}k\sin[2k(x-u_0t)]$. This nonlinear term generates harmonic sidebands of half amplitude and half the wavelength of the original wave which further with the same mechanism, generate sidebands at quarter original amplitude and wavelength and so on generating with increasingly shorter wavelengths. Therefore, the total amplitude which is the superposition of all these sideband harmonics is

$$\mathbf{u}_k(x,t) = \sum_n \frac{A}{2^n}\sin 2^n[k(x-u_0t)] \qquad \text{where}(n = 0,1,2,..) \tag{4.31}$$

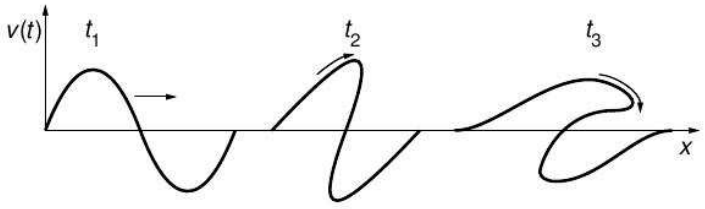

Figure 4.2: Steepening and breaking of a wave in a collisionless plasma. From *left to right* the steepening effect is presented at different times for a system without any dissipation. The wave breaking phenomenon is achieved at time t_3. Figure reprinted from [120]

Now ever shorter wavelength contribute, when the faster (shorter) wavelength waves have higher phase velocity, will overcome the slower (longer) wavelength waves and causes steepening of the wave until the gradient becomes so short that other processes take over[120]. Steepening causes shortening of the wavelength until the extension of the wave packet in real space becomes comparable to the internal dissipation scale, a ramp like structure (see Fig.4.2 at t_3) may form out of the wave front [27]. Suppose this ramp like structure forms at t_r, and for the time $t > t_r$, the wave will turn over and ultimately lead to wave breaking or collapse. Fig.4.2 shows schematically how this wave breaking evolves in time in a collisionless plasma. This wave breaking can be prevented only by additional processes which sets on when the wavelength of the ramp becomes so short that the terms of higher velocity gradients (in Eq.4.31) must be taken into account. In general, Eq.(4.31) in the wave frame of reference, its right hand is a function $\mathbf{F}(\mathbf{u})$ and can be further expanded to higher harmonics with respect to $\mathbf{u}$ such that

$$\frac{\partial \mathbf{u}}{\partial t} + \mathbf{u}\frac{\partial \mathbf{u}}{\partial x} = \frac{\partial}{\partial x} D \frac{\partial \mathbf{u}}{\partial x} - \beta \frac{\partial^3 \mathbf{u}}{\partial x^3} + ... \tag{4.32}$$

The first term on the right is a diffusive term with diffusion coefficient $D(x)$. As we are ignoring diffusion term, so $D(x)$ be considered as zero. The second term with arbitrary coefficient β is the lowest order contribution of wave dispersion to the evolution of wave amplitude and shape. By performing Fourier analysis for a harmonic perturbation $\mathbf{u} = A\exp i(kx - \omega t)$, the procedure yields the following dispersion relation

$$\omega - kc + k^3\beta = 0 \tag{4.33}$$

Thus a wave if not breaking, can be balanced and remain steepen until the dispersion term start competing with the nonlinearity. In the following sections we will show the interaction between nonlinearity and dispersion by calculating the solitary wave solutions using KdV perturbation and Sagdeev pseudo-potential method and further explain the conditions in which these kind of nonlinear waves intimately related with collisionless shock waves.

4.2.2 Ion Acoustic Solitary wave

A soliton or solitary wave is a hump or dip shaped nonlinear wave of relatively stable profile as an arbitrary pulse or disturbance and can be regarded as a linear superposition of sinusoidal wave trains with different frequencies. If each of these linear waves propagates with the same velocity then the medium is called as non-dispersive and the pulses travels without deforming its shape. If the velocity of each wave train is different, then the pulse spread with time and the medium is called dispersive medium. These stable stationary structures are special kind of "wave" which can be formed when the "dispersion" and "nonlinear" effects compromise with each other in the media [121]. The small but finite amplitude solitary waves commonly known as KdV solitons are governed by the Korteweg-de-vries (KdV) type equation. Solitary waves are not only of fundamental mathematical interest but over the years have gained the interest in large number of applications. These waves are frequently observed while studying in shallow water waves [122], in space plasmas[123], in laser plasma interactions [124, 125] and other plasma phenomenon such as ion acoustic solitons [126], dust acoustic solitons [127]. These nonlinear waves which represent the plasma states far from thermodynamic equilibrium, can be created in laboratory plasmas under controlled conditions. In the present report, the focus is on the the ion-acoustic solitons resulting from the interaction of intense laser pulses with plasmas.

Solitary waves in relativistic plasma

The behavior of nonlinear one-dimensional relativistic ion-acoustic solitons and their existence have been studied analytically by many researchers [128, 129] in different plasma models. When the speed of electrons and ions in a plasma approaches the velocity of light, relativistic effects modify the behavior of the solitons [130]. Such fast solitons which propagate in a collisionless plasma with group velocity close to the speed of light and may acts as a tool for photon and particle acceleration[131, 132]. Relativistic plasma solitons in laser plasma interactions, were first found numerically using computer simulations [24] and later also detected in laboratory experiments [124].

Electrostatic ion-acoustic (EIA) solitons [133], which are of prime interest in this thesis, are the solitons which are formed under the influence of electrostatic fields only. Several authors study the behavior of EIA solitons in relativistic plasmas [134, 135]. The first analytical observation of existence of EIA solitons in electron-ion plasma have been given by Sagdeev [27]. These solitons exist for certain range of Mach number M, otherwise destroy their symmetry and convert into shock waves [27, 113]. The formation and propagation of EIA solitons are observed experimentally first in 70's by Ikezi [136, 137]. Experiments have been also performed by Ikezi group for large-amplitude ion acoustic waves to explain nonlinear collisionless damping [138, 139]. Later, they also explained by his experiments, the ion trapping instabilities [140] and the particle reflection [141] phenomenons which results in generation of laminar collisionless shock waves. Numerically, such types of electrostatic solitary waves in laser plasmas have been observed by [118] which loses its symmetry by accelerating ions by reflection from the tip of the solitary wave. In our numerical simulations discussed in $\mathrm{Ch.6}$, we also observed such types of electrostatic ion-acoustic solitary waves and the related ion acceleration from the wave front.

4.2.3 Shock wave in Collisionless Plasma

A shock wave can occur in collisional as well as in collisionless plasmas[3]. Collisionless shocks (CS) occur generally in dilute hot gases which are in the state of fully ionized plasmas and are hot enough for binary collisions to become completely unimportant. The first conclusive evidence of existence of CS came from astrophysics, i.e. the plasma flow from the Sun, the solar wind is highly supersonic while encountering with the earth magnetic fields, a strong shock wave may formed. However, the vast majority of astrophysical shocks evolve under condition of highly dilute matter are generally collisionless in nature, e.g. the Earth bow shock. In laboratory experiments, first evidence of CS waves had been reported in 1965[26], since then the research on this topic has developed into its own discipline. In addition to wave type, collisionless shocks are classified according to the level of turbulence which causes the dissipation. The low Mach numbers shocks are classified as laminar with smooth profiles of plasma parameter and fields and a low value of turbulent drag rate ($\langle \delta \mathbf{E} \delta n \rangle$). For high Mach numbers, the increasing level of $\langle \delta \mathbf{E} \delta n \rangle$ broadens the $\mathbf{E}$ and $\mathbf{B}$ profiles and the shocks formed are turbulent shocks. There are various types of shocks that may develop in a collisionless plasma such as electrostatic shocks, magnetized shocks, MHD shocks etc[142], but the prime interest of this thesis is on electrostatic collisionless (EC) shocks. Considering them here in brief, for small Mach number $\mathrm{M} = v_s/c_s$ where

[3] In collision dominated plasmas; the matter is so dense that the shock formation proceeds on time scales longer than the binary collisional time scale i.e; $\tau_{coll} \simeq \lambda_{coll}/v_{th}$. So all shocks whose width Δ_{sh} is comparable to or larger than the collisional mean free path $\lambda_{coll} = (\sigma_{coll} N)^{-1}$ (where σ_{coll} is the collisional cross-section and N is matter density), are known as collisional shocks[142]. On the other side, in collisionless shocks (CS), the mean free path of individual particles is much larger than the characteristic scales of the shock structure, i.e.$\lambda_{coll} \gg \Delta_{sh}$ and effective collisions and pressure support are not mediated by particle - particle interactions, but by collective forces [143].

$c_s = T_e + \gamma_i T_i/m_i$ having $T_e/T_i \gg 1$, due to the dispersive spreading[4] of the ion acoustic waves (see Eq. 4.33), the electrostatic shocks are generated which further depends upon the electron density and temperatures as a function of electrostatic potential Φ[144].

Particle reflection by collisionless shocks had been first suggested and inferred as an important mechanism for shock dissipation by [27]. To infer about the reflection of particles from the shock on the smaller scale or to elucidate the internal physical structure of shocks, one has to direct to numerical simulations which in addition to analytical methods, are the most valuable tool for investigating collisionless plasma processes. First one dimensional simulations for electrostatic shocks have been performed by very small number of particles and in a small simulation boxes by [145] and observed strong plasma heating. The first indication for reflection of particles from shock wave front is given by [146]. Later, [108, 109] confirmed that in the large simulation boxes, at higher Mach numbers, the collisionless electrostatic shocks indeed reflect ions back upstream when the Mach number exceeds a certain critical value and the wave structure is strongly perturbed and damped.

Although the acceleration of particles by shocks is supposed to exist widely in space and astrophysical plasmas [107], yet it is not easy to confirm experimentally. In the progress of laser technology, the laser plasma interactions also provides a possible way to produce collisionless shocks in the laboratory and CS can be generated by high intensity relativistic laser pulse with solid or gas jet targets. Electrostatic collisionless shocks by laser plasma interactions have been first observed by optical probe, which could not resolve the shock wave front and be able to distinguish only different typologies of shocks[147]. Later the proton projection imaging (PPI) technique able to resolve the shock front with simultaneous measurement of shock propagation velocity, associated electrostatic field with high spatial and temporal resolution[110]. Ions located deep in the plasma can be accelerated to high energy by collisionless shocks and is of high interest at the moment because of the narrow energy spectrum of the accelerated ions. A detailed discussion about the generation of collisionless shocks by laser plasmas interactions and related ion acceleration is performed in Ch.3., Sec. 3.3.

4.3 Nonlinear Wave Methodology

We will now explain the nonlinear plasma dynamics by going beyond the standard linear hypothesis (discussed in sec.4.1). There exist various nonlinear methods for the analytical treatment of nonlinear plasma equations such as reductive perturbation method (RPM), Lax pair scheme, inverse scattering method and pseudo-potential methods. Lax scheme and scattering method give exact solutions while the perturbation method is an approximation and studies small deviations from linear wave theory. The pseudo-potential method are valid for arbitrary amplitudes, but assume a truly stationary structure. Here we will discuss in detail the Korteweg-de-Vries (KdV) perturbation method for the small amplitude solitary waves and the Sagdeev pseudo-potential method for large amplitude waves. Usually solitary waves or solitons are solutions to a system of coupled ordinary differential equations for the potential A and Φ. All other quantities like plasma density (n) and generalized momentum (P) can be calculated from A and Φ. The stability properties of the soliton, the life time of existence of such structures and the nonlinear evolution of solitons with perturbations, can be calculated using above defined analytic methods.

[4] In a non-dissipative medium, due to the nonlinear evolution of a dispersive wave disturbance many small wavelength waves are formed. In such modes where the faster wavelength waves having higher phase velocity, will overcome the slower wavelength waves which results in steepening of the density or potential pulse and formation of a trailing ion-acoustic shock wave.

4.3.1 Reductive perturbation method

Concept of reductive perturbation method was given by Gardner and Morikawa (1960) and later explained in a more general formulation by Tanuiti and his coworkers. Reductive perturbation method keeps a balance between the nonlinearity and dispersion. This method establishes a systematic way for the reduction of fairly general nonlinear system to a single nonlinear equation describing the behavior of higher order harmonics. With the help of this method, one can derive the Nonlinear Schrodinger, Korteweg-de Vries (KdV), modified Korteweg-de Vries (m-KdV) and the Kadomtsev Petviashvili (KP) equations. For this, the following scales transformation is used

$$\xi = \varepsilon^{\alpha}(x - \mathbf{u}t) \qquad \text{and} \qquad \tau = \varepsilon^{3\alpha}t \tag{4.34}$$

where α is the scaling parameter. Instead of using the independent variables x and t, solving equation using scale transformations involves going into a frame of reference which is moving with constant velocity u with respect to the fixed frame. Many of these transformations follow a standard pattern in which one is interested in relatively small deviations from some equilibrium state of a physical system. The method of scale transformations is simply used to suppress the secular terms, in order to extend the range of validity of the asymptotic expansion [148].

So by combining this transformation with a perturbation expansion of the dependent variables, here we will use K-dV perturbation method to track the asymptotic behavior of the wave. In this contest, the decisive influence on the development of the theory of nonlinear waves was exerted by the idea of Korteweg-de Vries which possibly simplify the initial equations by keeping the nonlinear and dispersive terms of the same order of accuracy.

Derivation of KdV Equation- Ion acoustic Solitons

K-dV model is universal in the sense that it applies to any wave motion with weak nonlinearity and weak long wave dispersion. The KdV equation is a hyperbolic partial differential equation (PDE) and describes a reversible dynamic process. The KdV equation is the fundamental equation describing the propagation of nonlinear waves in a medium with weak dispersion effects, having solutions as stable solitary wave structures i.e., solitons. The KdV equation is the nonlinear PDE for $\mathbf{u}(x,t)$ which we get from Eq.(4.32) by neglecting diffusion term D and is described as follows:

$$\frac{\partial \mathbf{u}}{\partial t} + \alpha \mathbf{u}\frac{\partial \mathbf{u}}{\partial x} + \beta \frac{\partial^3 \mathbf{u}}{\partial x^3} = 0 \tag{4.35}$$

This is a generic asymptotic equation that describes weakly nonlinear waves with weak long wave dispersion. $\mathbf{u}$ is the velocity of the wave and α and β are nonlinear and dispersion coefficient respectively. In above, term $\frac{\partial \mathbf{u}}{\partial t}$ is the rate of change of the wave profile $\mathbf{u}$ in a reference frame moving with the linearized phase velocity of the wave. The term $\mathbf{u}\frac{\partial \mathbf{u}}{\partial x}$ is an advective nonlinearity and $\frac{\partial^3 \mathbf{u}}{\partial x^3}$ is a linear dispersion term.

Here we will illustrate this technique on the specific problem of one-dimensional motion of ion-acoustic waves by K-dV perturbation method in an unmagnetized, electron-ion collisionless plasmas by considering cold ions and Boltzmann distributed electrons, in a plane geometry. Rewriting the linearized continuity Eq.(4.4) for the ion fluid as

$$\frac{\partial n}{\partial t} + \frac{\partial (n\mathbf{u})}{\partial x} = 0 \tag{4.36}$$

where n is the ion number density. Similarly the linearized ion momentum equation from Eq.(4.5) is

$$\frac{\partial \mathbf{u}}{\partial t} + \mathbf{u}\frac{\partial \mathbf{u}}{\partial x} = -\frac{e}{m_i}\frac{\partial \Phi}{\partial x} \tag{4.37}$$

where $\mathbf{u}$ is the ion fluid velocity and Φ is the electrostatic potential, m_i and e are the mass and charge of the ions. The electrons (having charge $-e$) are Boltzmann distributed and their density is given by $n_e = n_0 \exp(e\Phi/K_B T_e)$, where n_0 is the initial common density at equilibrium, K_B is the Boltzmann constant and T_e is the electron temperature. Therefore the Poisson's Eq.(4.6) becomes:

$$\frac{\partial \mathbf{E}}{\partial x} = -\frac{\partial^2 \Phi}{\partial x^2} = 4\pi e\left(n - n_0 e^{\left(\frac{e\Phi}{K_B T}\right)}\right) \tag{4.38}$$

We now normalize the above three equations, the ion density n to n_0, the ion velocity u to the ion acoustic speed c_s defined by $c_s^2 = K_B T_e/m_i$, potential Φ to $K_B T_e/e$, the time t to the inverse of Ω_p^{-1} where $\Omega_p^2 = 4\pi n_0 e^2/m_i$ is the ion plasma frequency and space x to the electron Debye length λ_D defined by $\lambda_D^2 = K_B T_e/4\pi n_0 e^2$. So the resulting reduced set of equation becomes

$$\begin{aligned}
\frac{\partial n}{\partial t} + \frac{\partial (n\mathbf{u})}{\partial x} &= 0 \\
\frac{\partial \mathbf{u}}{\partial t} + \mathbf{u}\frac{\partial \mathbf{u}}{\partial x} &= -\frac{\partial \Phi}{\partial x} \\
\frac{\partial^2 \Phi}{\partial x^2} &= e^{\Phi} - n
\end{aligned} \tag{4.39}$$

Now using the perturbation theory, we will make use of the following expansion

$$e^{\Phi} = 1 + \Phi + \frac{\Phi^2}{2} + \frac{\Phi^3}{6} + ... \tag{4.40}$$

Thus writing the dependent variables $n, \mathbf{u}$ and Φ in terms of ε by applying some initial conditions such that $\mathbf{u}_0 = 0$ since plasma is initially at rest, $\Phi_0 = 0$ as plasma is initially neutral; $n_0 \neq 0$, yet $\frac{\partial n_0}{\partial x} = 0$, the plasma is initially uniform and all temporal derivatives of equilibrium quantities are constant. The physical parameters n, u and Φ are expressed as a power series in terms of ε about the equilibrium as

$$\begin{aligned}
n &= 1 + \varepsilon n_1 + \varepsilon^2 n_2 + ... \\
\mathbf{u} &= \varepsilon \mathbf{u}_1 + \varepsilon^2 \mathbf{u}_2 + ... \\
\Phi &= \varepsilon \phi_1 + \varepsilon^2 \phi_2 + ...
\end{aligned} \tag{4.41}$$

To recover the K-dV equation, we must expand in the wave amplitude and keep one order higher than the linear theory. We will consider a perturbative approach which is appropriate in the long wavelength limit; i.e for $k \ll 1$, where dispersion relation is $\omega \simeq k$ and the group velocity approaches the phase velocity, $v_g \simeq \mathbf{v}_{\text{ph}} \simeq 1$. It often turned out that for the kdV equation, the term α in Eq. (4.34) usually takes the value of $1/2$ because this prescription is closely related to the validity of hyperbolic approximation and similarity transformation [149]. Identifying the wave number k as the small parameter of the order of $\varepsilon^{1/2}$ (using long wavelength approximation), we introduce the following transformation for this particular case

$$\begin{aligned}
\xi &= \varepsilon^{1/2}(x - t) \\
\tau &= \varepsilon^{3/2} t
\end{aligned} \tag{4.42}$$

so that the temporal and spatial derivatives takes the form

$$\frac{\partial}{\partial t} = \varepsilon^{3/2}\frac{\partial}{\partial \tau} - \varepsilon^{1/2}\frac{\partial}{\partial \xi}$$

$$\frac{\partial}{\partial x} = \varepsilon^{1/2}\frac{\partial}{\partial \xi} \tag{4.43}$$

Now solving the Poisson's equation from Eq.(4.39), by putting the values from Eq. (4.41) and Eq. (4.43), we find that the lowest order terms are proportional to ε and give $\Phi_1 = n_1$. Doing the same for continuity and momentum equation from Eqs. (4.39), we find that the lowest-order terms are proportional to $\varepsilon^{1/2}$ and these give

$$\frac{\partial \mathbf{u}_1}{\partial \xi} = \frac{\partial \Phi_1}{\partial \xi} = \frac{\partial n_1}{\partial \xi} \tag{4.44}$$

Since all vanish as $\xi \to \infty$, integration of the above equation gives

$$n_1 = \Phi_1 = \mathbf{u}_1 = \varphi \tag{4.45}$$

Thus our normalization is such that all the linear perturbations are equal and we denote all with a common term "φ". We now again collect the terms proportional to ε^2 from Poisson's equation (4.39) and to $\varepsilon^{5/2}$ from continuity and momentum equation (4.39). This yields the following set of equations:

$$\frac{\partial^2 \Phi_1}{\partial \xi^2} = \Phi_2 - n_2 + \frac{\Phi_1^2}{2} \tag{4.46}$$

$$\frac{\partial n_2}{\partial \xi} = \frac{\partial n_1}{\partial \tau} + \frac{\partial (n_1 \mathbf{u}_1)}{\partial \xi} + \frac{\partial \mathbf{u}_2}{\partial \xi} \tag{4.47}$$

$$\frac{\partial \Phi_2}{\partial \xi} = \frac{\partial \mathbf{u}_2}{\partial \tau} - \frac{\partial \mathbf{u}_1}{\partial \tau} - \mathbf{u}_1 \frac{\partial \mathbf{u}_1}{\partial \xi} \tag{4.48}$$

After some algebraic manipulations and second and higher order quantities are eliminated, replacing all the first order quantities by φ, we get the following KdV equation

$$\frac{\partial \varphi}{\partial \tau} + \varphi \frac{\partial \varphi}{\partial \xi} + \frac{1}{2}\frac{\partial^3 \varphi}{\partial \xi^3} = 0 \tag{4.49}$$

Thus ion waves of amplitude one order higher than linear wave are described by the Korteweg-de Vries equation where φ is the amplitude and ξ and τ are space-like and time-like variables respectively. The second term in Eq. (4.49) is easily recognized as the convective term $\mathbf{u}.\nabla\mathbf{u}$ leading to wave steepening. The third term arises from wave dispersion, the k dependence of phase velocity. For $T_i = 0$, ion acoustic waves obey the linearized dispersion relation having a Taylor expansion as $k \to 0$ of the form

$$\omega = k c_0 \left(1 - \frac{\beta k^2}{c_0}\right) \tag{4.50}$$

where c_0 is the phase velocity of the wave and factor β is determined by the particular type of medium considered and can be described as

$$\beta = c_0 \lambda_D^2/2 \qquad \text{and} \qquad c_0 = c_s = (T/m_i)^{1/2} \tag{4.51}$$

Here, λ_D is the electron Debye length, c_s is the ion acoustic speed, T is the effective temperature (equal to T_e when $T_i \ll T_e$) in energy units such that Boltzmann constant is unity and m_i is the ion mass.

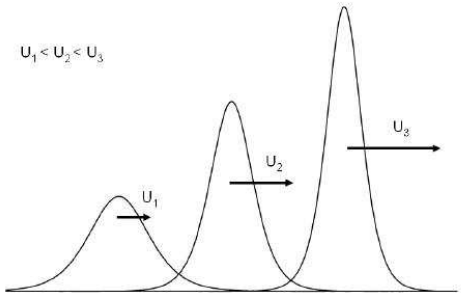

Figure 4.3: A single soliton travelling at three different speeds $\mathrm{U}_1 < \mathrm{U}_2 < \mathrm{U}_3$. It shows that, with the increase of speed, the soliton amplitude increases and the width decreases.

In a collisionless and non-isothermal plasmas where the electron temperature is much larger than ion temperature $(T_i \ll T_e)$, ion-acoustic solitary waves are driven by the electron pressure and ion inertia and the coupling between these species is being achieved by the electrostatic forces. The physics of the ion acoustic solitary waves in a collisional plasma is more complicated, since both the electrostatic forces and collisional effects enter into play [150]. Collisions derives both dissipative and resistive instabilities in the plasma if external free energy sources, such as density and velocities inhomogeneities are present and the waves become more nonlinear and turbulent [119].

Eq. (4.50) showing that the dispersive term is proportional to k^3. This is the reason for the third derivative term in Eq. (4.49). Dispersion must be kept in the theory to prevent wave steepening from spuriously nonlinear behavior. K-dV equation admits of the solution in the form of a soliton; i.e, a single pulse which retain its shape as it propagate with some velocity say U. Defining the new variable $\eta = \xi - U\tau$, so that $\partial/\partial\tau = -Ud/d\eta$ and $\partial/\partial\xi = d/d\eta$, so the Eq. (4.49) becomes:

$$-U\frac{d\varphi}{d\eta} + \varphi\frac{d\varphi}{\partial\eta} + \frac{1}{2}\frac{d^3\varphi}{d\eta^3} = 0 \tag{4.52}$$

This can be integrated

$$-U\int\frac{d\varphi}{d\eta}d\eta + \frac{1}{2}\int\frac{d\varphi^2}{d\eta}d\eta + \frac{1}{2}\int\frac{d}{d\eta}\left(\frac{d^2\varphi}{d\eta^2}\right)d\eta = 0 \tag{4.53}$$

If $\varphi(\eta)$ and its derivatives vanish at large distances from the soliton such as $(\mid \eta \mid \rightarrow \infty)$, the result is

$$U\varphi - \frac{1}{2}\varphi^2 - \frac{1}{2}\frac{d^2\varphi}{d\eta^2} = 0 \tag{4.54}$$

Multiply each term by $d\varphi/d\eta$ and then integrate once more, we get

$$\frac{1}{2}U\varphi^2 - \frac{1}{6}\varphi^3 - \frac{1}{4}\left(\frac{d\varphi}{d\eta}\right)^2 = 0 \tag{4.55}$$

Therefore

$$\left(\frac{d\varphi}{d\eta}\right)^2 = \frac{2}{3}\varphi^2(3U - \varphi) \tag{4.56}$$

This equation is satisfied by the soliton solution

$$\varphi(\eta) = 3U\ \mathrm{sech}^2[(U/2)^{1/2}\eta] \tag{4.57}$$

the above soliton solution tells us that the soliton have an amplitude $3U$ and the half width $(2/U)^{1/2}$, where U specified as the energy (speed) of the soliton. The larger the energy, the larger will be the speed and amplitude and the narrower will be the width of the soliton and is shown in Fig.4.3. So, we conclude that the solitary waves are basically a special kind of longitudinal wave in plasmas whose nature depends upon the nonlinear and dispersive effects present in the plasma. The above expression is derived by considering initially no ion streaming., i.e $u_0 = 0$ (initial ion speed). The relativistic effect on ion-acoustic waves completely depends upon the streaming of ions otherwise in the absence of ion streaming., i.e for u_0 equals to zero, the term u_0/c arising because of relativistic effect vanishes and relativistic effect has no influence on the solitary wave. A more general discussion about the relativistic effect on the ion acoustic solitary waves has been prescribed in [128, 135, 151].

4.3.2 Sagdeev pseudo-potential method

In section 4.2.3 we introduced ion-acoustic waves that have a phase velocity $\mathbf{v}_{\text{ph}} \sim \left(\frac{K_B T_e/m_i}{1+k^2\lambda_D^2}\right)^{1/2}$ i.e.Eq. (4.29). In Sec. 4.3.1, we considered the profile of a nonlinear ion-acoustic wave and found a solution for a single ion-acoustic soliton valid when the waves are weakly nonlinear, i.e. by using reductive KdV perturbation method for the small amplitude limit. To account for the full nonlinearity of plasma equations, we now employ another nonlinear method called Sagdeev pseudo-potential method which is exact, i.e non-perturbative and applicable for large amplitude ion waves.

Let the ion-acoustic wave is traveling with a velocity u_0 with respect to unperturbed plasma. If we go to the frame moving with the wave, the function $\Phi(x)$ will be constant in time, we see a stream of plasma impinging on the wave from the left with a velocity u_0. For simplicity, consider $T_i = 0$. so that all the ions are incident with the same velocity u_0. Now setting the $\partial/\partial t = 0$ in continuity equation (4.36), using the energy conservation, it gives $1/2m_i\mathbf{u}^2 + e\Phi = 1/2m_i u_0^2$ and $nu = n_0 u_0$, where $u(-\infty) = u_0$ and $n(-\infty) = n_0$. Thus the velocity of the ions in the shock wave comes out to be

$$\mathbf{u} = \left(u_0^2 - \frac{2e\Phi}{m_i}\right)^{1/2} \tag{4.58}$$

If n_0 is the density of the unperturbed plasma, the ion continuity equation then gives the ion density n_i in terms of density n_0 in the main plasma

$$n_i = \frac{n_0 u_0}{\mathbf{u}} = n_0\left(1 - \frac{2e\Phi}{m_i u_0^2}\right)^{-1/2} \tag{4.59}$$

The electrons assume a Maxwellian distribution and the electron density is given by the Boltzmann relation (see Eq. (4.27)). Thus the Poisson's equation (4.38) takes the form

$$\frac{d^2\Phi}{dx^2} = 4\pi e(n_e - n_i) = 4\pi e n_0\left[\exp\left(\frac{e\Phi}{K_B T_e}\right) - \left(1 - \frac{2e\Phi}{m_i u_0^2}\right)^{-1/2}\right] \tag{4.60}$$

The structure of this equation can be observed more clearly if we simplify it with the following dimensionless variables:

$$X \equiv \frac{x}{\lambda_D} = x\left(\frac{4\pi n_0 e^2}{K_B T_e}\right)^{1/2} \qquad \text{and} \qquad M \equiv \frac{u_0}{(K_B T_e/m_i)^{1/2}} \tag{4.61}$$

Where the term M is called the *Mach number* of the shock. Putting the values of Eq. (4.61) in Eq. (4.60) and normalizing the electrostatic potential Φ to $K_B T_e/e$, the Poisson's equation (4.60) takes the form

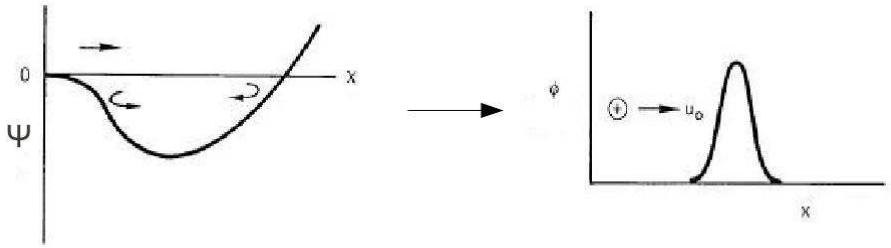

Figure 4.4: *Left frame*:- The upper arrow describing the trajectory of the pseudo-particle which is reflected at the right and returns. The lower arrows show the motion of a pseudo-particle that has lost its energy and is trapped in the potential well. *Right frame*:- Describes the trajectory of a soliton.

$$\frac{d^2\Phi}{dX^2} = e^{\Phi} - \frac{1}{\sqrt{1-\frac{2\Phi}{M^2}}} \tag{4.62}$$

The behavior of the solution of Eq. (4.62) was first explained by Sagdeev who used an analogy to an oscillator in a potential well. If the right-hand side of Eq. (4.62) is defined as $-d\Psi/dX$, the equation is the same as that of an equation of motion of a particle having position Φ and time X in classical mechanics: a "kinetic energy" term $\frac{1}{2}\left(\frac{d\Phi}{dX}\right)^2$ balances the potential energy $\Psi(\Phi)$. Integrating this equation in the form of an energy integral, we get

$$\frac{1}{2}\left(\frac{d\Phi}{dX}\right)^2 + \Psi(\Phi, M) = 0 \tag{4.63}$$

The function $\Psi(\Phi, M)$ is called the pseudo-potential energy and is given by

$$\Psi(\Phi, M) = 1 - e^{\Phi} + M^2\left(1 - \sqrt{1-\frac{2\Phi}{M^2}}\right) \tag{4.64}$$

For M lying in a certain range, this function has the shape as shown in the Fig.4.4. The total energy of the particle is zero, so a particle starting at the origin $\Phi = 0$ move up to a certain position Φ_m (where $\Psi(\Phi_m) = 0$), get reflected and return to $\Phi = 0$ making a single transit. So such a pulse is called as "soliton" as shown in right frame of Fig.4.4; a potential and density disturbance propagating with velocity $\mathbf{u}$.

Recalling that $\Phi = 0$ determines essentially the plasma equilibrium $\Psi(\Phi) = 0$. In general, we have the following conditions for $\Phi = 0$, for existence of soliton solutions:

$$\Psi(0, M) = \frac{d\Psi(0, M)}{d\Phi} = 0 \qquad \text{and} \qquad \frac{d^2\Psi(0, M)}{d\Phi^2} < 0 \tag{4.65}$$

In order for the anticipated type of motion to be possible, the potential must possess a maximum $\Phi_m \neq 0$ at the origin and a root, so at $\Phi_m > 0$,

$$\Psi(\Phi_m, M) = 0 \qquad \text{and} \qquad \frac{d\Psi(\Phi_m, M)}{d\Phi} > 0 \tag{4.66}$$

From Eq. (4.64), the constraint $\Psi''(\Phi = 0) < 0$ lead to $M > 1$, since

$$\frac{d\Psi(\Phi, M)}{d\phi} = \left(1 - \frac{2\Phi}{M^2}\right)^{-1/2} - \exp(\Phi) \tag{4.67}$$

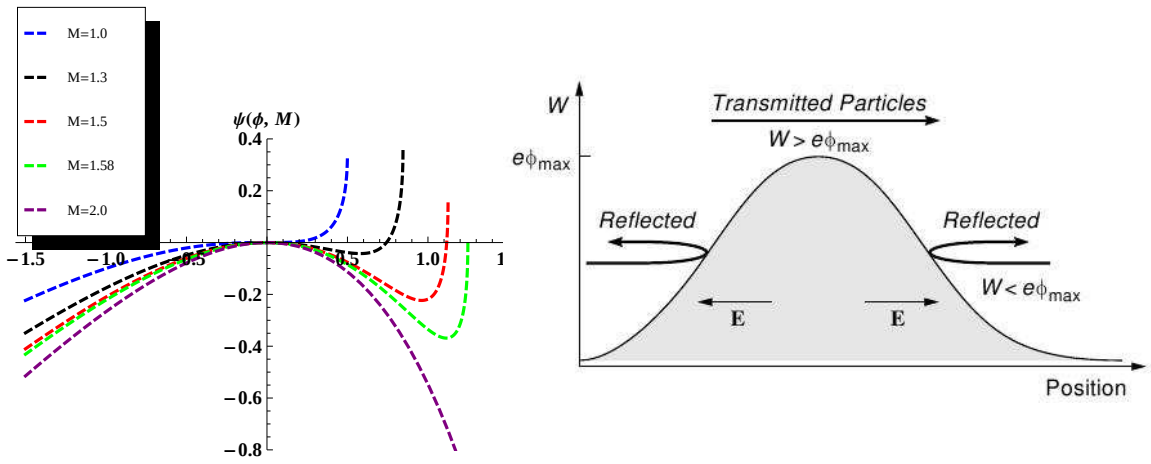

Figure 4.5: *Left frame:(a)* Variation of Sagdeev potential $\Psi(\Phi, \mathrm{M})$ with electrostatic potential ϕ. Positive potential solitary structure at five different Mach numbers (M) : $1.0, 1.3$, 1.5, 1.58 and 2.0 respectively. *Right frame:(b)* Symmetric reflection and transmission of particles from soliton.

$$\frac{d^2\Psi(\Phi, M)}{d\Phi^2} = \frac{1}{M^2}\left(1 - \frac{2\Phi}{M^2}\right)^{-3/2} - \exp(\Phi) \tag{4.68}$$

so at $\Phi = 0$ gives

$$\frac{d^2\Psi(0, M)}{d\Phi^2} = \frac{1}{M^2} - 1 < 0 \tag{4.69}$$

which gives $\mathrm{M} > 1$, means that the soliton speed should be supersonic. More investigation proves that neither negative potential solitons nor double layers exist in this case, while positive solitons arise from the physical requirement of real ion density as expressed by Eq. (4.59). When $\Phi \to \mathrm{M}^2/2$, we have $n \to \infty$. Accessible values of M are those for which the potential well yields a root Φ_m before the infinite compression limit is reached. So we find the largest possible value of M by imposing the requirement $\Phi = \mathrm{M}^2/2$,

$$n = \left(1 - \frac{2\Phi}{M^2}\right)^{-1/2} \text{ imposing } \quad R \to \Phi < \frac{M^2}{2} \tag{4.70}$$

Eq. (4.64) becomes

$$\Psi(\Phi = M^2/2) = M^2 + 1 - \exp\left(\frac{M^2}{2}\right) > 0 \tag{4.71}$$

The last term is in exponential form and by using a numerical estimation, the M[5] come out to be

$$M < 1.5852\,, \tag{4.72}$$

Left frame of Fig.4.5 explains about the existence conditions of large amplitude ion-acoustic waves. The allowable range of the normalized potential amplitude where ion acoustic solitary exists depends upon the Mach number. The potential well becomes deeper as Mach number (M) increases and ϕ increases as clearly seen in Fig.4.5b. The critical amplitude of the solitary wave is given by $\Phi_m \approx$

[5] We can also deduce this relation from the Newton's method: as we now $M = \sqrt{2\Phi}$, its function will be $f(\Phi) = 2\Phi + 1 - \exp(\Phi)$ and $f^{'}(\Phi) = 2 - \exp(\Phi)$. Now if $\Phi_0 = 1$, $\Phi_1 = \Phi_0 - \frac{f(\Phi_0)}{f(\Phi_0)} = 1.3922$ and $\Phi_2 = \Phi_1 - \frac{f(\Phi_1)}{f(\Phi_1)} = 1.2740$. Similarly $\Phi_3 = 1.2568$, solving for $M \to \sqrt{2\Phi} = 1.5852$.

$M^2/2 \approx 1.3$. So ion acoustic solitary waves in a cold ion plasma can exist for $1 < M < 1.58$ and $0 < \Phi < 1.3$ approximately. The solitary solutions turn into shock solutions for the conditions $M > 1.6$. Solving analytically, we found that the potential well is not formed for the Mach number $M > 1.6$, means solitary wave no longer exist anymore.

Right frame of Fig.4.5 shows the reflection mechanism of particles on the right side of wave front by the symmetric potential hump inside the soliton. Only particles with energies $1/2m\mathbf{v}_s^2 < e\Phi_m$ are reflected, while higher energy particles ($> 1/2m\mathbf{v}_s^2$) are transmitted through the potential hump. Clearly this happens only if the soliton moves because it is the motion which introduces the asymmetry. The low energy component may become asymmetrically reflected from the soliton potential with the asymmetries arising in the bulk velocities or in the particle fluids. The conditions of ion reflection changes when kinetic effects are included. Then the low energy particles in the distribution function may become reflected in continuous form from the soliton potential and asymmetry arise in a more natural way. In the next section, we will discuss an analytic oscillating model by taking into consideration the ion reflections from the leading edge of the potential barrier which leads towards the breaking of soliton symmetry.

4.4 Particle reflection

The process of ion reflection from the moving wave front is one of the important process in the entire physics of collisionless shocks. The plasma state is in the perturbed state after the passage of the solitary wave, The one reason of damping of the soliton can be due to the acquisition of energy by the ions reflected from the potential barrier. Particle reflection is required in supercritical shocks (M > 1), as to our knowledge. It is the only process that can compensate for the incapability of dissipative process inside the shock ramp to digest the fast inflow of momentum and energy into the shock. In order to establish the profile of the shock front in the ion-acoustic case, we proceed with the following analysis.

Now writing the Eq. (4.60), in terms of pseudo-potential energy $\Psi(\Phi)$, it becomes

$$\frac{d^2\Phi}{dx^2} = 4\pi e n_0 \left[\exp\left(\frac{e\Phi}{K_B T_e}\right) - \frac{u_0}{\sqrt{u_0^2 - \frac{2e\Phi}{m_i}}}\right] = -\frac{d\Psi(\Phi)}{dx} \tag{4.73}$$

which describes the potential profile Φ of ion acoustic wave when ion reflection is neglected. Integrating Eq. (4.73) once, we have our effective pseudo-potential energy $\Psi(\Phi)$ i.e; Eq. (4.64) in terms of ion density n_0 and propagation speed u_0:

$$\Psi(\Phi) = -4\pi n_0 \left(K_B T_e \exp\left(\frac{e\Phi}{K_B T_e}\right) + m_i u_0 \sqrt{u_0^2 - \frac{2e\Phi}{m_i}}\right) + C \tag{4.74}$$

Various periodic wave solutions can now be found depending on the choice of the integration constant C. A special case representing the value of C is given by $\Phi = 0$, which causes, $\frac{d\Phi}{dx}$, $\Psi(\Phi)$ and $\frac{d\Psi(\Phi)}{d\Phi}$ all to be zero, which results in a positive value of C., *i.e* from Eq. (4.74), it comes out to be $C = 4\pi n_0(K_B T_e + m_i u_0^2)$. This case is treated in the phase plane and gives a soliton solution and no shock solution as shown in Fig.4.4.

Now we will take account of the reflection of ions from the leading edge of the front, i.e in the region to the left of the location x_{M} of the first maximum Φ_{M}. The region $x < x_{\mathrm{M}}$ and $x > x_{\mathrm{M}}$ are labeled as I and II respectively as shown in Fig.4.6a. The shock profile can be determined by considering the ion reflection from the potential barrier. The net results is a peculiar kind of shock wave which connects

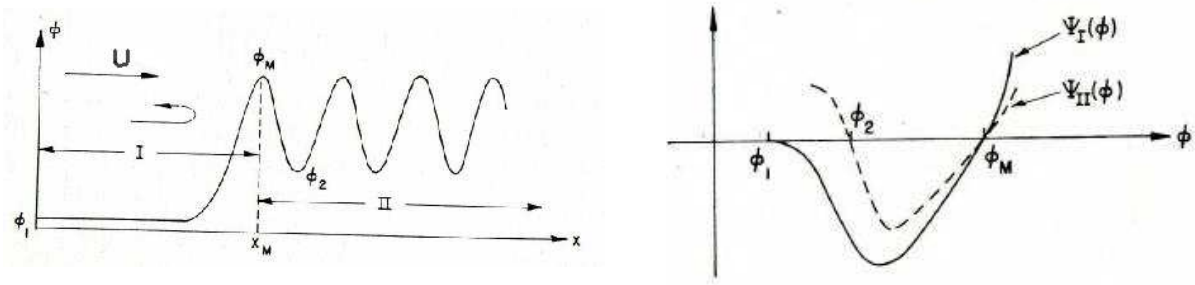

Figure 4.6: *Left frame*(a): An oscillatory electrostatic shock transition with some ions reflected from the leading edge. *Right frame*(b): Potential function $\Psi_I(\Phi)$ and $\Psi_{II}(\Phi)$ for the regions I and II of the electrostatic shock. Figure reprinted from [28].

two different plasma states; the unperturbed state in front of the shock and a state with intense ordered oscillations behind the shock front. However, the distribution of energy between the oscillations and the thermal motion depends on the actual collisionless dissipation mechanism. The shock profile as shown in Fig.4.6a, can be determined if the reflected ions are small in number and in the absence of dissipation $\Phi_1 = \Phi_2$ and $\lambda = \infty$ (whose results is a symmetric solitary wave). If ion reflections are taken into account, the potential in the region I of Fig.4.6a is described by an equation which differs from the Eq. (4.73) by presence of additional two terms on the right side:

$$-4\pi e n_0 f(\Phi_1)\left(\frac{u_0}{\sqrt{u_0^2-\frac{2e\Phi}{m_i}}}\right) \quad + \quad 8\pi e n_0 f(\Phi) \tag{4.75}$$

The first term correspond to the subtraction of the reflected ions from the total number of ions and the second term represents the contribution of the reflected ions. The quantity $n_0 f(\Phi)$ is the total density of the reflected ions at a point characterized by the potential Φ. The actual form of the function f can be easily calculated by giving the ion velocity distribution function for the reflected ions at $x = -\infty$. The potential jump Φ_1 is associated with ions that are reflected backwards from the potential barrier and escape to infinity, in this case here, we have considered such reflected particles are very small in number $(f \ll 1)$ and the potential jump Φ_1 is proportional to f [27]. However, the potential jump Φ_2 is associated with ions that are reflected forward by crossing the potential barrier and is proportional to the the square root of the number of reflected particles such that $\Phi_1 << \Phi_2$. The plasma state behind the front, i.e. in region II (Fig. 4.6a) is characterized by the quantities Φ_M and Φ_2, which determines the amplitude of the oscillations and their wavelength λ, i.e. Eq. (4.73) also hold in this region . Neglecting reflection effects on region II for the electrons and assuming $(K_B T_e/m_i)^{1/2} \gg u_0$ and assuming the electron density equal to the ion density at $x = -\infty$, the appropriate equations for the region I and II becomes[144]:

$$\mathbf{I}: \quad \frac{\partial^2\Phi}{\partial x^2} = -\frac{\partial \Psi_{\rm I}(\Phi)}{\partial \Phi} \equiv 4\pi e n_0 \left\{ [1+f(\Phi_1)]\exp\left(\frac{e\Phi}{K_B T_e}\right) - 2f(\Phi) - \frac{u_0[1-f(\Phi_1)]}{\left(u_0^2-\frac{2e\Phi}{m_i}\right)^{1/2}} \right\} \tag{4.76}$$

$$\mathbf{II}: \quad \frac{\partial^2\Phi}{\partial x^2} = -\frac{\partial \Psi_{\rm II}(\Phi)}{\partial \Phi} \equiv 4\pi e n_0 \left\{ [1+f(\Phi_1)]\exp\left(\frac{e\Phi}{T_e}\right) - \frac{u_0[1-f(\Phi_1)]}{\left(u_0^2-\frac{2e\Phi}{m_i}\right)^{1/2}} \right\} \tag{4.77}$$

By solving the potential equation at $x_{\rm M}$ in regions I and II with the boundary conditions of continuity of Φ and $d\Phi/dx$ at $x_{\rm M}$, we can find the potential profile (Fig.4.6b). Since $f(\phi_{\rm M})=0$, the integration constants in Eqs. $(4.76)\text{and}(4.77)$ can be chosen such that $\Psi_{\rm I}(\Phi_{\rm M})=\Psi_{\rm II}(\Phi_{\rm M})$. Therefore, $\frac{1}{2}(\frac{\partial\Phi}{\partial x})^2+\Psi_{\rm I,\,II}=0$ which implies that $\partial\Phi/\partial x$ is continuous at $\Phi=\Phi_{\rm M}$. Then potential Φ of $\Psi_{\rm I}$ potential makes its first swing along the solitonic path $\Phi_1\rightarrow\Phi_{\rm M}$ and on entering in region II oscillates indefinitely between $\Phi_{\rm M}$ and Φ_2 with the potential $\Psi_{\rm II}$.

Now, if we again consider the analogy with the particle motion in a potential well $\Psi(\Phi)$, it can be shown that the effect of the reflected ions make the total energy C negative which leads to a periodic structure behind the shock front (Fig. 4.6b). The decrease in the energy C is proportional to the number of reflected ions

$$-C\sim\int_0^{\Phi_{\rm M}}f(\Phi)d\Phi \tag{4.78}$$

Since the potential energy $\Psi(\Phi)$ varies quadratically at small Φ. the turning point Φ_2 is proportional the the square root of the energy $-C$

$$\Phi_2\sim\sqrt{-C} \tag{4.79}$$

and the oscillation period increases logarithmically as the energy is reduced i.e; $(\lambda\sim ln(1/-C))$. Thus the minimum value of the potential behind the front Φ_2 is

$$\Phi_2=\frac{2M}{\sqrt{M^2-1}}\left(\frac{T}{e}\int_0^{\Phi_{\rm M}}f(\Phi)d\Phi\right)^{1/2} \tag{4.80}$$

The value of $\Phi_{\rm M}$ is very close to the corresponding value in a solitary wave with the same Mach number. Now the ion reflection has another important effect on the solitary/shock wave, as the momentum transfer from shock wave front to the reflected ions retards the shock in the region of reflection. The wavelength at the front of these oscillations is given by[144]

$$\lambda\simeq\frac{1}{\sqrt{M^2-1}}\left(\frac{T_e}{\pi e^2n_0}\right)^{1/2}\ln\frac{\Phi_{\rm M}}{\Phi_2} \tag{4.81}$$

Shock ion reflection has incomparable importance in collisionless shock formation and can be efficiently treated by numerical simulations. Before in the next chapters, coming to discuss these problems in greater depth, I will present below a few other attempts which lead to the dissipation of electrostatic solitary waves other than particle reflection such as Landau damping and particle trapping.

4.5 Landau Damping of Electrostatic Waves

Here we will use kinetic approach to elucidate some of the properties of electrostatic ion-acoustic waves in terms of particle surfing and Landau damping which could not be derived by fluid techniques. Consider an electrostatic wave propagating in the $z-$ direction. In such a wave in one dimension, the electric field points in the Z direction, $\mathbf{E}=Ee_z$ and varies as $e^{i(kz-\omega t)}$. The distribution function similarly varies as $e^{i(kz-\omega t)}$ and depends only on $z-$ and is independent of x or y direction. So the Vlasov, Maxwell and Lorentz force equations produce no coupling of particle velocities $\mathbf{u}_x$, $\mathbf{u}_y$ in the $z-$ direction. This suggest to introduce the one dimensional distribution function which can be obtained by integrating over $\mathbf{u}_x$ and $\mathbf{u}_y$ as

$$f_s(\mathbf{u},z,t)\equiv\int f_s(\mathbf{u}_x,\mathbf{u}_y,\mathbf{u}_z,z,t)d\mathbf{u}_xd\mathbf{u}_y \tag{4.82}$$

From here, we emit the subscript z from $\mathbf{u}_z$ and read it as $\mathbf{u}$. Restricting to weak waves and neglecting nonlinearities, we linearize the one-dimensional distribution function as

$$f_s(\mathbf{u}, z, t) \simeq f_{s0}(\mathbf{u}) + f_{s1}(\mathbf{u}, z, t) \tag{4.83}$$

where $f_{s0}(\mathbf{u})$ is the distribution function of the unperturbed particles ($s = e, i$ for electron and ion respectively) in the absence of wave and f_{s1} is the perturbation produced by the electric field $\mathbf{E}$. The evolution of the f_{s1} is governed by the linear approximation of the Vlasov equation

$$\frac{\partial f_{s1}}{\partial t} + \mathbf{u}\frac{\partial f_{s1}}{\partial z} + \frac{q_s \mathbf{E}}{m_s}\frac{df_{s0}}{d\mathbf{u}} = 0 \tag{4.84}$$

As we are looking for a monochromatic, plane wave solution to this Vlasov equation, therefore putting $\partial/\partial t \to -i\omega$ and $\partial/\partial z \to ik$ and solving the resulting equation for f_{s1}, we get an equation for f_{s1} in terms of $\mathbf{E}$ as

$$f_{s1} = \frac{-iq_s}{(\omega - k\mathbf{u})m_s}\frac{df_{s0}}{d\mathbf{u}}\mathbf{E} \tag{4.85}$$

The above equations implies that the charge density associated with the wave is related to the electric field by

$$\rho_e = \sum_s q_s \int_{-\infty}^{+\infty} f_{s1} d\mathbf{u} = \left(\sum_s \frac{-iq_s^2}{m_s} \int_{-\infty}^{+\infty} \frac{f'_{s0} d\mathbf{u}}{\omega - k\mathbf{u}} \right) \mathbf{E} \tag{4.86}$$

The prime denotes the derivative with respect to $\mathbf{u}$, *i.e.* $f'_{s0} = df_{s0}/d\mathbf{u}$. By putting this charge density into the Poisson's equation $\nabla.\mathbf{E} = i\mathbf{k}\mathbf{E} = 4\pi\rho_e$, and by keeping the both sides proportional to $\mathbf{E}$, we can find the dispersion relation with the general analysis of waves in the dielectric medium. Considering a wave is propagating along the z-direction in an unmagnetized plasma, dispersion relation is given by

$$\varepsilon(\omega, \mathbf{k}) = 1 + \sum_s \frac{4\pi q_s^2}{m_s k} \int_{-\infty}^{+\infty} \frac{f'_{s0} d\mathbf{u}}{\omega - k\mathbf{u}} = 0 \tag{4.87}$$

The form of the dispersion relation can be written in more generalized form by combining the unperturbed electron and ion distribution function $f_{e0}(\mathbf{u})$ and $f_{i0}(\mathbf{u})$, to produce a single, unified distribution function:

$$f(\mathbf{u}) = f_{e0}(\mathbf{u}) + \frac{m_e}{m_i} f_{i0}(\mathbf{u}) \tag{4.88}$$

So the equation (4.87) takes the form

$$\varepsilon(\omega, \mathbf{k}) = 1 + \frac{4\pi e^2}{m_e k} \int_{-\infty}^{+\infty} \frac{f'(\mathbf{u}) d\mathbf{u}}{\omega - k\mathbf{u}} = 0 \tag{4.89}$$

In the above unified distribution function Eq. (4.88), for ion-acoustic waves, the proton play an important role because the large numbers of protons can move with the thermal speeds that are close to the the wave phase velocity and therefore can interact resonantly with the waves.

Landau Contour: The general dispersion relation Eq. (4.89) has a troubling feature, i.e. for real ω and k, its integrand of the wave phase velocity becomes singular at $\mathbf{u} = \omega/k$ unless $df(\mathbf{u})/d\mathbf{u}$ vanishes there. As the vanish of $df(\mathbf{u})/d\mathbf{u}$ is very unlikely, which means that if we assume k as real, then the value of ω can not be real except for a non-generic mode in which phase velocity happens to coincide with a velocity for which $df(\mathbf{u})/d\mathbf{u} = 0$. With ω/k complex, the point arises is how we can perform the integral-over $\mathbf{u}$ in the dispersion relation Eq. (4.89). Landau [152] developed a sophisticated derivation of the dispersion relation based on posing general initial data for electrostatic waves, evolving it forward

with time and identify the electrostatic modes by their late time sinusoidal behavior and finally read the dispersion relation for the modes from the late time evolution equations. So the dielectric function with the "Landau contour" $\pounds$ prescription can be written as

$$\varepsilon(\omega, \mathbf{k}) = 1 + \frac{4\pi e^2}{m_e k} \int_{\pounds} \frac{f'(\mathbf{u}) d\mathbf{u}}{\omega - k\mathbf{u}} = 0 \tag{4.90}$$

In most of the practical situations, electrostatic waves are weakly unstable or weakly damped, *i.e.* $\mid \omega_i \ll \omega_r \mid$ (subscript r and i denotes the real and imaginary part) and the amplitude changes a little over one wave period. The dielectric function Eq. (4.90) can be evaluated for $\omega = \omega_r + i\omega_i$ by using the Taylor series expansion away from the real axis. The on-axis real (ω_r) and imaginary (ω_i) values of the dielectric function can be computed by breaking the landau contour and using the Cauchy integral $\int_C$, it comes out to be [153]

$$\varepsilon(\mathbf{k}, \omega_r + i\omega_i) \simeq 1 - \frac{4\pi e^2}{m_e k^2} \left[\int_C \frac{f' d\mathbf{u}}{\mathbf{u} - \omega_r/k} + i\pi f'(\omega_r/k) + i\omega_i \frac{\partial}{\partial \omega_r} \int_C \frac{f' d\mathbf{u}}{\mathbf{u} - \omega_r/k} \right] = 0 \tag{4.91}$$

This is the dispersion relation for the limit $\mid \omega_i \mid \ll \omega_r$. A more detailed discussion is beyond the scope of the present work and can be found in Refs.[154, 153, 92].

4.5.1 Electrostatic Ion Acoustic Waves and conditions for Landau Damping

In section 4.1.3 using two-fluid theory, we studied that the ion acoustic waves are the analog of ordinary sound waves, occurs at low frequencies where the mean electron velocity is nearly close to the mean ion velocity., so the polarization is small while the the restoring force is due to the thermal pressure and not because of electrostatic field and the inertia is provided by the ions.

Suppose that the ions and electrons have Maxwellian velocity distribution but with different temperatures. Because of the much higher inertia, the protons have much smaller mean thermal speed than that of electrons and the one dimensional distribution function $f(\mathbf{u})$ of Eq. (4.91) which appears in the kinetic-theory dispersion relation has the form as shown in Fig.4.7. If $T_i \sim T_e$, then the contribution of the ion pressure and the electron pressure to the restoring force of the wave will be comparable. Thus the wave phase velocity will be $\omega_r/k \sim \sqrt{K_B(T_e + T_i)/m_i} \sim \sqrt{K_B T_i/m_i}$, which is the speed at which the ion contribution to $f(\mathbf{u})$ has its steepest slope (see Fig.4.7, the tick mark on the horizontal axis on left side $f_i(\mathbf{u})$). Therefore $\mid f'(\mathbf{u} = \omega_r/k) \mid$ will be large in this case, which means that there will be large number of ions that can surf on the wave which results in a large disparity occurs between the number of ions moving slightly slower than the wave (i.e. extracting energy from the latter) and the number moving slightly faster than the wave (i.e. give energy). The result is that, there will be strong Landau damping by the ions.

The strong Landau damping can be avoided if the electron temperature is much higher than that of ion temperature $T_e \gg T_i$. Then the wave phase velocity $\omega_r/k \sim \sqrt{K_B T_e/m_i}$ will be large compared to the ion thermal velocity $\omega_r/k \sim \sqrt{K_B T_i/m_i}$, so in the tail of the ion velocity distribution, there will be very few ions which can surf and damp the wave. Now, if we think about the Landau damping due to electrons in which the phase velocity $\omega_r/k \sim \sqrt{K_B T_e/m_i}$ is small compared to the thermal velocity of electrons $\sqrt{K_B T_e/m_e}$, thus the wave resides near the peak of the electron velocity distribution in which $f_e(\mathbf{u})$ is large enough that many electrons can surf but $f'_e(\mathbf{u})$ is small and there are nearly equal number of fast and slower electrons. The net surfing produces a very little Landau damping. Thus $T_e \gg T_i$ leads to successful propagation of ion acoustic waves.

The dispersion relation in the limit $\mid \omega_i \mid \ll \omega_r$ in Eq.(4.91) makes this physical argument quantitative. Now by using the assumptions $T_e \gg T_i$ and $\sqrt{K_B T_i/m_i} << \omega_r/k \ll \sqrt{K_B T_e/m_e}$, we find the

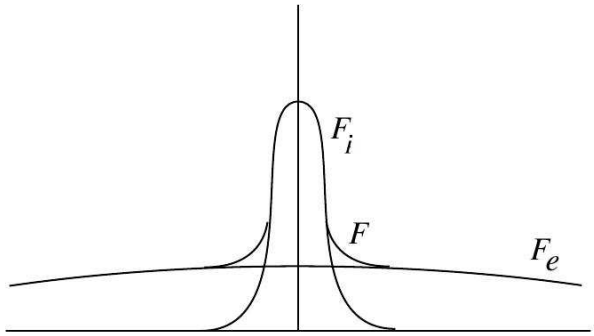

Figure 4.7: Ions F_i and Electrons F_e contribution to the net distribution function $F(\mathbf{u})$ in a thermal plasma. When $T_e \approx T_i$, the ion-acoustic phase velocity lies well within the ion distribution, having speed at which the surfing protons have maximum ability to Landau damp the wave, so the waves are heavily damped. When $T_e \gg T_i$, phase velocity is far out on the tail of proton distribution and there are very few ions at the phase velocity which can surf and damp the wave, so the wave can propagate and the little net damping is mostly by the electrons. Reprinted from [153].

real ω_r and imaginary ω_i part of the dispersion relation as:

$$\frac{\omega_r}{k} = \sqrt{\frac{K_B T_e/m_i}{1+k^2\lambda_D^2}} \quad \text{and} \quad \frac{\omega_i}{\omega_r} = -\frac{\sqrt{\pi/8}}{(1-k^2\lambda_D^2)^{3/2}}\left[\sqrt{\frac{m_e}{m_i}} + \left(\frac{T_e}{T_i}\right)^{3/2} \exp\left(\frac{-T_e/T_i}{2(1+k^2\lambda_D^2)}\right)\right] \tag{4.92}$$

The real part of the dispersion relation ω_r has been explained in the section 4.1.3, in Eq. 4.29 and is shown in the Fig.4.1, that for $k\lambda_D \ll 1$, the wave phase speed is $\sqrt{K_B T_e/m_i}$ and the waves are weakly damped as they can propagate for roughly $\sqrt{m_p/m_e} \sim 43$ periods before the strong damping takes place (here m_p is the proton mass). When the wavelength λ_D decreases (k increases) into the regime $k\lambda_D \geq 1$, the frequency of the wave asymptotes towards $\omega_r \approx \Omega_p$, i.e. the ion plasma frequency, in such a case the phase velocity decreases, so more ions can surf the waves and landau damping increases. Eq. (4.92) shows that damping becomes strong when $k\lambda_D \sim \sqrt{T_e/T_i}$ at which the ω_r/k decreases to the ion thermal velocity $\sqrt{K_B T_i/m_i}$, so more ions can surf and causes strong damping. When T_e/T_i decreases from $\gg 1$ towards unity, the ion damping starts becoming strong regardless how small can be the wave-vector k (exponential term of ω_i/ω_r in Eq. 4.92). Thus the Landau damping by ions can be reduced by raising the electron temperature.

4.6 Particle Trapping

When a plasma wave reaches large amplitude, either it has been injected into the plasma by external means or has grown to large amplitude due to instability, several non-linear effects sets in and particle trapping is one of them. Particle become trapped in a wave potential if the kinetic energy of the particle (W) in the wave frame is less than the potential energy of the wave. Trapping will be large for the resonant particles moving approximately at the same velocity as that of the wave and experiencing a nearly stationary electric wave potential

$$\Phi(x,t) = \Phi_0 \cos(kx - \omega t) = \Phi_0 \cos(kx') \tag{4.93}$$

in above the wave coordinates, i.e wave position and wave speed have been transferred into the wave frame by

$$x' = x - \left(\frac{\omega}{k}\right) t \qquad \text{and} \qquad \mathbf{v}' = \mathbf{v} - \frac{\omega}{k} \tag{4.94}$$

Now considering the motion of ions in the phase space $(x', \mathbf{v}')$, the total energy of the ion in the wave frame of reference is

$$\mathcal{E}_t = \frac{1}{2} m_i \mathbf{v}'^2 - Ze\Phi_0 \cos(kx')$$

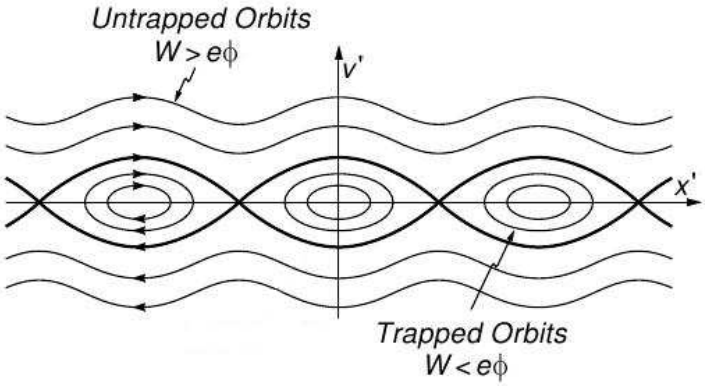

Figure 4.8: Phase space distributions of the particle orbits for the trapped (dashed lines) and untrapped (solid lines) particles moving in an electrostatic potential of a wave. Figure reprinted from [119].

$$= W - Ze\Phi_0 \cos(kx') \tag{4.95}$$

where m_i is mass of ions. The ions moves along the lines of this total constant energy $(\mathcal{E}_t)$ and is shown in the Fig.4.8. There are two types of curves in this phase space. The first ones are for low ions velocities exhibits closed lines. These closed trajectories describes the ions trapped in the wave potential. Second type of curves are of the ions having higher speed consists of open lines which corresponds to untrapped ions. The trapped ions trajectories have a negative total energy, i.e. $\mathcal{E}_t < 0$ and hence the trapped ions on such orbits bounce back and forth between the walls of the wave potential and exhibit an oscillatory motion which is periodic in the phase space. One can easily estimate the frequency of such bounce motion considering small amplitude oscillations of the ions near the bottom of the potential well, i.e. for ions having trajectories close to the center of the O− type trapped orbits. The cosine function for such ions can be expanded to the lowest order, yielding equation of motion:

$$m_i \frac{d^2x'}{dt^2} = -Ze\Phi_0 k^2 x' \tag{4.96}$$

which is the equation of a harmonic oscillator of frequency

$$\omega_t = \mid Ze\Phi_0 k^2/m_i \mid^{1/2} \tag{4.97}$$

and is known as the trapped ion frequency. Since $\nabla \mathbf{E} = -i\mathbf{k}\Phi$, which means the larger the wave field amplitude, the faster the trapped resonant ions will oscillate in the field. For the larger field amplitude, more ions will become trapped by the deepening of the potential trough and the widening of the wave resonance. We observed similar type of ion trapping phenomenons between the solitary waves in our 1D PIC simulations (e.g see Fig.6.6) and is described in the Ch.6

CHAPTER 5

Particle-In-Cell (PIC) Code

5.1 Introduction

Particle simulations are fundamental in many areas of applied research, including plasma physics, astrophysics and semiconductor device physics. These simulations often involves tracking of charged particles in electric and magnetic fields. The growth in the power of the computers over the past half century in order to study the basic science in general and plasma physics problems in particular, led to the development of a novel approach known as computational plasma physics. The plasma behavior which is generally studied by the well known basic laws of physics such as laws of Newton and Maxwell, but the consequences of these laws for a complex system consisting perhaps 10^{10} or more particles are frequently impossible to determine. In the present state-of-the art technology, highly parallel computers are becoming a more and more integral part of the scientific particle computation and makes it possible to study the plasma behavior and dynamics for complex systems.

This chapter serves as a brief introduction to the field of particle-in-cell (PIC) simulation of plasmas. To understand the complex dynamics of laser plasma interactions, involving collective and self-organization effects, requires the used of self-consistent electromagnetic, kinetic simulations. To, this aim, the particle-in-cell (PIC) method is by far the mostly used approach which gives primacy to the kinetic interactions among the constituent particles of plasma and the electromagnetic field. This approach provides a more accurate treatment of many local and quasi-local processes. We used the PIC approach to simulate our laser plasma interactions in which the electrons and ions are treated as computational particles (CPs), making no approximation to the basic laws of mechanics and the full range of collisionless plasma physics is included in our model.

5.2 Basic Model Equations

The scenario of intense laser-plasma interactions is characterized by strong kinetic effects such as the generation of very fast particles. Thus a fully kinetic approach is needed in which the theoretical basics for a kinetic description of a classical plasma is well established and will be studied by the Particle-in-cell (PIC) code. The goal is to study the Boltzmann equation for the distribution function coupled with the Maxwell equations for the electromagnetic (EM) fields. The collective dynamics of the particles of the plasma can be simulated by solving numerically the Boltzmann equation in the phase space for each particle species, where the distribution function $f = f(x, \mathbf{p}, t)$ evolves as

$$\frac{\partial f}{\partial t} + \dot{\mathbf{x}}\frac{\partial f}{\partial \mathbf{x}} + \dot{\mathbf{p}}\frac{\partial f}{\partial \mathbf{p}} = \frac{\partial f_{\text{coll}}}{\partial t} \tag{5.1}$$

in above, the coordinate $\mathbf{x}$ and the momentum $\mathbf{p}$ represents the generic vectors in the phase space while $\dot{\mathbf{x}} = \mathbf{v}$ is the particle velocity and $\dot{\mathbf{p}} = \mathbf{F}(\mathbf{x}, \mathbf{p}, t)$ is the Lorentz force on the computational particles and can be written as;

$$\mathbf{v} = \frac{\mathbf{p}c}{\sqrt{m^2c^2 + \mathbf{p^2}}} \qquad \text{and} \qquad \mathbf{F} = q \cdot \left(\mathbf{E} + \frac{\mathbf{v}}{c} \times \mathbf{B}\right) \tag{5.2}$$

The electric ($\mathbf{E}$) and magnetic ($\mathbf{B}$) fields are determined self-consistently with the dynamics of the particles which we described by the Vlasov's equation. The coupling of Vlasov equation with the Maxwell's equations is obtained by calculating the charge density $\rho(\mathbf{x}, t)$ and the current density $\mathbf{J}(\mathbf{x}, t)$ such as

$$\rho = \sum_{\alpha=e,i} q_\alpha \int f(\mathbf{x}, \mathbf{p}, t) d\mathbf{p}, \tag{5.3}$$

$$\mathbf{J} = \sum_{\alpha=e,i} q_\alpha \int \mathbf{v} f(\mathbf{x}, \mathbf{p}, t) d\mathbf{p} \tag{5.4}$$

Now in a full particle model, one follows both the motion of electrons and ions in the self-consistent electric and magnetic fields obtained from the Maxwell equations. Therefore using Maxwell equations, one has the choice to work directly with the $\mathbf{E}$ and $\mathbf{B}$ fields. Introducing total current and charge densities $\mathbf{J} = \mathbf{J}_e + \mathbf{J}_i$ and $\rho = \rho_e + \rho_i$, the Maxwell equations are:

$$\nabla \cdot \mathbf{E} = 4\pi\rho, \tag{5.5}$$

$$\nabla \times \mathbf{E} = -\frac{1}{c}\partial_t \mathbf{B}, \tag{5.6}$$

$$\nabla \cdot \mathbf{B} = 0, \tag{5.7}$$

$$\nabla \times \mathbf{B} = \frac{4\pi}{c}\mathbf{J} + \frac{1}{c}\partial_t \mathbf{E}. \tag{5.8}$$

Equations $(5.1$ and $5.5 - 5.8)$ form a self-consistent set of equations which in principle can be numerically solved like an initial value problem, using the appropriate boundaries conditions. For a simulation of laser plasma interactions, this corresponds an initial distribution function at $t = 0$ and defining the EM fields at one or more boundaries in order to describe the entrance of the laser pulse in the simulated plasma slab.

5.3 Lagrangian and Eulerian approach

In general, two different approaches have been employed to solve numerically the above mentioned Model equations (i.e. Boltzmann and Maxwell Equations) in $\mathrm{sec.}\ 5.2$. They corresponds to the choice of Lagrangian or Eulerian variables to integrate these Model equations. The Lagrangian approach corresponds to particle-in-cell (PIC) simulations in which there is a "discrete" description of the plasma as an ensemble of computational particles obeying individual equations of motion. In practice, PIC approach means going back to the most fundamental description of the plasma, having collection of single particles with mutual interactions. The current and electromagnetic (EM) fields are defined on the sites of a spatial grid and are calculated according to the distribution of the particles. PIC codes are the essential tools for computational plasma physics since the memory needed for multi-dimensional simulations is relatively small. The memory needed is proportional to $\mathrm{N_g} \times \mathrm{N_p}$ where $\mathrm{N_g}$ and $\mathrm{N_p}$ are the number of grid points and the number of particles per cell, respectively. Typically $\mathrm{N_p} \approx 10^1 - 10^3$ depending upon the the accuracy and resolution required while the number of grid points corresponds to $\mathrm{N_g} \approx (10^2)^{\mathrm{n}}$, where n be the dimensionality of the simulation $1 \leq \mathrm{n} \leq 3$. Nowadays, in the present available computer facilities it is possible to perform numerical PIC simulations also in fully $3\mathrm{D}$ geometry, with small values of $\mathrm{N_p}$.

The Boltzmann or Vlasov approach corresponds to the Eulerian or continuum description of the plasma. The Eulerian approach, directly finds the solution of Model equations (of $\mathrm{sec.}\ 5.2$), such that the numerical techniques are less developed and the numerical integration is less straightforward than

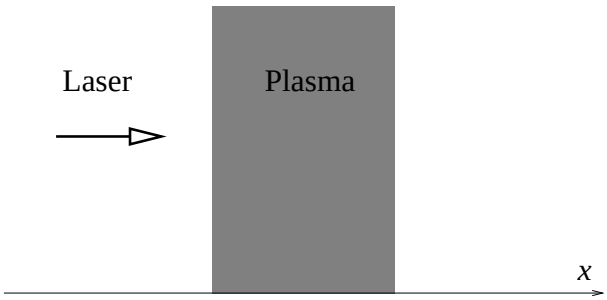

Figure 5.1: The essential one Dimensional geometry of PIC code.

the integration of individual equation of motions in PIC. Keeping all other things being equal, there would be no sense in the development of continuum codes. The major disadvantage is its very large memory requirements, since the memory scales as $\mathrm{N_g} \times \mathrm{N_v}$ where $\mathrm{N_v}$ is the number of grid-points in the momentum space. Therefore, the memory required by a 1D2P Vlasov code is comparable to that required by a 3D3P PIC code. Apart from the above description, continuum codes are free from problems of poor particle statics and can be used as a test for the dependence of PIC results upon number of particles. Continuum codes are noise free and make it possible to study the nonlinear dynamics for very long times and on very short spatial scales. These features helps to deeply understand some nonlinear phenomenons such as plasma wave-breaking[155], large amplitude wake-field generation[156] and Weibel instabilities[157]. Vlasov codes with respect to PIC codes having same spatial grid provide a better resolution for high plasma densities and sharp gradients and thus, is of particular importance to study the case of ultrashort laser-solid interactions. Due to these advantages, a complementary use of Vlasov and PIC codes may significantly improve the understanding of the nonlinear dynamics of collisionless plasma.

5.4 Numerical PIC Approach

We have used the particle-in-cell (PIC) code to simulate the interaction of the laser pulse with plasma slab. Fig.5.1 shows the essential concept of the code geometry; a laser pulse (a plane electromagnetic wave with some given temporal envelope) impinges on the plasma target, composed of electrons and ions (having such charge and number density that the plasma is globally neutral). All physical quantities depends on the single spatial coordinate x and on time t. We calculate the electric field $\mathbf{E}(\mathbf{x}, t)$, magnetic field $\mathbf{B}(\mathbf{x}, t)$ and distribution functions in the phase space of ions $f_i(\mathbf{x}, \mathbf{p}_\alpha, t)$ and of electrons $f_e(\mathbf{x}, \mathbf{p}_\alpha, t)$. The momentum space is generally fully three dimensional, *i.e.*, $\mathbf{p}_\alpha = (\mathbf{p}_x, \mathbf{p}_y, \mathbf{p}_z)$ for both ions and electrons.

5.4.1 How the code works

In the PIC code, the physics comes from the two parts; the fields produced by the particles and the motion of charge particles produced by the forces (fields). The fields are calculated through Maxwell equations by knowing the position of all the particles and their respective velocities while the forces on the particles are found using electric and magnetic fields by Newton-Lorentz equation of motion (Eq. 5.2). We use a sufficiently fine grained temporal grid to follow the plasma with acceptable accuracy and stability. Fields are calculated by use of the spatial grid. We calculate the fields from initial charge and current densities, then move the particles (small distance) and then recalculates the fields of particles at their new positions and velocities: this procedure is repeated for several steps. The grid provides a smoothing effect by not resolving the spatial fluctuations that are smaller than the grid size. At each

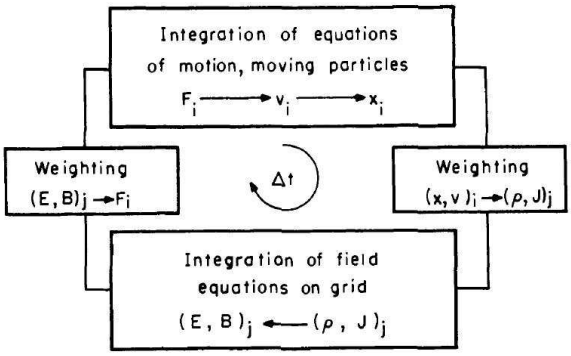

Figure 5.2: A typical cycle, one time step, in a particle simulation program. The particles are numbered i = 1, 2, ..., NP, the grid indices are defined as j. Figure reprinted from [158].

.

step in time, the program is solved for the fields from the particles and then moves the particles. There may be many number of steps in a characteristic period of the plasma and the same number of periods in a typical run, which adds up to hundreds or thousands of time steps in a given run. The particles are processed through the boxes shown in Fig.5.2, similarly as the forces and fields are calculated in the actual plasma.

The particle quantities, i.e. position and velocity are calculated by taking all of its values in $\mathbf{x}$ and $\mathbf{p}$ phase space. From the particles position and velocity, we can calculate the charge and current densities on the grid. The process of assigning charge and current densities implies some "weighting" to the grid points that is dependent on the particle position. Once the densities are established on the grid, then we use the numerical PIC method to calculate the electric and magnetic fields [158]. The PIC approach, reduces the plasma simulation to the simplest by considering the most fundamental description of plasma in terms of the collection of single charged particles which are moving under the action of self consistent electromagnetic fields. The accuracy of the approach increases with the number of particles employed at fixed number of grid cells. The higher particle number yield better statistics and reduce the fluctuations of local values of the distribution functions which are calculated by statistical averages.

5.4.2 The Particle approach

The PIC code approaches the plasma by an ensemble of computational particles (CPs), each of which represents a phase space volume element. The phase space is subdivided into small domains that are moving in time along the trajectories of single particles. Each computational particle follows a phase space trajectory that is determined through Lorentz force equation by electric $\mathbf{E}(\mathbf{x},t)$ and magnetic $\mathbf{B}(\mathbf{x},t)$ fields. These fields are evolved self- consistently in time using Maxwell's equations and the total current $\mathbf{J}(\mathbf{x},t)$ (i.e. the sum of the micro-currents of all the computational particles). The standard PIC approach considers only the collective interactions between the particles, although some collisional effects are introduced through the interactions of CPs with the field fluctuations [159].

In the above Eq. (5.1), the collisions are expressed in the term $\partial_t f_{\text{coll}}(\mathbf{x},\mathbf{p},t)$ including every kind of collisional process like Coulomb collisions or ionization. As we are studying the laser interactions with overdense plasma at an intensity of $\mathrm{I} = 10^{18} - 10^{20}\mathrm{W/cm}^2$, i.e in the relativistic regime, so the interaction can be treated as collisionless, because the collisions becomes increasingly ineffective at such high intensity. Thus the collisions are not relevant in our case (see $\mathrm{sec}2.8$ Ch. 2 for detail) and the laser interaction with plasma is fully collisionless. So setting the R.H.S term of Eq. (5.1) at 0, the Collisionless Boltzmann equation (called as Vlasov equation) in the phase space will be

$$\frac{\partial f}{\partial t} + \dot{\mathbf{x}}\frac{\partial f}{\partial \mathbf{x}} + \dot{\mathbf{p}}\frac{\partial f}{\partial \mathbf{p}} = 0 \qquad \text{or}$$

$$\left(\partial_t + \dot{\mathbf{x}}\partial_{\mathbf{x}} + \dot{\mathbf{p}}\partial_{\mathbf{p}}\right) f(\mathbf{x},\mathbf{p},t) = 0 \tag{5.9}$$

Now assuming the "particle" approach consists a discrete representation of the distribution function $f(\mathbf{x},\mathbf{p},t)$ as follows,

$$f(\mathbf{x},\mathbf{p},t) = f_0 \sum_{n=1}^{N_p} g[\mathbf{x}-\mathbf{x}_n(t)]\delta[\mathbf{p}-\mathbf{p}_n(t)], \tag{5.10}$$

where N_p is the number of quasi-particles or computational particles that provides a representation of the distribution function f. The constant f_0 is the proper normalization factor. $g[\mathbf{x}-\mathbf{x}_n(t)]$ is some analytical function defines the spatial shape of the quasi-particle while $\delta[\mathbf{p}-\mathbf{p}_n(t)]$ represents the Dirac delta function. Eventually, $g[\mathbf{x}-\mathbf{x}_n(t)]$ may also be considered as a delta function but is not convenient in practice because it would lead to an increased numerical noise in the current and fields.

The discrete representation in Eq.5.10 is a simple way to switch from an Eulerian description to a Lagrangian description where we can follow the trajectories of the computational particles in the phase space. Thus, in above equation the unknown quantities are the Lagrangian coordinates $x_n(t)$ and $\mathbf{p}_n(t)$ and the temporal evolution which can be deduced by introducing the Eq.5.10 into the Eq.5.9. By taking the partial derivative of f, we get

$$\begin{aligned}
\partial_t f &= -f_0 \sum_{n=1} \{\dot{\mathbf{x}}_n(t)\partial_{\mathbf{x}} g[\mathbf{x}-\mathbf{x}_n(t)]\delta[\mathbf{p}-\mathbf{p}_n(t)] \\
&\quad + g[\mathbf{x}-\mathbf{x}_n(t)]\dot{\mathbf{p}}_n(t)\partial_{\mathbf{p}}\delta[\mathbf{p}-\mathbf{p}_n(t)]\}\,, \qquad (5.11)\\
\dot{\mathbf{x}}\partial_{\mathbf{x}} f &= f_0 \sum_{n=1} \left\{ \frac{\mathbf{p}_n(t)}{m} \partial_{\mathbf{x}} g[\mathbf{x}-\mathbf{x}_n(t)]\delta[\mathbf{p}-\mathbf{p}_n(t)] \right\}, \qquad (5.12)\\
\dot{\mathbf{p}}\partial_{\mathbf{p}} f &= f_0 \sum_{n=1} \{\mathbf{F}[\mathbf{x},\mathbf{p}_n(t),t] g[\mathbf{x}-\mathbf{x}_n(t)]\partial_{\mathbf{p}}\delta[\mathbf{p}-\mathbf{p}_n(t)]\}\,. \qquad (5.13)
\end{aligned}$$

In above, we have used the property $f(\mathbf{x})\delta(\mathbf{x}-\mathbf{x}') = f(\mathbf{x}')\delta(\mathbf{x}-\mathbf{x}')$ and similarly for the δ'. Now summing all the above three terms and omitting arguments, we get

$$\sum_{n=1}^{N_p} \left(-\dot{\mathbf{x}}_n g_n' \delta_n - \dot{\mathbf{p}}_n g_n \delta_n' + \frac{\mathbf{p}_n}{m} g_n' \delta_n + \mathbf{F}_n g_n \delta_n' \right) = 0 \tag{5.14}$$

Now integrating above equation over momentum space $d\mathbf{p}$ by using the divergence theorem and recalling that the flux of $(\mathbf{F}(\mathbf{x},\mathbf{p},t) - \dot{\mathbf{p}}_n(t))\, g[\mathbf{x}-\mathbf{x}_n(t)]\delta[\mathbf{p}-\mathbf{p}_n(t)]$ is zero for $|\ \mathbf{p}\ | \to \infty$, then

$$\sum_{n=1}^{N_p} \left(-\dot{\mathbf{x}}_n(t) + \frac{\mathbf{p}_n(t)}{m} \right) g_n' = 0 \tag{5.15}$$

which has the obvious solution , independently on the form of g_n',

$$\dot{\mathbf{x}}_n(t) = \frac{\mathbf{p}_n(t)}{m} \tag{5.16}$$

because coordinates corresponding to different index n are independent. Now assuming the function g has similar properties to δ, i.e. $\int g(\mathbf{x}-\bar{\mathbf{x}})d\mathbf{x} = 1$ and $\int g'(\mathbf{x}-\bar{\mathbf{x}})d\mathbf{x} = 0$. Integrating above Eq.5.14 in space $d\mathbf{x}$, using the divergence theorem and recalling that the flux of $\left[\left(\frac{\mathbf{p}_n(t)}{m} - \dot{\mathbf{x}}_n(t) \right) g[\mathbf{x}-\mathbf{x}_n(t)]\delta[\mathbf{p}-\mathbf{p}_n(t)] \right]$ is zero for $|\ \mathbf{x}\ | \to \infty$, then we get

$$\sum_{n=1}^{N_p} \left(-\dot{\mathbf{p}}_n + \bar{\mathbf{F}}_n \right) \delta'(\mathbf{p}-\mathbf{p}_n) = 0 \tag{5.17}$$

We obtain the solution for momentum variable $\bar{\mathbf{p}}_n$ as

$$\dot{\mathbf{p}}_n(t) = \bar{\mathbf{F}}_n(\mathbf{x}_n, \mathbf{p}_n(t), t) \tag{5.18}$$

where

$$\bar{\mathbf{F}}_n(\mathbf{x}_n, \mathbf{p}_n(t), t) = \int \mathbf{F}(\mathbf{x}, \mathbf{p}_n, t) g(\mathbf{x} - \mathbf{x}_n) d\mathbf{x} \tag{5.19}$$

Thus in equations of motion (5.16) and (5.18), the problem of solving the kinetic equation for the distribution function f is reduced to the problem of solving a system of $2\mathrm{N_p}$ ordinary differential equations. In a 1D geometry each computational particle represents an infinite sheet. These particles are point like in momentum space, having $\mathbf{p}_n$ as a single definite value of the momentum and are extended in the coordinate space. The spatial shape is described by the function $g(\mathbf{x} - \mathbf{x}_n)$, centered over the average position $\mathbf{x}_n$. Quantity $\bar{\mathbf{F}}_n$ is the spatial average of the force $\mathbf{F}(\mathbf{x}, \mathbf{p}_n, t)$ on the $n-$th particle.

Solving our charge density $\rho(\mathbf{x}, t)$ and current density $\mathbf{J}(\mathbf{x}, t)$ from Eqs. (5.3) and (5.4), in terms of discrete particles representation of $f(\mathbf{x}, \mathbf{p}, t)$ (i.e Eq. 5.10), we get

$$\rho(\mathbf{x}, t) = f_0 \sum_{\alpha,n} \mathbf{x}_\alpha g[\mathbf{x} - \mathbf{x}_n]$$

$$\mathbf{J}(\mathbf{x}, t) = f_0 \sum_{\alpha,n} \mathbf{x}_\alpha \mathbf{v}_n g[\mathbf{x} - \mathbf{x}_n] \tag{5.20}$$

Once the sources, i.e charge and current densities in Eq.(5.20) are known, it remains now to find the numerical solution of Maxwell's equations to find the electromagnetic fields. We need to built a suitable algorithm to solve numerically Maxwell equations, so the charge and the fields are defined at the points on a numerical grid and are calculated on the basis of the particle distribution. Numerical grid is a finite set of spatial points of coordinates $\mathbf{x} = i\Delta\mathbf{x}$, with $i = 0, 1, 2, ..., N_g - 1$ the total number of grid points. The choice of the spatial resolution $\Delta\mathbf{x}$ is dictated by physical and numerical requirements. The spatial size of the grid is $L = N_g \Delta\mathbf{x}$; the system extends in space from $\mathbf{x} = 0$ to $\mathbf{x} = L$.

5.5 Numerical Algorithm

5.5.1 The Discrete Model Equations

The goal is to show the implementation of the typical numerical algorithms associated with PIC simulations. Let x be the only relevant spatial coordinate and all quantities are functions of (x, t) only. So the normalized Maxwell equations in the 1D geometry reduces to:

$$\partial_x E_x = \rho, \tag{5.21}$$
$$\partial_t E_x = -J_x, \tag{5.22}$$
$$\partial_t E_y = -J_y - \partial_x B_z, \tag{5.23}$$
$$\partial_t E_z = -J_z + \partial_x B_y, \tag{5.24}$$
$$\partial_x B_x = 0, \tag{5.25}$$
$$\partial_t B_x = 0, \tag{5.26}$$
$$\partial_t B_y = \partial_x E_z, \tag{5.27}$$
$$\partial_t B_z = -\partial_x E_y. \tag{5.28}$$

B_x is constant and uniform and thus taken equal to zero. Let us introduce now the auxiliary fields

$$F_{\pm} \equiv E_y \pm B_z \tag{5.29}$$
$$G_{\pm} \equiv E_z \pm B_y \tag{5.30}$$

Now looking at normalized set of Maxwell equations $(5.21 - 5.28)$, these fields in Eq.$(5.29 - 5.30)$ satisfy the equations

$$(\partial_t \pm \partial_x)F_{\pm} = -J_y, \tag{5.31}$$
$$(\partial_t \pm \partial_x)G_{\mp} = -J_z \tag{5.32}$$

Now integrating along the characteristic $x = \pm ct$ (having $c = 1$) to yield an advance scheme for the advance scheme up-to order $\mathcal{O}(\Delta t^2)$

$$F_{\pm}(x \pm \Delta x, t + \Delta t) = F_{\pm}(x, t) - \Delta t J_y(x \pm \Delta x/2, t + \Delta t/2), \tag{5.33}$$
$$G_{\pm}(x \mp \Delta x, t + \Delta t) = G_{\pm}(x, t) - \Delta t J_z(x \mp \Delta x/2, t + \Delta t/2), \tag{5.34}$$

where $\Delta x = c\Delta t$. Thus the discrete transverse fields will be interlaced with the phase space and transverse currents with time. The phase space will be defined at the cell boundaries $x = i\Delta x$ where $i = 0, 1, 2, .., N - 1$ and with the time-steps $t = n\Delta t$, having $n = 0, 1, 2....$ Therefore the transverse current will be defined at the cell centers $x = (i + 1/2)\Delta x$ and at the time-steps $t = (n + 1/2)\Delta t$

The value of Δx is bounded to the temporal resolution or time step Δt, which corresponds to the temporal discretization of all physical variables. The spacing of the grid points depends on the physics of the process to be simulated. The fields and densities are calculated on a grid composed of finite number of grid points spaced by Δx while the particle position is represented by the continuous variable x_n. Since we imagine that the particle is extended in space and its center position x_n will lie in the cell number i; i.e each particle at a given instant is located inside the cell, such that $i\Delta x < x_n < (i + 1)\Delta x$. Each particle will contribute to the source terms (i.e current and density) in the grid composing the parent and neighboring cells and the force on the particle will be evaluated from the value of fields in the parent and neighboring cells. The time step length then has to be chosen on the basis of the space resolution. It can be proven that the numerical scheme is stable when $c\Delta t \leqslant \Delta x$, and this implies that the particles move at most from one cell to neighboring one within one timestep.

The accuracy of the simulation results depends also on the number $\mathrm{N_p}$ of macro particles per cell that have been used: in fact in the denser plasma regions, if the maximum density is $\mathrm{n_0}$ then the minimum density difference that is possible to resolve is $\mathrm{n_0/N_p}$. The statistics can be improved by using large number of particles per cell. In a 1D3P geometry (one spatial and three momentum coordinate) each particle is represented by 4 numbers in double precision, hence by $4 \times 8 = 32$ bytes. One million of particles corresponds to 32Mbytes. To reduce statistical fluctuations, the number of particles per cell, $\mathrm{N_p/N_g}$ should be much larger than one. As a consequence, the memory needed to allocate currents and fields will be much less. Due to the low scaling of fluctuations with the number of variables ($\sim 1/\sqrt{\mathrm{N}}$), significant statistical fluctuations occur most of the time. The main disadvantages of the PIC code is probably the high noise level. The physical reason for noise is that the largest number of particles one can follow in simulation is orders of magnitude smaller than the true number of particles of plasma. The success of the PIC relies on the fact that collective plasma effects depends on the long-range coulomb interactions. Thus one may think of the "closest" interaction without significantly affecting the properties of collective plasma and this can be achieved by assigning a finite spatial width to the computational particles such as to soften the singularity of the Coulomb interactions.

CHAPTER 6

Solitary versus Shock wave Acceleration in Laser Plasma Interactions

The excitation of nonlinear electrostatic waves, such as shock and solitons, by ultra-intense laser interaction with overdense plasmas and related ion acceleration is investigated by numerical simulations. Stability of solitons and formation of shock waves is strongly dependent on the velocity distribution of ions. Monoenergetic components in ion spectra are produced by "pulsed" reflection from solitary waves. Possible relevance to recent experiments on "ion acceleration by collisionless shocks" is discussed.

6.1 Introduction

The generation of energetic ions of high flux with intense short laser pulses has been a subject of fundamental interest attracting wide attention in recent years. Energetic ions from laser plasma interactions are usually accelerated by induced quasistatic electric fields formed at the front side of target due to space charge separation when laser ponderomotive force pushes electron forward and backward in the interacting region [160]. Interacting with an overdense plasma (i.e. having electron density $\mathrm{n_e} > \mathrm{n_c}$, with $\mathrm{n_c} = 1.1 \times 10^{21}/\lambda(\mu\mathrm{m})^2$ cm^{-3} the cut-off density for the laser light), the light pressure of relativistically intense laser pulses sweeps out and compress the plasma, pushing its surface forward at high speeds. Such a combination of strong compression and plasma acceleration generate strong shock waves that propagate towards the bulk of the plasma. In moderately overdense and hot plasmas, where the shock waves are of collisionless nature, shock acceleration (SA) may lead to higher ion energies than the widely studied TNSA mechanism (Ch. 3, sec. 3.1) [14] and to monoenergetic spectra, as suggested on the basis of numerical simulations [78].

On the contrary, in "cold" overdense plasmas, ion acceleration also had been shown to occur via the so-called "hole boring" (HB) mechanism (see Ch.3, sec.3.2 for detail) [95, 105] by which the local radiation pressure creates a charge-separation field that sweeps up the ion density profile and accelerates ions with an average velocity, generally known as hole-boring velocity v_{hb}. The steepening of ion density eventually leads to wave-breaking producing a "fast" ion bunch with velocity $v_i \simeq 2v_{\mathrm{hb}}$ that penetrates into the plasma. Depending on the laser pulse duration, the HB acceleration process may generate a sequence of ion bunches. Now, since according to Silva *etal* [78], collisionless shocks are excited by the piston action of the laser pulse and their velocity $v_s \simeq v_{\mathrm{hb}}$, so that reflection from the shocks would generate ions with velocity $v_i \simeq 2v_s \simeq 2v_{\mathrm{hb}}$, one would expect shock acceleration (SA) to yield a cut-off velocity of ions which is equal to that predicted by the HB model. An important difference between the SA simulations by Silva etal[78] and the HB ones by Macchi etal.[95] is that a laser pulse with linear polarization (LP) was used in the first case, leading to efficient production of energetic ("fast") electrons which was absent in the simulations of Macchi etal[95] due to the use of circular polarization (CP). As a consequence, analysis of ion spectra alone may not discriminate between SA and HB mechanisms, and the latter may be confused when interpreting results of simulations or experiments on ion acceleration.

To point out how SA and HB should be discriminated from each other was one of the motivations

of the work reported here. We identified and aimed to analyze via 1D PIC simulations two issues which we consider to be characterizing for SA versus HB. The first issue is to establish when and whether ion acceleration occurs only at the front surface, as expected for HB, or also in the bulk of the target by reflection from a propagating shock, as expected for SA (we do not consider here rear surface acceleration as in TNSA, that may be easily distinguished in simulations). The second issue is the role of "electron temperature" which, in turn, should lead to differences between the cases of laser pulses with LP or CP, respectively.

6.2 Simulation with Linear Polarization

6.2.1 Solitary wave dynamics and ion acceleration

Numerical set-up

Since we focus on the basic aspects, we restrict to 1D PIC simulations for the sake of simplicity and high numerical resolution. As found in previous work[78], with respect to the 1D modeling the main differences found in two-dimensional (2D) simulations are that the shock front is obviously non-planar and that the intensity distribution in the focal spot leads to a radial dependence of the initial shock velocity, since the latter is determined by the local amplitude of the laser pulse (see below), in a way analogous to the hole boring acceleration in 2D[95]. The simulations in Ref.[78] showed only a few percent difference in the energy cut-off of ions between 1D and 2D, with the most energetic ions located along the axis (a feature which is common to other acceleration schemes). For what concerns the later evolution of the shock, with respect to a "realistic" 3D geometry we expect the 1D approximation to be reliable as far as the distance traveled by the shock remains smaller than the laser spot width, that is typically of several laser wavelengths; since the below described phenomena occur already when the shock has traveled only over a few wavelengths. We expect our findings not to be limited to the 1D planar geometry.

On the other hand, the issue of high numerical resolution (which is accessible in 1D) is very important because we found that the numerical results converged only for sufficiently high values of the number of particles per cell $\mathrm{N_p}$, although qualitatively similar features were observed also for lower $\mathrm{N_p}$. This suggests that kinetic effects play an essential role and thus low-density tails in the distribution functions must be resolved accurately. In addition, recent experiments on monoenergetic shock acceleration have shown narrow monoenergetic peaks that apparently contain a very low number of ions[79]; thus, whatever the mechanism of ion acceleration, a multidimensional simulation with insufficient particle statistics would not be able to resolve such features. In the simulations reported below, $\mathrm{N_p} = 800$ while the spatial and temporal resolution $\Delta\mathrm{x} = \mathrm{c}\Delta\mathrm{t} = \lambda/400$, where λ is the laser wavelength. Two dimensional simulations with such values of $\mathrm{N_p}$ and $\Delta\mathrm{x}$ would be extremely demanding on the computational side and are left for future work.

Short pulse excitation: solitary structures

We now analyze a representative simulation with the following set-up. The laser pulse is linear polarized with a peak amplitude $a_0 = 16$ and duration $\tau = 4\mathrm{T}$ [full width at half maximum (FWHM)], with T the laser period; the temporal profile is composed by 1T long, $\sin^2$-like rising and falling ramps and a 3T plateau. The plasma had a slab, square-like profile with initial ion and electron densities $\mathrm{n_i} = \mathrm{n_e} = 20\mathrm{n_c}$ and 15λ thickness. A laser pulse with central wavelength $\lambda_0 = 2\pi\mathrm{c}/\omega_0 = 1.0\mu$m,

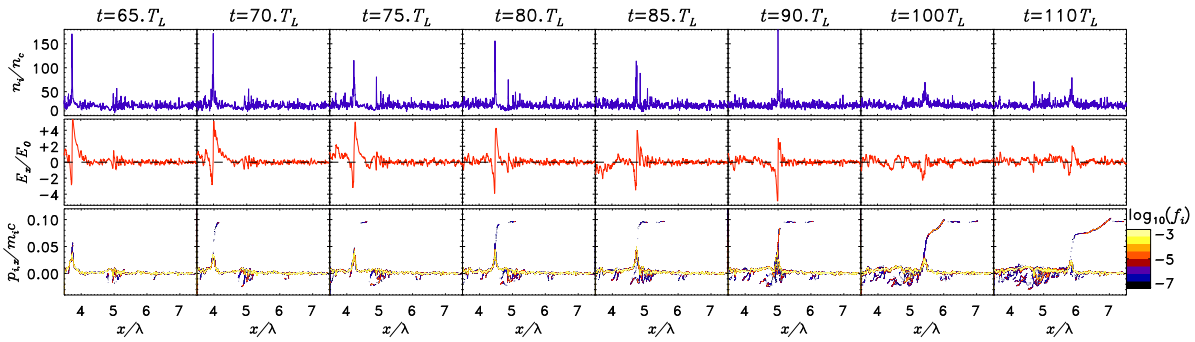

Figure 6.1: Snapshots of the evolution of a Solitary Acoustic Wave (SAW) at eight different times. The upper, middle and bottom rows show the ion density $\mathrm{n_i}$, the electrostatic field $\mathrm{E_x}$ and the contours of the $f_i(\mathrm{x},\mathrm{p_x})$ ion phase space distribution in a $\log_{10}$-scale. The laser pulse impinges from the left reaching the plasma boundary ($\mathrm{x}=0\lambda$) at $\mathrm{t}=0\mathrm{T}$. Simulation parameters are $a_0=16$, $\tau=4\mathrm{T}$ and $\mathrm{n_e}=20\mathrm{n_c}$. $\mathrm{n_i}$ is normalized to $\mathrm{n_c}$, $\mathrm{E_x}$ to $\mathrm{E_0}=\mathrm{m_e}\omega\mathrm{c}/\mathrm{e}$ and $\mathrm{p_x}$ to $\mathrm{m_p c}$.

propagating along the $\mathrm{x}-$direction and interacting with plasma having initial ion and electron temperature, $\mathrm{T_i}=\mathrm{T_e}=0\mathrm{keV}$. For reference, the laser pulse front reaches the front surface placed at $\mathrm{x}=0$ at the time $\mathrm{t}=0$.

In the early stage of the interaction, the laser pulse accelerates a fraction of high-energy, strongly relativistic electrons with energy of several $\mathrm{m_e c^2}$ which penetrate into the target and later recirculate across it, driving heating of bulk electrons. A solitary-like structure is generated at the front surface under the action of the laser pulse and then propagates into the plasma bulk at a constant velocity $v_s\simeq 0.05\mathrm{c}$. This value is close to the hole boring velocity v_{hb}, which in our case is calculated from Eq. 6.17(will discuss below) where the reflection coefficient is measured to be $\mathrm{R}\simeq 0.75$[1] in the simulation of Fig.6.1, yielding $v_{\mathrm{hb}}=0.06\mathrm{c}$. At $\mathrm{t}=65\mathrm{T}$, the solitary structure is located at $\mathrm{x}\simeq 3.7\lambda$ (first frame of Fig.6.1). The ion density has a very strong spike, reaching values up to $\simeq 9$ times the background density. The electric field around the density spike has a sawtooth shape. For reference we call the structure we observe a SAW (for Solitary Acoustic Wave).

The snapshots of SAW density and field profiles are qualitatively resemblant to those of solitonic solutions as described in Ref.[28]. As explained in sec.4.3.2 of Ch.4, a necessary and general condition for such solitons to exist with a velocity v_s is that the electrostatic potential energy jump $\mathrm{Ze}\Phi$ has a peak value

$$\mathrm{Ze}\Phi_{\mathrm{max}} < \mathrm{m_i} v_s^2/2\,, \tag{6.1}$$

so that background ions are not reflected by the SAW. Within a fluid model with the electrons in an isothermal Boltzmann equilibrium [28] at the temperature $\mathrm{T_e}$, the condition on the potential poses an upper limit on the Mach number $\mathrm{M}=v_s/c_s<1.6$, where $c_s=\sqrt{\mathrm{T_e}/\mathrm{m_i}}$ is the speed of sound. The other condition is that the soliton must be supersonic, i.e. $\mathrm{M}>1$

Numerical integration[2] of $\mathrm{E_x}$ over x for the SAW at $\mathrm{t}=65\mathrm{T}$ (first snapshot in Fig.6.1) yields $\mathrm{e}\Phi_{\mathrm{max}}\simeq 0.78\mathrm{E_0}\lambda\simeq 4.9\mathrm{m_e c^2}$, more than twice the kinetic energy $\mathrm{m_i}v_s^2/2\simeq 2.3\mathrm{m_e c^2}$. One thus

[1] Reflection coefficient can be estimated by using the energy conservation from Eq. 3.11 in sec. 3.2 of Ch.3 which implies $\mathrm{R}+\mathrm{T}=1-\mathrm{A}$, assuming negligible transmission ($\mathrm{T}=0$) and by calculating the amount of laser energy absorbed in overdense target, i.e. the absorption coefficient A, we can evaluate the amount of light reflected, i.e. reflection coefficient R.

[2] Since we have only discrete values of E_x, therefore what we actually do is $\sum E_x(i)dx$ and then we perform the integral, to calculate the electrostatic potential $\Phi=\sum E_x(i)dx$, starting from the point where E_x has a maximum value (top of SAW front).

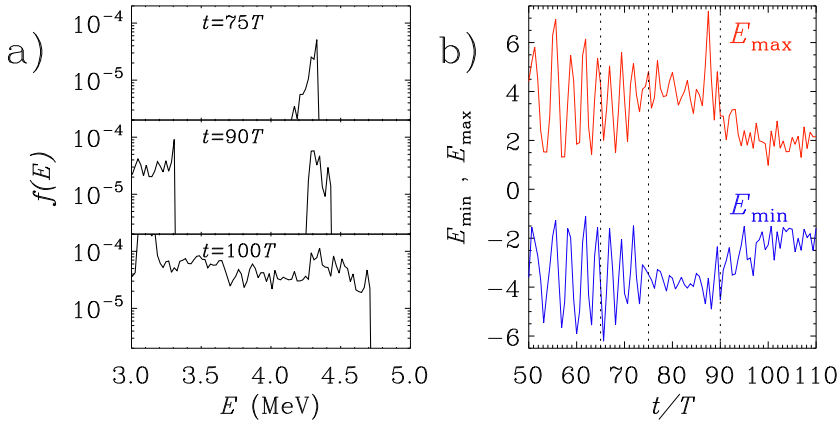

Figure 6.2: a): ion spectra from the simulation of Fig.6.1 at the times $t = 75T$, $90T$ and $100T$. Only ions in the same spatial range as Fig.6.1, i.e. $3.5 < x < 7.5$, are included in the spectra. b): temporal evolution of the maximum (red line) and the minimum value (blue line) of the electric field for the SAW structure observed in Fig.6.1. The vertical dashed lines mark the instants $t = 65T$, $75T$ and $90T$ at which ion reflection events start as seen in Fig.6.1.

would expect ion reflection to occur promptly from the SAW field. This occurs indeed in the simulation, producing a bunch of high-energy ions with very small momentum spread as can be observed at $t = 70T$ and $t = 75T$. However, violation of the condition Eq.(6.1) and consequent ion reflection do not destroy the SAW; at $t = 75T$, the SAW is still present with almost unperturbed velocity, and ion reflection has stopped. Between $t = 75T$ and $t = 85T$ a second bunch is formed in a very similar way, as observed between the third and fifth snapshot in Fig.6.1. Both bunches correspond to a monoenergetic high-energy peak in the spectrum, as shown in Fig.6.2-a; the FWHM of the peak at $t = 75T$ is less than 1%.

The SAW eventually "breaks" after $t \simeq 90T$ producing a third bunch with a higher number of ions as seen in seventh snapshot of Fig.6.1. As a consequence, the high-energy part of the spectrum broadens and monoenergetic features are lost, as seen in Fig.6.2-a at $t = 100T$. The SAW quickly loses its energy and slows down, so that ions are now reflected with lower energy, although a minor fraction exceeds the energy of the monoenergetic peaks generated at earlier times. Notice that the SAW collapse might not interpreted on the basis of the fluid existence condition alone, because the slowing of the SAW velocity would enforce such condition (unless the velocity falls below c_s). Apparently, the SAW breaking occurs after a "collision" with a slower, counter-propagating structure that can be noticed in the frames of Fig.6.1.

The observed behavior of the SAW is related to the observation that the electric field amplitude is not constant in time, but oscillates as shown in Fig.6.2-b. The temporal behavior of the maximum and minimum values suggests that the electron cloud around the ion density spikes oscillates back and forth. The amplitude of the oscillation tends to decrease with time. The quenching of the oscillation is particularly evident after the generation of the second fast bunch at $t \simeq 75T$. At this instant, the potential jump at the SAW front is $e\Phi_{max} \simeq 0.5E_0\lambda \simeq 3.1m_ec^2$, slightly above the stability threshold Eq. (6.1). Eventually, the overall amplitude greatly decreases after the generation of the third bunch, as also observed in the last frames in Fig. 6.1.

The onset of ion acceleration from the SAW as a sequence of generation of ion bunches with narrow energy spread, with the SAW conserving its velocity between subsequent acceleration events, has been observed in several of the simulations we performed, and further confirmed by simulations where test particles were put at various positions inside the plasma slab. Only those test particles located near to the

points where the incoming SAW reaches the threshold amplitude for ion reflection were accelerated. This observation is empirical and reproducible in simulations, although the frequency at which monoenergetic ion bunches are produced can not be estimated a priori as a function of the laser and plasma parameters. A few results of the test particle simulations have been discussed below in sec. 6.4

6.2.2 Effects of the ion energy distribution

The above reported observations led us to infer that the local phase space distributions of ions has a crucial role in determining both the stability of solitary waves and the possibility to generate true shocks whose signature would be, in the framework of fluid theory, the formation of a continuous flow of reflected ions. If the ions are "cold", i.e. have no energy spread, reflections from a moving potential barrier may occur either for none or for all the ions, since their initial conditions are the same. In the latter case, as soon as ion reflection begins, the wave would quickly lose its energy in the acceleration of the whole bulk of ions. This effect may prevent the formation of shocks and be crucial for the stability of solitary waves.

In order for a shock wave to form, it should be possible for the wave to "pick up" from the ion distribution only a fraction of the ions in an energy range for which a reflection condition analogous to Eq.(6.1) is fulfilled. If the ion distribution has a velocity spread, for a given value of Φ_{max} all ions with velocity $v_r > v_s - \sqrt{2e\Phi_{max}/m_i}$ will be reflected from the wave front. Thus a true shock may form in the presence of a sufficiently warm ion distribution. Fig.6.3 shows results of a simulation with identical parameters as Fig.6.1, but with the initial ion temperature $T_i = 1$ keV. Ion starts to reflect from SAW front at early time $30T$ and formation of a shock-like structure with "continuous" reflection of ions is observed at later stages at $85T$. The shock velocity is found to decrease slightly in time (as may be deduced also from the slope of the reflected ions feature in the phase space plot of Fig. 6.3) which could be interpreted as due to the wave energy transfer into reflected ions. Initially, as the fraction of reflected ions are small, a monoenergetic peak around 4.5MeV appears at $40T$ and $60T$ which further broadens

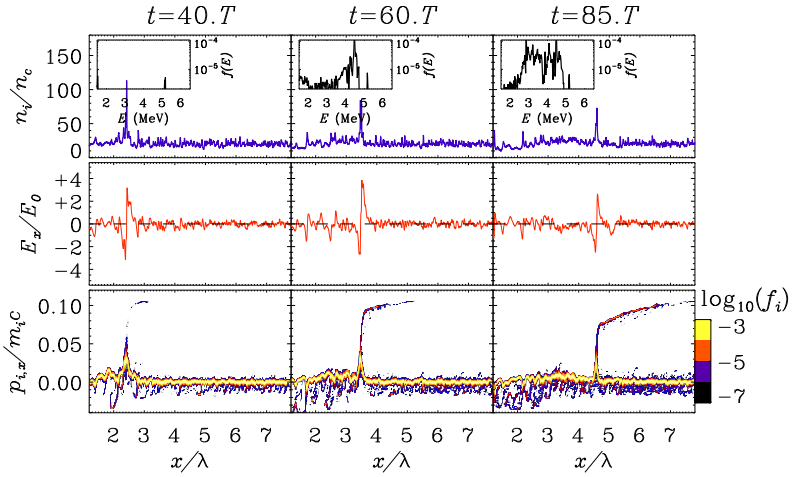

Figure 6.3: Snapshots at three different times of the n_i, E_x and $f_i(x, p_x)$ for a simulation identical to that of Fig.6.1 but for an initial ion temperature $T_i \simeq 2 \times 10^{-3} m_e c^2 = 1$ keV, showing the onset of ion reflection in large fraction than that of cold ions case. The scales are the same as in Fig.6.1 to show that the perturbation in n_i and E_x has a lower value in the present case. The insets show the corresponding ion spectra, limited to the ions in the region around the shock and excluding ions accelerated at the target boundaries.

with time as the shock slows down attempting to reflect more ions. The strength of electrostatic field and ion density also decrease with time (see upper and middle frames of Fig.6.3) which also gives the indication of shock deceleration along the propagation path.

Simulations have also been performed for an initial ion temperature $\mathrm{T_i} = 5 - 10$ keV, it is observed that increasing the initial ion distribution to higher value, the formed shock wave reflects ions in higher fraction and gets damped out faster giving all its energy to reflected ions. From the previously explained results for cold ions, i.e. of Fig.6.1 which says that a shock may not form because we can't have a steady and stable ion reflection. This indeed we observed for initial $\mathrm{T_i} = 1\mathrm{keV}$, having continuous ion reflection from the shock front which slows down with time (presumably due to energy loss to ions) and thus broadening the energy spectrum. The effect was more stronger for initial $\mathrm{T_i} = 5\mathrm{keV}$ because more ions in the distribution are reflected (for the same shock velocity). Now, lowering the initial $\mathrm{T_i} = 0.1\mathrm{KeV}$, we found that the acceleration is still "pulsed" as that of cold ion case but the bunches have longer duration and smaller spectral width which suggests that we are close to a good compromise for monoenergetic acceleration, and confirms that even a small ion temperature plays an important role. The initial warm ions study suggests that the role of initial ion temperature is quite important in formation of solitary or shock waves, their stability and related ion acceleration. The detailed study about the "optimal" initial ion temperature range in which the shock survives for a longer times and reflect ions of narrow spectral width is performed in the next chapter.

6.2.3 SAW breaking in the expanding sheath

The effect of the background ion distribution can be also noticed in the case in which the SAW generated at the front side of the plasma eventually reaches the rear side and propagates in the expanding sheath. The SAW overturns the slower ions and propagates in the sheath until it reaches the region in which the ion velocity is such that the ions are now reflected by the SAW potential (since the ions in the sheath move in the same direction of the SAW, their velocity in the rest frame of the SAW is lower than in the "laboratory" frame, hence they are reflected more easily). This mechanism was also described by [161]. Fig. 6.4 shows results from a simulation having the same parameters of Fig.6.1, but the plasma slab was only 3λ thick in order for the SAW to reach the sheath before losing much of its energy to reflected ions. Looking at the results shown in Fig.6.4, until $54\mathrm{T}$, there does not occur any ion reflection from the SAW front. As soon as the SAW reaches to the rear side, the threshold condition for ion reflection is reached, a few background slower ions turn back at the top of the SAW potential hill which results in a very high ion density peak at $54T$ and ions acquire the velocity $\sim 2v_s$. If the SAW reaches to the rear side after the laser pulse is over, the electric field in an expanding sheath (which decreases with time $\sim \mathrm{t}^{-1}$) becomes too small (see Fig.6.4 at $72\mathrm{T}$) such that SAW can not be further accelerated. Thus from this point onward, the SAW loses its energy in accelerating ions and breaks. Breaking occurs in the sheath in the region where the local velocity of ions is close to the SAW velocity, and leads to ion acceleration.

From the above results, our study suggests that generating highly monoenergetic ions by "shock acceleration" is not straightforward, as in our simulation we observe narrow spectra only as resulting from SAW "pulsations"[3] as a transient effect, since as shown in Figs.6.1 and 6.2 the SAW collapse ultimately produces a broad spectrum masking the monoenergetic peak. Especially in a plasma with "cold" ions producing a monoenergetic spectrum might be at odd with efficiency, because the reflection of a large fraction of ions by the moving structure (either a shock or a soliton) would ultimately cause a strong

[3] Ion acceleration is of "pulsed" nature, i.e. it occurs only at certain instants or points along the propagation path, and does not lead to the SAW disruption.

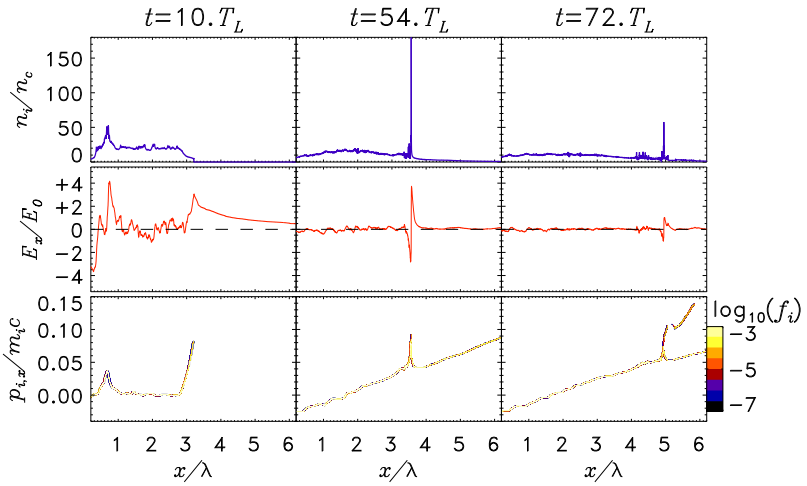

Figure 6.4: Snapshots at three different times of the $\mathrm{n_i}$, $\mathrm{E_x}$ and $f_i(\mathrm{x}, \mathrm{p_x})$ for a simulation identical to that of Fig.6.1 but for a shorter plasma slab $\ell = 3\lambda$, showing the breaking of the SAW in the expanding sheath at the rear side of the plasma.

loading effect decreasing its field and velocity. This is in qualitative agreement with the experimental results of [79] where the number of ions ($\sim 2.5 \times 10^5$) in the narrow spectral peak at ~ 22 MeV implies a conversion efficiency $< 10^{-8}$ of the 60 J pulse energy. The acceleration of a larger fraction of ions is also observed when the SAW undergoes disruption either by interacting with another structure or when entering the expanding sheath region at the rear surface of the plasma. Shock waves with "steady" acceleration of ions are generated in a plasma with initially "warm" ions, where a population of reflected ions can be formed.

6.2.4 Collective Oscillations of the Warm Plasma Foil

This is an analytical attempt of a simple theory for the observed oscillations in the field of the solitary wave structures observed in the simulations. Here we focus on a single solitary acoustic wave SAW as observed in our simulation results shown in Fig.6.1. The idea is that the cloud of electrons oscillates back and forth across the ion density spike.

Let us consider at a starting point, a thin foil with ion density $n_i(x) = N_i\delta(x)$. The foil(target) is immobile (it has zero velocity in the lab frame). The electrons have temperature T_e and spread out forming two symmetric sheaths on each side of the foil. A rough and essential schematic of the profile of electric field and ion density in a SAW is shown in the cartoon of Fig.6.5. The profile is quite similar to those of a very thin foil of warm plasma and can be calculated analytically for the electrons assuming a Boltzmann distribution and for a "truncated" energy distribution. The obvious physical difference between a thin foil and a SAW is that the latter moves at a velocity v, which for the moment we assume to be constant as in a steady state and non-relativistic ($v \ll c$). A simple analytical solution for the equilibrium state exists (see the appendix in Ref.[162]), with the electric field given by

$$E_0(x) = \frac{2T_e/e}{|x| + T_e/(\pi e^2 N_i)}\mathrm{sign}(x). \tag{6.2}$$

Now we introduce an oscillating perturbation and indicate the oscillating parts of each quantity as $E = \tilde{E}(x)e^{-i\omega t}$ (electric field), $n = \tilde{n}(x)e^{-i\omega t}$ (electron density), $v = \tilde{v}(x)e^{-i\omega t}$ (electron velocity).

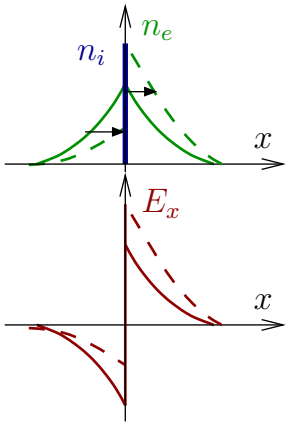

Figure 6.5: Collective oscillation of the electron cloud around the ion density spike consistent with $\Delta \mathrm{E_x} = \max(\mathrm{E_x}) - \min(\mathrm{E_x})$ remaining $\sim$ constant.

The system of 1D linearized fluid electrostatic equations are

$$\partial_t \tilde{n} + \partial_x (n_0(x)\tilde{v}) = 0, \tag{6.3}$$
$$m_e n_0(x)\partial_t \tilde{v} = -\gamma^* T_e \partial_x \tilde{n} - e\tilde{n}E_0(x) - e n_0(x)\tilde{E}, \tag{6.4}$$
$$\partial_x \tilde{E} = -4\pi \tilde{n} e. \tag{6.5}$$

From these we obtain

$$m_e \partial_x (n_0(x)\partial_t \tilde{v}) = -m_e \partial_t^2 \tilde{n} \tag{6.6}$$

and also

$$\begin{aligned} m_e \partial_x (n_0(x)\partial_t \tilde{v}) &= \frac{m_e}{4\pi e}\partial_t^2(\partial_x \tilde{E}) \\ &= \frac{\gamma^* T_e}{4\pi e}\partial_x^3 \tilde{E} \\ &\quad -e\partial_x(nE_0(x) + n_0(x)\tilde{E}) \end{aligned} \tag{6.7}$$

so that eventually we obtain an equation for $\tilde{\mathrm{E}}$

$$\omega^2 \tilde{E} = -\frac{\gamma^* T_e}{4\pi e}\partial_x^2 \tilde{E} - \frac{e}{m_e}\partial_x(E_0(x)\tilde{E}). \tag{6.8}$$

Because of symmetry we can study this equation for $\mathrm{x} > 0$ only. However we must notice that $\mathrm{E}_0(\mathrm{x})$ also has a contribution arising from the discontinuous ion density. Thus

$$\begin{aligned} \omega^2 \tilde{E} &= -\frac{\gamma^* T_e}{4\pi e}\partial_x^2 \tilde{E} - \frac{e}{m_e}\partial_x(E_0(x)\tilde{E}) \\ &\quad + \frac{4\pi e^2 N_i}{m_e}\delta(x)\tilde{E}. \end{aligned} \tag{6.9}$$

Notice that $E_0(x)$ is an odd function and that the above equation for $\tilde{E}$ may have either odd or even solutions. We are interested in even modes, $\tilde{E}(x) = \tilde{E}(-x)$ and, moreover, we only take long-wavelength modes and thus neglect the term arising from pressure forces (the one proportional to $\gamma^* \mathrm{T_e}$. Thus, for $x > 0$, we have

$$\omega^2 \tilde{E} = -\frac{e}{m_e}\partial_x(E_0(x)\tilde{E}) \tag{6.10}$$

and substituting for E_0

$$\omega^2 \tilde{E} = -\frac{2T_e}{m_e}\partial_x \left[\frac{\tilde{E}}{x + T_e/(\pi e^2 N_i)}\right] \tag{6.11}$$

To solve this equation one may define the auxiliary variables

$$f = \frac{\tilde{E}}{x + T_e/(\pi e^2 N_i)}, \qquad u = \frac{x^2}{2} + \frac{T_e x}{\pi e^2 N_i} \tag{6.12}$$

so that, being $\partial_x = [x + T_e/(\pi e^2 N_i)]\partial_u]$, we obtain

$$\omega^2 f = -\frac{2T_e}{m_e}\partial_u f \tag{6.13}$$

with solution

$$f = A \exp\left(-\frac{m_e \omega^2}{2T_e} u\right) \tag{6.14}$$

with A an arbitrary constant giving the amplitude of the perturbation. Switching back to x, $\tilde{E}$ and extending the solution to $x < 0$ we finally obtain

$$E_t = A\left(x + \frac{T_e}{\pi e^2 N_i}\right) \exp\left[-\frac{m_e \omega^2}{2T_e}\left(\frac{x^2}{2} + \frac{T_e x}{\pi e^2 N_i}\right)\right]. \tag{6.15}$$

The frequency ω is however not determined; the frequency spectrum is continuous, and the particular frequency will be determined by how the oscillation is excited.

6.2.5 Long pulse excitation: Multi-peak structures

When the laser pulse duration is increased with respect to the above reported simulations, we observe multiple peaks of the ion density and sawtooth oscillations of the electric field. Although a structure showing multiple oscillations behind a front is reminiscent of a collisionless shock wave as seen in textbooks, again for an initially cold ion plasma, we do not observe in general a steady ion reflection at the front. The density peaks move at different velocities and thus disperse in time. Hence the structure may be interpreted as a multi-peak SAW, generated due to pulsed hole boring acceleration at the front side [95] at a rate which is approximately the same for simulations having same pulse intensity and plasma density, so that a longer pulse duration allows acceleration of a sequence of ion bunches.

A representative "long pulse" simulation is shown in Fig.6.6. The laser pulse has peak amplitude $a_0 = 16$ (like the above reported "short pulse" simulations) with $5\mathrm{T}$ rise and fall ramps and a $55\mathrm{T}$ plateau. The plasma density and thickness are $20\mathrm{n_c}$ and 20λ, respectively. These parameters are close to those of previously reported $1\mathrm{D}$ simulations (see Fig.1 in Ref.[78]) and indeed some features observed in the ion phase space and density profiles look very similar. However, in our simulations the higher number of computational particles allows us to highlight additional details in the phase space distribution of Fig.6.6 (bottom row) such as vortex structures behind the front, corresponding to "trapped" ions bouncing between adjacent peaks where a potential well is formed. The observation of ions trapped in the multi-peak, nonlinear structure of the electric field and the quite broad distribution along the momentum axis of the most energetic ions suggest that those latter may be actually accelerated by "surfing" the longitudinal wave structure, rather than being merely reflected by the field at the front.

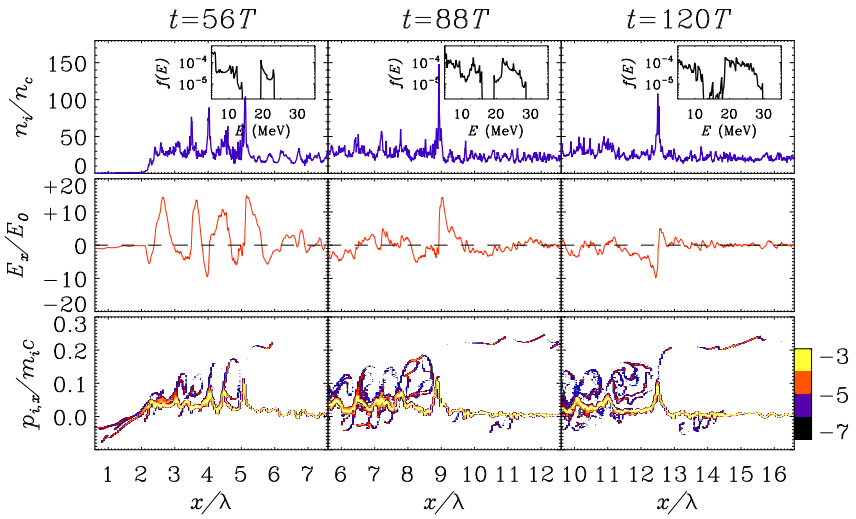

Figure 6.6: Snapshots of multi-peak structures at three different times from a "long pulse" simulation. The insets show the corresponding ion spectra, limited to the ions in the region around the SAW and excluding ions accelerated at the target boundaries. Simulation parameters are $a_0 = 16$, $\tau = 65\mathrm{T}$, $20\mu\mathrm{m}$ target and $\mathrm{n_e} = 20\mathrm{n_c}$. Units are the same as in Fig.6.1.

In addition, we observe significant oscillations of the electric field *ahead* of the wave front (i.e. of the rightmost density peak in Fig.6.6 at $56\mathrm{T}$), which may have been excited by fast electrons and are related to modulations in the momenta of the highest energy ions. The inset shows the spectrum of the reflected ions. During the first reflection event (first frame at $56\mathrm{T}$), the ion spectrum has a peak at $\sim 22\mathrm{MeV}$ and have narrow energy spread. Due to the further reflection events at $88\mathrm{T}$ and $120\mathrm{T}$ which occurs when the SAW potential exceeds the kinetic energy, i.e $(e\Phi_{\mathrm{max}} > m_i v_s^2/2)$, the spectrum doesn't remain of monoenergetic nature and get broader towards higher energy (compare the spectrum in inset of Fig.6.6 at different times, even neglecting the contribution of TNSA at the rear side). By the time $88\mathrm{T}$, the SAWs have been fully evolved and the leading SAW reflect ions of more than $22\mathrm{MeV}$ energy and the cut-off energy reaches up-to $\sim 30\mathrm{MeV}$ at $120\mathrm{T}$. Thus, the ion reflection which occur due to "pulsary action of SAW" is not easy to control and large number of ion reflection events masks the monoenergeticity.

In order to check the steady reflection of ions to sustain the quasi-monoenergetic nature in the spectra, we performed the simulation keeping all the other parameters same as of Fig.6.6 but for warm ions having initial ion temperature $\mathrm{T_i} = 1\mathrm{keV}$ and the results are shown in Fig.6.7. We observed that the SAW wave which turns into shock wave starts to reflect ions from early times and the ion reflection occurs is of

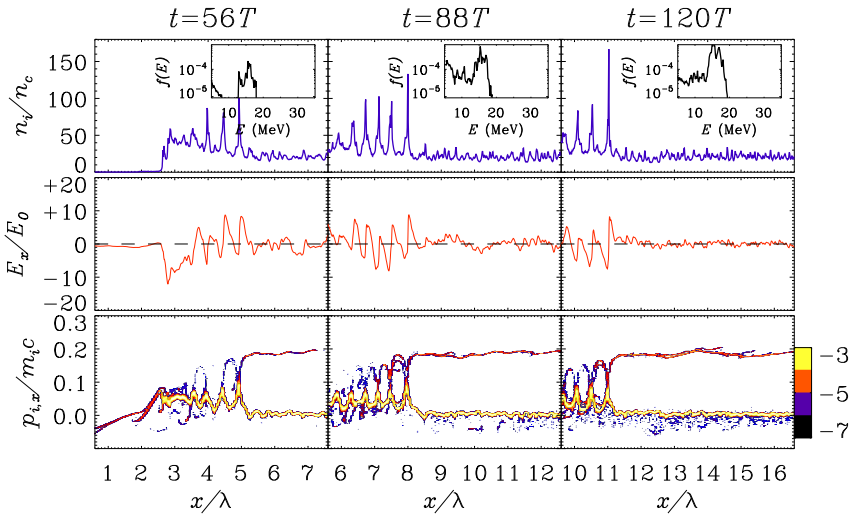

Figure 6.7: Warm ion simulation: Snapshots of the evolution of solitary acoustic wave (SAW) at three different times of a simulation having identical parameters as Fig.6.6, but with the initial ion temperature $\mathrm{T_i} = 1$ keV The insets show the corresponding ion spectra, limited to the ions in the region around the shock and excluding ions accelerated at the target boundaries.

"continuous and steady"[4] in nature. In attempt to reflect more number of ions, the SAW or shock wave front lags behind and is at 11λ irrespective of 12.5λ for cold ions simulation (Fig.6.6) at $120\mathrm{T}$ time duration. In addition, all the multi-peak structures moves almost at constant velocity with time and the corresponding ion density peaks remain there for much longer times. The vortex type structures between the peaks, corresponding to trapped ions is less formed with respect to cold ions simulation in which the particle trapping between the peaks is much more (compare phase space distribution of Fig.6.6 and Fig.6.7). Looking at the ion spectrum at $120\mathrm{T}$, as the wave front is reflecting steady ions, the energy spectra is much more quasi-monoenergetic and remains stable for more time irrespective of the cold ions case in which the spectrum becomes broad because of "non-steady"[5] nature of ion reflection. Although the cut-off ion energy is less in warm ions ($\sim 20\mathrm{MeV}$) than that of cold ion simulation ($\sim 30\mathrm{MeV}$) at $120\mathrm{T}$ time duration, as the shock slows down a bit, losing its energy in reflecting more ions but the spectrum is more stable and sustain quasi monoenergeticity for longer times.

The detailed description of the effect of the initial ion temperature on electrostatic shock generation and monoenergetic ion acceleration by reflection will be prescribed in the next chapter. We will show with 1D PIC simulations that there is "an initial ion temperature window" in which we can increase the number of reflected ions without any significant wave loading for which the shock moves almost with a constant velocity and reflect monoenergetic ions.

6.2.6 Effect of target density on ion dynamics and SAW generation

We also performed 1D PIC simulations for the interaction of a strong laser pulse in the range of $100\mathrm{fs}$ with an overdense target of $15\mu\mathrm{m}$ thickness at the same laser pulse amplitude of $a_0 = 16$. The laser pulse is of duration $\tau = 30\mathrm{T}$, such that; the temporal profile is composed by $2\mathrm{T}$ long, $\sin^2$- like rising and falling ramps and a $28\mathrm{T}$ plateau. A parametric scan have been performed at different target densities vary from $\mathrm{n_{e0}}(=\mathrm{n_{i0}}) = 5\mathrm{n_c} - 50\mathrm{n_c}$. We envision that the SAWs are excited within the plasma for some certain plasma densities, neither appear at low nor at very high plasma density. SAW are more

[4] steady means that the SAW or shock is reflecting ions almost at a constant rate and of less energy spread and can be observed from the slope of the phase space distribution in Fig.6.7 which is almost a straight line.

[5] Non-steady means, the ion reflection occurs at certain time intervals and may differ in energy.

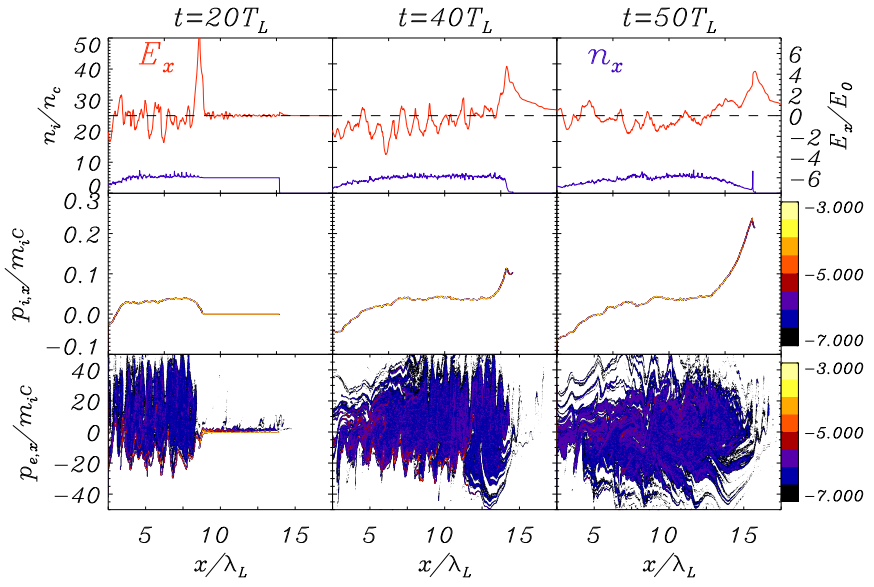

Figure 6.8: Snapshots of ion density $\mathrm{n_i}$, electrostatic field $\mathrm{E_x}$ and contour of ion $f_i(\mathrm{x},\mathrm{p_x})$ and electron $f_e(\mathrm{x},\mathrm{p_x})$ phase space distribution in a log_{10} scale at three different times, at laser pulse amplitude $a = 16$, $15\mu\mathrm{m}$ target thickness and $\mathrm{n_0} = 5\mathrm{n_c}$ plasma density. Note down the scales of $\mathrm{x}-$axis and $\mathrm{y}-$axis while comparing with Fig.6.9, Fig.6.10.

prominent and clearly visible around the plasma density of $n_0 = 10n_c - 20n_c$ and neither occur in higher plasma density of $n_0 = 50n_c$ nor at lower plasma density of $n_0 = 5n_c$.

Fig.6.8 shows the snapshots of the simulation performed at plasma density of $n_0 = 5n_c$. In this case we didn't find any SAW generation within or towards the rear side of the plasma. When a LP laser pulse impinges on the target surface, due to charge separation effects, a strong unipolar electrostatic field is generated (as shown in Fig.6.8 at 20T). A few ions gains an acceleration (as in Fig.6.8 b-c) and reaches towards the rear side of the target without much perturbation to the plasma. Therefore no SAW generation have been observed within the bulk of the plasma which can accelerate ions and the most effective ion acceleration occurs towards the rear side of the target. As the plasma density is not so much high, (as compare to our other simulations shown below at or above $n_0 = 10n_c$), the skin depth and the magnitude of the electric fields penetrating in the plasma increases which results in that electron bunches produced by the laser and transported through the target creates a strong electrostatic field that drives the surface ion acceleration. Due to very high electron heating, having momentum up-to $40m_ec$ as shown in electron phase space of Fig.6.8, the electron temperature across the target will be very high. As a consequence, the relative speed of sound $c_s \simeq \sqrt{T_e/m_i}$ might increases much enough such that the Mach number $M = v_s/c_s$ falls below one, which results in that it doesn't fulfill the fluid theory [28] according to which the lower limit for the existence of solitary waves is $M > 1$.

Fig.6.9 shows the snapshots for the simulation performed at plasma density of $n_0 = 10n_c$, keeping all the parameters same as of Fig. 6.8. In this case, more than one SAW are excited by the radiation pressure of laser from the target front surface which propagate within the plasma and drive the ions to twice its velocity by the wave breaking events; i.e. by reflection from the tip of the SAW. These SAWs which start reflecting ions from the early time duration, regains its position again after some time, exceeds the threshold potential and undergoes further wave breaking and ion reflection. Its interesting to see from Fig. 6.9 (a-c), how the first and second SAW interact with each other and they "exchange" ions, the ions accelerated by the middle SAW gets slowed and trapped by the leading SAW. Until the laser pulse is on, the first and second SAW starts to propagate initially with a velocity $v_s \simeq 0.11c$ (at 40T) and further propagate deep in the bulk by gradual reduction in velocity and density with time. The third solitary like structure which is quite visible at 40T lags behind (Fig.6.9b) with respect to time and get damped out (Fig.6.9c). As a consequence, by the time 120T, there exists only first SAW (can be observed form the ion density and electrostatic field) which propagate and reflect ions. Lower frames of phase space of

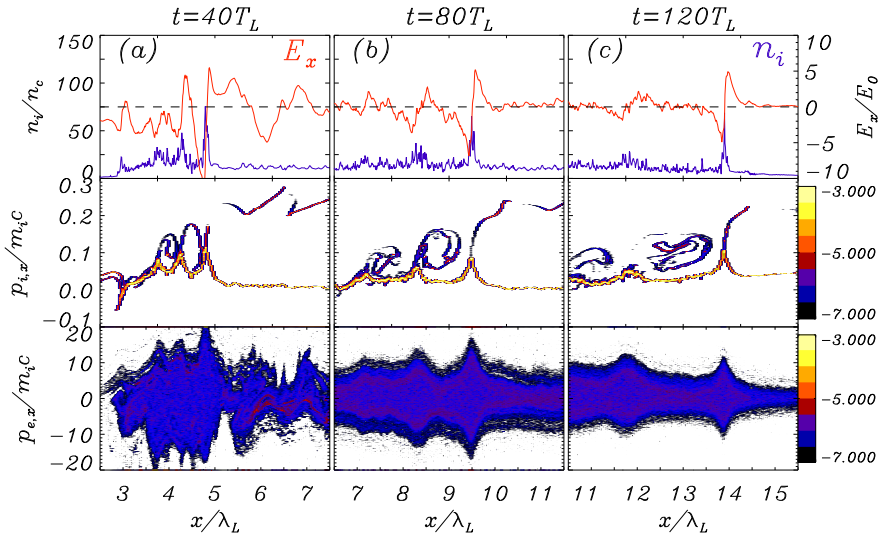

Figure 6.9: Snapshots of the evolution of solitary acoustic wave (SAW) at three different times. The upper row shows ion density(n_i), electrostatic field (E_x), while the middle and bottom rows show the ions and electrons phase space distribution in a log_{10} scale, having all the parameters same as of Fig.6.8 but at plasma density of $n_0 = 10n_c$.

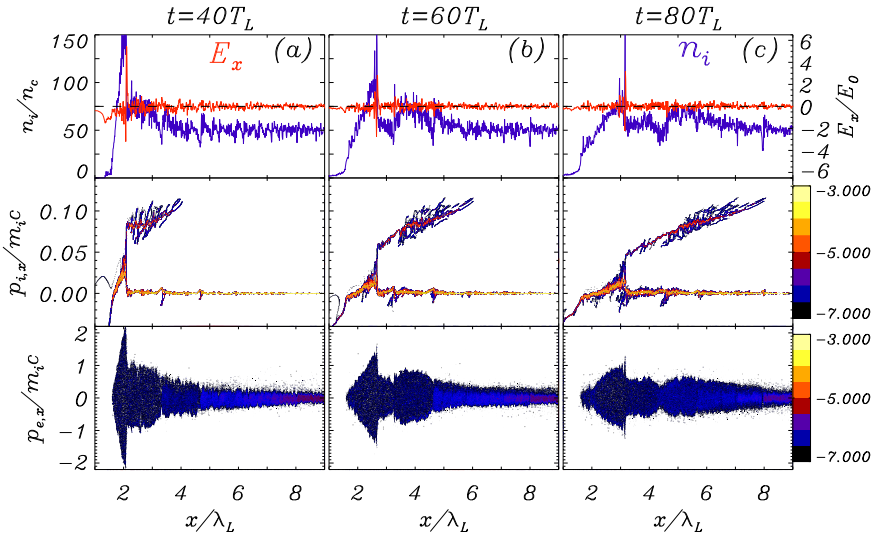

Figure 6.10: Snapshots of ion density $\mathrm{n_i}$, electrostatic field $\mathrm{E_x}$ and contour of ion $f_i(\mathrm{x},\mathrm{p_x})$ and electron $f_e(\mathrm{x},\mathrm{p_x})$ phase space distribution in a log_{10} scale at three different times, keeping all the parameters same as of Fig.6.9, but at plasma density of $\mathrm{n_0} = 50\mathrm{n_c}$. Notice down the $\mathrm{x}-$ and $\mathrm{y}-$axis scales while comparing with Fig.6.8 and Fig.6.9.

ions and electrons in Fig.6.9 shows that hot electron bunches have been formed within the target across these SAWs and as these SAWs structures move forward, similarly these hot electron bunches (or bulk electrons) moves along it. At $40\mathrm{T}$, these bulk electrons around the SAWs have momentum $\approx 20\mathrm{m_e c}$ (electron phase space Fig.6.9) and these bulk electrons get cool down along the propagation time and electron heating across the first SAW decreases to $\approx 10\mathrm{m_e c}$ at $120\mathrm{T}$.

Similar to above case, we also performed the simulation at plasma density $\mathrm{n_0} = 20\mathrm{n_c}$ in which we observed that three SAW′s are formed which start propagating within the plasma, but the ion reflection from the SAW front starts later. The first ion reflection occurs after time $40\mathrm{T}$ while by this time in $\mathrm{n_0} = 10\mathrm{nc}$ case (Fig.6.9), there occurs much more ion reflections and trapping between the multi-peak structures. These multi-peak SAWs propagate up-to later stages by reflecting ions at certain time intervals until there exists electrostatic field across it. Due to less reflection and less trapping of ions at $\mathrm{n_0} = 20\mathrm{n_c}$ case than that of $\mathrm{n_0} = 10\mathrm{n_c}$, the SAWs formed in this case remains stable for longer times. The reflection and particle trapping adds more nonlinearity to the plasma which leads towards the damping of the SAW. If the laser pulse is fairly long such that the oscillations excited within the plasma attain a sufficiently large amplitude at the end of the laser pulse for nonlinear effects to become important. For the LP pulses, due to strong electron heating, the plasma non-uniformity leads to a change in the wave vector of the plasma oscillations. As a result, some of the electrons are thrown out of the plasma region to the rear side which bounce back and further starts recirculating and get accelerated on the process of their interaction with plasma waves while the ions gain energy from their interaction with the localized electric field[163].

We have observed that the solitary acoustic waves (SAW′s) are formed at plasma densities up-to $\mathrm{n_0} = 25\mathrm{n_c}$ for the laser amplitude $a_0 = 16$ and didn't occur at higher plasma densities. Fig.6.10 shows the simulation performed at higher plasma density of $\mathrm{n_0} = 50\mathrm{n_c}$, having all the other parameters same as Fig.6.9. In this case, we didn't seen any clear generation and propagation of SAW like structures within the plasma which undergoes reflection and trapping phenomenons. It may be explained in such a way that as we increase the plasma density, the formed nonlinear electrostatic perturbations might be so slow that they get damped out at earlier times attempting to reflect large fraction of ions. A shock like reflection has been observed in the phase space plots of Fig.6.10, whose signature in the fluid theory is the continuous flow of reflected ions. We envision that a shock-like structure is generated on the front surface which is moving initially at $20\mathrm{T}$ with velocity $v_s \approx 0.05c$ and gradually decreases to $v_s = 0.02\mathrm{c}$

at $80\mathrm{T}$. The ion density is much higher across this shock-like front and is continuously reflecting ions in large fractions. Electron phase space plots also show that, the electrons are more heated across this shock-like structure than the rest of the plasma. From the slope of electrons spectrum, we calculated the bulk electron temperature (ignoring the fast oscillating electrons) which comes to be $\mathrm{T_e} = 2.6\mathrm{MeV}$. Now if the shock-like structure is propagating initially with a velocity $v_s = 0.05c$ at $20\mathrm{T}$, we evaluated the Mach number $\mathrm{M} = v_s/c_s$, (where $\mathrm{c_s} = \mathrm{K_B T_e/m_i}$), it comes out to be $\mathrm{M} = 0.9$ (the estimate is with classic formulas assuming a non-relativistic electron spectrum), which does not satisfy the existence condition of SAW/shock generation, i.e. $1 < \mathrm{M} < 1.6$. As the $\mathrm{M} < 1$, the structure we observed can not be called a shock wave. Thus, the above results performed at different plasma densities infer that the SAW/shock waves can be generated only up to certain range of laser and plasma parameters.

Simulations have also been performed for the same laser intensity $a_0 = 16$, by changing the target thickness and laser pulse duration to test the evolution of SAW. It is observed that by changing one of the parameters, results in the change of evolution of the SAW and the related phenomenons. For a fixed laser intensity, the role of target thickness, target density and laser pulse duration is important for the formation of solitary waves, evolution of solitary waves and the other dissipation phenomenons such as particle reflection and particle trapping. Below we will discuss a possible criterion for SAW/Shock generation.

6.2.7 Criterion for SAW or Shock generation versus Target density

Here we have tried to give a simple criterion to guess why in our 1D PIC simulations either shock or solitary acoustic waves (SAW's) are hardly observed for large density values. Since these structures are driven by the effect of the light pressure (or radiation pressure) exerted by the laser pulse at the surface, their initial velocity should be of the order of the "hole boring" velocity. This has been given e.g in Ref.[95] as

$$v_{hb} = a_0 \mathrm{c} \left(\frac{\mathrm{Z}}{\mathrm{A}} \frac{\mathrm{m_e}}{\mathrm{m_p}} \frac{\mathrm{n_c}}{\mathrm{n_e}} \right)^{1/2} \tag{6.16}$$

and compared with the velocity observed in simulations with *circular* polarization.

In comparing with the case of *linear* polarization (LP), where a_0 is given as the peak amplitude of the laser pulse, so that for LP the average over a period $\langle a^2 \rangle = a_0^2/2$. In addition, for LP, absorption is usually higher and thus the corresponding reduction in radiation pressure, $2\mathrm{I/c} \to (1 + \mathrm{R})\mathrm{I/c}$ with $\mathrm{R} < 1$ the reflection coefficient should be considered. Thus we would write the "hole boring" velocity for LP pulses

$$v_{hb} = a_0 \mathrm{c} \left(\frac{1 + \mathrm{R}}{2} \frac{\mathrm{Z}}{\mathrm{A}} \frac{\mathrm{m_e}}{\mathrm{m_p}} \frac{\mathrm{n_c}}{\mathrm{n_e}} \right)^{1/2} \tag{6.17}$$

which can be derived by the equation for the balance between the EM momentum flow and those of ions

$$(1 + \mathrm{R})\mathrm{I/c} = (\mathrm{m_i} v_i \mathrm{n_i}) v_i, \qquad \text{and} \qquad \mathrm{I} = \mathrm{m_e c^3 n_c} \langle a^2 \rangle \tag{6.18}$$

Here we consider $v_i \ll c$ as this is the relevant case to simulations but generalization to $v_i \lesssim c$ is possible (see Ref.[105]). To estimate v_s, we assume that SAWs are first generated as ion bunches by the radiation pressure acceleration and wave breaking at the front surface [95] and thus their energy is

$$\mathcal{E}_\mathrm{i} = \frac{1}{2} \mathrm{m_p v_s^2} = \frac{\mathrm{m_p}}{2} \left(\frac{\mathrm{Z}}{\mathrm{A}} \frac{\mathrm{m_e}}{\mathrm{m_p}} \frac{\mathrm{n_c}}{\mathrm{n_e}} a_0^2 \mathrm{c}^2 \right) = \frac{\mathrm{Z}}{2} \mathrm{m_e c^2} \frac{\mathrm{n_c}}{\mathrm{n_e}} a_0^2 \tag{6.19}$$

Thus for protons $\mathrm{Z} = \mathrm{A} = 1$, and considering the case of (Fig.6.9) having $\mathrm{n_e/n_c} = 10$ and $a_0 = 16$, this estimate gives us $v_s = 0.12c$, is in very good agreement with the initial SAW velocity of $v_s = 0.11c$ observed in simulations. Now let us consider the shock or soliton to be driven at velocity $v_s \simeq v_{hb}$. We need in any case v_s to be supersonic, i.e. $\mathrm{M} = v_s/c_s > 1$ where $c_s = (\mathrm{ZT_e/m_i})^{1/2} = (\mathrm{ZT_e/Am_p})^{1/2}$. To estimate the electron temperature, we used the so called "ponderomotive scaling"for $\mathrm{T_e}$ as explained in detail Eq. (2.70) in Ch.2, sec.2.8.3)

$$\mathrm{T_e} \simeq \mathrm{m_e c^2}(\gamma - 1) = \mathrm{m_e c^2}(\sqrt{1 + a_0^2/2} - 1) \simeq \mathrm{m_e c^2} a_0/\sqrt{2} \tag{6.20}$$

where the last equality holds for $a_0 >> 1$. For $a_0 = 16$, we obtain $\mathrm{T_e} \simeq 11.3\mathrm{m_e c^2}$, that seems fairly consistent with simulations. Hence posing $\mathcal{E}_\mathrm{i} > e\Phi_{\mathrm{max}}$, we obtain the criterion for the SAW or shock generation (assuming $R = 1$ for simplicity) as

$$\mathrm{M} > 1 \rightarrow a_0 > \frac{1}{2\sqrt{2}} \frac{\mathrm{n_e}}{\mathrm{n_c}} \tag{6.21}$$

corresponding to $a_0 > 3.55$ for $\mathrm{n_e/n_c} = 10$. This estimate, however is quite sensitive to the assumption of Eq. (6.20) for $\mathrm{T_e}$ because the classic formula assume a non-relativistic electron spectrum.

Thus from the above simple criterion in Eq. (6.21), we can guess whether a shock or soliton will be generated. This estimate might be generalized easily to $\mathrm{R} \neq 1$ and possibly to $v_s \lesssim c$; it should be taken with some care because the estimate for $\mathrm{T_e}$ is probably rough and less grounded than for v_{hb}, so at least numerical factors may be different in Eq. (6.21), but it might give us useful indication. Another important point to mention would be that in principle Eq. (6.21) is similar to the condition $\mathrm{n_e} < \mathrm{n_c}\gamma$ that is often mentioned as the condition for the plasma to be relativistically transparent for the laser light. However, in a step boundary plasma usually the condition is more restrictive (because of the ponderomotive compression itself) so that a window of parameters for shock acceleration probably exists. Nevertheless, relativistic transparency might explain why shock or solitons are not observed (at least in a clear way) also for too low densities, $\mathrm{n_e/n_c} \ll a_0$.

6.3 Simulation with Circular Polarization

Simulations has been performed also for circular polarization (CP) to compare the results for linear polarization (LP). To ensure that laser intensity is same as of LP case, we use a laser pulse which is lower by a factor of $\sqrt{2}$ than in LP case, we performed the CP simulations for the same parameters having laser pulse with a peak amplitude $a_0 = \frac{16}{\sqrt{2}} = 11.3$. The plasma had a slab, square-like profile with initial ion and electron densities $\mathrm{n_i} = \mathrm{n_e} = 10\mathrm{n_c}$ and 15λ thickness. Fig.6.11 shows the snapshots of two CP simulations performed for the above described parameters but at different lase pulse duration of $\tau = 30\mathrm{T}(100\mathrm{fs})$ and $\tau = 60\mathrm{T}(200\mathrm{fs})$ respectively. Fig.6.11 shows the effect of laser pulse duration on ion acceleration at front side of the plasma. In CP, we have observed the most effective ion accelerated from the front surface of plasma which starts in the form of small bunches which propagate into the plasma with a constant momentum of approx $1.3\mathrm{m_i c}$. When the CP laser pulse impinges on the plasma surface, the electrons are quickly pushed inward by the ponderomotive force, i.e by steady part of the $\mathbf{v} \times \mathbf{B}$ force. For CP, the oscillating component of the $\mathbf{v} \times \mathbf{B}$ force is zero, thats why there is very less electron heating and the interaction regime is completely different than that of LP pulses. In case of CP, all the ions get accelerated in the form of small bunches due to the hydrodynamics wave breaking, as the ion density is very high at the breaking and the faster ions move ahead than the slower ones. During the first breaking of the ion profile, with the formation of a bunch; the equilibrium between the

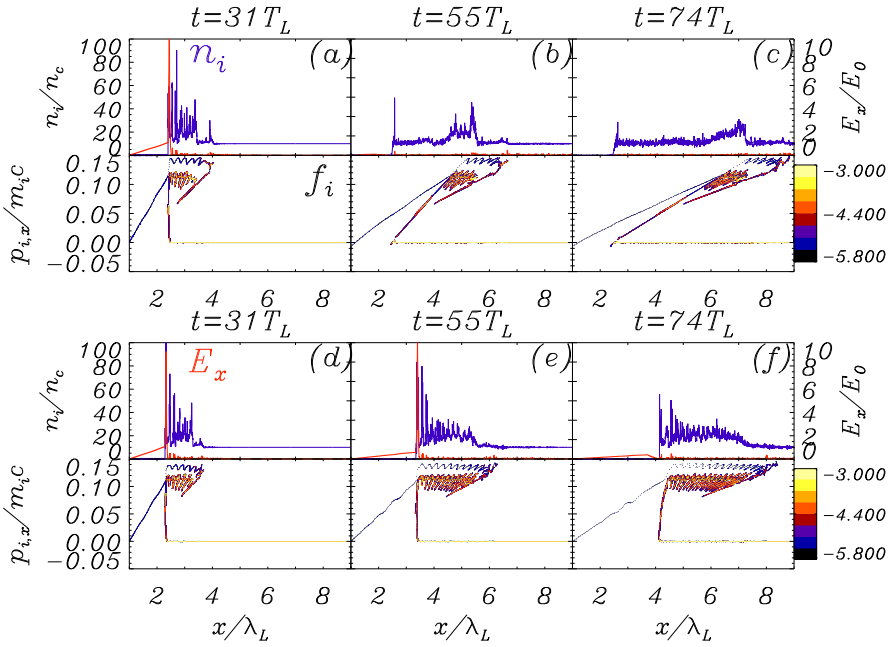

Figure 6.11: CP Simulation parameters: $a = 11.3$, target thickness $= 15\mu$m, plasma density $\mathrm{n_0} = 10\mathrm{n_c}$. Snapshots $(\mathrm{a}-\mathrm{c})$ shows the electric field $\mathrm{E_x}$, ion density n_i and ion phase space distribution f_i for the simulation done at laser pulse duration of $\tau = 30\mathrm{T}(100\mathrm{fs})$, The lower snapshots $(\mathrm{d}-\mathrm{f})$ shows the simulation results for laser pulse duration of $\tau = 60\mathrm{T}(200\mathrm{fs})$. Increase of laser pulse duration results in increase in number of ion bunches.

electrostatic and ponderomotive force on electrons is lost and if the laser pulse is not over yet at this stage, the electrons rearrange themselves to provide a new equilibrium and then the process of another bunch formation restarts.

As long as the laser impinges on the target, the number of bunch formation increases and when the laser is over, then there is no more bunch formation. Fig 6.11 shows a series of ion bunches formed until the laser pulse impinges on the target and then these bunches propagate with decreasing density with respect to time. Fig.6.11a, shows a large electrostatic field is there, when the laser is still impinges on the target, Fig.6.11b shows that when the laser pulse is stopped, there remains no electrostatic field E_x and then these formed bunches propagate ahead collectively with a uniform momentum. In CP, we did not observe fast electrons recirculation across the target as observed frequently in the LP case. Fig 6.11 $(\mathrm{d}-\mathrm{f})$ shows the snapshots at three different times of electrostatic field $\mathrm{E_x}$, ion density $\mathrm{n_i}$ and ion phase space distribution, for the $\tau = 65\mathrm{T}(210\mathrm{fs})$ laser pulse duration. It is shown clearly (at time $\mathrm{t} = 114\mathrm{T}$) that the number of bunch formation increases with increase in laser pulse duration as in the latter case (Fig.6.11$(\mathrm{d}-\mathrm{f})$), the number of ion bunches are more which can be observed clearly from the phase space distribution plots.

Fig.6.12 compares the absorption efficiency and ion energy spectrum for the CP versus LP simulations. For the CP case, the absorption into the ion bunches is approx 10% and is constant after the laser pulse is over which confirms that all the ions are getting accelerated by hole boring $-$RPA. For CP pulses, the absorption of electrons is very less as long as the laser is there and when laser pulse is over, the absorption is negligibly small. For LP, the absorption of electrons is very much in this case and is dominant during the interaction with the laser pulse. Later energy transfer towards ions occurs and with increase of time, the absorption efficiency of ions is increasing and of the electrons is decreasing, which confirms that the ions are getting some energy from the electrons. The ion energy spectrum for CP is

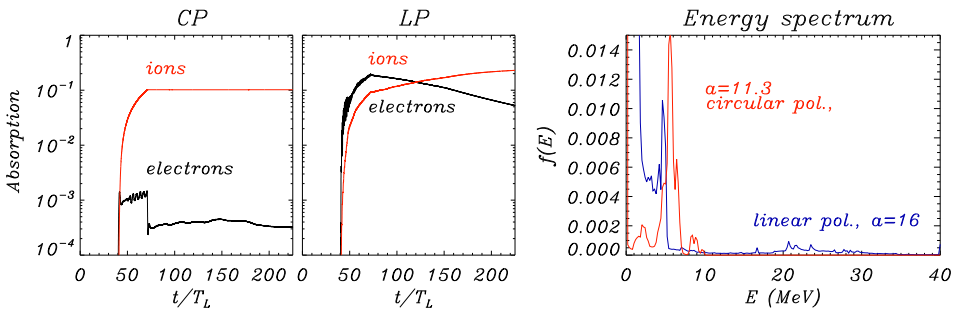

Figure 6.12: *Left frame:* Comparison of absorption efficiency of ions and electrons versus time. *Right frame:* ion energy spectrum from ID − PIC simulations performed with CP and LP pulses for the same laser and plasma parameters.

relatively narrow and a very prominent peak occurs around $8\mathrm{MeV}$, while the spectrum for LP is more thermal like, a peak occurs around $5\mathrm{MeV}$ and broad spectrum maximum up-to $30\mathrm{MeV}$. The reason for a more prominent peak for CP case is because of the fact that the ponderomotive force tends to focus the ion spatially at the end of the skin layer, creating a sharp peak [95] while for LP case, the strong electron heating leads to the explosion of the ion bunches and pile up few of these ions to higher energies lead to a broad energy spectrum. In CP, its relatively less electron temperature which also allows for a narrow energy spectrum [164].

With the aim to clarify many differences, similarities and possible overlaps between the SAW/shock acceleration (SA) and hole-boring (HB) by addressing issues such as role of radiation pressure versus fast electron generation, we have shown on the basic of numerical simulations that "soliton/shocks" driven by LP pulses (in an overdense ($\mathrm{n_e} > \mathrm{n_c}$), long-scalelength plasmas with a thickness typically $\mathrm{L} \gg \lambda$), produce energetic ion bunches as they propagate into the plasma bulk by a sequence of wave-breaking events. In contrast, for CP laser pulses the ion bunches generated by HB due to the action of radiation pressure, do no lead to further acceleration in the bulk.

6.4 Test Particle Simulations

We performed numerical ID PIC simulations by keeping all the parameters same as of Fig.6.1 but for a laser pulse duration of $\tau = 5\mathrm{T}$, such that the temporal profile is $2\mathrm{T}$ long, $\sin^2-$ like rising and fall ramps and $3\mathrm{T}$ plateau. In order to check the exact acceleration mechanism, simulations has been performed by placing a slab of "test particles (protons)" inside the plasma, at some distance from the surface in order that the test particles should not interact with the laser pulse, but will be reached by the shock wave at some instant. The goal is to see if and how much these test particles are accelerated by the shock. Test particles will move into the EM fields as the "real" particles, but they will not contribute to the charge and current densities; they are only there as a diagnostic.

Fig.6.13 shows the results performed for LP pulses, by placing the test particle at different positions inside the plasma slab. We placed the test particle slab at $2-3\lambda$ (second row from bottom in Fig.6.13) and at $3-4\lambda$ (the bottom frame in Fig6.13). We found that only those test particles located near to the points, where the incoming SAW reaches the threshold amplitude for ion reflection, get accelerated. As studied in sec.6.1, for LP pulses and cold background ions, during the laser pulse, the strong density perturbations are created in the form of SAWs, at the laser plasma interaction surface which propagate deep into the plasma bulk with velocity v_s and can extends up-to velocity $\approx 2v_{\mathrm{hb}}$. During propagation,

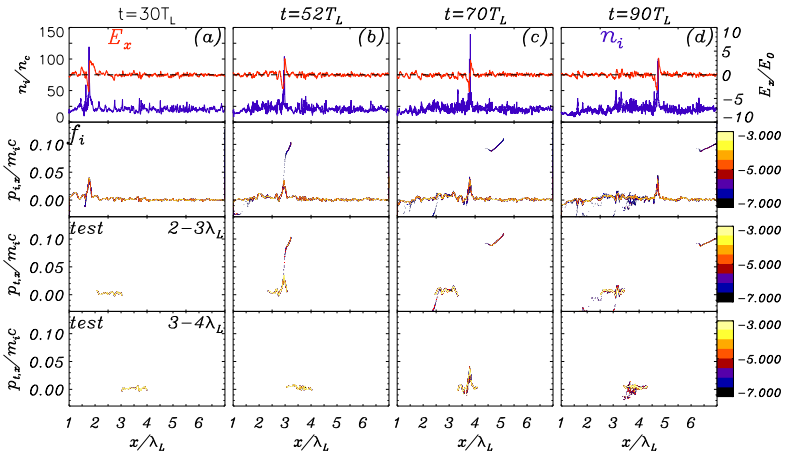

Figure 6.13: LP Simulations: Snapshots of ion density $\mathrm{n_i}$, electrostatic field $\mathrm{E_x}$ and contour of ion $f_i(\mathrm{x},\mathrm{p_x})$ and test particles $f_t(\mathrm{x},\mathrm{p_x})$ phase space distribution in a log_{10} scale at four different times. Test particle perturbation and acceleration confirms the formation of solitary or shock wave formation deep in the plasma Simulation parameters are $a_0 = 16$, $\tau = 5\mathrm{T}$, $10\mu\mathrm{m}$ target having density $\mathrm{n_0} = 20\mathrm{nc}$.

these SAWs further lead to secondary ion reflection from its front having velocity $v_r = 2v_s$. This is exactly what we observe in our simulations, we found that one SAW is formed from the front surface which start to propagate with velocity $v_s = 0.04c$. Up-to 2λ distance, the SAW does not reflect ions. The first ion reflection from SAW front occur at $48\mathrm{T}$ when the SAW is at 2.5λ. As we have placed a test particles slab at $2-3\lambda$ region. Thus those test particles within this slab which are near to 2.5λ, get accelerated and gains the same velocity as that of "real" background reflected ions (clearly be observed from phase space plots Fig.6.13 at $52\mathrm{T}$). As the SAW pass away $2-3\lambda$ region, the rest of the test particles remain in this region without any further acceleration. During the time, when the propagating SAW enters in the region $3-4\lambda$, there does not occur any ion reflection from the SAW front. Thus the SAW pass the test particles slab $3-4\lambda$ without accelerating the test particles of this region. Few perturbations can be observed to the rest of the test particles which is due to fast oscillating electrons and strong electron heating.

We performed the CP simulations at a laser amplitude $a_0 = 11.3$, by placing the test particle slab within the plasma at $2-3\lambda$, keeping all the other parameters same as of Fig.6.13. The result is shown in Fig.6.14. We found that the ions from the front surface get accelerated in the form of bunches by the hole boring mechanism which do not effect at all to the test particles placed within the plasma. Thus this results confirms that for CP pulses, no acceleration occurs in the bulk. Ion bunches propagated through the plasma in such a way, causing almost no perturbation within the bulk. Such bunches may not be considered as electrostatic solitons as for instance the value of electron temperature ($\mathrm{T_e}$) for CP case would be so low for the "Mach number" M to largely exceed the critical value ~ 6.5 above which one

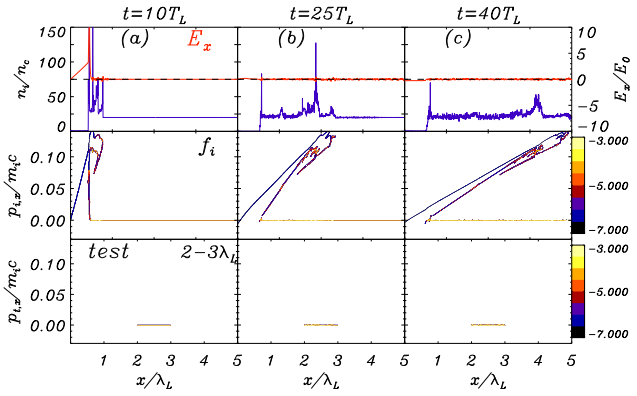

Figure 6.14: CP simulation: Snapshots of ion density $\mathrm{n_i}$, electrostatic field $\mathrm{E_x}$ and contour of ion $f_i(\mathrm{x},\mathrm{p_x})$ and test particles $f_t(\mathrm{x},\mathrm{p_x})$ phase space distribution in a log_{10} scale at three different times, keeping all the parameters same as of Fig.6.13, but using circular polarized pulses. The test particles within the plasma remain unperturbed shows the clear different between the hole-boring and shock acceleration processes.

does not have a shock but a “pure piston”. These findings confirm the crucial role played by the laser polarization or indirectly the effect of the electron temperature, in SAW/shock generation and the related ion acceleration.

In our opinion it may be clearer and more appropriate to talk about shock acceleration which implies the generation of a “true” electrostatic shock wave, able to propagate into the plasma bulk and to drive ion acceleration there or at the rear surface. With this fact, although Palmer etal[165] reported on “protons accelerated by a radiation pressure driven shock” in their experiment using a circularly polarized pulse, their data may be rather interpreted as evidence of hole boring acceleration. The analysis of data in the experiments by [166] and [167], where linear polarization was used, seems also compatible with the “hole boring” picture involving ion acceleration at the front surface, sustained by light pressure.

CHAPTER 7

Ion Temperature and Two-Dimensional Effects on the Formation of Shock and Solitary waves

In this Chapter we first investigated, using 1D PIC simulations, the role of the ion initial energy distribution plays in the formation of ion acoustic perturbations in form of solitons/shocks and in the related ion acceleration. Simulations performed at moderate intensity $\mathrm{I} = 10^{18} - 10^{19}\mathrm{W/cm^2}$ using linearly polarized pulses suggest the existence of an "optimal" initial ion temperature at which a shock wave reflects monoenergetic ions, as a result from a trade-off between beam monoenergeticity and efficiency. Circularly polarized pulses in initially warm plasmas exhibit a distinct transition from the laser driven piston scenario with all ions being reflected to the collisionless shock/soliton scenario having partial ion reflection. Preliminary 2D simulations suggest that the onset of surface rippling affects the width of the ion spectrum.

7.1 1D PIC Simulations

As shown in the sec.6.3 of previous chapter, for the circular polarized (CP) pulses, ions are accelerated only at the laser-plasma interaction surface and during the laser pulse, the ion spectrum extends up-to $2v_{\mathrm{hb}}$ [95]. For the LP pulses (as explained in sec.6.1), due to the large electron heating, the strong density perturbation are created in the form of solitary or shock waves at the surface which propagate deep into the plasma bulk having velocity $v_s \simeq v_{\mathrm{hb}}$. While propagating in the plasma, these solitary or shock waves may further lead to secondary ion acceleration by reflecting ions from its front having velocity $v_r = 2v_s$ (where v_r is the velocity of reflected ions). The above considerations tells that the hole boring process fixes the initial velocity for the solitary or shock waves while whether reflection would occur or not depends on the ratio between the shock velocity v_s and the relative speed of sound c_s [28]. As long as the shock velocity v_s is constant, the reflected ions should have velocity $2v_s$ and produce a monoenergetic peak in the spectrum.

The monoenergetic nature of the steady reflected ions (for warm ion simulations) or the shock stability is strongly dependent upon the laser pulse intensities and decreases with increasing laser intensities, as more kinetic effects come in along the ultra-relativistic regimes. Discussed below are the warm ion simulations performed at laser peak amplitude $a_0 = 4$ and $a_0 = 1$ corresponding to laser pulse intensity of $2.2 \times 10^{19}\mathrm{W/cm^2}$ and $1.4 \times 10^{18}\mathrm{W/cm^2}$ respectively. We observed that there exists a finite "ion temperature window" for which the shock wave reflect monoenergetic ions without any significant wave loading. With a further increase of initial $\mathrm{T_i}$, the shock wave attempts to reflect more number of ions, loses it velocity v_s along the propagation path and the reflected ion spectrum no longer remains monoenergetic.

7.2 Simulation results for $a_0 = 4$ amplitude

7.2.1 Proton Ion Simulations (Z/A = 1)

At initially cold ion background

In the early stage of the interaction, the LP pulse accelerates a fraction of strongly relativistic electrons with energy of several $\mathrm{m_e c^2}$ which penetrate into the target, recirculate across it and drive heating of the bulk electrons. Multi-peak structures in the form of two or three SAWs (depending upon laser pulse duration) are generated at the front surface under the action of the laser pulse which propagates into the plasma bulk initially with a constant velocity $v_s \simeq 0.06c$ but disperse with time, the later ones lagging behind than that of the the first SAW.

Left frames of Fig.7.1 show that the peaks of the ion (blue line) and electron densities (red line) overlap with each other. However, as the electron temperature is much higher than that of ion temperature, *i.e.* $\mathrm{T_e} \gg \mathrm{T_i}$, a bipolar charge separation electrostatic field of "sawtooth" shape is formed in the compressed plasma. This electrostatic field around the density spikes plays a key role in the acceleration of ions deeply located in plasma on the path of these SAWs. Moreover the reflection of ions from a moving electrostatic field front, is dependent on the stability threshold, i.e., the ratio $\Phi_{\mathrm{max}}/v_s^2$ where Φ_{max} is the potential jump at the front. This is what we observed for cold ion background ($\mathrm{T_i} = 0\mathrm{keV}$) simulation that when the electrostatic potential $(\mathrm{e}\Phi_{\mathrm{max}})$ around the SAW exceeds the kinetic energy $(1/2 m_i v_s^2)$, the ion reflection occurs from the SAW front[1]. As the electrostatic field amplitude is not constant along time but oscillates, due to this electric field oscillations the potential varies quickly around SAW and ion

[1] From Fig 7.1, at $156\mathrm{T}$, we estimate the first SAW electric field to have a peak value $\mathrm{E_{max}} \sim 0.8\mathrm{E_0}$, where $\mathrm{E_0} = \mathrm{m_e}\omega\mathrm{c/e}$ and a total first SAW extension $\mathrm{L} \sim 0.85\lambda = 1.7\pi\mathrm{c}/\omega$, from which we estimate $\mathrm{e}\Phi_{\mathrm{max}} = \mathrm{eE_{max}L} \simeq 4.27\mathrm{m_e c^2}$, which is ahead of the threshold energy $\mathrm{m_p} v_s^2/2 \simeq 3.58\mathrm{m_e c^2}$, thus SAW electrostatic potential $(\mathrm{e}\Phi_{\mathrm{max}} > \mathrm{m_i} v_s^2/2)$, crosses the stability threshold and the ion reflection promptly occurs. Further propagating ahead, the second and third ion reflection from SAW front occurs around $180\mathrm{T}$ and $224\mathrm{T}$ time instants. At these instants, the electrostatic potential is $\mathrm{e}\Phi_{\mathrm{max}} = 4.0\mathrm{m_e c^2}$ and $\mathrm{e}\Phi_{\mathrm{max}} = 3.8\mathrm{m_e c^2}$ respectively which is slightly above the stability threshold.

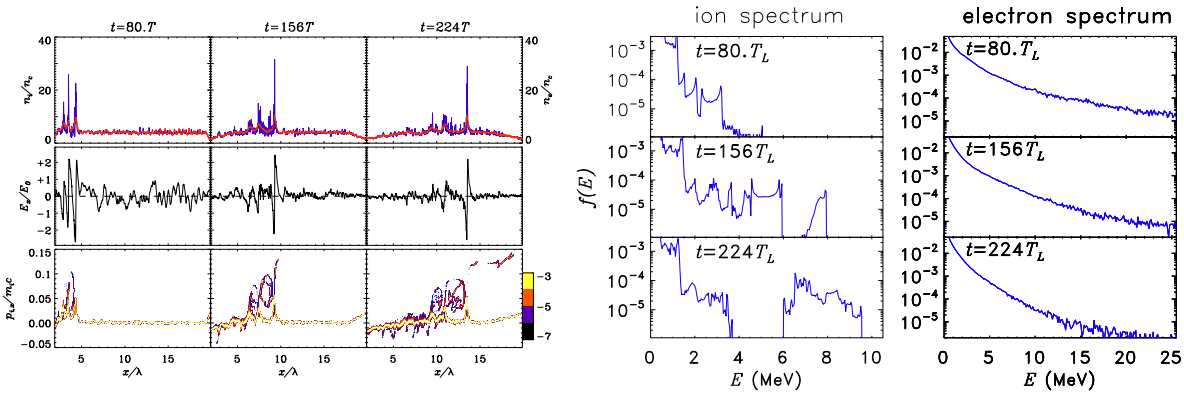

Figure 7.1: *Left frame (a)*: Snapshots of the evolution of SAW at three different times for an initial cold plasmas (*i.e.* $\mathrm{T_i} = \mathrm{T_e} = 0\mathrm{keV}$). The upper row shows the ion density $\mathrm{n_i}$ (blue line) and the electron density $\mathrm{n_e}$ (red line), middle row show the saw-tooth shape electrostatic field $\mathrm{E_x}$ and the bottom row shows the contours of the $f_i(\mathrm{x}, \mathrm{p_x})$ ion phase space distribution in a $\log_{10}$-scale. The laser pulse impinges from the left reaching the plasma boundary $(\mathrm{x} = 0\lambda)$ at $\mathrm{t} = 0\mathrm{T}$. *Right frame (b)*:The ions and electrons spectrum, including only the particles in the region around the SAW and excluding ions and electrons located near the target boundaries. Simulation parameters are $a_0 = 4$, $\mathrm{n_e} = 4\mathrm{n_c}$ and $\tau = 60\mathrm{T}$.

reflection is of pulsed nature, i.e. occur at some certain time intervals and is not uniform.

Looking at the slope of hot electrons (right frame of Fig.7.1), which are close to the SAWs we found that the slope becomes steeper from $140\mathrm{T}$ to $224\mathrm{T}$ time durations and the electrons get cooled down, *i.e.* the temperature of the hot electrons (which are close to SAWs) falls from $\mathrm{T_e} \approx 1.57\mathrm{MeV}$ (at $140\mathrm{T}$) to $\mathrm{T_e} \approx 1.29\mathrm{MeV}$ (at $224\mathrm{T}$). Now if we assume the SAW moving with a velocity $v_s \approx 0.0625c$ to be close to the stability threshold, therefore posing the Mach number $\mathrm{M} = 1.6$, we get an estimate of the hot electrons temperature $\mathrm{T_e} = (0.0625/1.6)2\mathrm{m_p c^2} \simeq 2.8\mathrm{m_e c^2} \approx 1.4\mathrm{MeV}$ that is fairly consistent with the value obtained from the electron spectra. Thus during the ions reflection events (*i.e.* from $140\mathrm{T}$ to $224\mathrm{T}$), the hot electrons temperature falls below the calculated threshold temperature, *i.e.* $\mathrm{T_e} \approx 1.4\mathrm{MeV}$, which results in that the relative speed of sound $\mathrm{c_s} \simeq \sqrt{\mathrm{ZT_e/Am_i}}$ decreases and hence the Mach number $\mathrm{M} = v_s/c_s$ increases slightly above the stability threshold $\mathrm{M} \geq 1.6$, for the ion reflection to occur which would not quench the SAW and the latter remains almost unperturbed for such small reflections with a slight change in velocity $v_s \simeq 0.06 \pm 0.005c$. The above calculations infer that the energy loss to the reflected ions may be at the expense of hot electrons energy.

SAW velocity and amplitude decrease significantly only over long times after a couple of pulsed ion reflections. The acceleration of a larger fraction of ions is observed when the SAW undergoes disruption either by interacting with another structure coming from opposite side or when it enters into the expanding sheath region at the rear surface of the plasma, where it breaks down resulting in continuous ion reflection. The appearance of the above mentioned pulsed ion reflection in the wake of the SAW might thus be interpreted as the result of a partial transition of the SAW towards a collisionless shock when ion reflection sets in. However, a stable shock may not form because the ions are cold in the present conditions as it is evident from the phase space plots in Fig.7.1. Monoenergetic peaks appear only as a result of such pulse acceleration in which the corresponding number of ions is relatively low. Acceleration of large fraction of ions leads to quenching and slowing down of the wave, resulting in broadening of the energy spectrum.

Warm ion simulations

In order to see the effect of initial ion distribution on soliton or shock evolution and to optimize its effect on ion reflection, we performed the simulations by increasing the initial ion temperature. Fig.7.2 shows results of a simulation with identical parameters as that of Fig.7.1, but with initial ion temperature $\mathrm{T_i} = 0.05$ keV. We observed that the ion reflection starts at earlier time, *i.e.* at $80\mathrm{T}$, a small fraction of ions ($\sim 0.1 \times 10^{-5}$) get reflected from the moving SAW front ($v_s \approx 0.057\mathrm{c}$), as a consequence a small monoenergetic peak of $\sim 6.5\mathrm{MeV}$ appear in the ion spectrum (inset, first frame of Fig.7.2). The second and third frame of Fig.7.2 substantially shows the clear picture of later stages, i.e., at $156\mathrm{T}$ and $180\mathrm{T}$, the SAW/shock is fully evolved by this time, having velocity $v_s \approx 0.0625\mathrm{c}$ and reflect ions of fraction ($\sim 0.6 \times 10^{-5}$) resulting in a sharp monoenergetic peak of $\sim 7\mathrm{MeV}$ smears out in the energy spectrum which doesn't affect the spectrum of the previous reflected ions and monoenergeticity remains stable for much longer time (inset of Fig 7.2). The electrostatic field is also less oscillating with respect to time than in the cold ions case and the SAW propagates in such warm plasma ($\mathrm{T_i} = 0.05\mathrm{keV}$) without much significant loss in its velocity. As a consequence, with respect to the "cold" ions case narrow monoenergetic peaks almost appear at all the times in the spectrum. Although the cutoff energy is less in this case i.e., $\sim 7.5\mathrm{MeV}$ instead of $\sim 9.5\mathrm{MeV}$ (for cold ions case), the ions spectrum remain monoenergetic for longer times. Therefore, a slight change of initial $\mathrm{T_i} = 0.05\mathrm{keV}$, the ion reflection from the SAW front becomes linear, monoenergetic and occurs in small fractions until SAW loses its energy and damps out in the rear sheath field.

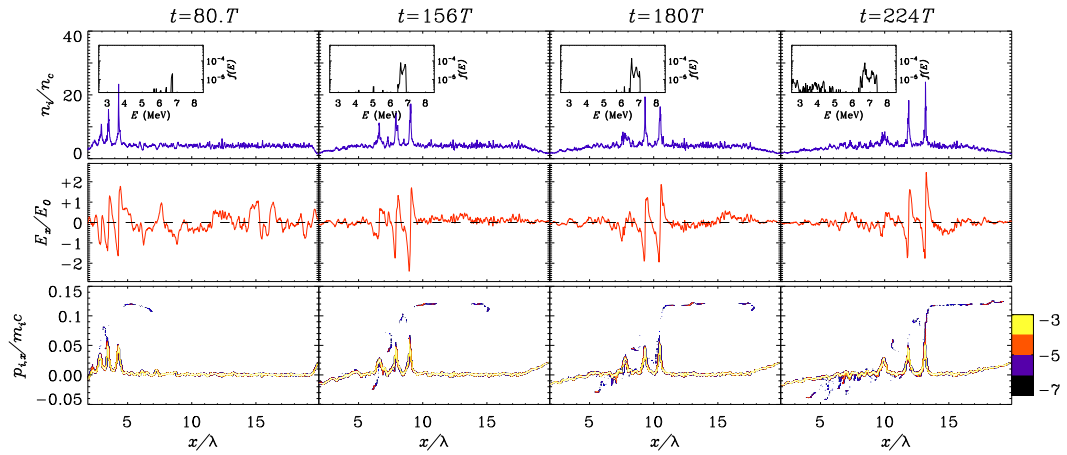

Figure 7.2: Snapshots at four different times of the $\mathrm{n_i}$, $\mathrm{E_x}$ and $f_i(\mathrm{x}, \mathrm{p_x})$ for a simulation identical to that of Fig.7.1 but for an initial ion temperature $\mathrm{T_i} \simeq 10^{-4}\mathrm{m_e c^2} = 0.05$ KeV, showing that the ion reflection is linear and of steady nature than that of the "cold ions" case. The insets show the corresponding ion spectra, including only the ions in the region around the SAW or shock wave and excluding ions located near the target boundaries.

The SAW velocity is found to decrease slightly in time for $\mathrm{T_i} = 0.05\mathrm{keV}$ such that by the time $224\mathrm{T}$, the leading SAW reaches up-to $\sim 13.3\lambda$ (see ion phase space Fig.7.2), while in the cold ions case (see Fig.7.1), the SAW is at $\sim 13.6\lambda$. For the initial $\mathrm{T_i} = 0.05\mathrm{keV}$, due to some initial ion distribution, there are always some ions having small energy spread in front of the leading SAW which are easy to reflect and in doing so, the SAW attempting to reflect more ions, loses some of its energy and lags behind. While in the cold ions case in which the front ions are at rest and ions get reflected only in the time intervals during which the electrostatic potential exceeds the kinetic energy of SAW. Now having an initial $\mathrm{T_i}$ means the ion distribution has some initial velocity spread, and for a given value of Φ_{max}, all ions with velocity $v_i > (v_s - \sqrt{2e\Phi_{\mathrm{max}}/m_i})$ will be reflected from the wave front. Since from $156\mathrm{T}$ time, the reflection is of more steady nature, so assuming that the background ions have velocity $v_i \approx v_s - \sqrt{2e\Phi_{\mathrm{max}}/m_i}$, the kinetic energy of front background ions can be estimated as

$$\mathcal{E}_{\mathrm{i}} = \frac{1}{2}\mathrm{m_i}\left(v_s - \sqrt{\frac{2\mathrm{e}\Phi_{\mathrm{max}}}{\mathrm{m_i}}}\right)^2 \tag{7.1}$$

It comes out to be $\mathcal{E}_i \approx 0.47 m_e c^2$. Now estimating for the electrostatic potential at $156\mathrm{T}$, it is $Ze\Phi_{\mathrm{max}} = 1.3 m_e c^2$ which is above than the threshold kinetic energy and satisfies the condition $Ze\Phi_{\mathrm{max}} > \mathcal{E}_i$. As a result the front background ions are easily reflected from the the leading SAW front.

With a further increase of initial ion temperature to $\mathrm{T_i} = 0.1\mathrm{keV}$ (Fig.7.3), i.e. the background ions have slightly more initial energy spread than that of $\mathrm{T_i} = 0.05\mathrm{keV}$ case (Fig.7.2), the leading SAW front picks up a very few ions at an early stage, *i.e.* at $40\mathrm{T}$ and reflect them. During the early stages, the SAW/shock is not fully evolved yet (having $v_s \sim 0.051\mathrm{c}$), so initially it reflect a few ions of slightly less energy $\sim 5\mathrm{MeV}$. By the time $80\mathrm{T}$, the SAW/shock gains the velocity up to $v_s \sim 0.059\mathrm{c}$ and reflects ions of slightly higher energy $\sim 7\mathrm{MeV}$. The two different energy types of reflected ions are clearly visible in the spectrum (see inset, Fig. 7.3a) and can also be deduced from the slope of the reflected ion feature in the phase space plots (Fig.7.3a). Now from $80\mathrm{T}$ onwards, the SAW/shock propagates within the bulk almost with a constant velocity $v_s \sim 0.062 \pm 0.002\mathrm{c}$ reflecting ions to double its velocity. The ion reflection at later stages is continuous in nature (Fig.7.3$(\mathrm{c}-\mathrm{d})$) and doesn't affect much to the existing

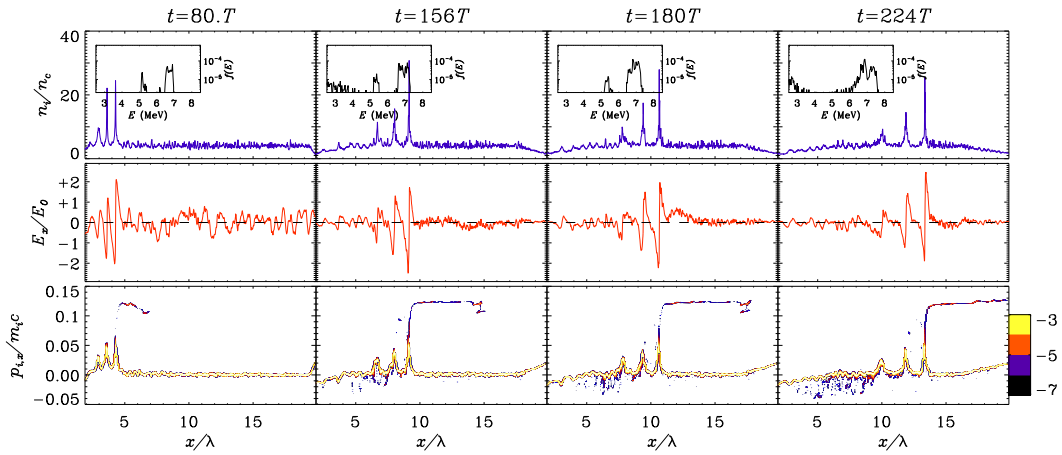

Figure 7.3: Snapshots at four different times of the $\mathrm{n_i}$, $\mathrm{E_x}$ and $f_i(\mathrm{x}, \mathrm{p_x})$ for a simulation identical to that of Fig.7.1 but for an initial ion temperature $\mathrm{T_i} \simeq 2 * 10^{-4}\mathrm{m_e c^2} = 0.1$ keV, showing the onset of "steady" ion reflection and in large fraction than that of the $\mathrm{T_i} = 0.05\mathrm{keV}$. The scales are the same as in Fig.7.1. The insets show the corresponding ion spectra, including only the ions in the region around the SAW or shock wave and excluding ions located near the target boundaries.

monoenergetic peak. Even neglecting the first ion bunch (formed at $40\mathrm{T}$) which comes to the rear side at time $224\mathrm{T}$, the later shock like ion reflection is quasi-monoenergetic and of energy $\sim 6.5 - 7.5\mathrm{MeV}$.

Evaluating for the fraction of reflected ions up-to $224\mathrm{T}$ time duration, it comes out to be approximately 1.5×10^{-5} for $\mathrm{T_i} = 0.1\mathrm{keV}$ case which is higher than that of 0.6×10^{-5} for the $\mathrm{T_i} = 0.05\mathrm{keV}$ case. The fraction of reflected ions for $\mathrm{T_i} = 0.1\mathrm{keV}$ in the spectral peak at $7\mathrm{MeV}$ implies a conversion efficiency of $\sim 5 \times 10^{-6}$ of the total pulse energy which is slightly high than that of conversion efficiency $\sim 10^{-7}$ for $\mathrm{T_i} = 0.05\mathrm{keV}$ case. Thus from the above two results shown in Fig.7.2 and Fig.7.3, there seems to be an "optimal" value of $\mathrm{T_i}$, small but non-vanishing, for which we can increase the fraction of reflected ions without any significant loss in SAW/shock velocity. We noticed that at this particular initial "ion temperature window" which occurs between $\mathrm{T_i} = 0.05\mathrm{keV} - 0.1\mathrm{keV}$, the SAW/shock remains stable for longer time without any significant wave loading and reflects monoenergetic ions. Increasing the initial $\mathrm{T_i}$ above $0.1\mathrm{keV}$, the ion reflection increases in large numbers and the shock doesn't sustain a constant velocity and decelerates with time which results in broadening of the ion spectrum and monoenergeticity is lost over longer times.

Fig.7.4 describes the simulation results performed at initial $\mathrm{T_i} = 1\mathrm{keV}$ and $5\mathrm{keV}$ respectively. We envision that the ion reflection occurs from the beginning is continuous and of shock-like, where the steady solutions of solitary waves change into shock waves. As according to the standard fluid theory [28], the possibility to generate "true" shocks would be the formation of continuous flow of reflected ions, which indeed we noticed in our simulations from $\mathrm{T_i} = 0.1\mathrm{keV}$ onwards. The fraction of reflected ions by the time $200\mathrm{T}$, for $\mathrm{T_i} = 1\mathrm{keV}$ are $\simeq 6 \times 10^{-5}$ which further increases to $\simeq 15 \times 10^{-5}$ for the $\mathrm{T_i} = 5\mathrm{keV}$ case. This reflected ions fraction is much higher than the previously studied warm ions simulations. Due to the higher number of reflected ions, the shock wave will lose its energy in reflecting more ions and lags behind (see the ion phase space at $200\mathrm{T}$ of Fig.7.4), i.e. the leading shock front is at 10.4λ for $\mathrm{T_i} = 5\mathrm{keV}$ case, while it is at 11.2λ for $\mathrm{T_i} = 1\mathrm{keV}$. The number of reflected ions, which increases with increasing initial $\mathrm{T_i}$ indirectly affects the stability of shock wave. If the latter reflects large number of ions, which means that the shock is losing or transferring more energy in reflecting more ions, so the shock front velocity decreases in time more quickly and the energy spectrum of the

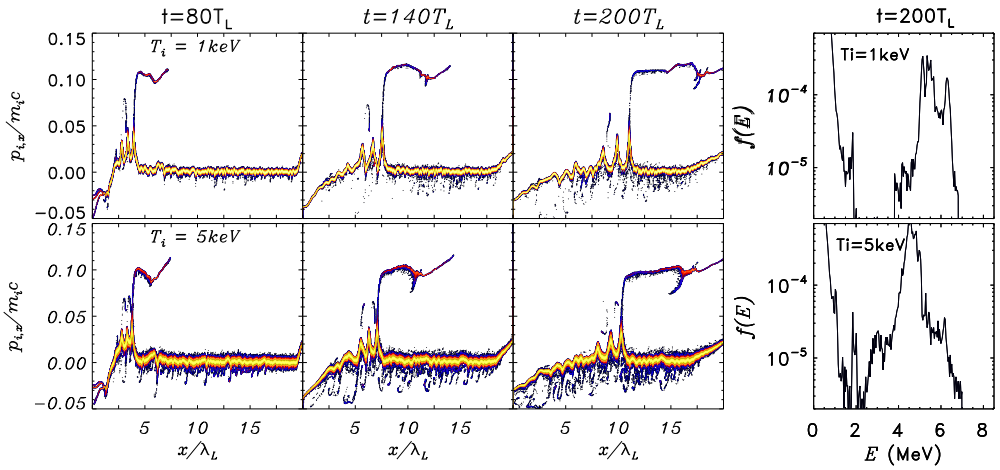

Figure 7.4: Snapshots at three different times of the ion phase space $f_i(\mathrm{x}, \mathrm{p_x})$ for the simulations performed at initial ion temperature of $\mathrm{T_i} \simeq 2 * 10^{-3}\mathrm{m_e c^2} = 1$ keV and $\mathrm{T_i} \simeq 1 * 10^{-2}\mathrm{m_e c^2} = 5$ keV respectively, showing the onset of "continuous" shock like ion reflection. All the other parameters are identical to Fig.7.1. The number of reflected ions increases with increasing the initial $\mathrm{T_i}$, and the shock decelerates more quickly with time. The right frame show the ion spectra at $200\mathrm{T}$ time duration, considering only the ions in the region around the shock wave and excluding ions located near the target boundaries.

reflected ions broadens towards lower energies which we indeed observed in the simulations performed at higher initial ion temperature, *i.e.* $\mathrm{T_i} = 5\mathrm{keV}$ and $10\mathrm{keV}$, where the spectral plateau occurs around $4 - 5\mathrm{MeV}$ energy which further shifts towards lower energies for high initial $\mathrm{T_i}$. The occurrence of spectral "plateau" (right frame of Fig.7.4 for $\mathrm{T_i} = 5\mathrm{keV}$) is because of shock deceleration, rather than due to further acceleration of the reflected ions in the rear side sheath.

Thus we infer that, increasing the initial $\mathrm{T_i}$, reflection of ions from the SAW/ shock wave front becomes "linear" in the sense that, given the wave some speed, we always have some ions in the tail of the distribution function which can be reflected. But for too high ion temperature there are too much reflected ions, so we fall back again in the case of excessive wave loading. With reference to the case of "true" shock formation in a plasma with warm ions, which starts from $\mathrm{T_i} = 0.1\mathrm{keV}$, where the ion reflection from the beginning is "continuous" in nature, the shock doesn't decelerate quickly and remain stable for longer time to reflect ions of same energy(Fig 7.3). Although there occurs a continuous ion reflections above $\mathrm{T_i} = 0.1\mathrm{keV}$ but the shock loses its energy more quickly in order to reflect more ions and decelerates. So due to excessive wave loading and shock deceleration, the latter doesn't remain in a position to reflect ions of same energy and the lower energy tail of the reflected ions broaden the energy spectrum. Now, lowering $\mathrm{T_i}$ from $0.1\mathrm{keV}$ to $0.05\mathrm{keV}$ implies that less ions are reflected, reflection is still linear and monoenergetic but is not of continuous nature. A further decrease in initial $\mathrm{T_i}$ below $0.05\mathrm{keV}$, we again fall back to cold ions case and the ion reflection neither remain linear nor sustain monoenergetic nature for longer times.

7.2.2 Carbon Ion Simulations

Heavy ions (*e.g.* carbon) can not be accelerated as efficiently as protons since, due to the lower charge to mass ratio $(\mathrm{Z/A})$ the electric force per unit mass is smaller on heavier ions. We performed the simulations for the carbon ions having $\mathrm{Z/A} = 1/2$ by replacing protons, keeping all the parameters same

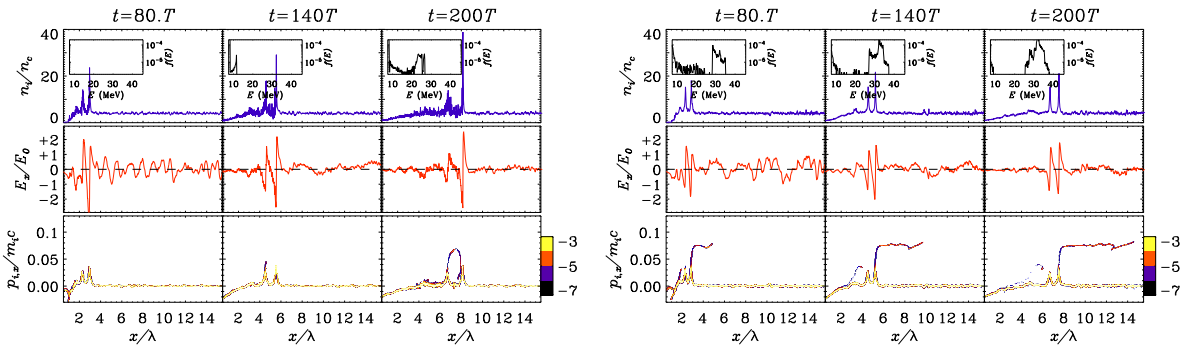

Figure 7.5: *Carbon ion simulation*: Snapshots at three different times of ion density $\mathrm{n_i}$, electrostatic field $\mathrm{E_x}$ and the ion phase space $f_i(\mathrm{x}, \mathrm{p_x})$ for the simulations performed at *Left frame: (a)* cold ion background $\mathrm{T_i} = 0$ keV showing the propagating of SAW without any ion reflection and *Right frame: (b)* $\mathrm{T_i} \simeq 2 * 10^{-3}\mathrm{m_e c^2} = 1$ keV respectively, showing the onset of "continuous" shock like ion reflection. A transition from SAW to shock wave is clearly observable. All the other parameters are identical to Fig.7.1. Although the number of reflected ions increases with increasing initial $\mathrm{T_i}$, but shock looses its energy to the reflected ions and lags behind. The insets show the corresponding ion spectra, including only the ions in the region around the SAW or shock wave and excluding ions located near the target boundaries. Simulation parameters are $a_0 = 4$, $\tau = 60T$ and $n_e = 4n_c$.

as of Fig.7.1. Fig.7.5 (left frame) shows the simulation performed for initially cold ions $(\mathrm{T_i} = 0\mathrm{keV})$. Two SAWs are formed from the target front surface which propagates initially at a velocity $v_s \approx 0.042\mathrm{c}$ (at 80T) and later disperse with time. We did not observe any ion reflection from the leading SAW while the second SAW undergoes some ion reflection. The ion reflected from the second SAW get trapped by the huge electrostatic field of the first SAW. Due to the ion reflection, the second SAW loses its velocity to $v_s = 0.039\mathrm{c}$ by the time 200T, giving some of its energy to reflected ions while the first SAW propagates with almost constant velocity $v_s \approx 0.041c$ without much loss in its energy. Calculating for the SAW electrostatic potential[2] which does not exceed the stability threshold condition $(\mathrm{Ze}\Phi_{\mathrm{max}} < \mathrm{m_i} v_s^2/2)$ and SAW propagates without any ion reflection as shown in phase space plots of Fig.7.5 (left frame). Therefore in a cold carbon ion background, ion reflection is hardly to occur from the SAW front and the latter remains symmetric for much longer times. These simulation results confirms that the stability condition (Eq.6.1) is strongly dependent upon the $\mathrm{Z/A}$ factor as for the carbon ions case, the potential energy term is lowered by a factor of 2 than that of kinetic energy term.

Fig.7.5(right frame) shows the same simulation as above but with an initial ion temperature $\mathrm{T_i} = 1\mathrm{keV}$, We envisioned the SAW turns into shock wave and the shock front is moving with a velocity $v_s \approx 0.04c$ at 80T, reflecting ions to double its velocity $v_i = 2v_s \approx 0.08c$. As a consequence a peak of $\sim 30 - 35\mathrm{MeV}$ smears out in energy spectrum (inset Fig.7.5 right frame at 80T). Because of continuous ion reflection from the shock front, its velocity decreases to $v_s \approx 0.034c$ at 200T as a result the spectrum of reflected carbon ions get broader.

Estimating the electrostatic field at 80T, the leading shock wave have an electric field peak value $\mathrm{E_{max}} \approx 0.41\mathrm{E_0}$ and a total shock extension $\mathrm{L} \approx 0.6\lambda = 1.2\pi\mathrm{c}/\omega$, as a result the electrostatic potential energy comes out to be $\mathrm{Ze}\Phi_{\mathrm{max}} \simeq 9.3\mathrm{m_e c^2}$. Due to the initial velocity distribution, the front background ions have some initial velocity spread. Calculating the kinetic energy of front background ions at 80T

[2] Estimated at 80T, the first SAW have have an electric field peak value $\mathrm{E_{max}} \approx 0.24\mathrm{E_0}$, where $\mathrm{E_0} = \mathrm{m_e}\omega\mathrm{c/e}$ and a total SAW extension $\mathrm{L} \sim 0.7\lambda \approx 1.4\pi\mathrm{c}/\omega$. From this we can estimate $\mathrm{Ze}\Phi_{\mathrm{max}} = \mathrm{ZeE_{max}L} \simeq 6.3\mathrm{m_e c^2}$ (using $\mathrm{Z} = 6$ for carbon), which is quite below of the threshold kinetic energy $\mathrm{m_i} v_s^2/2 \simeq 19.4\mathrm{m_e c^2}$, where $\mathrm{m_i}$(carbon mass) $= 12\mathrm{m_p}$(proton mass). Computing again the electrostatic potential at 200T which have a peak value $\mathrm{E_{max}} \approx 0.5\mathrm{E_0}$ and SAW extension $\mathrm{L} \sim 0.7\lambda \approx 1.4\pi\mathrm{c}/\omega$ it comes out to be $\mathrm{Ze}\Phi_{\mathrm{max}} \simeq 13.2\mathrm{m_e c^2}$ which is still below the threshold kinetic energy $\simeq 17.6 m_e c^2$

from the Eq.7.1, it comes out to be $\mathcal{E}_{\rm i} = 8.6{\rm m_e c^2}$, which is below than that of electrostatic potential energy of shock $Ze\Phi_{\rm max} \simeq 9.3{\rm m_e c^2}$. Thus the shock front reflect the front background ions and is clearly observable in phase space plot of Fig.7.5 (right frame). This simulation study confirms that carbon ions can be accelerated with some optimal initial ion temperature.

7.3 Simulation Results for $a_0 = 1$ amplitude

In order to find an "optimal ion temperature ${\rm T_i}$" resulting from a trade-off between beam monoenergeticity and efficient ion acceleration, we also performed the simulations at a bit lower relativistic laser intensity ${\rm I} = 1.4 \times 10^{18}{\rm W/cm^2}$ corresponding to laser pulse amplitude $a_0 = 1$ to check the effect on the "initial ion temperature window" for which we can efficiently reflect small number of ions without any significant wave loading, i.e. the SAW or shock velocity remains stable for much longer times and reflect ions of monoenergetic nature.

7.3.1 Warm ion simulations

Fig.7.6 shows the snapshot at a fixed time duration $200{\rm T}$ of the simulations performed by varying the initial ion temperatures in the ${\rm T_i} = 0 - 5{\rm keV}$ range. In a cold ion background as shown in Fig.7.6a, an ion nonlinear wave is launched into the target, in the form of SAW or multi-peak structures which undergo ion reflection by solitary pulsations. Due to the strong electric field oscillations, the ion reflection from the SAW front occurs at some certain instants along the propagation path and is quite a nonlinear phenomenon. Due to the multiple ion reflections of different energies, the spectrum of the latter is no longer monoenergetic (see Fig.7.7a). With a slight change in the initial ion temperature ${\rm T_i} = 10{\rm eV}$(Fig.7.6b), the time of event of ion reflection from SAW changes, such that the SAW starts

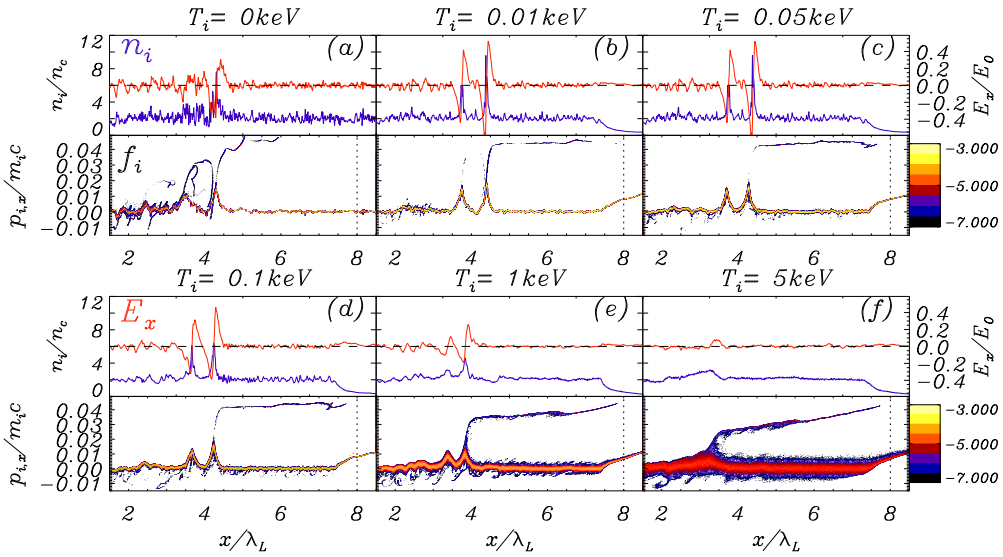

Figure 7.6: LP simulations: Snapshots of n_i, E_x and the contours of the $f_i(x, p_x)$ ion phase space in a $\log_{10}$-scale showing evolution of electrostatic shock wave and the ion dynamics at a fixed time interval of ${\rm t} = 200{\rm T_L}$, for six different cases: *(a:)* for an initial cold ions $T_i = 0$ keV, *(b:)* for an initial ion temperature $T_i = 0.01$ keV, *(c:)* for initial $T_i = 0.05$ keV, *(d:)* for initial $T_i = 0.1$ keV, *(e:)* for initial $T_i = 1$ keV, *(f:)* for initial $T_i = 5$ keV respectively. Simulation parameters are $a_0 = 1$, $n_e = 2n_c$, $8\mu m$ target and pulse duration $\tau = 60T$.

to reflect ions at early times, *i.e.* at $100\mathrm{T}$ than that of cold ions case in which the first ion reflection occurs around $150\mathrm{T}$. The leading SAW propagating with a velocity $v_s \approx 0.024c$, reflect small fraction of ions (1.5×10^{-5}) in the narrow spectral peak of $1.1\mathrm{MeV}$(Fig.7.7b) implies a conversion efficiency 2×10^{-6} of the $28\mathrm{J}$ pulse energy. We noticed that the electric field amplitude is quite stationary and the SAW is more stable in this case and thus reflects ions of constant velocity. As a consequence, with respect to "cold ions" case, the reflected ions are of monoenergetic nature. So even changing a slight initial ion temperature (i.e. $10\mathrm{eV}$), the ion reflection become "linear" in the sense that, at the given wave speed v_s, we always have some ions in the tail of the distribution function which can be reflected. Thus in order for just a minority of the ions to be reflected, the ion distribution must have an initial velocity spread.

We also performed other simulations in range of initial ion temperature from $\mathrm{Ti} = 20\mathrm{eV}$ to $100\mathrm{eV}$, two of which are shown in Fig.7.6$(\mathrm{c}-\mathrm{d})$ having initial ion temperature $50\mathrm{eV}$ and $100\mathrm{eV}$ respectively. We see that the number of reflected ions increases by increasing the initial ion temperature as there are now more ions in the range which the SAW front can easily pick and reflect to twice the shock velocity such that the fraction of reflected ions for $\mathrm{T_i} = 50\mathrm{eV}$ are $\sim 4\times10^{-5}$ which further increases to $\sim 6\times10^{-5}$ for $\mathrm{T_i} = 100\mathrm{eV}$. The increase of the ions number can be observed from the variation of the monoenergetic peak shown in Fig.7.7$(\mathrm{b}-\mathrm{d})$. So in this initial ion temperature range from $\mathrm{T_i} = 10\mathrm{eV} - 100\mathrm{eV}$, we observed that the fraction of reflected ions increases without much significant wave loading and the shock propagates almost at a constant velocity ($v_s \approx 0.025 \pm 0.001c$), reflect ions of monoenergetic nature which is also observed in the phase space plots of Fig.7.6$(\mathrm{b}-\mathrm{d})$ showing a straight line.

Fig.7.6(e-f) shows the result at initial $\mathrm{T_i} = 1\mathrm{keV}$ and $\mathrm{T_i} = 5\mathrm{keV}$ respectively having shock-like ion reflection. The ion reflection from the beginning is continuous and steady. The fraction of reflected ions is 14×10^{-5} for $\mathrm{T_i} = 1\mathrm{keV}$ which further increases to 30×10^{-5} for $\mathrm{T_i} = 5\mathrm{keV}$ and is much higher than that of previous warm ion results (Fig.7.6(b-d)). As a result, in order to reflect more ions, shock loses its energy, lags behind and is at $\approx 3.8\lambda$(Fig.7.6e) and 3.2λ(Fig.7.6f) for $\mathrm{T_i} = 1\mathrm{keV}$ and $\mathrm{T_i} = 5\mathrm{keV}$ respectively and the reflected ions have a broad energy spectrum (Fig.7.7(e-f)). The density peaks and the electrostatic field are clearly observable in case of $\mathrm{T_i} = 1\mathrm{keV}$(Fig.7.6e) which means that shock wave still exists and is propagating forward by reflecting ions while in case of $\mathrm{T_i} = 5\mathrm{keV}$ (Fig.7.6f), the density peaks and electrostatic field are completely lost by the time $200\mathrm{T}$ which means that the shock

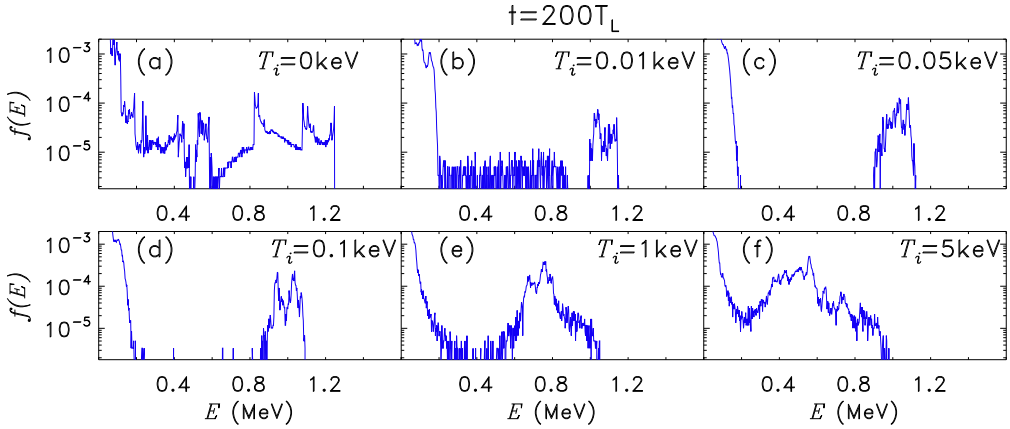

Figure 7.7: Snapshots at fixed $\mathrm{t} = 200\mathrm{T_L}$ time duration of the corresponding ion spectrum for six different cases as shown in Fig. 7.6 including only the ions in the region around the SAW or shock wave and excluding ions located near the target boundaries.

wave doesn't exist anymore and has damped out by losing all its energy to reflected ions.

Thus from the above simulation results described in sec. 7.3 and 7.4, at laser pulse amplitude of $a_0 = 4$ and $a_0 = 1$ respectively, we envision that at a lower amplitude $a_0 = 1$, the SAW is able to reflect monoenergetic ions even with a slight initial ion distribution, i.e. $\mathrm{T_i} = 10\mathrm{eV}$. For the $a_0 = 1$ case, the range of initial ion temperature window in which the SAW/shock reflect monoenergetic ions is large and is between $\mathrm{T_i} = 10\mathrm{eV} - 100\mathrm{eV}$. Now with the increase in laser intensity to $a_0 = 4$, more nonlinear and kinetic effects come into play and we observe a narrow range of initial ion temperature window, i.e. between $\mathrm{T_i} = 50\mathrm{eV} - 100\mathrm{eV}$ at which the SAW/shock remains stable for longer times and reflect ions of narrow energy spread. Further increasing the laser pulse amplitude to $a_0 = 16$, there is hardly any optimal initial ion temperature at which the reflected ions are monoenergetic. Although the number of reflected ions increase with increase in initial T_i, but because of other nonlinear effects and instabilities, the shock velocity does not remain constant for much time and loses its energy along the propagation path. Formation of monoenergetic ion spectra seems to be more favored for moderate values of laser amplitude $a_0 \sim 1 - 4$.

7.4 2D Simulation Results

We will now discuss our preliminary results of the 2D PIC simulations[3] performed at a laser amplitude of $a_0 = 1$ and for the "warm ions" having initial $\mathrm{T_i} = 0.1\mathrm{keV}$, keeping all the parameters same as that of Fig.7.6d, at lower resolution $\Delta x = \lambda/100$ and $\mathrm{N_p} = 100$ particle per cell. The simulation box is set as $140\mu\mathrm{m} \times 15\mu\mathrm{m}$ and the laser beam has Gaussian intensity distribution with the diameter of $5\mu\mathrm{m}$ in the transverse $\mathrm{y}-$ direction.

Fig.7.8 shows the proton density in the configuration space in which a double layer front in the form

[3] the simulations were made with the help of Andrea Sgattoni by the 2D PIC code "ALaDyn".

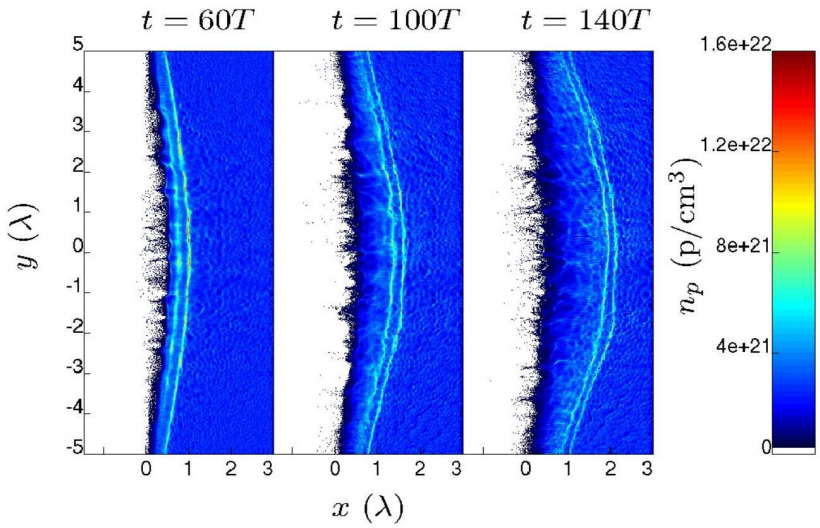

Figure 7.8: 2D PIC simulation: Snapshots at three different time durations of a shock wave, showing the proton density in the configuration space. The simulation is identical to the 1D simulation shown in Fig.7.6d at an initial $\mathrm{T_i} = 0.1\mathrm{keV}$. Laser pulse is P-polarized having waist $w_o = 5\lambda$ having $N_p = 100$ and $\Delta_x = \Delta_y = \lambda/100$, Simulation parameters are $a_0 = 1$, $\tau = 50\mathrm{T}$ and $\mathrm{n_e} = 2\mathrm{n_c}$.

of a damped or short shock wave is formed at the target front surface. We observed that the double layer front shows a transverse modulation with time. The development of transverse ripples on the shock front causes a different evolution of the shock with time and the shock slows down more quickly than that of 1D simulations (Fig.7.6d), resulting in broadening of the energy spectrum. When the ripple amplitude increases and becomes comparable to the shock wavelength, the instability may enter the nonlinear phase and the shock velocity starts to decrease. Lower frames of Fig.7.9 shows that modulations in the longitudinal momentum (p_x) as a function of the transverse coordinate (y) are present on the shock surface. As a consequence, the reflected ions from the shock front are of different energy and don't display a monoenergetic spectrum. The decrease in the shock speed can be observed from the slope of the reflected ions shown in Fig.7.9(upper frames), which broadens towards lower energy side.

The quick deceleration of shock speed might be explained in such a way that a small initial ion temperature produces the perturbation growth of ripples on the surface of a uniform target and interaction of a shock wave with periodic or localized perturbations ahead of the shock front distorts the shape of the shock front and can cause a Richtmyer-Meshkov (RM) type instability growth[168]. Now due to strong electron heating, the plasma is strongly perturbed. The shock wave which is formed within the bulk when hits the perturbed interface, ripples on the reflected and transmitted shock surface are induced which lead to the generation RM instability which is further driven by the shear velocity left by the rippled shocks at the plasma interface. Such interactions which lead to complicated flows may be caused by the variation in the density and pressure gradients. 2D simulations results have highlighted more clearly the growth of instabilities and perturbations which we didn't predict in our 1D simulation results, and 2D simulations at high numerical resolution are much demanding in order to study such interactions in more detail.

The evolution of RM instability has a close relationship with the compressibility of the system. Therefore, the combination of compressibility phenomenons such as the shock interaction with interface

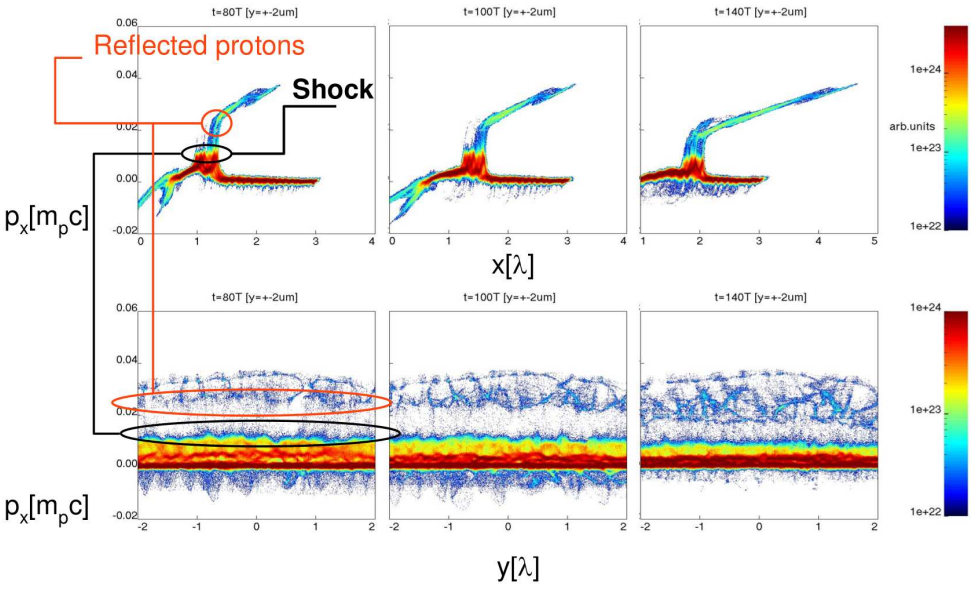

Figure 7.9: 2D PIC simulation: Snapshots at three different $60\mathrm{T}, 100\mathrm{T}$ and $140\mathrm{T}$ time durations of a shock wave. In this we cut the selection with a transverse coordinate $y = [-2 : 2]\lambda$ from the Fig.7.8. A strong modulation instability is present which slows down the shock and the reflected ions don't display a monoenergetic spectrum and becomes less energetic with time.

which includes the linear and nonlinear growth and subsequent transition to turbulence flow across a wide range of Mach numbers and is quite a challenging task for theorists and experimentalists[169]. 2D simulations results show the onset of rippling at the shock front. This rippling apparently leads to a broad ion spectrum, in contrast to the monoenergetic spectrum observed in 1D simulations for the same parameters. Work is needed to understand the instability mechanism which leads to deceleration of shock speed and to identify the possible stabilization strategies for monoenergetic ion acceleration.

7.5 Simulations with Circular Polarized Pulses

In this part, we will explain the effect of initial electron temperature ($\mathrm{T_e}$) on electrostatic SAW/shock generation and related ion acceleration, in an overdense plasma irradiated with intense femtosecond circular polarized (CP) pulses. The laser pulse is circularly polarized with a peak amplitude $a_0 = 1/\sqrt{2} = 0.71$, and have duration $\tau = 200\mathrm{T}$, the temporal profile is composed by $20\mathrm{T}$ long, $\sin^2$-like rising and falling ramps and a $180\mathrm{T}$ plateau. All the other parameters are same as of Fig.7.6a. Fig.7.10 shows the snapshots at a fixed time $200\mathrm{T}$ for different initial electron temperature $\mathrm{T_e}$. As we increase the initial $\mathrm{T_e}$, a distinct transition from the laser driven piston scenario with all ions being reflected to the collisionless electrostatic shock/soliton scenario having partial ion reflection has been found. The results in Fig.7.11($\mathrm{b-e}$) show that at low and finite value of initial $\mathrm{T_e}$, we can enhance the accelerated ion energy with respect to initially cold electrons (Fig.7.11a)

When the target is initially cold ($\mathrm{T_e} = 0$), in contrast to LP pulses in which the hot electrons are easily generated and we observe the generation of solitary acoustic waves (SAW) which propagate and reflect ions as studied in Fig.7.6a), for CP pulses, there is no effective heating mechanism and a "quasi-stationary double layer" structure is maintained for a longer time as shown in Fig.7.10a. Calculating the hole boring velocity, it comes out to be $v_{\mathrm{hb}} = 0.01c$ and is in good agreement with the HB formula (Eq.6.17 of Ch.6). Until the laser pulse is on, the ions are getting reflected continuously by the laser-

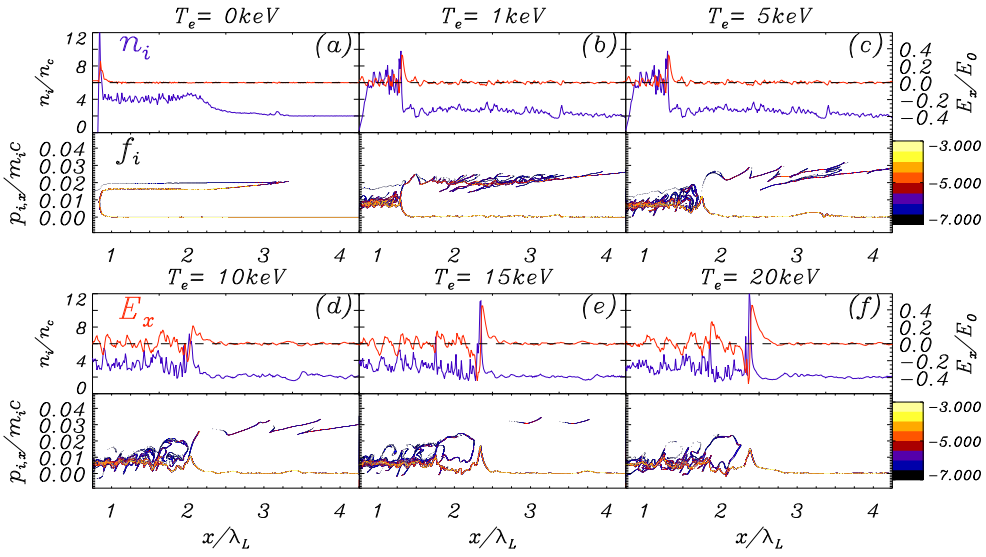

Figure 7.10: CP case: Snapshots at fixed $\mathrm{t} = 200\mathrm{T_L}$ time duration of the simulations performed at different initial $\mathrm{T_e}$ using CP pulses. Simulation parameters are $a_0 = 0.71$, $\tau = 200\mathrm{T}$ and $\mathrm{n_e} = 2\mathrm{n_c}$. The result shows that at some finite initial $\mathrm{T_e}$, electrostatic perturbations in form of solitary or shock waves can be generated also for circular polarized pulses.

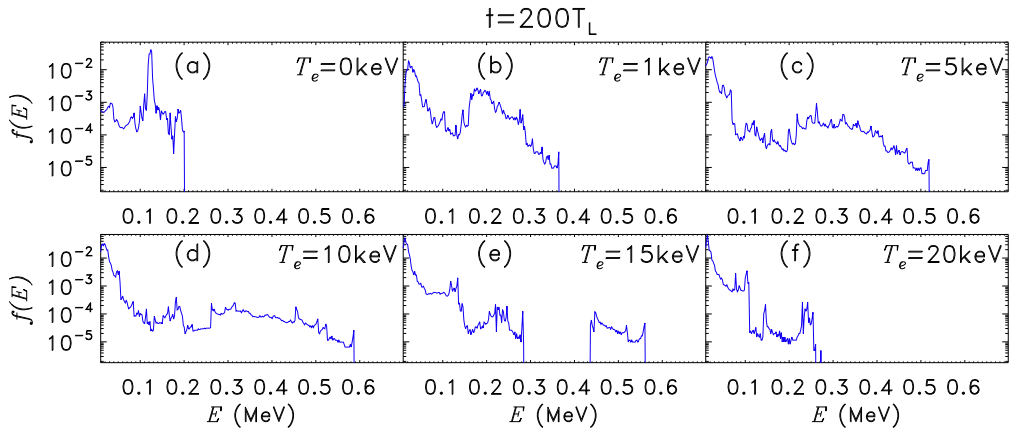

Figure 7.11: Snapshot of the corresponding ion spectrum for six different cases as shown in Fig.7.10 including only the ions in the region around the SAW or shock wave and excluding ions located near the target boundaries. The spectrum shows the increase of cutoff energy from $0.2\mathrm{MeV}$ to $0.6\mathrm{MeV}$

driven piston, to twice the piston velocity (equal to the hole boring (HB) velocity v_{hb}). As a result, we get two sharp peaks in the ion phase space having velocity $0.01\mathrm{c}$ and $0.02\mathrm{c}$, corresponding to about $0.1\mathrm{MeV}$ and $0.02\mathrm{MeV}$ energy in the ion spectrum. From previous studies of HB[95], we also know that the formation of the highest energy peak is related to wave breaking of the ion density spike at the laser-plasma interface. This HB acceleration mechanism is quite promising and successful for CP pulses since the final reflected ions are very monoenergetic as shown in Fig.7.11a.

Now, in a warm electron plasma $(\mathrm{T_e} > 0)$, wave breaking is affected by the electron temperature because the electron pressure prevents the formation of sharp density spikes. It is difficult to predict the consequences on the ion spectrum but qualitatively is not surprising that everything becomes more turbulent and the spectrum broadens up (Fig.7.11$(\mathrm{b}-\mathrm{d})$). As we know for soliton or shock generation, the Mach number $\mathrm{M} = v_s/\mathrm{c_s}$ plays a crucial role which indirectly is strongly dependent on $\mathrm{T_e}$. For CP pulses, when the initial $\mathrm{T_e} = 0$, the ions which are kept cold and immobile, will be influenced and reflected by the laser piston action and there is hardly any ion transmission occur within the plasma as the background ions remain unperturbed. Now with the rise of initial $\mathrm{T_e}$, we can see clearly in Fig.7.10$(\mathrm{b}-\mathrm{e})$ that some ions (clear from the ion density peaks) are getting "detached" from the hole boring front and then the non-linear phase space structures occurs between the density peaks. The ion reflection and trapping phenomenons can be clearly observed in the phase space in Fig.7.10$(\mathrm{c}-\mathrm{e})$. So as compared to the cold electron case, when the initial $\mathrm{T_e} > 0$, we observed some sort of ion-acoustic perturbations which can transmit and propagate in the plasma. We also observed that for $\mathrm{T_e} = 0$, the electric field is unipolar and positive (Fig.7.10a), while as we increase the initial $\mathrm{T_e}$, the electric fields turns to be bipolar and at initial $\mathrm{T_e} = 15 - 20\mathrm{keV}$ (Fig.7.10$(\mathrm{e}-\mathrm{f})$), the bipolar electric field is quite large and of sawtooth shape in which some ion acoustic waves start to propagate along the path. Fig.7.11 shows the reflected ion energy at different initial $\mathrm{T_e}$. We observed that with increase of initial $\mathrm{T_e}$, the final cut off energy of the reflected ions increases up-to $\sim 0.5\mathrm{MeV}$(Fig.7.11e) which is three times higher than that of cold electrons case(Fig.7.11a).

Now looking at the initial warm electrons case $(\mathrm{T_e} \neq 0)$, whether these perturbations in the ion phase space are merely some nonlinear ion-acoustic wave, or soliton/ shock wave, we will find out the Mach number (M). As for the $\mathrm{T_e} = 0$ case, in which the electron temperature is negligibly small, so the ion acoustic velocity $\mathrm{c_s} = \mathrm{ZT_e/m_i}$ will be very small or hardly zero. Thus the Mach number $\mathrm{M} = v_s/\mathrm{c_s}$ will be quite large and will exceed the critical value $\mathrm{M_{cr}} \simeq 6.5$ above which one does not

have a shock but a pure piston. This is what we observed here in $\mathrm{T_e} = 0$ case (Fig.7.10a), that the ions are accelerated by the laser driven piston. Thus formation of true shocks is inhibited for CP pulses at initial $\mathrm{T_e} = 0$ because of the reduced electron heating. Now for initial electron temperature, $\mathrm{T_e} = 1\mathrm{keV}$, the ion acoustic velocity has a finite value $\mathrm{c_s} = 0.001\mathrm{c}$. Calculating for the hole boring front velocity, which comes $v_{\mathrm{hb}} = 0.011c$. So the Mach number, $\mathrm{M} = 11$ has some finite value as compared to $\mathrm{T_e} = 0$ case. Increasing further the initial electron temperature $\mathrm{T_e} = 5\mathrm{keV}$ (Fig.7.10c), the ion acoustic speed increases to $\mathrm{c_s} = 0.0023\mathrm{c}$ and the Mach number decreases to $\mathrm{M} \approx 5.7$ and we may call the perturbation as a strong turbulent shock. Further increasing the initial $\mathrm{T_e} = 10\mathrm{keV}$ case, due to variation in the v_s and c_s, the Mach number decreases to $\mathrm{M} \approx 4$. Looking carefully at the ion phase space in Fig.7.10$(\mathrm{c} - \mathrm{d})$, we observed that as we increase the initial $\mathrm{T_e}$, the ion reflection from the shock front has decreased. For the higher Mach number, the shock is quite turbulent and reflects a continuous flow of ions of different energies. As the Mach number decreases, the shock no longer remains so strong to reflect ions in large fractions. Thus ion reflection decreases with decrease in Mach number. For initial $\mathrm{T_e} = 15\mathrm{keV}$, the Mach number further decreases to $\mathrm{M} \approx 1.7$, as a result the shock may transit to solitary waves and reflection occurs at some finite time intervals (Fig.7.10e). Further increase the $\mathrm{T_e} = 20\mathrm{keV}$, the ion reflection is completely stopped (Fig.7.10f). These simulation results infer that SAW or shock waves can be generated also with the CP pulses, having some initial electron distribution.

CHAPTER 8

Conclusion and Future work

8.1 Conclusion

In this section we will summarize the results of our thesis. In chapter 6 which is based on our investigation reported in Ref.[170], we have highlighted that a super-intense laser pulse interacting with an overdense plasma may drive the generation of both solitary and multiple- peak structures depending upon the laser pulse duration. The structures are generated due to the combined action of radiation pressure acting as a piston at the front surface ("hole boring" acceleration) and of the heating of electrons by the laser pulse, which occurs only for linear polarization. Possibly novel features observed in the dynamics of solitary structures include a strong collective oscillation of the electric field, and the "pulsed" nature of ion acceleration by reflection from the wave front. Monoenergetic peaks appear only as a result of such pulse acceleration in which the corresponding number of ions is relatively low. Acceleration of larger fractions of ions leads to quenching and slowing down of the wave, resulting in broadening of the energy spectrum. In particular, in a cold-ion background, wave loading effects prevent true shock wave formation and efficient monoenergetic acceleration.

The background ion distribution plays an important part in the ion acceleration dynamics. For instance, appearance of a "classic" shock wave-like structure with continuous reflection of ions from the wave front is observed only for some finite initial ion temperature. Comparing with previous work, we argue that the simple picture of "shock acceleration" as specular reflection from a moving front might not fully explain the features observed in simulations. There we envision a possibly novel mechanism of ion "surfing" acceleration in a nonlinear ion "wave" driven by pulsed radiation pressure acceleration at the laser-plasma interface. Conditions on laser and plasma parameters for the generation and stability of both shock- and soliton-like waves have been presented. Circularly polarized pulses drive "hole boring" or "pure piston" acceleration at the plasma surface, accelerated ions propagate through the plasma in a purely ballistic way causing almost no perturbation in the plasma and do not generate nonlinear solitary or shock waves in an initially cold plasma. In general, the dynamics of shock acceleration in the plasma bulk appears to be more complex than the simple picture of reflection from a moving wall.

Further investigations by 1D PIC simulations performed in chapter 7 prove that in a cold ion background plasma using LP pulses, ion reflection occur by solitary "pulsations". This is a "nonlinear" phenomenon and is not easy to control, whenever it occurs because it involves too many ions and sooner or later results in broadening of ion spectrum. Our study suggests that obtaining monoenergetic spectra is not straightforward, even when neglecting the side effect of the sheath field. We observe monoenergetic peaks in the simulations only when short-duration ion bunches are accelerated by solitary waves generated by the laser-plasma interaction or with the shock waves generated at some "optimal" initial ion temperature. Even with a slight increase of the initial ion temperature, ion reflection becomes "linear" in the sense that there always are some ions in the tail of the energy distribution function which can be reflected and there occurs "steady" ion reflection. For too high initial ion temperature, due to "continuous" ions reflection there are too much reflected ions and the shock loses its velocity more quickly, as a consequence we fall back in energy due to excessive wave loading. Our "warm ions" simulations suggests that

it can be possible for given laser and plasma parameters, to find an "optimal" ion temperature T_i resulting from a trade-off between beam monoenergeticity and efficiency, since a small number of reflected ions decrease wave loading. For the CP pulses, we envision that the role of initial electron temperature is quite important in generation of ion acoustic perturbation in form of soliton/shock waves. Both the electron and and ion energy distribution (determined by laser-plasma interaction) plays important role in shaping these coherent fields and accelerating ions. The electron energy determines their propagation velocity while the ion distribution affects how ions are reflected by these waves and can turn them from ion acoustic solitary waves to ion acoustic shocks.

8.2 Future work

The results presented in this thesis illustrate several interesting physical phenomena and provide a basis for further investigations as direct extensions of our work. In this regard, we suggest below some open problems which can be addressed in the future.

A key issue to be further clarified for potential application is whether having a monoenergetic spectrum is not compatible with efficiency, as suggested by our simulations and also by the recent experiment of Haberberger et al. [79]. In this latter experiment, it was suggested that the shock waves are not driven directly by radiation pressure but rather by electron heating, and that the particular structure of the CO_2 laser pulse plays an important role. The mechanism for both shock generation and acceleration need to be further studied by simulations, although simulating the actual experimental parameters is very demanding, mostly because of the long duration of the laser pulse. Although we showed by 1D PIC simulations that shock acceleration may be very monoenergetic in a proper range of the ion temperature, so far preliminary tests in 2D simulations have failed to obtain a similar spectrum. The reason seems to be related to the fast transverse rippling of the shock surface. An extended investigation in 2D will be needed to characterize such phenomenon and to give directions for its theoretical interpretation. The pulsations of the electric field we observed in solitary waves is a new phenomenon that is interesting on its own. A refinement of the very simple "thin foil" model presented in Sec.6.2.4 Ch.6, taking into account the drift and the detailed structure of the solitary wave, may also warrant further investigation.

Acknowledgement

Thanks to the committee of the “Galileo Galilei Graduate School” in the University of Pisa for selecting and giving me the opportunity to do my research here and providing me the fellowship to go on with the thesis work. My sincere thanks and heartfelt gratitude to **Dr. Andrea Macchi** and **Prof. Francesco Pegoraro**, for not only guiding me with his experience and knowledge but also for providing a very informal and relaxed environment. I am deeply indebted to them for their sagacious suggestions, constructive and healthy criticism, and perpetual encouragement that I have been perceiving throughout the PhD studies. It was indeed a great experience to work under their scholarly guidance and supervision. My warm thanks to *Dr Andrea Macchi* for his kind help and guidance from the first day of the PhD work. I am really grateful to him for timely help and sparing so much time to read critically my entire thesis to bring this into the present form.

I owe my deepest gratitude to Prof. Marco Borghesi from Queen University of Belfast and Dr. Matteo Passoni from Politecnico di Milano who give their precious time in reading this thesis and suggesting important points. I convey special acknowledgement to Ilaria Fierro for her indispensable help dealing with administration and bureaucratic matters during my stay.

My parents deserve special mention for their inseparable support and prayers. My Father, in the first place is the person who showed great confidence in me and encouraged me to come away from the home and pursue my PhD work. My Mother, is the one who raised me with her caring and gentle love. Thanks to my siblings and fiancee for being continuously supportive and caring. Last but not the least I would like to convey my deepest love and sincere thanks to the “GOD” for everything.

Bibliography

[1] T. H. Maiman, "Stimulated Optical Radiation in Ruby,"*Nature* **187** (Aug., 1960) 493–494.

[2] D. Strickland and G. Mourou, "Compression of amplified chirped optical pulses,"*Optics Communications* **55** (Oct., 1985) 447–449.

[3] M. Nisoli, S. Stagira, S. de Silvestri, O. Svelto, S. Sartania, Z. Cheng, M. Lenzner, C. Spielmann, and F. Krausz, "A novel-high energy pulse compression system: generation of multigigawatt sub-5-fs pulses,"*Applied Physics B: Lasers and Optics* **65** (Aug., 1997) 189–196.

[4] T. Tajima and J. M. Dawson, "Laser electron accelerator," *Phys. Rev. Lett.* **43** (1979) 267–270.

[5] P. Kaw, "Nonlinear Effects of Laser Propagation in Dense Plasmas,"*Applied Physics Letters* **15** (July, 1969) 16–18.

[6] M. S. Sodha, L. A. Patel, and R. P. Sharma, "Effect of nonlinear absorption on self-focusing of a laser beam in a plasma,"*Journal of Applied Physics* **49** (July, 1978) 3707–3713.

[7] S. J. Gitomer, R. D. Jones, F. Begay, A. W. Ehler, J. F. Kephart, and R. Kristal, "Fast ions and hot electrons in the laser–plasma interaction," *Physics of Fluids* **29** (1986) 2679–2688.

[8] F. N. Beg, A. R. Bell, A. E. Dangor, C. N. Danson, A. P. Fews, M. E. Glinsky, B. A. Hammel, P. Lee, P. A. Norreys, and M. Tatarakis, "A study of picosecond laser–solid interactions up to 10^{19} W cm^2," *Physics of Plasmas* **4** (1997) 447–457.

[9] K. Krushelnick *et al.*, "Multi–MeV Ion Production from High-Intensity Laser Interactions with Underdense Plasmas," *Phys. Rev. Lett.* **83** (1999) 737.

[10] E. L. Clark, K. Krushelnick, M. Zepf, F. N. Beg, M. Tatarakis, A. Machacek, M. I. K. Santala, I. Watts, P. A. Norreys, and A. E. Dangor, "Energetic Heavy-Ion and Proton Generation from Ultraintense Laser-Plasma Interactions with Solids," *Phys. Rev. Lett.* **85** (2000) 1654.

[11] A. Maksimchuk, S. Gu, K. Flippo, D. Umstadter, and V. Y. Bychenkov, "Forward ion acceleration in thin films driven by a high-intensity laser," *Phys. Rev. Lett.* **84** (2000) 4108–4111.

[12] R. A. Snavely *et al.*, "Intense high-energy proton beams from petawatt-laser irradiation of solids," *Phys. Rev. Lett.* **85** (2000) 2945–2948.

[13] G. F. Knoll, *Radiation detection and measurement*. Wiley, New York, 2nd ed. ed., 1989.

[14] S. C. Wilks, A. B. Langdon, T. E. Cowan, M. Roth, M. Singh, S. Hatchett, M. H. Key, D. Pennington, A. MacKinnon, and R. A. Snavely, "Energetic proton generation in ultra-intense laser-solid interactions," *Phys. Plasmas* **8** (2001) 542.

[15] G. A. Mourou, T. Tajima, and S. V. Bulanov, "Optics in the relativistic regime,"*Rev. Mod. Phys.* **78** (Apr, 2006) 309–371.

[16] P. Mulser and D. Bauer, *High Power Laser-Matter Interaction*, vol. 238 of *Springer Tracts in Modern Physics*. Springer, 2010.

[17] T. Baeva, S. Gordienko, and A. Pukhov, "Theory of high-order harmonic generation in relativistic laser interaction with overdense plasma,"*Physical Review E* **74** (Oct., 2006) 046404.

[18] H. Hora, "Theory of relativistic self-focusing of laser radiation in plasmas,"*Journal of the Optical Society of America (1917-1983)* **65** (Aug., 1975) 882–886.

[19] G. C. Das, J. Sarma, Y.-T. Gao, and C. Uberoi, "Dynamical behavior of the soliton formation and propagation in magnetized plasma,"*Physics of Plasmas* **7** (June, 2000) 2374–2380.

[20] F. Mottez, "Instabilities and Formation of Coherent Structures,"*Astrophysics and Space Science* **277** (June, 2001) 59–70.

[21] T. Umeda, "Generation of low-frequency electrostatic and electromagnetic waves as nonlinear consequences of beam-plasma interactions,"*Physics of Plasmas* **15** (June, 2008) 064502.

[22] R. A. Cairns *et al.*, "Electrostatic solitary structures in non-thermal plasmas," *Geophysical Research Letters* **22** (1995) 2709–2712.

[23] M. Buchanan and J. Dorning, "Nonlinear electrostatic waves in collisionless plasmas,"*Phys. Rev. E* **52** (Sept., 1995) 3015–3033.

[24] S. V. Bulanov, T. Z. Esirkepov, N. M. Naumova, F. Pegoraro, and V. A. Vshivkov, "Solitonlike Electromagnetic Waves behind a Superintense Laser Pulse in a Plasma,"*Phys. Rev. Lett.* **82** (Apr, 1999) 3440–3443.

[25] O. B. Shiryaev, "Regimes of the interactions of high-intensity plane electromagnetic waves with electron-ion plasmas,"*Physics of Plasmas* **15** (Jan., 2008) 012308.

[26] J. W. M. Paul, L. S. Holmes, M. J. Parkinson, and J. Sheffield, "Experimental Observations on the Structure of Collisionless Shock Waves in a Magnetized Plasma,"*Nature* **208** (Oct., 1965) 133–135.

[27] R. Z. Sagdeev, "Cooperative Phenomena and Shock Waves in Collisionless Plasmas," *Reviews of Plasma Physics* **4** (1966) 23.

[28] D. A. Tidman and N. A. Krall, *Shock Waves in Collisionless Plasmas*, ch. 6. Wiley/Interscience, New York, 1971.

[29] P. Gibbon, *Short Pulse Laser Interaction with Matter*. Imperial College Press, 2005.

[30] P. Maine, D. Strickland, P. Bado, M. Pessot, and G. Mourou, "Generation of ultrahigh peak power pulses by chirped pulse amplification,"*IEEE Journal of Quantum Electronics* **24** (Feb., 1988) 398–403.

[31] G. Cook, "Pulse compression-key to more efficient radar transmission," *IEEE Proc. IRE* **48** (1960) no. 310, .

[32] Wikipedia. `http://en.wikipedia.org/wiki/Chirped_pulse_amplification`.

[33] P. Maine, D. Strickland, M. Pessot, J. Squier, P. Bado, G. Mourou, and D. Harter, "Chirped pulse amplification: Present and future," *NASA STI/Recon Technical Report N* **89** (1988) 14434.

[34] S. Backus, C. G. Durfee, M. M. Murnane, and H. C. Kapteyn, "High power ultrafast lasers,"*Review of Scientific Instruments* **69** (Mar., 1998) 1207–1223.

[35] G. Chériaux and J.-P. Chambaret, "Ultra-short high-intensity laser pulse generation and amplification,"*Measurement Science and Technology* **12** (Nov., 2001) 1769–1776.

[36] S. C. Wilks, W. L. Kruer, M. Tabak, and A. B. Langdon, "Absorption of ultra-intense laser pulses," *Phys. Rev. Lett.* **69** (1992) 1383–1386.

[37] T.-Y. B. Yang, W. L. Kruer, A. B. Langdon, and T. W. Johnston, "Mechanisms for collisionless absorption of light waves obliquely incident on overdense plasmas with steep density gradients,"*Physics of Plasmas* **3** (July, 1996) 2702–2709.

[38] J. H. Eberly and A. Sleeper, "Trajectory and mass shift of a classical electron in a radiation pulse,"*Phys. Rev.* **176** (Dec, 1968) 1570–1573.

[39] L. D. Landau and E. M. Lifshitz, *The Classical Theory of Fields*. Elsevier, Oxford, 2nd ed., 1975.

[40] A. Macchi, "An introduction to ultraintense laser-plasma interactions," *Laser Plasma Lecture Notes* (2011) .

[41] T. W. B. Kibble, "Frequency shift in high-intensity compton scattering,"*Phys. Rev.* **138** (May, 1965) B740–B753.

[42] B. Quesnel and P. Mora, "Theory and simulation of the interaction of ultraintense laser pulses with electrons in vacuum,"*Phys. Rev. E* **58** (Sep, 1998) 3719–3732.

[43] D. Bauer, P. Mulser, and W. H. Steeb, "Relativistic Ponderomotive Force, Uphill Acceleration, and Transition to Chaos," *Phys. Rev. Lett.* **75** (1995) no. 25, 4622–4625.

[44] P. W. Milonni and J. H. Eberly, *Lasers*. Wiley-VCH, Oct., 1988.

[45] G. Schmidt and T. Wilcox, "Relativistic particle motion in nonuniform electromagnetic waves,"*Phys. Rev. Lett.* **31** (Dec, 1973) 1380–1383.

[46] S. Guérin, P. Mora, J. C. Adam, A. Héron, and G. Laval, "Propagation of ultraintense laser pulses through overdense plasma layers,"*Physics of Plasmas* **3** (July, 1996) 2693–2701.

[47] G.-Z. Sun, E. Ott, Y. C. Lee, and P. Guzdar, "Self-focusing of short intense pulses in plasmas," *Physics of Fluids* **30** (1987) 526–532.

[48] A. Macchi, S. Veghini, and F. Pegoraro, ""Light Sail" acceleration reexamined," *Phys. Rev. Lett.* **103** (2009) 085003.

[49] M. Tabak, J. Hammer, M. E. Glinsky, W. L. Kruer, S. C. Wilks, J. Woodworth, E. M. Campbell, M. D. Perry, and R. J. Mason, "Ignition and high gain with ultrapowerful lasers," *Physics of Plasmas* **1** (1994) 1626–1634.

[50] P. Mora, "Theoretical model of absorption of laser light by a plasma,"*Physics of Fluids* **25** (June, 1982) 1051–1056.

[51] R. Fedosejevs, R. Ottmann, R. Sigel, G. Kühnle, S. Szatmari, and F. P. Schäfer, "Absorption of femtosecond laser pulses in high-density plasma,"*Phys. Rev. Lett.* **64** (Mar, 1990) 1250–1253.

[52] W. L. Kruer, *The Physics of Laser Plasma Interactions*. Addison-Wesley, New York, 1988.

[53] V. L. Ginzburg, *Propagation of Electromagnetic waves in plasmas*, vol. 1. 1964.

[54] F. Brunel, "Not-so-resonant, resonant absorption," *Phys. Rev. Lett.* **59** (1987) 52–55.

[55] P. Gibbon and A. R. Bell, "Collisionless absorption in sharp-edged plasmas," *Phys. Rev. Lett.* **68** (1992) 1535–1538.

[56] W. L. Kruer and K. Estabrook, "$\mathbf{J} \times \mathbf{B}$ heating by very intense laser light," *Phys. Fluids* **28** (1985) 430.

[57] W. Rozmus and V. T. Tikhonchuk, "Skin effect and interaction of short laser pulses with dense plasmas,"*Phys. Rev. A* **42** (Dec, 1990) 7401–7412.

[58] M. D. Rosen, "Scaling laws for femtosecond laser-plasma interactions," vol. 1229 of *Society of Photo-Optical Instrumentation Engineers (SPIE)*, pp. 160–169. May, 1990.

[59] G. J. Pert, "Inverse bremsstrahlung in strong radiation fields at low temperatures,"*Phys. Rev. E* **51** (May, 1995) 4778–4789.

[60] M. Chaker, J. C. Kieffer, J. P. Matte, H. Pepin, P. Audebert, P. Maine, D. Strickland, P. Bado, and G. Mourou, "Interaction of a 1 psec laser pulse with solid matter," *Physics of Fluids B: Plasma Physics* **3** (1991) no. 1, 167–175.

[61] K. G. Estabrook, E. J. Valeo, and W. L. Kruer, "Two-dimensional relativistic simulations of resonance absorption,"*Physics of Fluids* **18** (Sept., 1975) 1151–1159.

[62] D. W. Forslund, J. M. Kindel, K. Lee, E. L. Lindman, and R. L. Morse, "Theory and simulation of resonant absorption in a hot plasma,"*Phys. Rev. A* **11** (Feb., 1975) 679–683.

[63] S. C. Wilks and W. L. Kruer, "Absorption of ultrashort, ultra-intense laser light by solids and overdense plasmas," *IEEE J. Quant. Electr.* **33** (1997) 1954–1968.

[64] G. Malka and J. L. Miquel, "Experimental confirmation of ponderomotive-force electrons produced by an ultrarelativistic laser pulse on a solid target,"*Phys. Rev. Lett.* **77** (Jul, 1996) 75–78.

[65] K. B. Wharton *et al.*, "Experimental measurements of hot electrons generated by ultraintense ($10^{19}\mathbf{W/cm^2}$) laser-plasma interactions on solid-density targets," *Phys. Rev. Lett.* **81** (1998) 822–825.

[66] M. H. Key *et al.*, "Hot electron production and heating by hot electrons in fast ignitor research," *Physics of Plasmas* **5** (1998) 1966–1972.

[67] Z.-M. Sheng, Y. Sentoku, K. Mima, J. Zhang, W. Yu, and J. Meyer-Ter-Vehn, "Angular Distributions of Fast Electrons, Ions, and Bremsstrahlung x/ γ-Rays in Intense Laser Interaction with Solid Targets,"*Physical Review Letters* **85** (Dec., 2000) 5340–5343.

[68] P. M. Nilson *et al.*, "Scaling hot-electron generation to high-power, kilojoule-class laser-solid interactions," *Phys. Rev. Lett.* **105** (2010) 235001.

[69] H. Chen, S. C. Wilks, W. L. Kruer, P. K. Patel, and R. Shepherd, "Hot electron energy distributions from ultraintense laser solid interactions," *Physics of Plasmas* **16** (2009) 020705.

[70] M. Roth *et al.*, "Fast ignition by intense laser-accelerated proton beams,"*Phys. Rev. Lett.* **86** (Jan, 2001) 436–439.

[71] S. Bulanov, T. Esirkepov, V. Khoroshkov, A. Kuznetsov, and F. Pegoraro, "Oncological hadrontherapy with laser ion accelerators," *Physics Letters A* **299** (2002) no. 2–3, 240–247.

[72] M. Allen, P. K. Patel, A. Mackinnon, D. Price, S. Wilks, and E. Morse, "Direct Experimental Evidence of Back-Surface Ion Acceleration from Laser-Irradiated Gold Foils," *Phys. Rev. Lett.* **93** (2004) 265004.

[73] J. Fuchs *et al.*, "Comparison of Laser Ion Acceleration from the Front and Rear Surfaces of Thin Foils," *Phys. Rev. Lett.* **94** (2005) 045004.

[74] A. Pukhov, "Strong field interaction of laser radiation,"*Reports on Progress in Physics* **66** (Jan., 2003) 47–101.

[75] T. Esirkepov, M. Borghesi, S. V. Bulanov, G. Mourou, and T. Tajima, "Highly Efficient Relativistic-Ion Generation in the Laser-Piston Regime," *Phys. Rev. Lett.* **92** (2004) 175003.

[76] I. N. Ross, P. Matousek, M. Towrie, A. J. Langley, and J. L. Collier, "The prospects for ultrashort pulse duration and ultrahigh intensity using optical parametric chirped pulse amplifiers,"*Optics Communications* **144** (Feb., 1997) 125–133.

[77] J. Denavit, "Absorption of high-intensity subpicosecond lasers on solid density targets," *Phys. Rev. Lett.* **69** (1992) 3052–3055.

[78] L. O. Silva, M. Marti, J. R. Davies, R. A. Fonseca, C. Ren, F. S. Tsung, and W. B. Mori, "Proton shock acceleration in laser-plasma interactions," *Phys. Rev. Lett.* **92** (2004) 015002.

[79] D. Haberberger *et al.*, "Collisionless shocks in laser-produced plasma generate monoenergetic high-energy proton beams,"*Nature Physics* **8** (Jan., 2012) 95–99.

[80] A. J. Kemp and H. Ruhl, "Multispecies ion acceleration off laser-irradiated water droplets," *Physics of Plasmas* **12** (2005) no. 3, 033105.

[81] K. Flippo *et al.*, "Laser-driven ion accelerators: Spectral control, monoenergetic ions and new acceleration mechanisms,"*Laser and Particle Beams* **25** (Feb., 2007) 3.

[82] B. M. Hegelich *et al.*, "MeV Ion Jets from Short-Pulse-Laser Interaction with Thin Foils," *Phys. Rev. Lett.* **89** (2002) 085002.

[83] P. K. Patel *et al.*, "Isochoric heating of solid-density matter with an ultrafast proton beam," *Phys. Rev. Lett.* **91** (2003) 125004.

[84] S. Kar *et al.*, "Plasma Jets Driven by Ultraintense-Laser Interaction with Thin Foils," *Phys. Rev. Lett.* **100** (2008) 225004.

[85] J. Fuchs *et al.*, "Laser-Foil Acceleration of High-Energy Protons in Small-Scale Plasma Gradients," *Phys. Rev. Lett.* **99** (2007) 015002.

[86] B. M. Hegelich *et al.*, "Laser acceleration of quasi-monoenergetic MeV ion beams," *Nature* **439** (2006) 441.

[87] B. J. Albright, L. Yin, B. M. Hegelich, K. J. Bowers, T. J. T. Kwan, and J. C. Fernández, "Theory of Laser Acceleration of Light-Ion Beams from Interaction of Ultrahigh-Intensity Lasers with Layered Targets," *Phys. Rev. Lett.* **97** (2006) 115002.

[88] A. P. L. Robinson, A. R. Bell, and R. J. Kingham, "Effect of target composition on proton energy spectra in ultraintense laser-solid interactions,"*Phys. Rev. Lett.* **96** (Jan, 2006) 035005.

[89] M. Passoni and M. Lontano, "One-dimensional model of the electrostatic ion acceleration in the ultraintense laser-solid interaction," *Laser and Particle Beams* **22** (2004) 163–169.

[90] A. V. Gurevich, L. V. Pariiskaya, and L. P. Pitaevskii *Sov. Phys. JETP* **22** (1966) 449.

[91] J. E. Crow, P. L. Auer, and J. E. Allen, "The expansion of a plasma into a vacuum," *Journal of Plasma Physics* **14** (1975) 65–76.

[92] L. Landau and E. Lifshitz, *Fluid mechanics*. Course of theoretical physics. Butterworth-Heinemann, 1987.

[93] M. Passoni and M. Lontano, "Theory of light-ion acceleration driven by a strong charge separation," *Phys. Rev. Lett.* **101** (2008) 115001.

[94] A. P. L. Robinson, M. Zepf, S. Kar, R. G. Evans, and C. Bellei, "Radiation pressure acceleration of thin foils with circularly polarized laser pulses," *New J. Phys.* **10** (2008) 013021.

[95] A. Macchi, F. Cattani, T. V. Liseykina, and F. Cornolti, "Laser acceleration of ion bunches at the front surface of overdense plasmas," *Phys. Rev. Lett.* **94** (2005) 165003.

[96] A. Macchi, S. Veghini, T. V. Liseykina, and F. Pegoraro, "Radiation pressure acceleration of ultrathin foils," *New Journal of Physics* **12** (2010) 045013.

[97] G. Marx, "Interstellar vehicle propelled by terrestrial laser beam," *Nature* **211** (1966) 22–23.

[98] J. D. Jackson, *Classical Electrodynamics*, ch. 7.3. John Wiley and Sons, Inc., 3rd ed., 1998.

[99] Y. Sentoku, T. E. Cowan, A. Kemp, and H. Ruhl, "High energy proton acceleration in interaction of short laser pulse with dense plasma target,"*Physics of Plasmas* **10** (May, 2003) 2009–2015.

[100] E. L. Clark *et al.*, "Measurements of Energetic Proton Transport through Magnetized Plasma from Intense Laser Interactions with Solids," *Phys. Rev. Lett.* **84** (2000) 670–673.

[101] M. Zepf *et al.*, "Proton acceleration from high-intensity laser interactions with thin foil targets,"*Phys. Rev. Lett.* **90** (Feb, 2003) 064801.

[102] H. Habara *et al.*, "Ion acceleration from the shock front induced by hole boring in ultraintense laser-plasma interactions,"*Phys. Rev. E* **70** (Oct, 2004) 046414.

[103] A. Macchi, M. Passoni, and M. Borghesi, "Superintense laser-plasma ion acceleration," *Rev. Mod. Phys.* **to be published** (2012) .

[104] T. Schlegel *et al.*, "Relativistic laser piston model: Ponderomotive ion acceleration in dense plasmas using ultraintense laser pulses,"*Physics of Plasmas* **16** (Aug., 2009) 083103.

[105] A. P. L. Robinson, P. Gibbon, M. Zepf, S. Kar, R. G. Evans, and C. Bellei, "Relativistically correct hole-boring and ion acceleration by circularly polarized laser pulses," *Plasma Phys. Contr. Fusion* **51** (2009) 024004.

[106] J. F. L. Simmons and C. R. McInnes, "Was Marx right? or How efficient are laser driven interstellar spacecraft?," *Am. J. Phys.* **61** (1993) 205–207.

[107] S. F. Martins, R. A. Fonseca, L. O. Silva, and W. B. Mori, "Ion dynamics and acceleration in relativistic shocks," *The Astrophysical Journal Letters* **695** (2009) L189.

[108] D. W. Forslund and C. R. Shonk, "Formation and Structure of Electrostatic Collisionless Shocks," *Phys. Rev. Lett.* **25** (1970) 1699–1702.

[109] D. W. Forslund and J. P. Freidberg, "Theory of Laminar Collisionless Shocks," *Phys. Rev. Lett.* **27** (1971) 1189–1192.

[110] L. Romagnani *et al.*, "Observation of collisionless shocks in laser-plasma experiments,"*Phys. Rev. Lett.* **101** (Jul, 2008) 025004.

[111] M. S. Wei *et al.*, "Ion acceleration by collisionless shocks in high-intensity-laser–underdense-plasma interaction," *Phys. Rev. Lett.* **93** (2004) 155003.

[112] A. Ravasio *et al.*, "Proton radiography of a shock-compressed target," *Phys. Rev. E* **82** (2010) 016407.

[113] R. J. Taylor, D. R. Baker, and H. Ikezi, "Observation of collisionless electrostatic shocks,"*Phys. Rev. Lett.* **24** (Feb, 1970) 206–209.

[114] G. Sorasio, M. Marti, R. Fonseca, and L. O. Silva, "Very high mach-number electrostatic shocks in collisionless plasmas," *Phys. Rev. Lett.* **96** (2006) 045005.

[115] L. Romagnani *et al.*, "Dynamics of electric fields driving laser acceleration of multi–MeV protons," *Phys. Rev. Lett.* **95** (2005) 195001.

[116] Emmanuel d'Humières, E. Lefebvre, L. Gremillet, and V. Malka, "Proton acceleration mechanisms in high-intensity laser interaction with thin foils," *Physics of Plasmas* **12** (2005) 062704.

[117] M. Chen *et al.*, "Collisionless electrostatic shock generation and ion acceleration by ultraintense laser pulses in overdense plasmas," *Physics of Plasmas* **14** (2007) 053102.

[118] A. Zhidkov, J. Koga, A. Sasaki, and M. Uesaka, "Radiation damping effects on the interaction of ultraintense laser pulses with an overdense plasma," *Phys. Rev. Lett.* **88** (2002) 185002.

[119] F. F. Chen, *Introduction to plasma physics and controlled fusion*, vol. 1. 1974.

[120] R. A. Treumann and C. H. Jaroschek, "Fundamentals of Non-relativistic Collisionless Shock Physics: II. Basic Equations and Models,"*ArXiv e-prints* (May, 2008) , arXiv:0805.2162.

[121] S. Novikov, S. V. Manakov, L. P. Pitaevskii, and V. E. Zakharov, *Theory of solitons: The inverse scattering method*. 1984.

[122] N. J. Zabusky and C. J. Galvin, "Shallow-water waves, the Korteweg-de Vries equation and solitons," *Journal of Fluid Mechanics* **47** (1971) 811–824.

[123] J. I. Vette, "Summary of Particle Populations in the Magnetosphere," in *Particles and Field in the Magnetosphere*, B. M. McCormack & A. Renzini, ed., vol. 17 of *Astrophysics and Space Science Library*, p. 305. 1970.

[124] M. Borghesi *et al.*, "Macroscopic Evidence of Soliton Formation in Multiterawatt Laser-Plasma Interaction," *Phys. Rev. Lett.* **88** (2002) 135002.

[125] M. Borghesi *et al.*, "Electric field detection in laser-plasma interaction experiments via the proton imaging technique," *Physics of Plasmas* **9** (2002) no. 5, 2214–2220.

[126] H. Washimi and T. Taniuti, "Propagation of ion-acoustic solitary waves of small amplitude,"*Phys. Rev. Lett.* **17** (Nov, 1966) 996–998.

[127] N. N. Rao, P. K. Shukla, and M. Y. Yu, "Dust-acoustic waves in dusty plasmas,"*phys of plasmas* **38** (Apr., 1990) 543–546.

[128] G. C. Das and S. N. Paul, "Ion-acoustic solitary waves in relativistic plasmas,"*Physics of Fluids* **28** (Mar., 1985) 823–825.

[129] Y. Nejoh and H. Sanuki, "Large amplitude Langmuir and ion-acoustic waves in a relativistic two-fluid plasma,"*Physics of Plasmas* **1** (July, 1994) 2154–2162.

[130] K. Nishikawa and P. K. Kaw, "Propagation of solitary ion acoustic waves in inhomogeneous plasmas,"*Physics Letters A* **50** (Jan., 1975) 455–456.

[131] K. Mima, T. Ohsuga, H. Takabe, K. Nishihara, T. Taijma, E. Zaidman, and W. Horton, "Wakeless triple-soliton accelerator,"*Phys. Rev. Lett.* **57** (Sep, 1986) 1421–1424.

[132] P. K. Kaw, A. Sen, and T. Katsouleas, "Nonlinear 1d laser pulse solitons in a plasma,"*Phys. Rev. Lett.* **68** (May, 1992) 3172–3175.

[133] J. F. McKenzie and T. B. Doyle, "A unified view of acoustic-electrostatic solitons in complex plasmas,"*New Journal of Physics* **5** (Mar., 2003) 26.

[134] G. C. Das, B. Karmakar, and S. N. Paul, "Propagation of solitary waves in relativistic plasmas,"*IEEE Transactions on Plasma Science* **16** (Feb., 1988) 22–26.

[135] R. K. Roychoudhury and S. Bhattacharyya, "Ion-acoustic solitary waves in relativistic plasmas,"*Physics of Fluids* **30** (Aug., 1987) 2582–2584.

[136] H. Ikezi, R. J. Taylor, and D. R. Baker, "Formation and Interaction of Ion-Acoustic Solitions,"*Physical Review Letters* **25** (July, 1970) 11–14.

[137] H. Ikezi, "Experiments on ion-acoustic solitary waves,"*Physics of Fluids* **16** (Oct., 1973) 1668–1675.

[138] N. Sato, H. Ikezi, N. Takahashi, and Y. Yamashita, "Large-Amplitude Ion Acoustic Waves in a Plasma,"*Physical Review* **183** (July, 1969) 278–287.

[139] H. Ikezi and Y. Kiwamoto, "Observations of Nonlinear Landau Damping of Ion-Acoustic Waves,"*Physical Review Letters* **27** (Sept., 1971) 718–721.

[140] H. Ikezi, Y. Kiwamoto, K. Nishikawa, and K. Mima, "Trapped-Ion Instabilities in Ion-Acoustic Wave,"*Physics of Fluids* **15** (Sept., 1972) 1605–1612.

[141] H. Ikezi, T. Kamimura, M. Kako, and K. E. Lonngren, "Laminar electrostatic shock waves generated by an ion beam,"*Physics of Fluids* **16** (Dec., 1973) 2167–2175.

[142] R. A. Treumann and C. H. Jaroschek, "Fundamentals of Non-relativistic Collisionless Shock Physics: I. The Shock Problem,"*ArXiv e-prints* (May, 2008) , arXiv:0805.2132.

[143] R. A. Treumann, "Fundamentals of collisionless shocks for astrophysical application, 1. Non-relativistic shocks,"*The Astronomy and Astrophysics Review* **17** (Dec., 2009) 409–535.

[144] S. S. Moiseev and R. Z. Sagdeev, "Shock Waves in a Rarefied Plasma in a Weak Magnetic Field,"*Soviet Physics Doklady* **7** (Mar., 1963) 813.

[145] R. C. Davidson, N. A. Krall, K. Papadopoulos, and R. Shanny, "Electron heating by electron-ion beam instabilities,"*Phys. Rev. Lett.* **24** (Mar, 1970) 579–582.

[146] D. Biskamp and H. Welter, "Ion Heating in High-Mach-Number, Oblique, Collisionless Shock Waves,"*Physical Review Letters* **28** (Feb., 1972) 410–413.

[147] A. R. Bell, P. Choi, A. E. Dangor, O. Willi, D. A. Bassett, and C. J. Hooker, "Collisionless shock in a laser-produced ablating plasma,"*Phys. Rev. A* **38** (Aug, 1988) 1363–1369.

[148] M. J. Ablowitz and H. Segur, "Solitons and the inverse scattering transform," *Philadelphia, PA, Society for Industrial and Applied Mathematics (SIAM Studies in Applied Mathematics, No. 4), 1981.Ch.4* **4** (1981) p276.

[149] T. Taniuti, "Reductive Perturbation Method and Far Fields of Wave Equations," *Progress of Theoretical Physics Supplement* **55** (1974) 1–35.

[150] S. V. Vladimirov and M. Y. Yu, "Nonlinear ion-acoustic waves in a collisional plasma,"*Phys. Rev. E* **48** (Sep, 1993) 2136–2139.

[151] B. Das and P. Chatterjee, "Speed and shape of solitary waves in relativistic warm plasma," *Czechoslovak Journal of Physics* **56** (2006) 389–398.

[152] L. Landau *J.Phys. USSR* **10** (1946) no. 25, .

[153] R. D. Blandford and K. S. Thorne, *APPLICATIONS OF CLASSICAL PHYSICS*. California Institute of technology, Ch.20, 2004-2005.

[154] V. P. Maslov and M. V. Fedoryuk, "The Linear Theory of Landau Damping,"*Sbornik: Mathematics* **55** (Feb., 1986) 437–465.

[155] A. Bergmann and P. Mulser, "Breaking of resonantly excited electron plasma waves," *Phys. Rev. E* **47** (1993) 3585–3589.

[156] J. Krall, G. Joyce, and E. Esarey, "Vlasov simulations of very-large-amplitude-wave generation in the plasma wake-field accelerator,"*Phys. Rev. A* **44** (Nov, 1991) 6854–6861.

[157] F. Califano, F. Pegoraro, and S. V. Bulanov, "Spatial structure and time evolution of the weibel instability in collisionless inhomogeneous plasmas,"*Phys. Rev. E* **56** (Jul, 1997) 963–969.

[158] C. K. Birdsall and A. B. Langdon, *Plasma Physics Via Computer Simulation*. Institute of Physics, Bristol, 1991.

[159] T. H. Dupree, "Kinetic Theory of Plasma and the Electromagnetic Field,"*Physics of Fluids* **6** (Dec., 1963) 1714–1729.

[160] P. Mora, "Plasma expansion into a vacuum," *Phys. Rev. Lett.* **90** (2003) 185002.

[161] A. Zhidkov, M. Uesaka, A. Sasaki, and H. Daido, "Ion acceleration in a solitary wave by an intense picosecond laser pulse," *Phys. Rev. Lett.* **89** (2002) 215002.

[162] A. Macchi, F. Ceccherini, F. Cornolti, S. Kar, and M. Borghesi, "Electric field dynamics and ion acceleration in the self-channeling of a superintense laser pulse," *Plasma Physics and Controlled Fusion* **51** (2009) 024005.

[163] S. V. Bulanov, N. M. Naumova, and F. Pegoraro, "Interaction of an ultrashort, relativistically strong laser pulse with an overdense plasma,"*Physics of Plasmas* **1** (Mar., 1994) 745–757.

[164] T. V. Liseikina and A. Macchi, "Features of ion acceleration by circularly polarized laser pulses," *Appl. Phys. Lett.* **91** (2007) 171502.

[165] C. A. J. Palmer *et al.*, "Monoenergetic proton beams accelerated by a radiation pressure driven shock," *Phys. Rev. Lett.* **106** (2011) 014801.

[166] K. U. Akli *et al.*, "Laser Heating of Solid Matter by Light-Pressure-Driven Shocks at Ultrarelativistic Intensities," *Phys. Rev. Lett.* **100** (2008) 165002.

[167] A. Henig *et al.*, "Laser-Driven Shock Acceleration of Ion Beams from Spherical Mass-Limited Targets," *Phys. Rev. Lett.* **102** (2009) 095002.

[168] S. Atzeni and J. M. ter Vehn, *The Physics of inertial Fusion*. Oxford Science Publications, 2004.

[169] M. Brouillette, "The richtmyer-meshkov instability," *Annual Review of Fluid Mechanics* **34** (2002) 445–468.

[170] A. Macchi, A. S. Nindrayog, and F. Pegoraro, "Solitary versus shock wave acceleration in laser-plasma interactions,"*Phys. Rev. E* **85** (Apr, 2012) 046402.